

**OREGON HEALTH & SCIENCE UNIVERSITY
SCHOOL OF MEDICINE – GRADUATE STUDIES**

DEVELOPMENT OF CHEMICAL BIOLOGY TOOLS TO FOLLOW SIGNAL
TRANSDUCTION IN CELLS

By

Alix Thomas

A DISSERTATION

Presented to the Chemical Physiology and
Biochemistry program and the Oregon Health
& Science University
School of Medicine in
partial fulfillment of
the requirements for the degree of

Doctor of Philosophy

September 2024

Table of Contents

LIST OF FIGURES	iv
LIST OF ABBREVIATIONS	v
ACKNOWLEDGEMENTS.....	vii
ABSTRACT.....	viii
Chapter 1: Introduction.....	1
INVENTING NEW CHEMICAL BIOLOGY TOOLS	1
OPTICALLY ACTIVE INDICATOR OF SIGNAL TRANSDUCTION	4
Fluorescent dyes as indicators.....	4
Fluorescent proteins.....	6
Self-labeling fluorescent indicators	12
Bioluminescence-based indicators	16
De novo design of ligand binding protein	17
MODIFICATION OF BIOMOLECULES WITH BIORTHOGONAL CHEMICAL GROUPS.....	19
Cycloadditions	19
Photo-sensitive chemical tools.....	21
Genetic code expansion.....	25
THE PUZZLE OF PARP1 DEPENDENT ADP-RIBOSYLATION: NEED FOR TOOLS	27
PARP1 role in DNA damage response.....	28
PARP1-catalyzed ADP-ribosylation linkages	29
State of the art tools to detect ADP-ribosylation	30
OVERVIEW OF GPCRS AND CANNABINOID RECEPTOR 1.....	32
G protein-coupled receptors and biased signaling	32

Cannabinoid receptor 1 signaling	34
CHEMICAL BIOLOGY TOOLS TO HELP UNRAVEL INDIVIDUAL LIPID FUNCTION	37
Engineering tools to track lipid in cells	38
Bifunctional lipids for lipid visualization and interactome screen	41
Chapter 2: FRET-based biosensors for measuring dynamic changes in ADP- ribosylation.....	44
ABSTRACT.....	44
INTRODUCTION	45
MATERIAL AND METHODS.....	47
RESULTS.....	54
DISCUSSION.....	71
OUTLOOK AND FUTURE WORK	74
Chapter 3: Cannabinoid Receptor Signaling is Dependent on Sub-Cellular Location.....	78
ABSTRACT.....	78
INTRODUCTION	79
MATERIAL AND METHODS.....	82
RESULTS.....	89
DISCUSSION	106
OUTLOOK AND FUTURE WORK	110
Chapter 4: Trifunctional fatty acid derivatives: PE’s mitochondrial interactome	112
ABSTRACT.....	112
INTRODUCTION	112
MATERIALS AND METHODS	115
RESULTS.....	124
DISCUSSION.....	140
OUTLOOK AND FUTURE WORK	146
Concluding remarks.....	151
Appendix.....	152
FIGURES	152
TABLE INTERACTOME	159
References.....	178

LIST OF FIGURES

Figure 1-1. Representation of the change in conformation of a cAMP sensor.....	8
Figure 1-2. Structure of calcium saturated jGCaMP8.....	10
Figure 1-3. Representation of SNIFIT-GABA	14
Figure 1-4. Representation of a coumarin-caged lipid	23
Figure 1-5. Upon DNA damage, PARP1 is activated and, in complex with HPF1, initiate ADP-ribosylation.....	29
Figure 1-6..Representation of the heterotrimeric G protein activation by a GPCR	32
Figure 1-7. Tagged lipid derivatives.	41
Figure2-1. Sensor design of pARS.	54
Figure 2-2. A. Fluorescence emission spectrum of pARS.....	57
Figure 2-3. PARP1 kinetics	58
Figure 2-4. pARS in live cell.....	60
Figure 2-5. pARS Semi-quantification in live cell	62
Figure 2-6. Bar graph representing the maximum FRET ratio (CFP/YFP) of HeLa cells transfected with 32 different variant (cassettes).....	63
Figure 2-7. A. Sensor design of mARS	68
Figure 2-8. mARS characterization	71
Figure 2-9. Tentative representation of WWE domains (PDB 3V31) bond to poly-ADP-ribose (PAR).	75
<i>Figure 3-1. Immuno-fluorescence experiment comparing CB1 expression between untransfected (WT) or CMVCB1 (+/CB1) HeLa cells.</i>	<i>89</i>
Figure 3-2. Expression level and N-terminal modification direct CB1's sub-cellular localization and impact downstream cAMP signaling	90
Figure 3-3 Quantification of CB1 expression constructs	93
Figure 3-4. Location bias drives emCB1 to couple to G α i/o and pmCB1 to couple to G α s.....	94
Figure 3-5. Introducing a clickable TCO*A in CB1 without interfering with signaling or trafficking provides an alternative method to distinguish EM-CB1 to PM-CB1	99
Figure 3-6. CB1 activation leads to a transient increase in calcium levels via influx of extracellular calcium and intracellular release	102
<i>Figure 3-7. Confocal micrographs showing HeLa Kyoto cells transfected with CB1-F180.....</i>	<i>103</i>
Figure 3-8. Additional evidence from CB1-F180 post-translational labeling and change in [cAMP] levels shows that CB1 localization in endo-membrane affects G-protein coupling	104
Figure 3-9. Tentative representation of the contradictory effect of activated CB1 on cAMP levels depending on receptor location.	105

Scheme 4-1. Synthesis of trifunctional PE.....	124
Scheme 4-2 Synthesis of trifunctional PA.....	124
Figure 4-1 TF-lipid loading.....	126
Figure 4-2 TF-lipid TLC.....	127
Figure 4-4 TF-PE subcellular localization.....	133
Figure 4-5. Proteomic analysis.....	135
Figure 4-6. Comparison of PE and PA.....	138
Figure 4-7 PE protein hits.....	140

LIST OF ABBREVIATIONS

PeT	Photoinduced electron transfer
GFP	Green fluorescent protein
YFP	Yellow fluorescent protein
CFP	Cyan fluorescent protein
CB1	Cannabinoid receptor 1
FRET	Förster resonance energy transfer
cAMP	Cyclic adenosine monophosphate
AC	Adenylyl cyclase
FP	Fluorescent protein
PKA	Protein kinase A
FHA	Forkhead associated domain
cpFP	Circularly permuted fluorescent protein
GPCR	G protein-coupled receptors
GRK	G protein-coupled receptor kinase
BiFC	Bimolecular fluorescent complementation
hAGT	<i>O</i> ⁶ -alkylguanine-DNA alkyltransferase
BRET	Bioluminescence resonance energy transfer
RLuc	<i>Renilla</i> luciferase
CuAAC	Copper-catalyzed azide–alkyne cycloaddition
IEDAC	Inverse electron-demand Diels-Alder cycloaddition
ICL	Intracellular loop
LTP	Lipid transport proteins
TCO	Trans-cyclooctene
DEAC	7-diethylamino coumarin
DAG	Diacylglycerol

DMSO	Dimethylsulfoxide
DDR	DNA damage response
ncAA	Non-coding amino acid
GCE	Genetic code expansion
aaRS	Aminoacyl-tRNA synthetase
UAA	Unnatural amino acid
MMS	Methyl-methanesulfonate
NAD	Nicotinamide adenine dinucleotide
NLS	Nuclear location sequences
ADPr	ADP-ribose
PTM	Post-translational modification
PARylation	Poly(ADP-ribosylation)
PA	Phosphatidic acid
PC	Phosphatidylcholine
PE	Phosphatidylethanolamine
PG	Phosphatidylglycerol
PS	Phosphatidylserine
PDD	PDD00017273
PM	Plasma membrane
POR	NADPH-cytochrome P450 reductase
SSB	Single strand breaks
SRS	Stimulated Raman scattering
SERCA	Sarco/endoplasmic reticulum Ca ²⁺ ATPase
DSB	Double strand breaks
MARylation	Mono(ADP-ribosylation)
ARH3	ADP-ribosyl hydrolase 3
PARG	Poly(ADP-ribosyl) glycohydrolase
TAG	Triacylglycerol
TCEP	Tris(2-carboxyethyl)phosphine
TLC	Thin layer chromatography
WWE	Tryptophan-tryptophan-glutamate
WIN	WIN55,212-2

ACKNOWLEDGEMENTS

I would like to begin by expressing my deepest gratitude to my mentor, Dr. Carsten Schultz, for the opportunity to work in his lab. Thanks to the freedom and trust he has provided, I have been able to learn from my mistakes and develop as a scientist throughout my PhD journey.

I would like to thank my dissertation advisory committee -- Braden Lobingier, Michael Cohen, David Farrens, Fikadu Tafesse, Kimberly Beatty and James Frank -- for their insightful feedback and guidance, which have significantly shaped my graduate studies.

Throughout my PhD, I have been fortunate to be surrounded by fantastic individuals both inside and outside the lab. This supportive environment has made the entire experience incredibly joyful. I am grateful for all the assistance, advice, and challenging discussions from my labmates. A special thank you goes to Aurelien for his inspiring conversations and mentorship. I also want to acknowledge the members of the neighboring lab, especially Brandon and Danny, for their scientific discussions and constant camaraderie.

None of this would have been possible without the love and support of my family and friends. I want to thank Grace for being my greatest support and inspiration, James for being an ever-present friend, Gabe for being an excellent landlord and many others that have defined my graduate life. Finally, thank you to my family for supporting this adventure far from home in the US.

ABSTRACT

Signal transduction is the mechanism by which the cell converts a stimulus into a specific response. This process typically involves a series, or cascade, of molecular events tightly regulated across time and space. This includes binding, modification, and translocation of biomolecules. These reactions ultimately lead to a precise response from the cell in order to appropriately adapt to their environment, and failure to do so can often result in a “disease state”. Understanding these events is of fundamental importance to design appropriate therapies, leading to an ever-growing need for tools to precisely analyze signaling. Optical tools are particularly well-suited for studying signal transduction because light is minimally invasive to biological systems, allowing for dynamic tracking of cellular events in live cells. Additionally, optical tools offer high spatial resolution, down to the level of a single molecule.

The goal of my PhD has been to develop and adapt optical chemical biology approaches to study signal transduction in cells. In pursuing this goal, I developed genetically encoded FRET sensors to monitor with high temporal resolution PARP1-dependent ADP-ribosylation in live cells (Chapter 2). I explored CB1 location-dependent functionality by adapting genetic code expansion to generate novel tagging strategies in live cells (Chapter 3). Finally, I characterized chemically engineered lipid probes designed to follow lipid transport, metabolism and protein-interactions (Chapter 4).

Chapter 1: Introduction

In my PhD, I focused on the development and application of an array of chemical biology tools to monitor various cell regulation mechanisms. This ranged from the development of genetically encoded FRET sensors to monitor dynamic post translational modifications in live cells, to characterization of chemically engineered lipid probes for lipid profiling.

Tool development in chemical biology exist at the interface between molecular engineering and biology. In the absence of a structured collaborative effort, often lacking in the academic field, it is important to possess both a deep understanding of the biology and the necessary skills to design and develop these tools. I started my PhD with a purely engineering mindset and over time gained a deeper and deeper appreciation for biology and its scientific method. Tool development and this shift in perspective defined my PhD, and combined with the opportunity in my lab to work with many different chemical biology approaches, led me to work on a diverse set of tools and biology fields, with a particular focus on signal transduction. Accordingly, the first part of my introduction covers two different classes of chemical biology tools I worked on particularly adapted to study signal transduction, while the second part briefly discusses three distinct fields of molecular biology and the conceptual approach for identifying potential needs for new tools in these areas.

INVENTING NEW CHEMICAL BIOLOGY TOOLS

As scientists, our fundamental objective is to formulate hypotheses that, through rigorous work, lead to significant advancements in our research area. Intrinsicly, most research is based on theoretical advancement or the discovery of new principles. This means that novelty echoes with success. When developing tools, we aim at creating or improving technologies that enable or enhance the study of biological processes or therapies. This process can add a layer of complexity compared to the wider field of biomedical research as the success of these tools is not only measured by their novelty but also their usability and reliability.

Defining scientific methods

The traditional scientific methodology relies on the formulation of hypotheses which are rigorously tested through the gathering of empirical evidence. If the test results support the hypothesis, then it is considered as new insight until it is disproved (if it is ever). Of note, in the words of D.Boorstin, “The greatest obstacles to discovery is not ignorance – it is the illusion of knowledge”; hypothesis testing always involves a certain amount of assumptions and can limit the recognition of paradigm shift. Still, hypothesis-driven deduction has defined scientific inquiries since the formalization of scientific methods and continues to guide researchers in their investigations today.

Six years ago, as a fresh graduate student learning about grant writing, I was taught that framing your research project as a hypothesis-driven deduction is the sole acceptable approach. Proposing to address a lack of data or a knowledge gap in a scientific area through a screen would be qualified as “fishing expedition”, a red flag in grant writing drastically decreasing the chance of funding. While this approach remains valid in grant writing, a shift in the scientific method occurred 20 years ago with the Omics revolution -- the ability to

measure changes in large number of genes, proteins, metabolites or lipids in an un-discriminated fashion. Omics has opened a new path in scientific method, so-called “data-mining-inspired induction”, where the gathering of data can, in itself, be sufficient to justify the inquiry. While this method defies the potential bias of the hypothesis driven method described above, it presents its own challenges in the form of understanding and analyzing the large set of data in a comprehensive and reproducible way. However, the methodology has been successfully adopted, mostly by implementing a cycling between generation of omics-driven ideas followed by careful testing(2).

In the recent years, the explosion of machine learning models has amplified the use of omics-driven research, assisting in the analysis of data sets. This can be pushed as far as presenting insight founded purely on correlative analysis from large data sets, bypassing the formulation of a mechanistic model, analogous to how some AI engine are generated today using machine learning (following the law of big numbers). This methodology has been met with fierce resistance by the scientific community, proposing instead “synergistic merging of big data with big theory”(3). In any case the field of big-data is still evolving and improving their methods in order to increase reliable insight. Yet, these strategies and new methodologies are already so successful that, just in the time of my PhD, I have observed a dramatic shift in how omics-driven methodologies, adopted 20 years ago, are presented. The universal hypothesis-driven deduction, modeling how we systemically used to present our science, has given room to a hybrid form of omics-driven induction followed by deductive testing.

Adapting scientific methods to develop molecular biology tools

Practically, when starting a new molecular biology research project, most scientist will go through a two-step approach: first step is learning and understanding the field and the second

step is to formulate a research question based on the information you gathered and synthesized. After these two steps, one can either formulate a hypothesis or run a big data collection screen to address the proposed research question. Either way, experiments are run, data is collected, and results are analyzed, with the end goal of discovering a new mechanistic insight. With hypothesis testing, however, the preliminary data collection stage is filled with great uncertainty. Most researchers design “go or no-go” experiments, meant to determine if a hypothesis is worth exploring or not. But in response to a “no-go” result, many will go through iterations of reshaping the hypothesis until one seems to be correct. With omic-driven induction, this first stage of testing and re-deigning is by-passed, the data tells you what the most probable path to answers is, mitigating the risk taken with hypothesis formulated research projects.

Tool development, on the other hand, currently only has a singular approach, analogous to the “go or no go” approach of molecular biology. It requires precise design; novelty is not always enough and several elements of engineering need to be taken into account. This includes the ease of implementation, the efficiency, the adaptability and, in some cases, scalability. If possible, the tool design should be accommodated for use in different models and experiment conditions, permit consistency between operators, and have some form of normalization. Together these factors define the tools usability and reliability and need to be pondered against the potential for novelty in order to promote its impact. All of these factors are highly stringent and amplified by the wide variety of pre-existing molecular biology tools, making tool design a challenging and possibly risky endeavor. For this reason, testing tool quickly is challenging as all the factors described above often need to be tested in sequential round of experiments, each round potentially making the tool obsolete. Many

designs are flawed and tools fail, but the quicker the tool is tested, the quicker you can adapt or move on. With the advent of AI, iteration could become the rule of success, similarly to how omics screens in biology have partially offset the risk inherent in formulating a hypothesis. In order to address challenges as medical science complexifies, and molecular tools with it, it will be critical to adapt new methodologies.

OPTICALLY ACTIVE INDICATOR OF SIGNAL TRANSDUCTION

Molecular imaging reveals the timing and location of biochemically defined molecules, signals, or processes as they emerge, interact, and vanish across time and space. As a result, molecular imaging synergistically integrates principles from physics, chemistry, physiology, biochemistry, and genetics (adapted from Roger Tsien)(4).

Fluorescent dyes as indicators

Fluoresceins and rhodamines, which belong to the xanthene dye family, are some of the most widely utilized fluorophores. Modification of fluorescein and rhodamine structures has led to extension of the absorption and emission spectra into the infrared and improvement in brightness and photostability of the dyes(5-7). The unique open-closed equilibrium of fluoresceins and rhodamines has allowed the construction of photoactivatable fluorophores(8), fluorogenic enzyme substrate(9) and indicators (10)with extremely high contrast. The spirolactone-forming equilibrium of these dyes can be influenced by the polarity of the medium and their protonation state, making rhodamines and fluoresceins effective environmental sensors(11). Those properties have sparked the design of fluorescent indicators synthesized with built-in sensing ability, allowing noninvasive monitoring of

signal transduction inside cells. For example, some first designs involved either inherent sensitivity to pH(12), or solvent polarity(13).

Additionally, attaching an ion chelator to a fluorophore can create probes that exhibit increased fluorescence upon ion binding. This effect can be achieved through diverse photophysical mechanisms, for example by altering the molecule electronic conjugation or photoinduced electron transfer (PeT). Those fluorescent chemical indicators were widely adopted for intracellular Ca^{2+} first synthesized in the 1980s by the Tsien lab(14, 15). The first Ca^{2+} indicator, BAPTA, relied on a shift in electronic conjugation upon binding to Ca^{2+} , shifting its maximum absorbance from 254 nm to 203 nm(16). The overlapping absorbance with proteins and lack of membrane permeability limited BAPTA applications in cell and led to the development of a new generation of Ca^{2+} indicators. These were improved by enhancing cell permeability, shifting to suitable wavelengths with increased brightness and optimization of the dynamic range. To achieve this, BAPTA was coupled to fluorescein or rhodamine, generating fluo-1, -2 and -3 as well as rhod -1 or -2(17, 18). The change of fluorescence for these indicators relies on PeT. Before binding of Ca^{2+} , electron transfer from BAPTA to the photoinduced dye reduces fluorescence. Binding of Ca^{2+} to BAPTA reduced the PeT efficiency leading to an increase in fluorescence.

A major advantage of those fluorophore probes over genetically encoded sensors is the broad range of ion specificity and affinity available, as well as the ease of use by bypassing the need for transfection, making them suitable for experiments in primary cells. However, robustly targeting the chemical indicators to a specific cell sub-compartment is challenging, and extruding of the indicators from cells makes long experiments difficult(19). New methods combining flexible scaffolds with advances in protein engineering have opened new

possibilities in targeting fluorescent indicator, as well as enzyme substrate and photoactivatable fluorophores to a specific subcellular compartment(20), some of which will be discussed below.

Fluorescent proteins

In the 90s, the development of genetically encoded fluorescent indicators revolutionized the field of cell and molecular biology. Most of these fluorescent proteins originated from mutants of the green fluorescent protein (GFP) from the jellyfish *Aequorea Victoria*. GFP was discovered in 1962(21) and recombinantly expressed in *E.coli* in 1994, demonstrating that only oxygen was required for proper folding and maturation of the chromophore. This highlighted its suitability as a fluorescent tag in living organisms(22). Following this discovery, brighter GFP mutants with optimized spectra were engineered to overcome the low quantum yield and broad spectrum of the original GFP(23), simultaneously giving birth to blue and cyan-emitting mutants(24). Around the same time, the structure of GFP and its fluorophore chemical structure was solved(25), further enabling the design of new variants with longer (red-shifted) emission wavelength. This led to the generation of yellow fluorescent protein (YFP) and cyan fluorescent protein (CFP) which, to this day, is one of the best pairs for Förster Resonance Energy Transfer (FRET)(26). Today, fluorescent proteins exist in a broad range of colors spanning the visible spectrum from violet to far-red, and continue to be improved(27). Most notably, due to the low light scattering, absorbance, and autofluorescence from endogenous molecules at higher wavelengths, far-red fluorescent proteins remain a major focus, with ongoing efforts to enhance their quantum yield(28).

FRET-based biosensors

FRET describes the energy transfer from a donor fluorophore to an acceptor fluorophore via non-radiative dipole-dipole coupling when both fluorophores are in close proximity ($<100\text{\AA}$), the dipole moments of both fluorophores are at an appropriate angle, and the emission spectra of the donor fluorophore sufficiently overlaps with the excitation spectra of the acceptor fluorophore. The orientation of the dipoles, together with the distance between the fluorophore defines the efficiency of the energy transfer through space. This was demonstrated by Lubert Stryer and his graduate student, Haugland, in a breakthrough paper: by attaching a donor fluorophore to one end and an acceptor fluorophore to the other end of poly-L-proline peptides ranging in length from 12 to 46 \AA . They observed a decrease in energy transfer efficiency with increasing peptide length in agreement with the predictions of the Förster equation(29). Those characteristics are ideal to generate intrinsically ratiometric fluorescent changes from protein-protein interaction and protein re-conformation(30).

A generalized design for FRET biosensors, categorized as “intramolecular”, consists of inserting a protein domain or molecular switch that changes conformation upon ligand binding or enzymatic modification between a pair of donor and acceptor fluorescent proteins(Figure 1-1). For example, kinase activity biosensors have a kinase-specific peptide substrate linked to a phosphoamino-acid binding domain. Phosphorylation by a kinase induces substrate-binding domain interaction, leading to conformational change and significant FRET variation(31). This design was widely adopted to monitor not only kinase activity but also dynamics changes in metabolites like cAMP(Figure 1-1)(32) or for diverse post translational modifications such as methylation(33), O-GlcNAcylation(34) and more recently histone H3 Lys-9 trimethylation and Ser-10 phosphorylation(35) among others.

Intramolecular FRET-based biosensors have been widely successful as they combine the advantage of high signal-to-noise ratio, efficient expression in cells and simple ratiometric readout. However, it is challenging to achieve high sensitivity. The reason for this is that the two main parameters defining FRET efficiency, distances between the FPs and relative orientation, are hard to predict and rationally design. In a single sensor protein, the fluorophores are always fairly close giving rise to a basal FRET level. We and other groups have engineered optimized cassettes or backbones in order to facilitate rapid screening and optimization of biosensors in which the change in dipole moment adds to changes in fluorophore distance(36, 37).

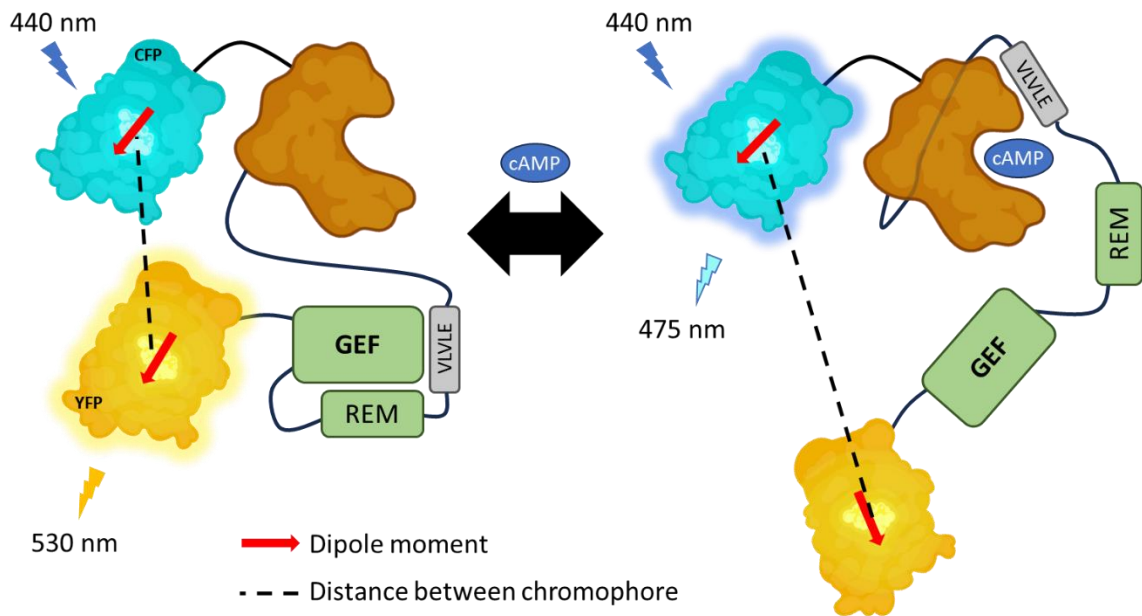


Figure 1-1. Representation of the change in conformation of a cAMP sensor based on the regulatory domain of EPAC. Following cAMP binding, the VLVLE sequence binds to the regulatory domain, leading to a change in distance and dipole/dipole angle between the CFP and YFP(32).

Another FRET sensor design relies on the co-expression of two interacting proteins each containing either the donor or acceptor FP. They are typically referred to as bimolecular FRET-based sensors or “intermolecular” sensors. Although intermolecular FRET biosensors

can present the advantage of higher FRET change other intramolecular biosensors, their signal can be affected by unbalanced expression level between the donor and acceptor(38). An example of bimolecular FRET sensor is the protein kinase A (PKA) sensor BimAKAR, which is derived from the intramolecular FRET sensor AKAR(39). BimAKAR consists of a PKA substrate fused to a YFP acceptor co-expressed with a CFP donor fused to Forkhead-associated (FHA) domain, a binder of phosphothreonine. FHA binds to the phosphorylated substrate leading to an increase in FRET that was shown superior to the AKAR sensor(40).

FP FRET biosensors simple design and intrinsic ratiometric readout have made them some of the most applied optical tools to study cell signal transduction. However, some inherent limitations have dampened their popularity over the years. First, the use of two fluorescent proteins limits the potential for multiplexing as well as imaging in animal because of absorption and scattering (this can be partially remedied by using fluorescence life time imaging). Second, the maximum dynamic range of intramolecular FRET biosensor achievable is relatively small compared to other modern biosensors.

Single fluorescent protein biosensors

The first circularly permuted fluorescent protein (cpFP) originated from the Tsien lab after their discovery that opening of new N and C termini at specific residues in proximity to Tyr145 in GFP was well tolerated with retained fluorescence. The circular permutation with new termini led to equilibrium shifts between the deprotonated and protonated chromophore, modulating the emission intensity(41). To test if conformational changes at those residues could lead to dynamic variation in emission intensity, calmodulin was inserted at residue Tyr145. Ca²⁺ binding to calmodulin caused deprotonation of the chromophore, increasing emission by 7-fold. This construct, named camgaroos, became the first example of a

circularly permuted fluorescent protein biosensor(41). Camgaros inspired the design of the improved Ca^{2+} indicators GCaMP and pericams, where M13 is attached to the N-terminus and calmodulin to the C-terminus (Figure 1-2) (42, 43). GCaMP has since then gone through many iterations and is widely successful in monitoring Ca^{2+} in complex systems.

Recently, several highly successful cpFP-based neurotransmitter sensors have been reported. G Protein-Coupled Receptors (GPCR) feature seven transmembrane alpha helices. When a GPCR is bound to a ligand in its orthosteric pocket, the TM5 and 6 helices undergo a conserved conformational

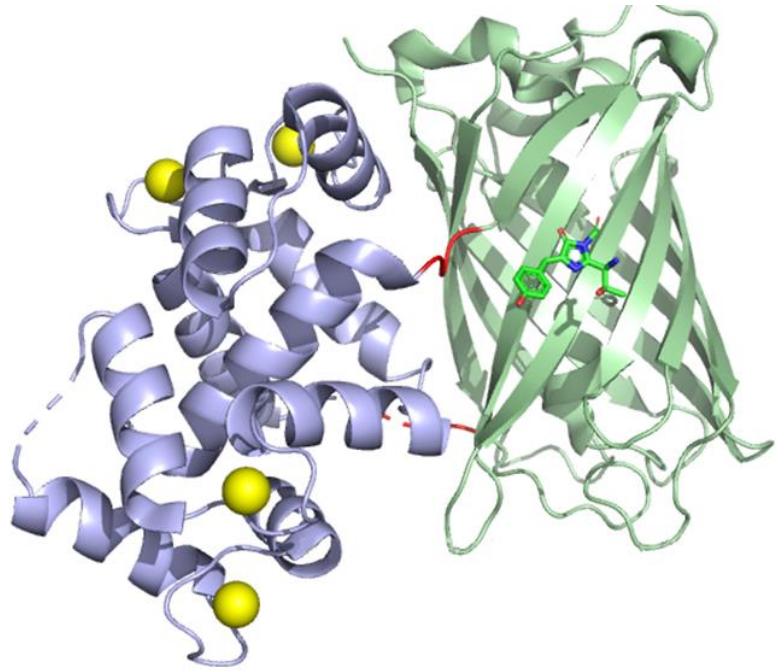


Figure 1-2. Structure of calcium-saturated jGCaMP8 (PDB 7ST4)(1). Ca^{2+} ions are shown in yellow, Calmodulin/M13 in light blue and GFP in light green. The chromophore was moved to the foreground for visibility.

change with TM6 moving outward from the receptor core to facilitate activation of the G protein complex(44). The extent of this conformational change varies between GPCRs and can reach up to 14 Å in the β 2-Adrenergic Receptor-G(45). This allosteric domain movement can be exploited to design cpFP biosensor to measure neurotransmitter and other GPCR ligands. Some early example are the dopamine biosensors dLight(46) and GRAB(47) which are both based on the insertion of a cpFP between TM5 and 6 of dopamine D1 receptor and

dopamine D2 receptor respectively. Sensors following a similar design can detect norepinephrine(48), serotonin(49), acetylcholine(50) and more.

Circularly permuted biosensors have several advantages over other FRET-based biosensors. The single-color excitation increases the possibility for multiplexing. Due to their small size, they are easier to fuse to a large sensor molecule and express and traffic better in cells. Lastly, the dynamic range achieved between bound and apo state is typically higher than in the more limited FRET-based biosensors. However, cpFP biosensors are more challenging to design. Typically they require a large screen to optimized the sensor fusion site and the linkers. Additionally, their reliance on changes in the protonation state of their chromophore renders them environmentally-sensitive, which can affect quantification and make them more adapted to binary read-out (such as Ca^{2+} spike measurement or action potential)(51).

Bimolecular fluorescent complementation

Following the discovery that GFP can fold and fluoresce after the rearrangement of the original sequence, it was hypothesized that splitting GFP at the loop between residues 157 and 158, leaving 7 β -strands from the *N*-terminal part of the fluorophore and 4 strands of the *C*-terminus, could recover when they are re-assembled(52). Each monomer of an antiparallel leucine zipper heterodimer was fused to the *N*-terminal and *C*-terminal fragment of the split GFP and expressed in similar amounts in *E-coli*. Transformed colonies turned green demonstrating the ability to reconstitute GFP from its peptide fragments. Bimolecular fluorescent complementation (BiFC) exploits this property of GFP by fusing each FP fragment to two interacting proteins of interest which can dimerize with a signaling molecule.

Most BiFC probes are used to investigate protein-protein interactions. By combining BiFC with FRET it is possible to visualize ternary complex formation. An assay has been developed where proteins A and B are fused to non-fluorescent Venus fragments, and protein C is fused to Cerulean. Interaction between A and B reconstitutes Venus, serving as a FRET acceptor. If C interacts with A or B, both FPs come in close proximity enabling FRET and indicating ternary complex formation(53).

Importantly, most protein-protein interaction in cells are highly transient and the reconstituted form of split GFP is more often than not more stable than the interaction of interest itself. For this reason, BiFC is a useful tool to look at the interaction onset but are unable to resolve the reversibility of the interaction(54). Alternatively, SplitFAST, recently derived from the fluorogenic reporter FAST(55), is a reversible split fluorescent reporter that can spatiotemporally monitor the formation and dissociation dynamics of the protein-protein complex(56). This tagging systems belong to the family of chemical-genetic fluorescent tools, which offer interesting variations to FP for the generation of biosensors.

Self-labeling fluorescent indicators

So far, we have shown that fluorescein and rhodamine derived dyes as well as genetically encoded fluorescent proteins are fantastic non-invasive tools to develop indicators of molecular changes in live cells. In 2003, the first self-labeling protein tag, later named SNAP-tag, was engineered from human DNA repair protein *O*⁶-alkylguanine-DNA alkyltransferase (hAGT)(57, 58). SNAP-tag can selectively react with *O*⁶-benzylguanine derivatives enabling orthogonal labeling of the protein with a large variety of different organic molecules(59). Later, CLIP-tag(60) and HaLoTag(61), both both engineered to function independently of the SNAP-tag (referred to as “orthogonal”), were engineered and

implemented in optical sensors (also referred to as chemigenetic biosensors). In the context of fluorescent indicator development, combining the optical properties of organic dyes with the cell specificity, sub-cellular targeting and existing molecular recognition motifs that genetically encoded sensors offer can lead to new biosensors with unique properties and versatility.

A disadvantage associated with FP FRET-based biosensors is their broad absorption and emission spectra and small Stokes shifts(62), which can lead to cross-talk when attempting simultaneous read out of multiple biosensors(63, 64). Chemigenetic biosensors are not as limited in this way because of the superior optical properties of small molecule dyes. Another disadvantage is that most FP FRET-based biosensors rely on a conformational change of the receptor upon ligand binding, as described above with the cAMP EPAC sensor (Figure 1-1)(32). Self-labeling fluorescent indicators can by-pass the need for change in conformation of the receptor by labeling the protein tag with a synthetic fluorophore tethered to a receptor protein ligand. In doing so, the ligand, covalently attached to the protein tag, is bound in a “close confirmation” to the receptor until it is out-competed by the agonist of interest. This induces a “release” of the fluorescent protein tag, which can be exploited for the generation of fluorescent indicators(65, 66)(Figure 1-3). Because the sensor is based on competitive binding, the K_d of the analyte for the receptor has to be lower than the range studied.

One of the first examples of a biosensor using this strategy is the GABA-snifit, a FRET biosensor capable of detecting micromolar concentrations of GABA in live cells(67). The sensor consists of a SNAP-tag labeled with the fluorescent GABA_B receptor antagonist, and a CLIP-tag labeled with a second fluorophore compatible for FRET and attached to the GABA_B receptor. Both fluorophores are in close proximity in the closed conformation and

upon physiological increase in GABA, the antagonist is out-competed leading to a shift of the sensor from a closed to an open conformation and a decrease in FRET(Figure 1-3). The FRET readout permits quantification of the GABA concentration at the cell surface. Similar scaffolds can be derived to quantify other analytes if a proper binding protein and suitable ligand exists, and was successfully adapted to quantify acetylcholine, anticholinesterase, and NAD^+ to name a few(68, 69).

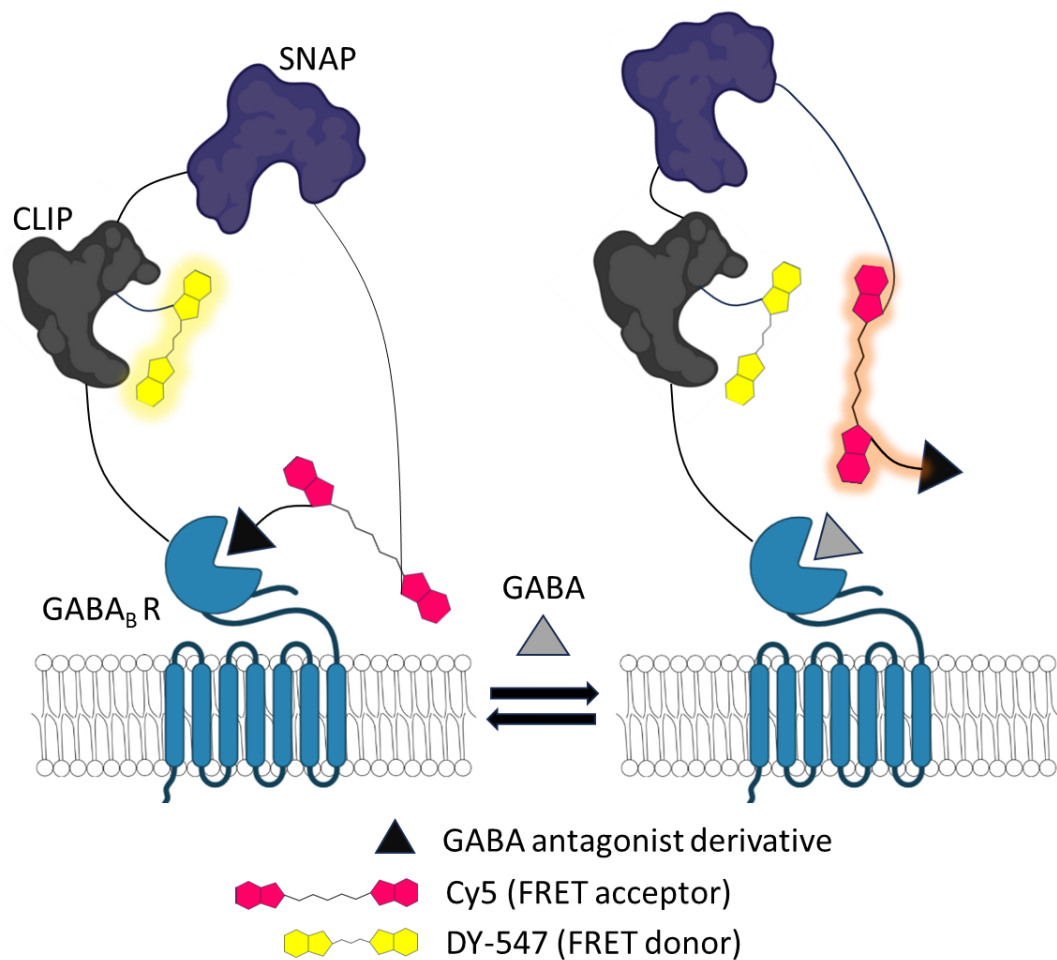


Figure 1-3. Representation of SNIFIT-GABA. SNAP-tag is labeled with Cy5 functionalized with a GABA antagonist CGP51783 derivative. CLIP-tag is labeled with DY-547. In the absence of GABA, the derivative is bound to the receptor, keeping SNIFIT in a close conformation with low FRET. Upon increase in GABA concentration, the CGP51783 derivative is outcompeted leading to the open conformation of SNIFIT and increase in FRET(67).

SNIFIT biosensors offer high specificity and sensitivity, making them powerful tools for detecting ligand concentrations, particularly with transmembrane receptors. However, their reliance on the efficient and specific labeling of both tags can complicate their implementation in cellular assays. Moreover, while most dyes used are fluorogenic, background fluorescent, tissue penetration of the dyes and the inherent bulkiness of the scaffold can still be problematic and potentially prohibitive for live animal studies. Recently, new scaffold of chemigenetic biosensors have emerged relying on the use of a single self-labeling protein. Because of the demonstrated faster labeling kinetics and higher fluorogenic potential of HaLoTag7 (HT7), it has become the self-labeling protein predominantly utilized in generating those novel biosensors(70).

One such scaffold originated from the finding that exchanging the CFP/YFP pair of pre-existing FRET-based biosensors with an eGFP donor and a HT7(71, 72) labeled with a red-shifted silico-rhodamine dye acceptor can lead to biosensors with unprecedented dynamic ranges, likely by reducing the spectral overlap of the FRET pair in the open state. This was demonstrated by generating sensors for Ca^{2+} , ATP and NAD^+ . Remarkably, replacing the eGFP with the non-fluorescent ShadowG(73) enabled the conversion of the FRET NAD^+ sensor into an intensimetric sensor with reasonable dynamic range and, more importantly, state-of-the-art fluorescence lifetime changes(74).

Alternatively, another strategy using HaloTag took advantage of the fluorescent equilibrium of silico-rhodamine, which exist predominantly in its non-fluorescent form (lactone) in water and partially switches to its fluorescent zwitterionic form after covalent binding to Halo-Tag, increasing the fluorescence by 100 fold(75). Recognizing that protein binding does not fully shift the equilibrium of the dye, a circularly permuted Halo-Tag was generated by inserting

a recognition domain in close proximity to the fluorophore binding site in order to modulate the fluorophore environment and shift its equilibrium. This led to the successful development of red-shifted Ca^{2+} and voltage indicators with superior optical properties to comparable red-shifted FPs sensors(76).

Bioluminescence-based indicators

Fluorescent indicators require excitation by incident light, which can lead to undesired phototoxicity and autofluorescence, particularly when imaging in deep tissue. Bioluminescent proteins do not require light for excitation. Instead, they rely on enzymes called luciferases which consume a small molecule, generally referred to as luciferin, to emit light(77). Bioluminescence resonance energy transfer (BRET) is the transfer of a donor bioluminescence to an acceptor fluorescent protein and follows a similar modular principle as FRET(78). Biosensors using BRET have been developed to follow dynamic signal transduction. One of the earliest examples is a BRET sensor engineered to follow the ubiquitination dynamics of arrestin2 modulated by GPCR activation. For this, the authors fused *Renilla* luciferase (RLuc) to β -arrestin and GFP to ubiquitin. Ubiquitination of β -arrestin brought RLuc and GFP in close proximity leading to an increase in BRET and quantifiable ubiquitination(79). Other BRET sensors were developed with an architecture close to previously described FRET sensor such as the sensor for cAMP, CAMYEL, with the Epac1 domain sandwiched between the fluorescent protein citrine and RLuc(80).

In the past, bioluminescence was predominantly used in macroscopic imaging as single cell imaging was prohibited by the low activity of the luciferase. New, brighter luciferases, such as NanoLuc, have enabled robust single cell measurements in addition to tuning of emission

wavelengths, analogous to previous and on-going development of fluorescent proteins, allowing for more efficient BRET(81, 82). This led to the improvement of several pre-existing BRET biosensors(83, 84). Notably, a voltage indicator, LOTUS-V, was engineered closely following pre-existing FRET biosensor designs by fusing on each termini of a voltage-sensing domain NanoLuc and Venus(85).

Ideally, an existing FRET biosensor could be converted to a BRET sensor by replacing the FRET pair with the spectrally appropriate BRET pair. Unfortunately, perhaps because of the different structural arrangement required, this generally does not yield efficient BRET. Strategies have been developed to circumvent this limitation and enable rapid conversion of a FRET sensor into a BRET sensor. By fusing the luciferase onto the donor of a FRET pair, it is possible to transfer energy from the luciferase to the FRET donor which then successively transfers the energy to the FRET acceptor(86). A similar approach was used to convert the hybrid chemigenetic biosensor ChemoG (previously described) into a bioluminescent biosensor (ChemoL)(74).

Engineering of bioluminescent proteins still requires, relative to their fluorescent counterpart, more development in synthetic chemistry and protein engineering. However, constant improvement in scaffold design and optimization will help facilitate the development of new biosensors and applications.

De novo design of ligand binding protein

Most biosensors used to monitor signal transduction in live cells depend on two key factors: native protein binding domains that bind the effector with affinity within the useful physiological concentration range, and the appropriate structural and dynamic properties of linker arrangements.

Most biosensor designs starts with an existing native protein domain that will elicit a specific change of conformation upon “sensing” the signal of interest. Unfortunately, the availability of these domains is limited and they often lack specificity. Moreover, engineering of such domains into a biosensor often reduces affinity or specificity which makes optimization of dynamic range a challenging prospect.

In the early 2000s, researchers initiated a concerted effort to develop a general method for creating new small molecule-binding proteins using computational design. However, 10 years later, protein-binding interaction design remained an unsolved problem(87). Rapid progress in computational methods to predict optimal energy binding, shape complementarity and crucially structural pre-organization in the unbound state has shifted the paradigm. It is now possible to computationally generate accurate protein binding domains. The first step is defining a ligand binding interaction with specific residues which is then built into a scaffold. In a second step, the ligand pocket is refined by optimizing shape complementarity in relation to the pre-organized site (unbound state)(88, 89). Those methodologies are improving at an incredibly fast pace and are already being applied in generating new biosensors(90, 91). Ideally, the domain rearrangement following binding of the ligand could be conserved so that an existing ligand binding domain could be swapped with another to rapidly adapt an efficient biosensor scaffold to different ligand following distinct chemotype. This would considerably reduce the time spent on optimization of the scaffold, the major challenge when generating sensors with a large dynamic range.

MODIFICATION OF BIOMOLECULES WITH BIORTHOGONAL CHEMICAL GROUPS

Genetically encoded proteins, such as the ones described above, are powerful tools for tracking and modulating cellular events mediated by proteins. Yet they are sometimes unsuitable for studying other molecules such as glycans and lipids biology. These are notoriously hard to study because of their large diversity and lack of genetic templates.

To overcome these limitations, chemical biologists have developed a set of chemical functional groups that can be inserted into a molecule of choice to serve as a reactive handle while, ideally, have a minimal effect on the function of said molecule. Critically, these functional groups must be selective and non-disruptive to the cell. Some of this work was recently highlighted when Carolyn Bertozzi, a pioneer in the field, was awarded the Nobel Prize in Chemistry for applying “click chemistry” to study living organisms. Today the biorthogonal toolkit is vast and a few of these tools will be discussed below.

Cycloadditions

Copper-catalyzed azide–alkyne cycloaddition (CuAAC)

More generally referred to as “click chemistry”, CuAAC is the reaction where an azide, a mild electrophile, reacts with a terminal alkyne(92, 93). To proceed rapidly, this reaction requires a Cu(I) catalyst, a cytotoxic metal ion which prevents its application *in vivo*, but is otherwise rapid, simple and produces a stable triazoles. Most importantly both azides and alkynes are very small and will not react with endogenous biomolecules making them one of the most reliable and widely used bioorthogonal chemical reaction(94).

The first example of using CuAAC in biology was by “decorating” a Cowpea mosaic virus with azides or alkynes on reactive lysine and cysteine residues, followed by click of a fluorescein derivative(95). This established the azide-alkynes methodology for the study of most biological processes in the cell(96, 97) through for example biomolecule visualization in fixed cells or pulldown of the molecule of interest from cell lysates. In order to expand this technique to *in vivo*, alternative mechanisms have been developed to by-pass copper catalysis.

Inverse electron-demand Diels–Alder reaction

Another type of bioorthogonal cycloaddition are the Diels-Alder ligation. The discovery that strain-promoted [3 + 2] cycloaddition between cyclooctynes and azides could react bioorthogonally without the need of a catalyst, a reaction named inverse electron-demand Diels-Alder cycloaddition (IEDAC), has led to many applications in molecular biology(98). This reaction was further developed and improved with the trans-cyclooctene (TCO), which react with the electron-deficient tetrazine much more rapidly than cyclooctynes (Strain-promoted IEDAC or SPIEDAC)(99) Due to its fast kinetics, the reaction can be easily implemented in live organism(100, 101). Tagging molecules in live animals or cells can be challenging because of residual fluorescence from unreacted dye. One key aspect of SPIEDAC is the efficiency and rapidity of the ligation(102), which limits the amount of unreacted dye. Moreover, tetrazine attachment can make the dye fluorogenic, further helping by limiting background fluorescence(103).

Because of its relative bulkiness and isomerization to a cis configuration over-time rendering it non-reactive, alternative strained alkenes of smaller size and higher stability have been utilized such as cyclopropenes(104). While their reactivity is typically inferior to TCO, they

have enabled studies of molecules not compatible with TCO. For example, they were incorporated using genetic code expansion (GCE) into enzymes or GPCRs(104, 105).

Photo-sensitive chemical tools

Click chemistry has proven invaluable to study biomolecules but it does not confer spatial or temporal control over the molecule of interest. Temporal control is often desirable when studying biological system as most biomolecules in living organism are in constant flux. Spatial control permits researchers to investigate cellular processes at the subcellular level or a subpopulation of cells within a complex tissue. To this end, photosensitive chemical tools have been one of the most powerful approaches by using light as an inducer. Light is powerful because it can be minimally invasive in most cells and delivered to a precise location at a given time. For applications in biology, it is important that the chemical group absorption is above 350 nm to minimize cytotoxicity, that the biomolecule remains sufficiently soluble in water and that the photochemical byproduct, if there is any, is inert in cells. Another important parameter is the *apparent rate constant* of the substrate, or how quickly the substrate becomes active upon exposure to light, which typically needs to be faster than the expected rate of response of the biological system when looking at fast, transient kinetics. This ensure that the activation of the photochemical product is not the limiting factor in the biological response.

The choice of a chemical group to attach to the molecule of interest will often depend on the available chemistry and wavelength absorption. Luckily, the toolkit of photo-sensitive chemical tools is vast and rapidly expanding.

Photo-cage: coumarin groups

Most biomolecules rely on highly specific interaction with their binding partner in order to be active. This means that the interaction between two molecules is dependent on strict molecular structures and electrostatic behavior. Adding a given chemical group, referred to as a “caged” group, to the molecule can disrupt this tight chemical balance thus preventing interaction with binding partners in the cell. Ideally this leads to an inert molecule that will not signal or get metabolized.

Photo-cage groups can be removed with light and exist in a wide variety of forms(106)(Figure 1-4). Among this family, the coumarin cage possesses advantageous characteristic such as its intrinsic fluorescence, which allows visualizing the caged molecule before uncaging and can sometimes facilitates characterization of release rate. The development of coumarin cages originated from the discovery that 7- methoxycoumarinyl-4-methyl derivatives can be used as photoactivatable phosphate-releasing groups(107). To make coumarin cages bio-compatible they have been optimized to increase water solubility and to shift absorption maximum above 350 nm. Remarkably, 7-diethylamino coumarin (DEAC) derivatives were shifted up to about 405 nm for their absorbance maximum and were used to uncage GABA, for example(108).

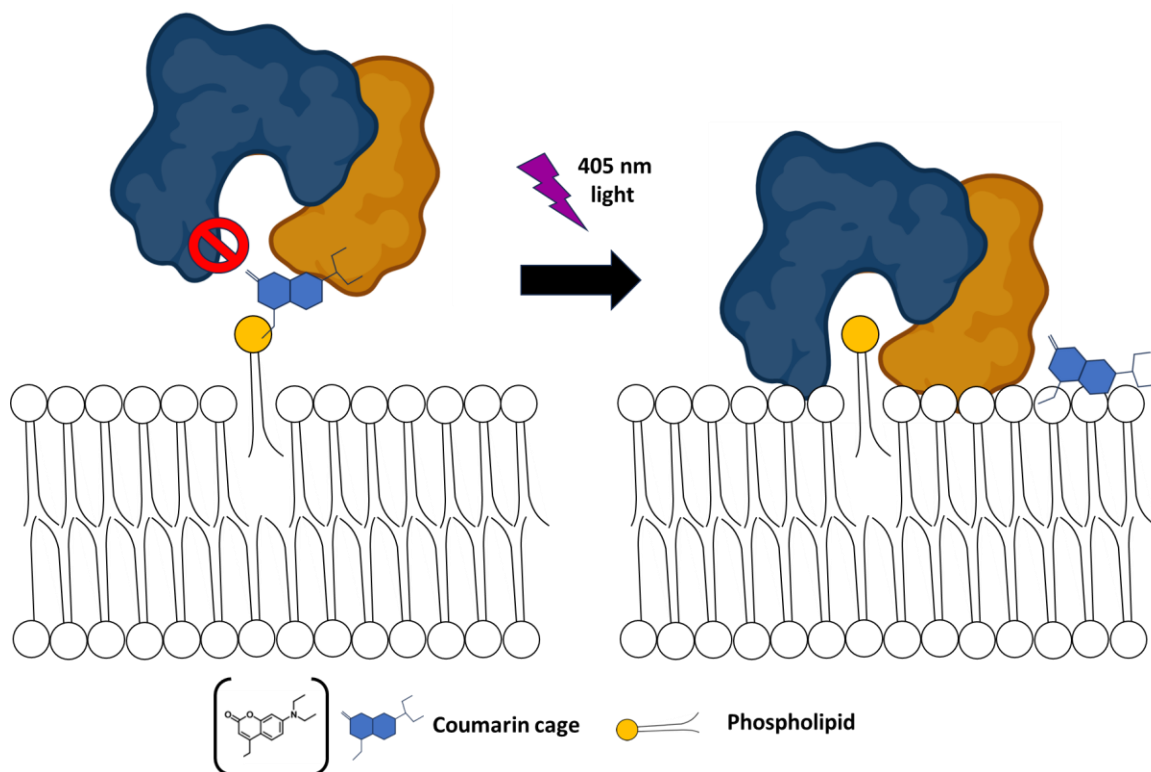


Figure 1-4. Representation of a coumarin-caged lipid (yellow headgroup). The coumarin cage prevents lipid-protein binding. After uncaging, the lipid is “freed” and can enter the protein binding site.

Photoswitches

We have seen that photo-cages allow for optical control of a molecule’s function. However, while the uncaged molecule provide the advantage of being unaltered, the caged molecule can have dramatically altered properties, for example by increasing its cell permeability or influence its subcellular location preference. Additionally, uncaging is an irreversible process. Another approach to control a biomolecule function is to insert photoisomerising groups into its structure. Irradiation with light promotes reversible isomerization from a planar to a globular structure(109). Ideally this results in one isomer that conserve its original

functions while the other one loses its potency. The most common approach to generate these photoswitchable biomolecule is to insert the photoisomer into the perimeter of the molecule, referred to as “azo-extension”, or substitutes a functional group with similar properties to the photoisomer, referred to as “azo-insertion”(110, 111). Due to their robust photochemical behavior the most used photoswitching isomers are azobenzenes(112). The advantages of this approach over caged-molecules are reversibility and smaller impact on the biophysical properties of the molecule. However, the inserted isomer can potentially affect binding or specificity of the active form. For this reason a meticulous structure-activity relationship study is necessary when designing such molecules. Several successful lipid tools, among others, were developed using this scaffold(113, 114).

Photolabeling: diazirines

Many interactions in cells are electrostatic in nature, highly transient, and modulated by specific cellular context. A variety of techniques exist to investigate transient protein-protein interactions. Identifying small molecule interactions can be more challenging because of their higher diffusion rate. In order to stop the diffusion of a molecule, a photoactivable group can be added that generates highly reactive species when exposed to light(115), which will readily form covalent bonds with nearby biomolecules (photo-crosslinking)(116). The interactor can then be directly identified using a variety of molecular biology methodologies. One class of compounds that have been successfully used for photo-crosslinking are diazirines. After photo-activation, diazirines form a carbene that will rapidly react with carbon-hydrogen bonds, oxygen-hydrogen bonds, or nucleophiles(117). Diazerines can also form a diazo isomer which react with acidic amino acids, specifically glutamate(118, 119). The diazirine stability, high reactivity after light activation and small size has made it one of

the most popular and efficient photolabeling reagent. However, it is most efficient in hydrophobic environments like membranes or protein pockets, as the carbene labeling efficiency decreases in aqueous conditions (117). For this reason, diazirines have been predominantly used to study bio membrane and lipids interactions(120, 121).

Genetic code expansion

Biorthogonal chemistry enables very precise control over small molecules in cells or live animals provided they are bioavailable. Proteins and other macromolecules, however, are more challenging to manipulate using this type of chemistry. One straightforward way to equip a protein of interest with a useful chemical group, while minimally perturbing its structure and function, is to incorporate an unnatural or non-coding amino acid (ncAA). A large variety of ncAA have been synthesized over the years with useful chemical groups like the ones described above, and several methods have been developed to efficiently insert them into proteins *in vitro*(122-124).

The translation of protein with ncAAs *in vivo* requires increasing the encoding of amino acid in living cells from 20 to 21 or more. This was achieved by using a method named genetic code expansion (GCE). In this approach, an orthogonal pair of aminoacyl-tRNA synthetase (aaRS) and tRNA are engineered, often through directed evolution, to selectively incorporate the desired ncAA over canonical amino acids. This works by having the orthogonal aaRS aminoacylate only its corresponding orthogonal tRNA, with minimal activity towards the host's tRNAs. Similarly, the orthogonal tRNA is aminoacylated only by the orthogonal aaRS(125-127). Moreover, the tRNA typically recognizes the stop codon amber(TAG) as it is not assigned to a canonical amino acid and is the least used of the three stop codons in mammalian cells(128).

Over the past 20 years, a large number of methodological advances in GCE have permitted the incorporation of ncAAs in multiple cell types including mammalian cells. Unique molecular biology approaches have emerged from being able to equip proteins with chemical groups at a specific site(129). For example, the incorporation of an amino acid with a photocrosslinkable group, such as a diazirine, can permit capture of protein-protein interactions in vivo with spatial and temporal control(130, 131). Some other successful applications are the incorporation of photocaged UAAs. Photocaging of serine and tyrosine can facilitate studies on phosphorylation(132) while caging of key lysine or cysteine in the active site of enzymes can confer spatio-temporal control over their activity(133).

TCO*-modified ncAAs, such as TCO*-L-lysine(134), allow for precise attachment of fluorophore dyes to target proteins with minimal linkage size and potential for fluorogenicity(103). This makes them highly appealing for protein tagging, especially in super-resolution microscopy. The use of larger antibodies or fluorescent proteins in super-resolution can introduce displacements of up to 20 nm, which can affect imaging accuracy(135), making the smaller linkage size of TCO*-modified ncAAs a valuable advantage. For example, a study has shown that introduction of TCO*Lys into a set of proteins combined with fluorogenic tetrazine-dyes can enable efficient biorthogonal labeling for super resolution microscopy in fixed and live cells(103).

While GCE is a powerful technique, its application in mammalian cells remains challenging. The efficiency of ncAA incorporation at an amber codon varies widely, from 10% to 100%. This inconsistency is due to several interconnected factors: the efficiency of tRNA decoding and peptide bond formation on the ribosome, the position of the amber codon within the gene, and perhaps most critically, competition with the release factor eRF1. Additionally,

reassignment of the amber codon is in general well tolerated but complicates generation of stable cell lines and generates non-negligible off target effects.

Constant improvement of aaRS/tRNA pairs and new amber suppression technologies are helping to offset those limitations. For example, the creation of mutants of eRF1 with decreased recognition of the amber codon can facilitate ncAA incorporation(136). More excitingly, a recent study generated a phase-separated compartment enriched with the aaRS, suppressor tRNA, and mRNA of choice. This enabled a localized GCE system where only the stop codon of the mRNA of interest is suppressed, with minimal impact on cytosolic mRNA sharing the same stop codon(137).

THE PUZZLE OF PARP1 DEPENDENT ADP-RIBOSYLATION: NEED FOR TOOLS

The transfer of ADP-ribose (ADPr) from nicotinamide adenine dinucleotide (NAD⁺), named ADP-ribosylation, is a post-translational modification (PTM) catalyzed by ADP-ribosyltransferase (ART) enzymes. These enzymes are present in every living organism and can transfer onto substrate protein ADPr via N-, O-, or S- glycosidic linkages(138). ADP-ribosylation has a variety of functions, from directly regulating an enzyme activity to recruiting protein binding partners(139, 140). Similarly to many other PTMs, ADP-ribosylation is reversible and tightly regulated in cells, with the dynamic processes of “writing” and “removing” as key features of the signaling function(141). In humans, a sub-family of ARTs known as poly-ADP-ribose polymerases (PARPs) consists of 17 distinct members(142), each exhibiting a wide variety of domain architectures that contribute to their functions(143). Among this sub-family, divergent evolution has led to a variety of ADPr modifications. Notably, some PARPs such as PARP1 and PARP2, are capable of adding

multiple ADPr in a chain on a substrate amino acid, a process named poly(ADP-ribosylation)(PARylation)(144).

PARP1 role in DNA damage response

Historically, the study of PARP enzymes originated from research on DNA damage responses. It was later found that PARP1, PARP2, and PARP3 are allosterically activated in response to DNA damage, with PARP1 responsible for the majority of PARP activity. PARP1 is highly expressed in cells and localized in the nucleus. PARP1 binds to DNA including single strand breaks (SSBs)(145), double strand breaks (DSBs)(146), stalled replication forks(147), and other forms(148, 149). PARP1's main role upon binding to DNA damage sites is to catalyze ADP-ribosylation of itself and many other substrate proteins, such as histone and DNA repair proteins(150, 151)(Figure 1-5). For example, PARP1 is involved in regulating DNA replication under stress conditions, where it stabilizes stalled replication forks by promoting fork reversal. Inhibition of PARP1 increases replication fork speed and can lead to replication stress (152). Correspondingly, inhibiting poly(ADP-ribosyl) glycohydrolase (PARG), the main PAR remover in cells, induces persistent fork stalling and cell death(153), highlighting the importance of PARG in preserving PARP1 maintenance of genome stability. Cancer cells with defective DNA damage response are highly sensitive to PARP1 inhibition, establishing PARP1 as a target for chemotherapeutic approaches in ovarian, pancreatic or prostate cancers(154, 155). Although the critical role of PARP1 in maintaining genome stability is well established, the precise ADP-ribosylation mechanisms by which it functions remain to be fully understood.

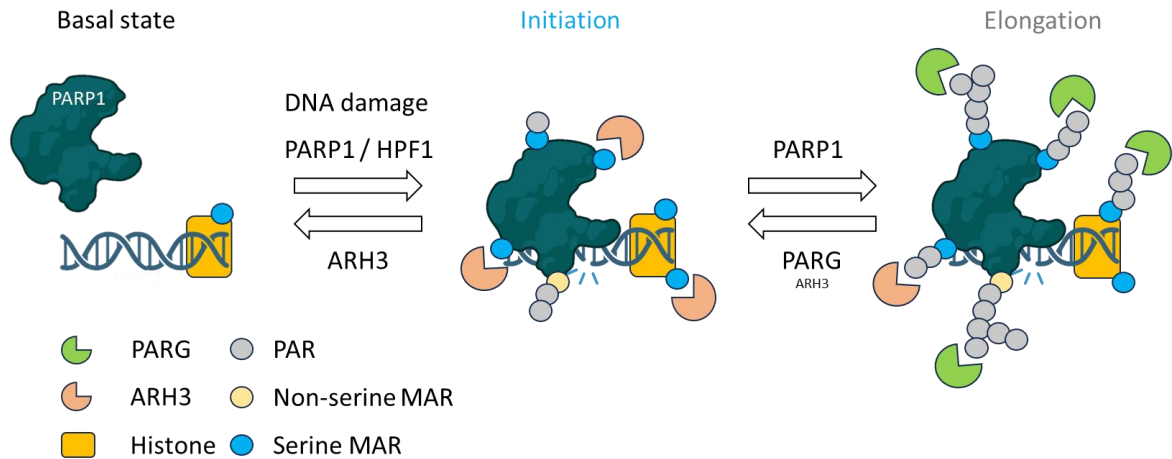


Figure 1-5. Upon DNA damage, PARP1 is activated and, in complex with HPF1, initiate ADP-ribosylation predominantly on serine residues. PARP1 alone can then elongate the initial MARylation. ARH3 hydrolyzes MARylation off of serine, with minimal activity on PAR, while PARG hydrolyzes rapidly PAR.

PARP1-catalyzed ADP-ribosylation linkages

ARTs catalyze the transfer of an ADP-ribose from NAD^+ onto a nucleophilic acceptor amino acid within the protein substrate (in the context of PTM). The nucleophile attack occurs on the C1'' atom of NAD^+ . For PARylating enzyme, such as PARP1, the modification can be extended with repeated addition of an ADP-ribose on the 2' or 2'' hydroxyl group of the initial ADP-ribose for chain elongation or branching, respectively.

The catalytic core in all PARP enzymes is conserved. In PARP1, the nicotinamide-binding pocket contains a His-Tyr-Glu triad where His862 and Tyr896 bind NAD^+ while Glu988 is critical for catalysis(141). Removal of Glu988 abolishes PAR elongation activity, switching the activity to exclusively mono(ADP-ribosylation) (MARylation)(156).

Despite extensive study and a good understanding of the PARP1 catalytic pocket, profiling of acceptor amino acid substrates that PARP1 targets has remained challenging. Historically, PARP1 has been described to modify glutamate and aspartate side chains(157-159). Consensus recognition motifs such as $\text{PX}\underline{\text{E}}$ or $\text{PXX}\underline{\text{E}}$ have been suggested(159). However, a

paradigm shift has occurred with the discovery that Histone PARylation factor (HPF1) can transfer the catalytic preference of PARP1 to serine residues(160-163). Furthermore, MS-based analysis suggests that glutamate and serine residues are predominantly PARylated and MARylated, respectively(163).

The high number of PARP1 substrates and regulators(164, 165) together with the high dynamic nature of PARylation and MARylation make *in vivo* studies on PARP1 substrate specificity challenging. Indeed, under normal physiological condition, PARP1-dependent ADP-ribosylation is low and highly transient due to the high activity of removers, such as PARG or the serine-linked mono(ADP-ribose) remover ADP-ribosyl hydrolase 3 (ARH3)(166) (Figure 1-5). For this reason, most studies investigating PARP1 activity under physiological condition have done so in the absence of PARG or ARH3 activity in order to capture the resulting accumulation of ADPr by mass spectrometry (MS) or immunoblotting(159, 163, 167). Probes with high temporal resolution and sufficient sensitivity to detect low physiological level of ADPr could significantly help decoding the regulation and functions of those different linkages and lead to better clinical targeting.

State of the art tools to detect ADP-ribosylation

Significant efforts in the recent years have been invested in developing tools to improve the study of ADPr-specific linkages. The Kraus lab has pioneered the conversion of protein domains recognizing ADPr into recombinant antibody-like ADP-ribose binding proteins. The Matic lab, using new chemical biology approaches, has generated new recombinant site-specific antibodies which have revolutionized the field(168, 169). Additionally, new methods for MS-based identification of specific ADPR linkages have permitted to detect proportion of ADPr linkage and PARP1 target substrates, as described above(163, 170).

Advances in the development of antibodies and MS workflows have been tremendous for the identification of the wide range of ADPr acceptor but are still hampered by three inherent challenges of PARP1-dependent ADP-ribosylation. One, the low level and highly dynamic nature of this PTM can lead to a loss of the heterogeneity between PAR and MAR and often requires enrichment methods. Two, most ADPr linkages, but particularly ester linkages on acidic residues, are labile. Robust protocols might only partially limit the loss of the ADPr unit. Third, evidence suggests that PARP1 activity in response to DNA damage occurs in multiple waves, each contributing to signaling associated with unique ADPr-linkage, making it crucial to monitor PARP1-dependent ADP-ribosylation with precise temporal resolution(171).

Optical indicators of ADP-ribosylation applicable to live cells could help solve some of these challenges. To date, the most exciting application of such indicator has been by using functionalized recombinant antibodies(171): a monovalent antibody with the SpyTag peptide can be conjugated to a fluorescently functionalized SpyCatchers to generate a fluorescent indicator of, for example, serine-linked MARYlation. Although highly specific and sensitive, this tool is hindered by the need for a harsh permeabilization protocol for antibody penetration, and a non-quantifiable read-out.

An alternative approach is to use genetically encoded fluorescent indicators. Several split protein biosensors for PAR have been developed taking advantage of the numerous PAR-binding protein domains like the tryptophan-tryptophan-glutamate (WWE) domain that recognize isoADPr, an intermediate molecule of a PAR chain(140). For example, WWE was fused to both parts of a dimerization-dependent GFP. Upon binding to PAR, the split GFP dimerizes, leading to fluorescence. The construct was capable of detecting PAR formation in

cells and its sensitivity was further improved by replacing the split-GFP with a split-luciferase, enabling detection of PAR formation in live animals(172). As described before, a drawback of bimolecular fluorescent complementation approaches is the lack of reversibility, an important feature of ADP-ribosylation. In addition, this readout cannot be quantified. In order to investigate low transient increase in PARP1 activity in live cell, generating alternative quantifiable optical tools with high sensitivity and reversibility is urgently needed.

OVERVIEW OF GPCRS AND CANNABINOID RECEPTOR 1

G protein-coupled receptors and biased signaling

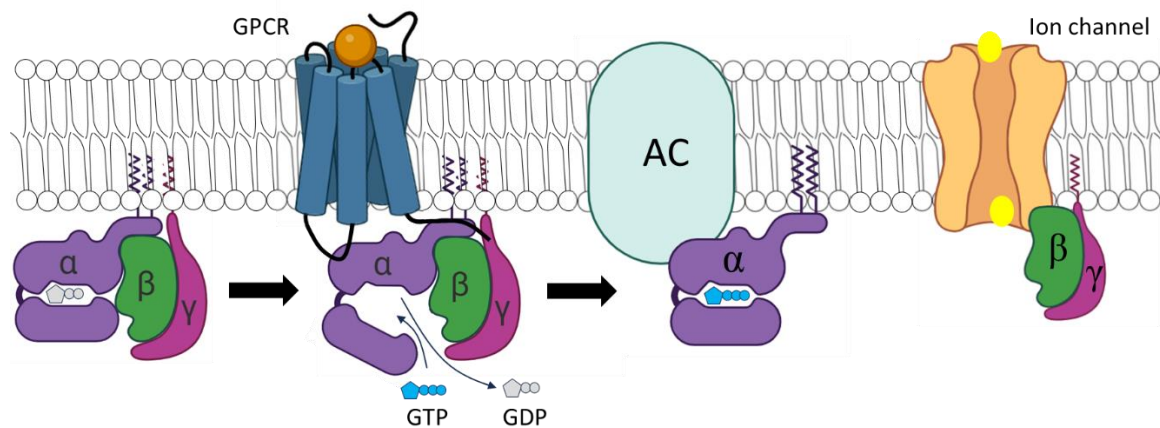


Figure 1-6..Representation of the heterotrimeric G protein activation by a GPCR. Adapted from Weis & Kobilka(173)

The G protein-coupled receptor (GPCR) family is the largest group of membrane surface receptors(174). Human GPCRs are categorized into five distinct families: the rhodopsin family, the adhesion family, the frizzled/taste family, the glutamate family, and the secretin family(175). These receptors play a crucial role in transmitting signals from the extracellular environment to dedicated intracellular signaling pathways(44).

As their name suggests, GPCRs primarily function by interacting on their intracellular side with heterotrimeric GTP-binding proteins (G proteins), which consist of α , β , and γ subunits.

Binding of a ligand (or agonist) causes conformational changes of the receptor which leads to “activation” of the heterotrimer by exchange of a GDP for GTP and dissociation into $G\alpha$ and $G\beta\gamma$ that separately activate intracellular effector molecules(44). The G protein complex reforms after $G\alpha$ hydrolyses GTP back into GDP. The G protein complex can then re-associates with the GPCR (Figure 1-6). The variety of existing α , β , and γ subunits allows for the formation of a large number of G proteins combination, which serve as a scaffold to enable a wide array of responses from GPCRs.

Moreover, activation of GPCRs can also lead to phosphorylation of the receptor by a G protein-coupled receptor kinase (GRK) followed by binding of arrestins. Binding of arrestins prevent the G protein heterotrimer from binding back to the receptor, induces endocytosis, and promotes a variety of additional signaling cascades(176).

Agonists can stimulate both pathways described above. By causing different receptor conformations upon binding, agonists can preferentially stimulate G protein pathways over arrestin pathways, and vice versa, a phenomenon referred to as biased agonism(177). Another form of bias of GPCR signaling is linked to the sub-cellular location of the GPCR during activation.

GPCRs were once believed to function only at the cell surface. This view stemmed from the fact GPCRs main role is to “sense” extracellular signals and that many GPCR ligands, too bulky or hydrophilic, cannot easily cross the plasma membrane. Internalized receptors were thought to either be degraded or recycled, suggesting that endocytosis served only to attenuate GPCR signaling. Evidence shows that internalized GPCRs can activate signaling from intracellular compartments. For example, the $G\alpha_s$ -coupled beta-2 adrenergic receptor was shown to signal from endosomes, influencing cAMP production(178-180). Importantly,

this endosomal signaling specifically drives GPCR-mediated gene transcription by producing cAMP on early endosomes, whereas plasma membrane signaling of the receptor contributes minimally to this transcriptional response, making the two pools functionally different. Furthermore, emerging evidences show that several GPCRs can localize at the Golgi, independently from internalization(179, 181). For example, the opioid receptors mu and delta can be activated and couple to Gai/o at the Golgi apparatus(182). Activation of these intracellular GPCRs inherently requires the delivery of the ligand to these compartments. Interestingly, GPCRs ligand physio-chemical properties are highly varied. Some ligands cannot cross the plasma membrane and will require active transport while other can passively diffuse through the membrane to enter the cell. This can lead to preferential activation of the pool of GPCRs localized intracellularly over the one at the plasma membrane and vice-versa, modulating GPCR signaling.

Cannabinoid receptor 1 signaling

Initial research on Δ^9 -THC, the major psychoactive biomolecule in marijuana, led to the discovery of cannabinoid receptor 1, a class A GPCR, in rat brain tissue(183). CB1 is a member of the cannabinoid receptor family and is one of most highly expressed GPCRs in the brain(184). In the brain, neuronal CB1 receptors are localized predominantly on presynaptic terminals where they act as retrograde neuromodulators(185). Other than the nervous system, CB1 is also expressed at lower level in peripheral tissues, such as adipose tissue and the pancreas to name a few(186).

CB1 mainly couples to Gi/o proteins, leading to a reduction in cAMP through inhibition of adenylyl cyclase (AC) by Gai/o, inhibition of voltage-gated Ca^{2+} channel by G $\beta\gamma$ as well as binding of G $\beta\gamma$ to GIRK channels leading to potassium efflux and hyperpolarization of the

cell membrane. Those mechanisms participate to the reduction of neurons excitability (187). CB1 has been shown to also couple with lower efficacy to $G_{\alpha s}$ and $G_{\alpha q/11}$. In neuroblastoma cells, $G_{\alpha s}$ coupling was reported in response to the synthetic agonist CP55,940(188), an observation facilitated by treatment with the $G_{\alpha i/o}$ suppressor Pertussis toxin(189). In human embryonic kidney 293 cells, it was suggested that CB1, in response to the agonist WIN55,212-2, increases intracellular Ca^{2+} by coupling to $G_{\alpha q}$. Interestingly, this was WIN55-specific, as the effect was not observed with the agonists Δ^9 -THC, HU-210, CP55,940, 2-AG, methanandamide, and cannabidiol(190). A recent cryo-EM structure of CB1 revealed that the interaction between $G_{\alpha i}$ and CB1 mainly occurs between the $\alpha 5$ helix of $G_{\alpha i}$ and the intracellular loop 2 (ICL2) of CB1. This interaction was found to be weaker compared to the interactions between ICL2 and their respective G proteins in other GPCRs, and has been suggested as the reason for CB1's ability to interact with G proteins other than $G_{\alpha i/o}$ (191). In any case, conflicting evidence have been gathered on CB1 over the years, particularly in terms of its differential G protein coupling and its activation of the cAMP versus pERK pathways(192-194).

An interesting feature of CB1 is its relative long N-terminus (110 amino acids) compared to other members of the class A GPCR family. How the N-terminus of CB1 regulates its trafficking and signaling remains to be understood. For instance, CB1 lacks a conventional signal peptide and its two N-linked glycosylation sites in the N-terminus are not required for translocation of the receptor to the plasma membrane(195). Furthermore, truncation of the N-terminus or addition of a signal sequence have been shown to increase translocation of CB1 to the plasma membrane(195). For signaling, it was found that truncation of the first 103 residues of CB1 does not affect the binding of its agonist CP-55940 or G protein

signaling(196). However, the same study has shown that a disulfide bond in the N-terminus, between C98 and C107, modulates the effect of the CB1 allosteric ligands Org 27569 and PSNCBAM-1. Additionally, splicing variants of CB1 with truncated N-terminal regions, while they were only detected as mRNA in tissues, have unique pharmacological profile. Indeed, it was shown that 2-AG act as an inverse agonist for these variants at a potency similar to its agonist activity for CB1(197, 198). It is possible that these variants are expressed in a subset of cells and are yet to be discovered.

Studying CB1 trafficking has been challenging due to large intracellular pools of the receptor in both recombinant or endogenous expressing cells(199), making it difficult to discern between CB1 in transit and established intracellular pools of CB1. Still, several studies have suggested that intracellular CB1 can be involved in signaling(200). A pivotal study has identified, using immunogold electron microscopy, that CB1 localizes in mitochondria of hippocampal astrocytes where it directly controls cellular respiration and glucose metabolism through cAMP regulation(201, 202). Developing new visualization tools for CB1, particularly compatible with super-resolution microscopy, could help identify and characterize further the role of the intracellular CB1 pool.

CB1 investigations have historically suffered from a lack of highly specific antibodies(203). Specific monoclonal antibodies for both N-terminal and C-terminal could help discover new CB1 functional roles. Additionally, some antibodies can probe the receptor activation state of GPCRs(204). These antibodies, through directed evolution, can be used to stabilize the active conformation of the receptor and therefore serve as conformation biosensors(205, 206). Another approach to tag endogenous receptor pool is through ligand directed labeling. This method uses a ligand of the receptor functionalized with a dye and a reactive group that can

form a covalent bond with specific nucleophilic amino acid (such as cysteine or lysine). For the study of GPCRs and other functional proteins, “traceless affinity labeling” was developed that allow for the dissociation of the ligand after the labeling reaction(207). For example, it enabled the specific labeling of endogenous opioid receptors in living brain slices(208). Traceless probes for CB1 are still under development; however, recent efforts have resulted in the design of CB1 fluorescent probes by conjugating NBD or TAMRA dyes to CB1’s pharmacophores(209). In the study, an innovative modular design allowed for the screening of various CB1 ligands and led to the identification of several probes that retained their affinity for CB1 after dye attachment. The probes were successfully utilized to label CB1 in live tetracyclin-inducible Hek293 cells. Although these probes are not traceless due to the absence of reactive groups that can form covalent bonds with nearby nucleophiles, they demonstrate the potential of such probes in investigating the interplay between receptor localization and pharmacology.

CHEMICAL BIOLOGY TOOLS TO HELP UNRAVEL INDIVIDUAL LIPID FUNCTION

Part of this chapter is adapted with permission from the chapter “Chemical Biology of Lipids” in Advanced Chemical Biology (Wiley 2023), by Scotland Farley, Alix Thomas, Aurélien Laguerre, and Carsten Schultz

Advances in our understanding of the genome have enabled precise manipulation of nucleic acids and proteins, leading to significant molecular insights. However, lipids present a unique challenge. Unlike proteins and nucleic acids, lipid structures cannot be directly altered through genetic manipulation. Moreover, their diversity, complex biosynthesis, small size, rapid metabolism, and lateral diffusion within cellular membranes make them difficult to

label and track, limiting our ability to study them with the same precision afforded to proteins and nucleic acids.

Lipids are broadly categorized into three major classes based on their structural backbones: glycerolipids, sphingolipids, and sterols. Each class is characterized by a distinct biosynthetic pathway, biophysical properties and functions. Glycerolipids, built on a glycerol backbone, are the most abundant lipids. Central to their metabolism is diacylglycerol (DAG), produced from sequential acylation by fatty acyl-CoA molecules of glycerol-3-phosphate, which can be converted into various phospholipids, such as phosphatidylcholine (PC), phosphatidylethanolamine (PE) or phosphatidic acid (PA) as well as the neutral lipid triacylglycerol (TAG). Sphingolipids are derived from a sphingosine backbone to which one N-linked acyl chain can be added. Sterols are a more distinct class of lipids with a four-ring structures serving as a backbone.

We will discuss here the advantages and limitations of various chemical biology approaches to study individual lipids in cells.

Engineering tools to track lipid in cells

Two main approaches have emerged for the visualization and characterization of lipids in cells. One relies on the use of proteins, such as antibodies or genetically encoded sensors based on lipid binding domain. The other relies on the chemical modification of lipids to generate synthetic lipid probes (Figure 1-7).

Immunostaining as well as genetically encoded construct such as small tags and sensors have been widely used for the study of proteins. These molecular biology tools have been successfully applied to study lipids but their availability and usability can be limited.

Hundreds of proteins possess lipid binding domains. A subset of these domains, when soluble, have been derived into fluorescent protein indicators. Typically, by fusing a FP to a lipid binding domain, one can follow the translocation of the probe from the un-bound state in the cytosol to the bound state at the membrane where the lipid is being biosynthesized. If the lipid is metabolized, the anchoring moiety is lost and the indicator will diffuse away from the membrane. Those indicators can be expressed in live cells and do not require addition of exogenous lipids, making them well suited to look at physiological changes in lipid concentration. However, the nature of the translocation readout restricts their application by making them specificity adapted to look at rapid increases in lipid at the plasma membrane, such as after activation of phospholipases(210, 211). Other than their scarcity, it is important to keep in mind that overexpression of the lipid binding domain can lead to buffer effects, for example by slowing down the metabolism of the bound lipid.

A method to overcome the limited availability and application of lipid binding protein is by synthesizing modified lipid probes. Radiolabeled lipids have been used to investigate lipid metabolism in cells but their experimental utility is limited because of low spatial resolution at the single cell level(212). Another technique is the direct fusion of a fluorophore to the structure of the native lipid, for example with BODIPY or NBD(213), allowing visualization of the lipid in live cells. However, in comparison to proteins, lipids are very sensitive to modification. Studies have shown that fluorophore conjugation can affect biophysical properties of the lipids as well as masking the lipid functional group (Figure 1-7). This can lead to changes in the lipid membrane partitioning, where the fluorophore dictates the sub-cellular localization of the lipid (214, 215). Interestingly, for reasons unknown, lipids labelled with aromatic groups such as coumarin or the fluorophores aforementioned preferentially

localize to the ER and Golgi(216). An alternative to aromatic dyes are polyene tags, typically attached at the end of the lipid tail and comparatively smaller to aromatic dyes (Figure 1-7). These lipid probes were shown to not suffer from the same limitation as the dyes described above. However, because of their maximum absorption around 350 nm and proportion to photo-bleach, polyene are more challenging to utilize for *in vivo* experiments(217) and not widely applicable.

Another approach to fluorescently tag lipid probes for tracking in cells is the addition, typically on the lipid tail, of an alkyne for click chemistry. The small size and hydrophobic nature of the alkyne limits functional interactions to permit faithful monitoring of the lipid dynamics (Figure 1-7). However, because of the cytotoxicity of the copper catalysis, this method requires to fix cells after different time point to investigate the dynamics of the lipid probe by fluorescence. In addition, fixation and permeabilization reagents compatible with click chemistry will extract cellular lipids, including the probe, which can make this application challenging(218). Multifunctional lipid derivatives, described below, can avoid some of these challenge by photo-crosslinking the probe to nearby proteins. Nevertheless, it would be much preferred if minimally labeled native lipid species could be traced in real time with good spatial resolution in an intact cell. With Stimulated Raman scattering (SRS) imaging, a vibrational spectroscopic imaging technique, one could theoretically do so(219). Each chemical group of a biomolecule has a specific molecular vibrational spectrum associated to it that can be used as a natural (tag-free) or quasi tag-free label. SRS is capable of imaging down to micromolar concentrations of a given small molecule in real time provided functional groups such as double bonds exhibit unique sharp Raman peak features. Carbon-deuterium (C-D) and alkene-deuterium (C=C-D) bonds are spectrally isolated from

the endogenous Raman bands, as is the alkyne bond, which makes alkyne lipid derivatives well suited for SRS imaging(220). While successful studies have already used SRS to look at lipid metabolism, the detection sensitivity still needs to be improved to detect the sub-micromolar concentrations of lipids in cells(221).

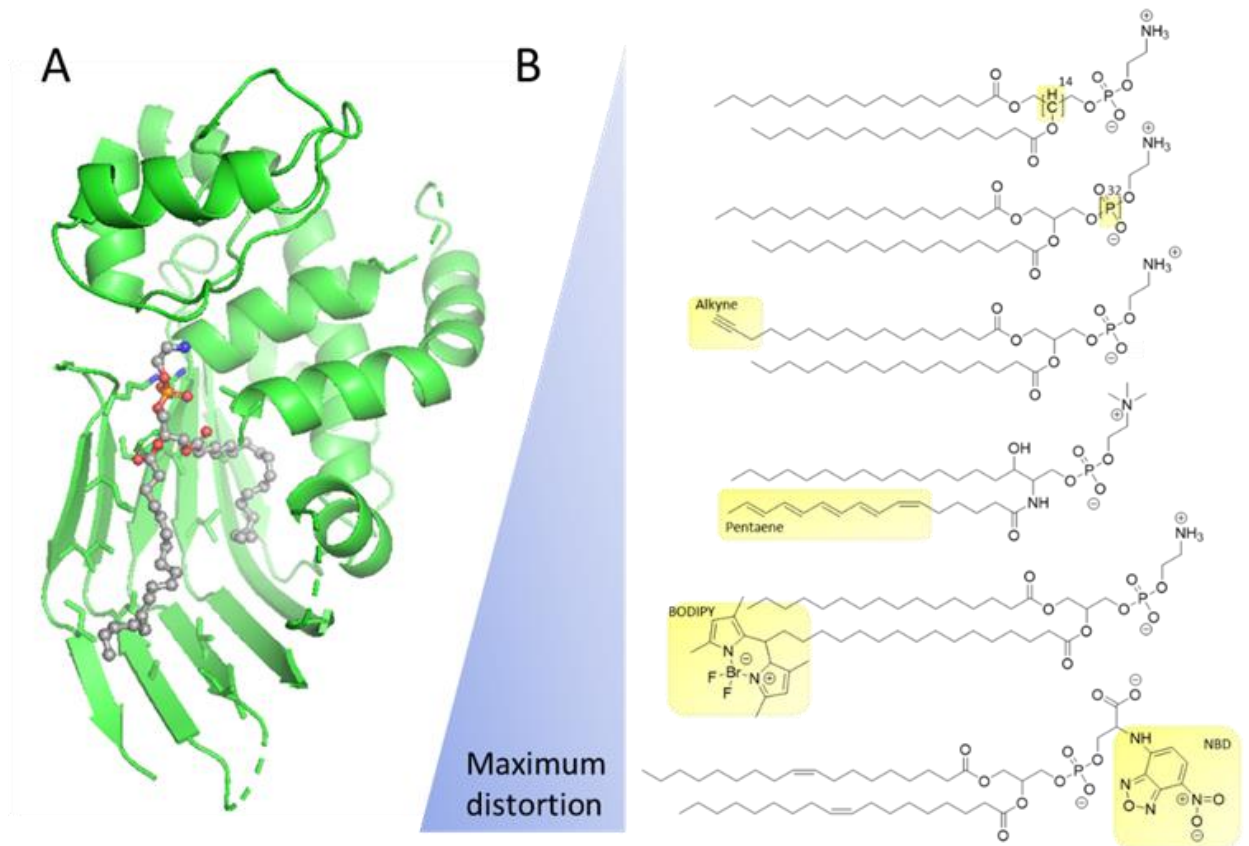


Figure 1-7. Tagged lipid derivatives. (A) Crystal structure of the PE-bound N-terminal domain of Atg2 (PDB 6A9J). (B) The incorporation of a radioactive label provides the least severe modification while the addition of a large fluorophore such as BODIPY might alter the location, recognition and metabolism severely compared to the endogenous lipid.

Bifunctional lipids for lipid visualization and interactome screen

As mentioned above, a challenge of tagging lipid post cell fixation is the inevitable washing away of the lipid probe together with the cellular lipids. By adding a diazirine to the acyl chain, the probe can be photo-crosslinked to nearby molecule (see Chapter1, photosensitive chemical tools), essentially fixing the probe at its current position and can then be

fluorescently tagged for visualization. Many different lipid probes bearing an alkyne and a diazirine were designed, named bifunctional lipid derivatives(222), to study phospholipids(120), fatty acid(223) and many others(222, 224).

Another important application of bifunctional lipids is to screen for and identify lipid-protein interaction. The weak lipid-protein interactions and the limited availability of lipid-binding antibodies have made identifying protein binders particularly challenging. By using photo-crosslinking to covalently link the lipid to its binding proteins and using the alkyne group to pull down the lipid probe along with its bound proteins, both challenges can be effectively overcome. This type of approach, for example, allowed the identification of new protein binders of ceramide(225).

Lipids are rapidly metabolized in cells and bifunctional lipids are subject to rapid turnover as well. This can be useful if one is interested in tracking lipid metabolism in cells but it can make it challenging to discern between the original lipid and metabolization products when visualizing the probe or identifying protein binders. To prevent lipid metabolism and signaling, it is possible to add a coumarin cage on the lipid headgroup. This enables spatial and temporal control over the lipid biological function and was applied to generate many different “caged” lipids(226, 227). Some of these coumarin cages can be released by illumination with 400 nm light and are orthogonal to the photo-activation of the diazirine at 350nm (Figure 1-4). This means that this photo-cage group can be appended to the bifunctional lipid generating trifunctional lipid derivatives with two photoactivable groups functionally orthogonal. By uncaging the probe prior to photo-crosslinking, visualization and identification of protein interactors can be achieved with unparalleled precision. Many

trifunctional lipids were synthesized such as sphingosines, phospholipids, and fatty acids(228-231).

Additionally, a feature of the trifunctional lipids is their systematic localization in endomembranes, primarily ER and Golgi, prior to uncaging. As described above, the aromatic coumarin group is likely driving this subcellular localization. This feature allows to observe potential transport of the lipid across organelle by photo-crosslinking and fixing cell at different time point after uncaging. For example, after uncaging of TF-phosphoinositol, a rapid transfer from endomembranes to the plasma membrane was observable within a few minutes(229).

Chapter 2: FRET-based biosensors for measuring dynamic changes in ADP-ribosylation

Alix Thomas, Kapil Upadhyaya, Daniel Bejan, Hayden Adoff, Varik Harris, Michael Cohen
& Carsten Schultz

Portions of this chapter are adapted from: Thomas et al, A genetically encoded sensor for real-time monitoring of poly-ADP-ribosylation dynamics in-vitro and in cells. Acs Sensor(232)

ACKNOWLEDGMENT STATEMENT: Thanks to Kapil Upadhyaya for synthesizing isoADPr and purifying the recombinant WWE domain, Daniel Bejan for performing Western Blot experiments and providing input on experiment designs, Hayden Adoff for performing imaging experiments, Michael Cohen and Carsten Schultz for contributing to the experimental design, analyzing the data, and editing the manuscript.

ABSTRACT

ADP-ribosylation, the transfer of ADP-ribose (ADPr) from nicotinamide adenine dinucleotide (NAD⁺) groups to proteins, is a conserved post-translational modification (PTM) that occurs most prominently in response to DNA damage. ADP-ribosylation is a dynamic PTM regulated by writers (PARPs), erasers (ADPr hydrolases), and readers (ADPR binders). PARP1 is the primary DNA damage-response writer responsible for adding a monomer (MARylation) or polymer (PARylation) of ADPR to proteins. Monitoring the *in vitro* and in-cell kinetics of these enzymes in real time, along with the turnover of the ADP-ribose motif, can be pivotal in designing effective drug inhibitors and unraveling the regulation of the write-erase cycle. Successful antibodies, mass spectrometry and

genetically-encoded sensors have allowed the specific detection of ADPR with temporal resolution, yet they may fail to capture the complete ADPR cycle or have proven to be technically challenging to implement in an assay. Here, we describe two genetically encoded FRET probes for semi-quantitative monitoring of PARylation (pARS) and MARylation (mARS) dynamics. With a ratiometric readout and excellent signal-to-noise characteristics, we show that both sensors can monitor PARP1-dependent PARylation or MARylation with temporal and spatial resolution. pARS provided unique insights into PARP1-mediated PARylation kinetics *in vitro* and high-sensitivity detection of PARylation in live cells, even under mild DNA-damaging conditions. We also show that pARS can be used to determine the potency of PARP inhibitors *in vitro* and, for the first time, in live cells in response to DNA damage. The robustness and ease of use of pARS make it an important tool for the PARP field. While mARS requires more characterization, we believe its use in combination with pARS will facilitate study of PARylation and MARylation dynamics, furthering our understanding of PARP1 regulation and signaling.

INTRODUCTION

PARP1 is a critical first responder to various types of cell DNA damage(233). The binding of PARP1 to damaged DNA leads to its activation via long-range allostery. Active PARP1 catalyzes ADP-ribosylation of itself and other protein targets (e.g., histones) using nicotinamide adenine dinucleotide (NAD⁺) as a substrate(234, 235). PARP1-mediated ADP-ribosylation leads to the recruitment of DNA damage response (DDR) proteins and, ultimately, DNA repair(138). DDR-defective cancer cells are uniquely and profoundly sensitive to the loss of PARP1, referred to as synthetic lethality. This finding inspired the

clinical development of PARP1 inhibitors, five of which are FDA-approved for the treatment of DDR ovarian and breast cancer(236).

For years, it was thought that PARP1 predominately generates polymers of ADP-ribose, a process called poly-ADP-ribosylation (PARylation) on glutamate and aspartate residues of protein targets. Yet recent studies show that PARP1 catalyzes mono-ADP-ribosylation (MARylation) on serine residues of protein targets(160), a process significantly enhanced by the co-factor protein HPF1(161, 162). The initial site of serine MARylation may become a starting point for further serine PARylation; however, a recent proteomics study showed that serine in PARP1 targets is predominately MARylated and not PARylated(163), suggesting that in cells, PARylation occurs predominately on glutamate/aspartate.

Like other PTMs, glutamate/aspartate PARylation and serine MARylation are reversible. ADP-ribose hydrolase 3 (ARH3) is the only known serine MARylase in cells(166, 237), whereas poly-ADP-ribose glycohydrolase (PARG) is the predominant PARylase in cells. The rapid reversal (minutes timescale) of PARylation by PARG under DNA damage conditions is critical for faithful DNA repair; knockdown of PARG or inhibition of PARG activity results in defects in DNA repair, underscoring the critical role of PARylation in the DNA damage response(238).

The transient nature of PAR in cells makes it challenging to study PARylation using conventional methods such as Western blotting. An effective approach to tracking the spatiotemporal dynamics of PARylation in live cells is using a genetically encoded sensor. A typical sensor design is based on a domain that recognizes PAR with high specificity and selectivity. Such PAR-binding domain-based sensors have been described(172, 239, 240).

However, they suffered from a low signal-to-noise ratio and were only shown to detect PAR levels qualitatively under strong PARP1 activation conditions.

Here, we describe the design and characterization of a highly sensitive and specific Förster Resonance Energy Transfer (FRET) based sensor, which we call pARS, that dynamically monitors PARP1-dependent PARylation *in vitro* and in live cells (Figure 1). We observed PARP1-mediated PARylation kinetics on the seconds time scale, which revealed sigmoidal kinetics suggesting allosteric modulation of PARP1. pARS could semi-quantitatively measure changes in PARylation in live cells in response to increasing DNA damage. Finally, we find that pARS can be used for determining PARP inhibitor potency in live cells, demonstrating its potential for screening PARP inhibitors in a cellular context.

MATERIAL AND METHODS

Chemicals

Protease inhibitor cocktail (Roche Diagnostics), mass spectrometry grade proteases (Thermo Fisher), ADPr (Sigma), isoADPr (synthesized by Kapil Upadhyaya for this study), DB008 (provided by the Cohen lab)(241), Olaparib (Selleck Chemical), PDD00017273 (SigmaAldrich), AZD5305 (Selleck Chemical), DNase I (Roche Diagnostics), NAD⁺ (Sigma), methyl methanesulfonate (Thermo Fisher), Hoechst (Thermo Fisher), activated DNA (Sigma).

pARS overexpression and purification for *in-vitro* characterization

pARS was overexpressed in *Escherichia coli* Rosetta (DE3) cells. A one-liter culture was grown at 37 °C in LB-Miller broth containing kanamycin (50 µg/ml) with vigorous shaking (120 rpm) to an optical *A*₆₀₀ of ~0.7 before expression was induced by addition of IPTG to

a final concentration of 0.5 mM. After further growth for 3 h, cells were harvested by centrifugation at $6000 \times g$ for 20 min, and lysed by sonification in 40 ml of Buffer A [50 mM Tris (pH 7.5), 150 mM NaCl, 10mM beta mercaptoethanol, 1 U of DNase I and a tablet of cOmplete™ ULTRA protease inhibitor cocktail (Roche Diagnostics, Indianapolis, IL, USA)]. The cell lysate was cleared by centrifugation at $20\,000 \times g$ for 30 min at 4 °C, and the supernatant was filtered using a 0.22 μ m filter and loaded onto a 5 ml Ni-NTA column (Thermo, Hispur Ni-NTA) pre-equilibrated in Buffer A. Resin was then washed with 10 column volumes of Buffer A, 10 column volumes of Buffer B [50 mM Tris (pH 7.5), 10 mM imidazole, 150 mM NaCl, 10mM beta mercaptoethanol], followed by 100 ml of Buffer C [50 mM Tris (pH 7.5), 20 mM imidazole, 150 mM NaCl, 10mM beta mercaptoethanol] before the protein was eluted with Buffer C supplemented with 400 mM imidazole. The Ni-NTA eluate was reconcentrated using Amicon spin filter, filtered using 0.22 μ m filter and further purified using a 5mL HiTrap Heparine HP column with an FPLC chromatography system (AKTA prime). The column was equilibrated with Buffer A and the sample was applied to the column with a flow rate of 3 ml/min. Elution was done following a 3-step program: 5 column volumes of Buffer A, 40 column volumes of gradient from 0 to 100% of Buffer D [50 mM Tris (pH 7.5), 1 M NaCl, 10 mM beta mercaptoethanol], and 5 column volumes of Buffer D at a flow rate of 3 ml/min. Fractions were analyzed on SDS-Page. Selected fraction was reconcentrated using Amicon spin filter following manufacturer's protocol.

Full spectrum acquisition and kinetics

Excitation–emission spectra and kinetics were measured using a Cary Eclipse fluorescence Spectrophotometer (Agilent). Data acquisition was carried out in Hepes buffer (50 mM

HEPES, 150 mM NaCl, 4 mM MgCl₂ pH 7.5) supplemented with fresh 0.2 μM tris(2-carboxyethyl)phosphine (TCEP). For kinetics experiments PARP1 was added at 5 nM and pARS at 250 nM. The reaction was started after collection of a one-minute baseline by manual addition of NAD⁺ at various concentrations. Kinetics measurements were collected at one second intervals with excitation at 440 nm and emission at 475 and 527 nm under constant agitation. FRET change was calculated by dividing the acceptor fluorescence intensity by the donor fluorescence intensity and normalization to baseline fluorescence. Maximum reaction rates were independently measured from the sigmoidal fit for each curve at different substrate concentrations. *K_m* values were estimated using nonlinear regression analysis and curve fitting using the Michaelis–Menten function in Prism (GraphPad).

***In vitro* steady state PARP1-autoPARylation measurements with pARS**

PARP1 was added at RT to a final concentration of 10 nM in HEPES buffer (50 mM HEPES, 150 mM NaCl, 4 mM MgCl₂ pH 7.5) supplemented with fresh 0.2 μM TCEP. Inhibitors of various concentrations were pre-incubated before addition of NAD⁺ at 100 μM. The reaction proceeded at 30 °C for 30 min before quenching of the reaction with 10 μM Olaparib. PARG (10 nM) or NUDT16 (3 μM) were added to the reaction mixture and incubated at 30 °C for 90 min. pARS (0.5 μM) was added to the mixture and transferred to a 384 well plate for imaging on a Tecan plate reader using 440 excitation and sequentially collecting emission at 475 and 527 nm (+/- 10 nm). FRET change was calculated by dividing the acceptor fluorescence by the donor fluorescence and normalization to a condition without PARP1. IC₅₀ values were estimated using three-parameter regression analysis and curve fitting with no further constraints using Prism.

Binding assay on agarose gel

pARS or WWE domain were incubated at various concentration with 1 kb DNA (0.1 μ M) at room temperature in 50 mM HEPES, 150 mM NaCl, 4 mM MgCl₂ pH 7.5 for 5 min. The mixture was then loaded on a 1% Tris-acetate (fisher) agarose gel supplemented with ethidium bromide and ran for 20 min at 100 V. The gel was imaged on a BioRad imager in the UV channel (for DNA) and green fluorescence channel (for pARS).

Stable cell line generation expressing pARS

Flp-In-293 cells were purchased from Thermo Fisher Scientific (cat # R75007), cultured in DMEM supplemented by 10% FBS and grown at 37 °C with 5% CO₂. Stable expression of pARS was achieved by transient transfection of pARS and pOG44 using Lipofectamine 2000 (ThermoFisher Scientific, Cat # 11668019). To ensure sufficient genetic diversity, 40% confluent cells in a T75 flask were transfected to provide more than 10 colonies upon addition of 100 μ g/mL hygromycin (ThermoFisher Scientific, Cat #10687010) for selection. Following transfection and selection, all hygromycin-resistant HEK293 Flp-In cells were sorted for expression, expanded, and frozen for further experimentation. HEK293 Flp-In cells expressing pARS were maintained in 50 μ g/mL hygromycin.

Live cell imaging acquisition

Cells were seeded in eight-well Lab-Tek microscope dishes for 24 h (to reach 60-70% confluence) before transfection in full growth DMEM medium. 150 ng of the pARS sensor were mixed with 0.3 μ l of JetPrime in 20 μ l of the manufacturer's buffer, incubated for 15 min and added to the cells. After overnight incubation the transfection medium was replaced with fresh full growth medium. 48 h later cells were imaged at 37 °C in full medium. Imaging was performed on a dual scanner confocal microscope Olympus Fluoview 1200, using a 63x

(oil) objective. The FRET sensor was excited using a 440 nm laser (at a laser power of 1.0%) and the signal was collected in the CFP/YFP emission channels. For DNA damage stimulation, cells were treated with 1 mM H₂O₂ or 10mM MMS or UV light irradiation. For the FRAP assay, cells were irradiated with 100% 375 nm laser for 4 s. For full field of view irradiation (Figure 5), cells were pre incubated with various concentration of Hoechst for 5 min then washed with fresh full growth medium before starting imaging. Cells were irradiated with the 375 nm laser and ~20mW/cm² for 1 sec.

Microscopy image analysis

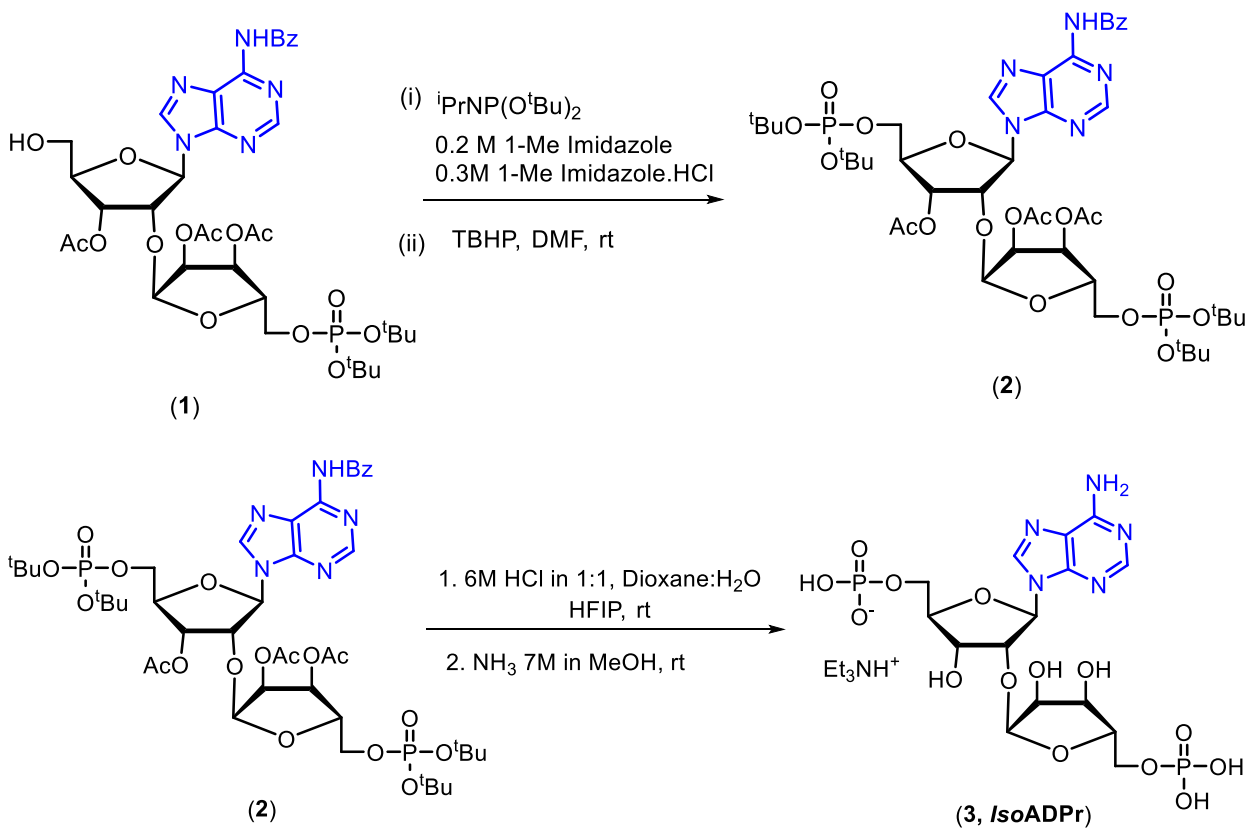
All images were analyzed with FIJI software(242). Primarily, multi-channel images were separated into single channels and converted to 32-bit. Each channel was then smoothed and the time course experiment was duplicated and stacked using the Z project function (using the CFP channel). Using the stacked channel image, region of interest in the nucleus of each cell were manually defined. A ratiometric image of the Venus channel divided by the CFP channel was then generated, the previously acquired ROI mask was superimposed to the time course experiment and the multi-measure function was applied to it. From this stack, we extracted mean single cell values from the time course experiment. Those values were then exported to an excel file for further analysis. The ratio was normalized to baseline and plotted on Graphpad.

Statistics

For experiment in cells, we report means \pm standard errors. All the experiments were performed in biological triplicates except unless otherwise indicated. For *in-vitro*

experiments, we report means \pm standard errors unless specified otherwise in the figure legend.

Synthesis of IsoADPr (Done by Kapil Upadhyaya)



Scheme 2-1. Compounds were synthesized by Dr. Kapil Upadhyaya. See Methods section in <https://doi.org/10.1101/2024.06.11.598597>

RESULTS

To detect PARP1-mediated PARylation, we designed a FRET-based sensor that contains the specific PAR-binding domain WWE from the ubiquitin E3 ligase RNF146, sandwiched between a well-established pair of fluorescent proteins with mTurquoise (mTurq) as a donor and the yellow fluorescent protein mVenus as acceptor(37, 243, 244)

(Figure 1). When PARP1 was PARylated *in vitro*, the sensor oligomerized on PAR units resulting in a strong increase in FRET compared to baseline level

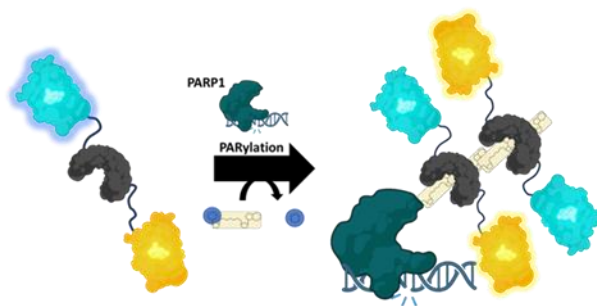


Figure2-1. Sensor design of pARS. Generated using BioRender

(Figure 2-1 and 2-2A). The addition of trypsin led to the cleavage of the sensor and a loss of the observed FRET(Figure 2-2A). Because the FRET change depends on the oligomerization of the sensor onto PAR chains, the molecular ratio of pARS over PARylated PARP1 is critical in setting the dynamic range. An excess of the sensor can lead to a reduced dynamic range, attributable to residual, unbound sensor. At the same time, an insufficient sensor-to-PAR ratio may cause signal loss due to the increased distance between each sensor molecule. We show here that a molecular ratio of 50/1 pARS-to-PARP1 is optimal to maximize the dynamic range of the sensor (Figure 2-2B). Surprisingly, we noticed that upon adding DNA without PARP1, pARS exhibited an increase in FRET comparable to the addition of auto-PARylated PARP1 (Figure 2-2F). We investigated if pARS can directly bind to DNA, which would lead to an unwanted increase in FRET. pARS and DNA were incubated at different pARS concentrations in the presence or absence of DNase. Starting at 5 μ M pARS, we observed a shift in DNA migration and smearing of the sensor, which was prevented by adding DNase, indicating that pARS binds to DNA in the micro-molar range *in vitro* (Figure 2-2G-H). Next,

we incubated a recombinant WWE domain with DNA and found that WWE binds to DNA with a similar affinity to pARS. The WWE-Y145A mutant, which cannot bind to PAR, also loses its ability to bind to DNA, suggesting that WWE binds DNA and PAR. Accordingly, we prevented unspecific FRET increase of pARS by using lower DNA concentration when performing PARP1 reactions.

We next assessed the ability of pARS to distinguish MAR from PAR. The smallest known unit of PAR recognized by the WWE domain is isoADPr, which is the unique repeating unit of PAR(243, 244). Dr. Kapil Upadhyaya synthesized isoADPr by an improved synthetic path(245, 246) (see Methods, Scheme 2-1) and incubated pARS with isoADPr before adding prePARylated PARP1. isoADPr effectively blocked the PARylated PARP1-mediated FRET change. In contrast, pre-incubation with ADPr, which does not bind to the WWE domain(243), did not significantly impact the PARylated PARP1-mediated FRET change (Figure 2-2C). These results demonstrate the specificity of pARS for PAR versus MAR. pARS specificity was further tested using enzymes that can degrade PAR: NUDT16, a pyrophosphatase, and PARG, an O-glycohydrolase(247). Treatment of PARylated PARP1 with these enzymes led to a complete loss of FRET (Figure 2-2D), further confirming the selectivity of pARS for detecting PAR. Finally, we utilized pARS to determine the potency, in a 384 well plate format, of the clinically approved PARP1 inhibitors Olaparib and AZD5305 as well as DB008(241), a low potency PARP1 inhibitor. We obtained IC₅₀ values of 3.4 and 3.1 nM for Olaparib and AZD5305 respectively, and 850 nM for DB008, in alignment with previous reports(248, 249) (Figure 2-2E).

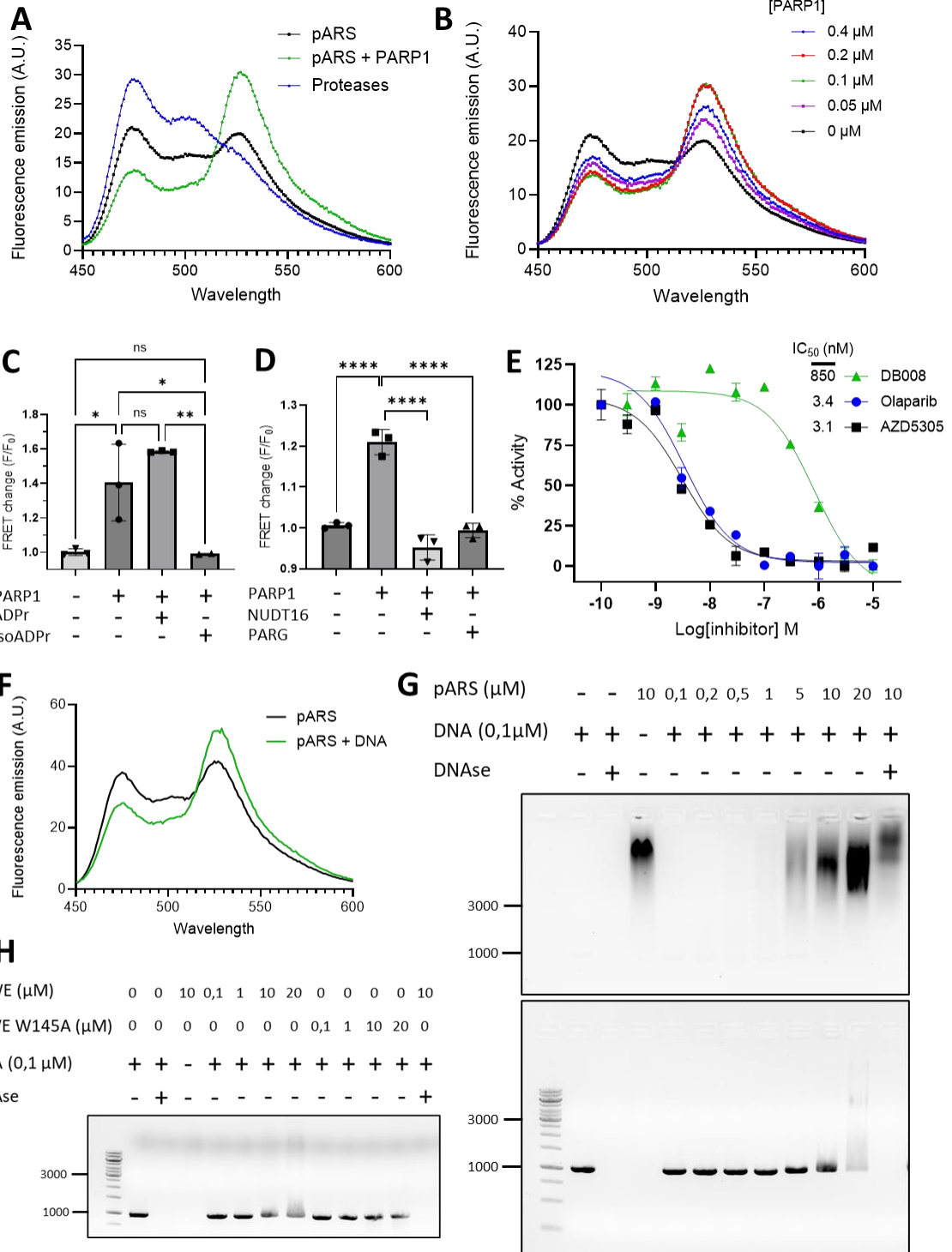


Figure 2-2. A. Fluorescence emission spectrum of pARS (5 μ M) excited with 440 nm (+/- 10) light with or without PARP1 (100 nM). B. Fluorescence emission spectrum of pARS (5 μ M) excited with 440 nm (+/- 10) light with different concentration of auto-modified PARP1. A ratio of 50 to 1 (pARS-to-PARP1) gives the best dynamic range. C. FRET change of pARS upon PARP1 activity with or without pre-incubation with 10 μ M ADPr or isoADPr. D. FRET change of pARS upon PARP1 activity with or without the remover enzymes NUDT16 and PARG. E. pARS FRET reporter assay to assess potency of Olaparib, AZD5305, and DB008 against PARP1 (10 nM) in a plate reader. * $p < 0.05$, ** $p < 0.01$, * $p < 0.005$, **** $p < 0.001$ (One way Anova). At least three independent experiments. F. Fluorescence emission spectrum of pARS (5 μ M) excited with 440 nm (+/- 10) light with or without DNA (0,1 mg/mL). G.H. DNA binding of pARS and WWE PBD were assessed with a dose response of respective purified proteins with 0.1 μ M DNA (1 kb).**

To accurately monitor PARP1 kinetics *in vitro*, we added the sensor to PARP1 before initiating the PARP1 reaction. This allowed us to follow PARP1 activity in real time on the second timescale. We found that increasing NAD^+ concentrations increased the rate and magnitude of the FRET change. Interestingly, we observed a delayed increase in the reaction rate and the optimal fitting curve of our data corresponded to an allosteric/sigmoidal model, suggesting allosteric modulation of PARP1 (Figure 2-3A). As expected, the maximum reaction velocity increased with the NAD^+ concentration following a hyperbolic fit. We determined a K_m for PARP1 of 8.62 μ M (Figure 2-3B), consistent with prior published K_m values on full length PARP1(250). Intriguingly, decreasing the temperature to 15° C during the PARP1 auto-PARylation reaction appeared to increase either the total amount of PAR chains or their length, as reflected by the gradual higher maximum product concentration when the reaction proceeded at a lower temperature (Appendix 2-1). Finally, we investigated PAR removal by PARG in real-time (Figure 2-3C). The addition of PARG rapidly reduced FRET following an exponential decay model. Inhibition of PARG using the selective small molecule PARG inhibitor PDD00017273 (PDD), prevented the PARG-mediated FRET decay. By examining the kinetics of PARP1 and PARG with resolution at the seconds timescale, we hope to facilitate and expand the range of applications compared to previously established PAR reporters(172, 251, 252), and open new avenues for characterizing the

regulation of PARP1-mediated PARylation by modulators and inhibitors, and how mutations in PARP1 and PARG can impact their activities.

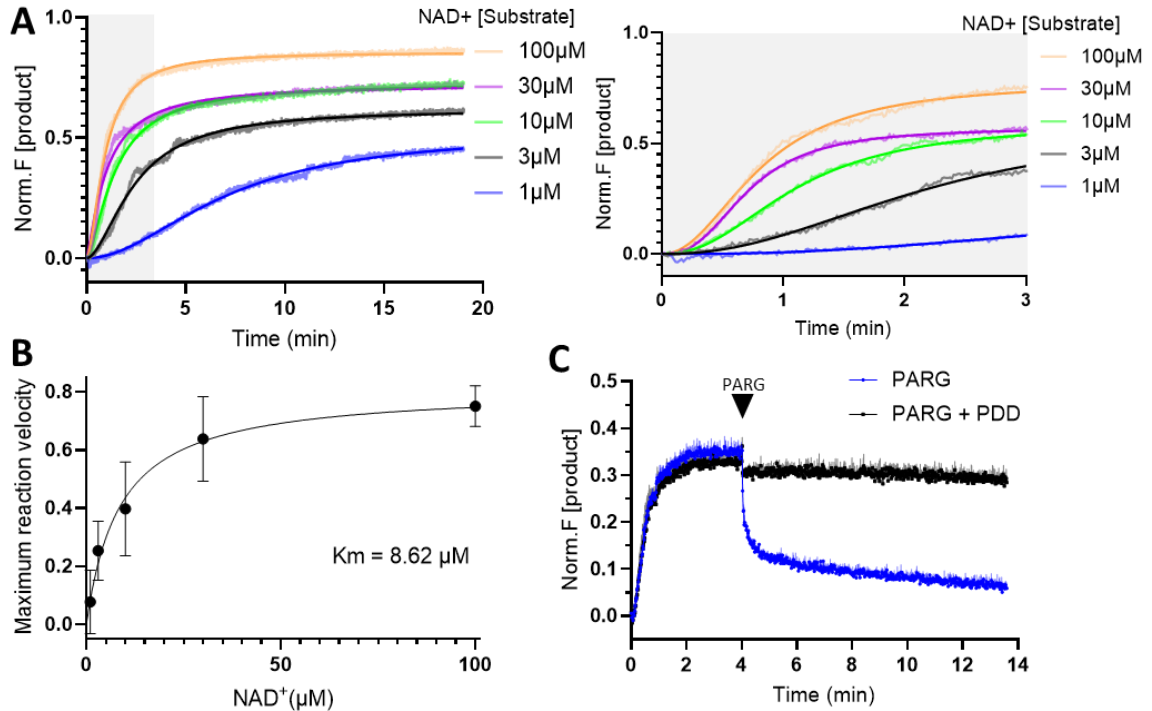


Figure 2-3. PARP1 kinetics **A.** PARP1 (5 nM) dependent PAR formation under various NAD⁺ concentrations. Curve was fitted using an allosteric/sigmoidal non-linear regression model. In grey is a zoom of figure A showing sigmoidal fit in early time points. **B.** Normalized reaction velocities from (A) for determining K_m via Michaelis-Menten kinetics of PARP1. **C.** PARP1 (5 nM) dependent PAR formation at 10 μM NAD⁺ (37°C) with the addition of PARG (20 nM) in the presence or absence of PDD (1 μM). Data is shown as Mean ± SEM of two independent experiments.

Having established pARS as a robust sensor for monitoring PARP1-dependent PARylation *in vitro*, we next sought to evaluate pARS in live cells. We expressed pARS in HeLa cells and performed live-cell FRET imaging. Multiple nuclear location sequences (NLS) were added to the sensor on its N- and C-terminus to achieve complete nuclear expression of pARS (Figure 2-4A). Upon treatment of cells with 1 mM H₂O₂, which induces DNA damage, we observed an increase in FRET (7.16-fold increase relative to standard deviation) followed by a gradual decrease back to baseline within 20 min. Treatment with the PARP1/2 inhibitor

Olaparib (1 μ M) fully abolished the response, while adding the PARG inhibitor PDD (1 μ M) potentiated the increase in FRET and prevented the decay of the signal, consistent with the notion that PARG is the major PARylase in cells (Figure 2-4B). Alternative induction of DNA damage using methyl-methanesulfonate (MMS) led to an increase in FRET almost identical to H₂O₂ (Figure 2-4D-E). Next, we determined if PARP1 was the major PAR writer in cells. Beyond PARP1, PARP2 is a closely related family member that also PARylates proteins in response to DNA damage. We expressed pARS in WT, PARP1 KO, and PARP2 KO U2OS cells and treated with H₂O₂. PARP2 KO cells showed the same H₂O₂-induced FRET increase as WT cells; by contrast, the H₂O₂-induced FRET increase was abolished entirely in the PARP1 KO cells (Figure 2-4C). These results show that in U2OS cells, the PARylation response after DNA damage is primarily dependent on PARP1 with minimal contribution of PARP2. This confirmed previous observations of PARP2 mainly catalyzing the synthesis of branched PAR chains(165). Together, these results demonstrate that our sensor can reliably follow the spatiotemporal dynamics of PARylation mediated by PARP1 in response to DNA damage in live cells. To confirm our *in vitro* experiments that pARS functions via oligomerization of several sensor molecules, we generated variant “homo” versions of pARS with either two mTurquoise or two mVenus fluorescent proteins on each end of the WWE domain. When expressing both constructs, we observed an increase in FRET after treatment with H₂O₂ (Figure 2-4F), albeit with lower sensitivity, suggesting that the mechanism of action is similar *in vitro* and in cellulo.

Additionally, we showed that pARS binds to the site of DNA damage after irradiation with a 375 nm laser similar to the previously reported probes, GFP-WWE and ddGFP-WWE(171, 172) (Figure 2-4H). Mutating Tyr145 to alanine in the WWE domain of pARS, leading to

loss of PAR binding, abolished the FRET changes of the sensor in live cells(243) (Figure 2-4G). Taken together, our results show that the FRET increase of pARS upon DNA damage in live cells is driven by the oligomerization of the sensor on PAR.

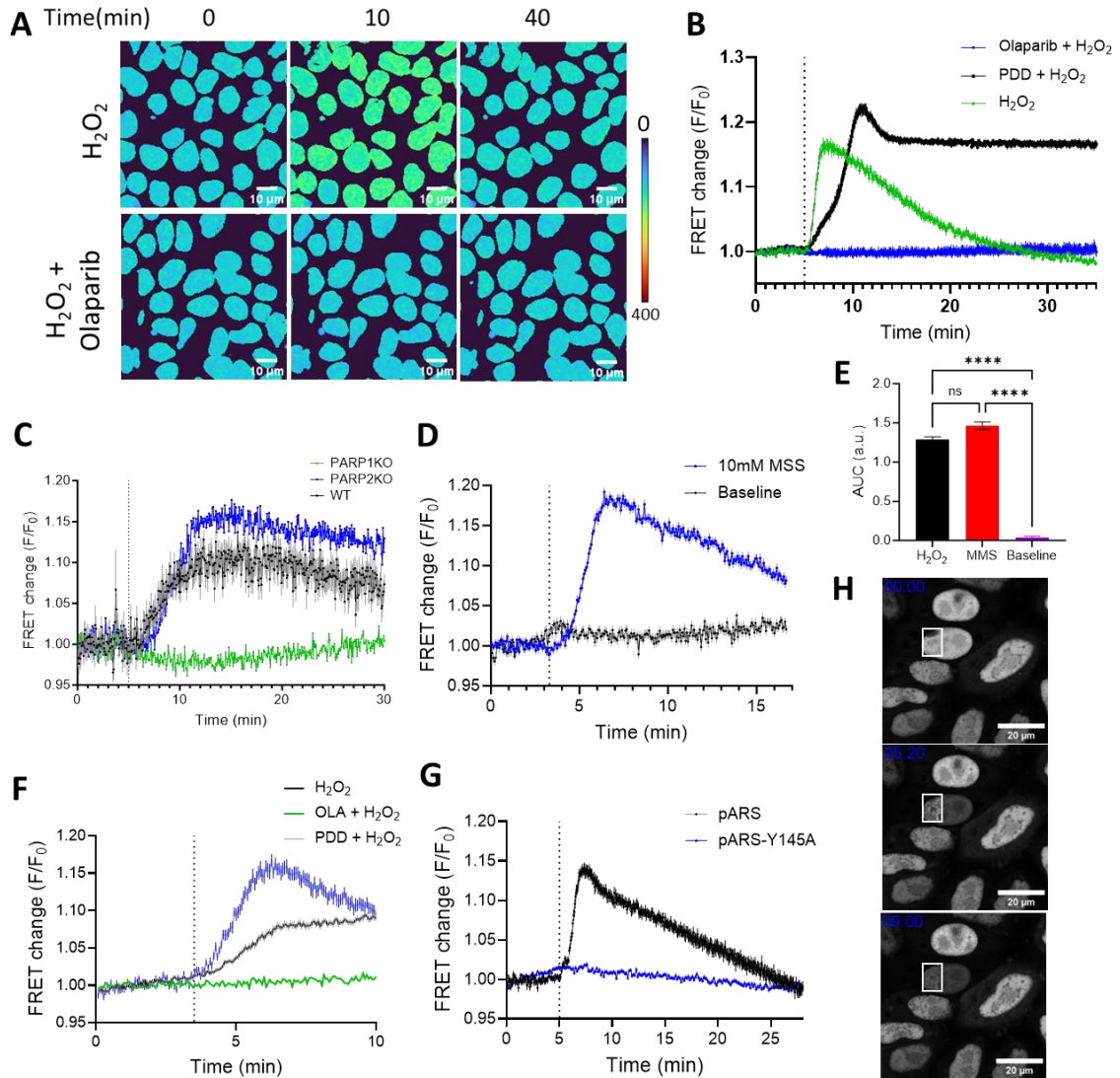


Figure 2-4. pARS in live cell **A.** FRET ratio (CFP/YFP) of HeLa cells transfected with pARS at different time points after treatment with 1 mM H_2O_2 with or without PARP1 inhibitor Olaparib. Colors are representative of the CFP/YFP ratio of pixel intensities after background subtraction. **B.** Average of 27, 24 and 26 HeLa cell traces showing FRET changes of pARS after treatment with 1 mM H_2O_2 , with or without pretreatment with PDD or Olaparib. **C.** Average of 35, 55 and 43 cell traces showing FRET changes of the pARS sensor in U2OS cells WT, PARP1KO or PARP2KO after treatment with 10 mM MMS. Data is shown as mean \pm SEM of two independent experiments. **D.** Average of 176 and 136 cell traces showing FRET change of the pARS sensor in HeLa cells after treatment with 10 mM MMS. Data is shown as mean \pm SEM of three independent experiments. **E.** FRET changes of pARS after treatment with 1 mM H_2O_2 or 10 mM MMS. **F.** Average of 119, 54 and 32 traces of HeLa cells co-expressing homoTurq-pARS and homoVenus-

pARS after treatment with 1 mM H₂O₂, with and without pretreatment with Olaparib or PDD. **G.** FRET changes of pARS in 23 cells or the “dead” pARS-Y145A sensor in 72 cells after treatment with 1 mM H₂O₂. **H.** Confocal micrograph representing different time points of FRAP experiment using 375 nm laser at 100% laser power on HeLa Kyoto cells transfected with pARS (See supplemental video). Data are shown as Mean ± SEM of three (A,B,C) or two (D,E) independent experiments. *p < 0.05, **p < 0.01, ***p < 0.005, ****p < 0.001 (One way Anova)

Treatments such as millimolar concentrations of H₂O₂ or MMS induce massive DNA damage within cells but are often the standard used for detecting PARP1-mediated PARylation in cells using more conventional methods such as Western blotting. Given the excellent signal-to-noise of our sensor, we wanted to know if we could detect lower levels of PARylation in live cells using milder DNA damage conditions. We therefore used a 375 nm laser combined with different concentrations of Hoechst, a dye potentiating DNA damage induction by UV irradiation(253) (Figure 2-5A). By subjecting HEK 293 cells stably expressing pARS to minimal irradiation (0.1% laser power), we characterized the range of PARP1 activity, from saturation with 10 μM Hoechst to a 10% increase of maximum FRET in the presence of 0.2 μM Hoechst (Figure 2-5B,C). We did not observe any increase in FRET after laser irradiation in cells transfected with pARS-Y145W, demonstrating the absence of photobleaching potentially contributing to the increase in FRET (Figure 2-5D). These results demonstrate the tunability of the sensor and its ability to semi-quantitatively monitor changes in PARylation dynamics upon minor changes in the DNA damage response in live cells.

Lastly, we sought to demonstrate the utility of pARS for determining the potency of PARP1 inhibitors in live cells. We used 375 nm irradiation in the presence of 1 μM Hoechst, which induced about 80% of the dynamic range of the sensor. This ensured that the FRET signal was not saturated. Incubation of HEK 293 cells stably expressing pARS with increasing concentrations of Olaparib led to a dose-dependent decrease in the FRET response (Figure 2-5E). We then calculated the area under the curve for each dose-response. We obtained an

IC₅₀ of Olaparib in live HEK293 cells of 11.9 nM (Figure 2-5F), which fits in the median of literature values ranging from 3 nM to 250 nM obtained using Western blotting(241, 250, 254). Together, these results demonstrate that pARS is useful for evaluating PARP1 inhibitor potency in live cells.

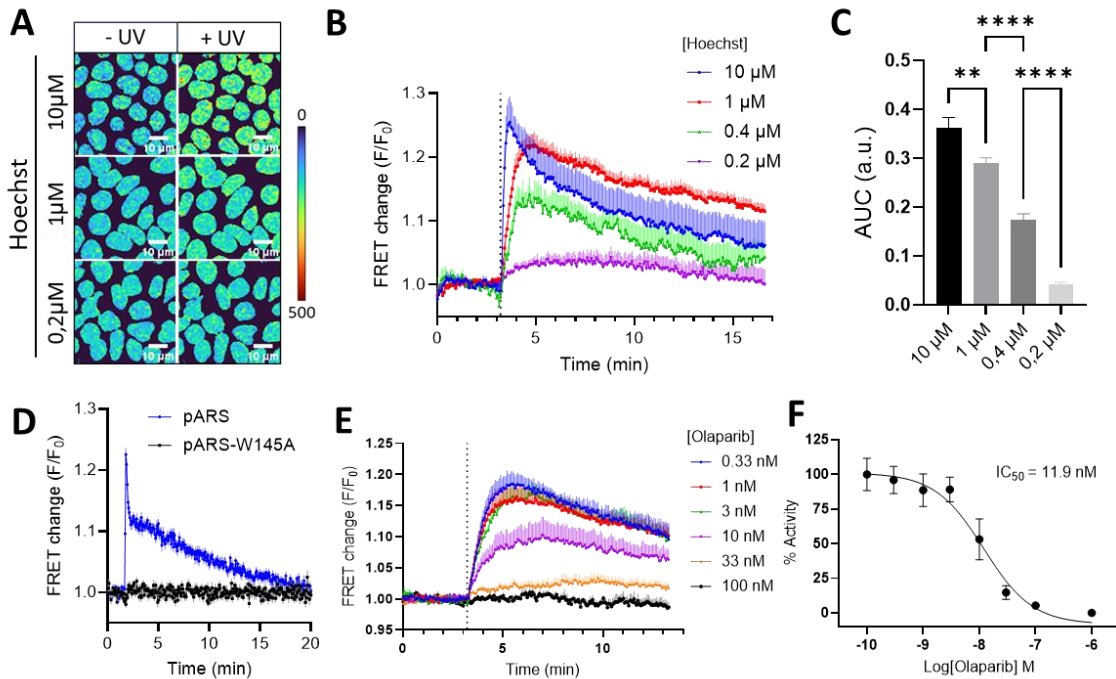


Figure 2-5. pARS Semi-quantification in live cell **A.** FRET ratio (CFP/YFP) before and after UV irradiation of HEK 293 cells stably expressing pARS. Cells were treated with 10, 1, or 0.2 μM of Hoechst 5 min before the experiment. Colors are representative of the CFP/YFP ratio of pixel intensities after background subtraction. **B.** FRET changes of pARS over time as in (A) after irradiation with 375 nm laser for 1 s. **C.** Bar graph representing the area under the curve (AUG) of each trace in (B) between 3.2 and 5 min. **D.** Average of 19 and 20 cell traces showing FRET changes of the pARS sensor or pARS-W145A in HEK 293 cells after irradiation with a 375 nm laser for 10sec. **E.** FRET changes of pARS stably expressed in HEK 293 pretreated with 1 μM Hoechst and irradiated with a 375 nm laser for 1 s. Cells were treated with various concentrations of Olaparib. **F.** Dose response curve assessing Olaparib potency in live cells. Values were derived from area under the curve values of Figure 4D traces. Data is shown as Mean \pm SEM of three (A,B,C) or two (D,E,F) independent experiments. * $p < 0.05$, ** $p < 0.01$, *** $p < 0.005$, **** $p < 0.001$ (One way Anova)

We show that our ratiometric readout and high signal-to-noise ratio can be applied to evaluate PARP1 inhibitor potency in live cells. However, the dynamic range can be further improved

which could help look at physiological change of PARP1 activity, such as an increase in PARylation during S phase of the cell cycle. To do so we elected to use pre-engineered “cassettes” developed in the lab which consist of 32 different combinations of circular permuted fluorescent proteins and linkers(37). By inserting our WWE recognition domain into each construct of the cassette, we rapidly generated the 32 different constructs and tested each in HeLa cells. We successively treated each cell population with 1 mM H₂O₂ and observed a range of responses from a ~20% decrease in dynamic range, to an increase of ~50% with the best construct relative to our original pARS sensor (Figure 2-6). In this pARS variant, the linker between mTurquoise and WWE was extended from 4 to 8 amino acids, and cp173Venus was replaced with Venusd. This optimized sensor will help in investigating low transitory PARP1 activity in cells in the future.

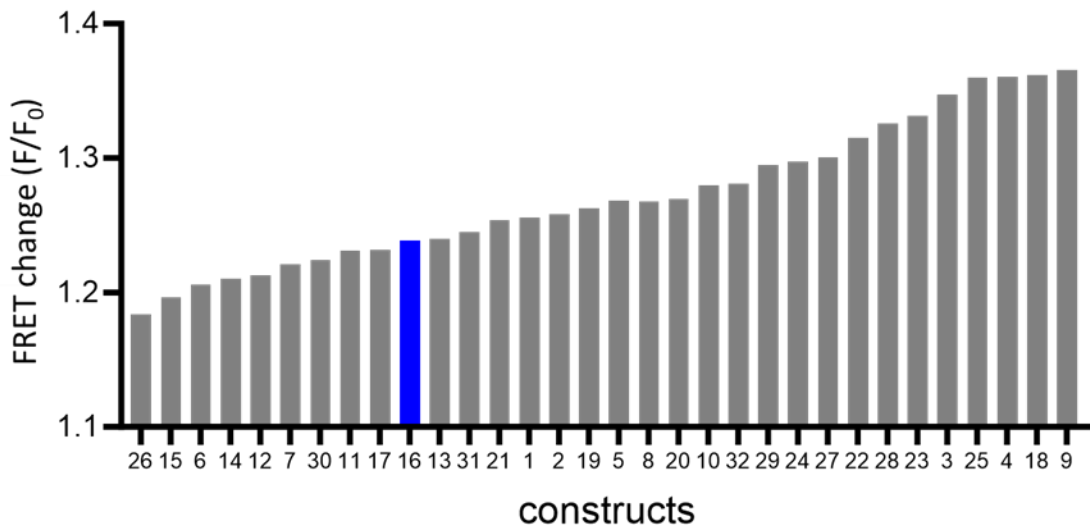


Figure 2-6. Bar graph representing the maximum FRET ratio (CFP/YFP) of HeLa cells transfected with 32 different variant (cassettes) of pARS after treatment with 1 mM H₂O₂. Each bar represent the average of single cell traces collected in one biological replicate for each construct. The blue bar represents the original pARS.

Development of a PARP1-dependent MARYlation FRET sensor

Following the discovery of serine ADPr and the HPF1-PARP1 complex, recent findings have shown the prevalence of mono-ADPr upon DNA damage, shifting the field of research not only on PARP1-dependent PARylation but the interplay between MARYlation and PARylation. Although recognition sequences for mono-ADP-ribosylation have been identified and characterized, no genetically-encoded sensor has been developed to monitor this process in live cells. To detect PARP1-mediated MARYlation, we designed an intramolecular FRET-based sensor (mARS) that contains a 10 amino acid peptide corresponding to the tail of histone H3 from which Serine10 is specifically MARYlated by PARP1, the pair of fluorescent proteins mTurq as a donor and mVenus as an acceptor, a flexible EV linker and the specific MAR-binding domains Macro 2 and 3 from PARP14(255). We hypothesized that in the basal state, the mARS sensor will have an open conformation with low FRET signal. After DNA damage, the serine (S10) of the histone H3 peptide will be MARYlated by PARP1 and Macro 2 and 3 can bind to the modified residue leading to a strong FRET signal (Figure 2-7A). We expressed mARS in HeLa cells and performed live-cell FRET imaging. Similarly to pARS, multiple nuclear location sequences were added to the sensor to achieve complete nuclear expression. Upon treatment of cells with 1 mM H₂O₂, we observed an increase in FRET followed by a gradual decrease back to baseline within 25 min (Figure 2-7B-C). Treatment with the PARP1/2 inhibitor Olaparib (1 μM) fully abolished the response (Figure 2-7B). To confirm that the FRET increase observed is dependent on the MARYlation of S10, we mutated the serine to an alanine and reproduced the experiment. Surprisingly, we observed the same change in the FRET response after treatment with H₂O₂ (Figure 2-7D). To further investigate the mechanism of action of the sensor we generated variant “homo”

versions of pARS with either two mTurquoise or two mVenus fluorescent proteins on each end of the Macro 2/3 and histone H3 peptide and co-expressed them in HeLa cells. We did not observe an increase in FRET after treatment, suggesting that the mechanism of action is intra-molecular, as hypothesized (Figure 2-7E).

Several key residue mutations of the macro domains of PARP14 have been identified as sufficient to abrogate binding of the domains to mono-ADPr. The mutation G1055E and D1235A were shown to interfere with macro2 and macro3 binding to ADPr respectively. We mutated both residues on mARS which abolished the FRET changes of the sensor in live cells (Figure 2-7F), indicative that the sensor mechanism is dependent on the binding affinity of macro 2 and 3 for mono-ADPr. With those results, we aimed to determine if the sensor was MARYlated by PARP1, and, if so, to identify the substrate residues using enzymatic and chemical treatment. We transfected HeLa cells with mARS and induced DNA damage by treating the cells with 1 mM H₂O₂ for 10 min and immunoprecipitated mARS using GFP-Trap beads. Repeated washes were performed to remove PARP1, which shares a similar molecular weight with mARS, making it difficult to distinguish between the two on a Western blot. Without on-bead treatment, we observed a band with both the pan MAR antibody 33204 and the serine MAR specific antibody 33205 (Figure 2-7G). Following treatment with ARH3, an enzyme that hydrolyzes serine ADP-ribosylation, the serine MAR band completely disappeared, as expected, while the pan MAR band was markedly reduced. Neither the mono-ADP ribosylhydrolase 1 (MacroD1), which removes ester-linked MAR, nor the glycohydrolase PARG affected either band. However, chemical treatment with hydroxylamine, which cleaves ADPr ester bonds, partially decreased the pan MAR band. Taken together, these results show that mARS is MARYlated predominantly on serine

residues as well as on other residues, likely glutamates and aspartates, following DNA damage. MD2 and 3 of PARP14 have been reported to be auto-ribosylated(256, 257). ADP-ribosylated serine residues in the KS motif accounts for most of serine MAR observed in humans (160, 258). Two such motifs are present on each of the PARP14 macro domain used as recognition domains in mARS. Given how mARS appeared to be predominantly MARYlated on serine, we mutated those serine residues into alanine, generating a Δ SMacro-mARS mutant, to test if the KS motif of the macro domains contributed to the FRET change observed after DNA damage. In HeLa cells transfected with Δ SMacro-mARS, a FRET increase was observed. However, mutating S10 of the histone H3 peptide did not abolish the response, suggesting that other residues are modified and contribute to the observed FRET change (Figure 2-7H). Further investigation will be needed to identify the modified residues.

We sought to confirm the specificity of mARS for PARP1-dependent MARYlation. Mutating E988Q in the PARP1 active center reduces its elongation activity 2800-fold, essentially turning PARP1 into a MARYlating only enzyme (259, 260). We co-transfected PARP1-KO U2OS cells with mARS or pARS and either mCherry-PARP1 or mCherry-PARP1-E988Q. In cells transfected with mChP1, H₂O₂ treatment resulted in an increase in FRET for both mARS and pARS (Figure 2-8A-B). In contrast, cells transfected with mCherry-PARP1-E988Q did not show a significant increase in FRET for pARS, while mARS, although reduced, still exhibited a marked increase in FRET. Importantly, we confirmed the activity of mCherry-PARP1 in our cell model by Western blot (Figure 2-8C).

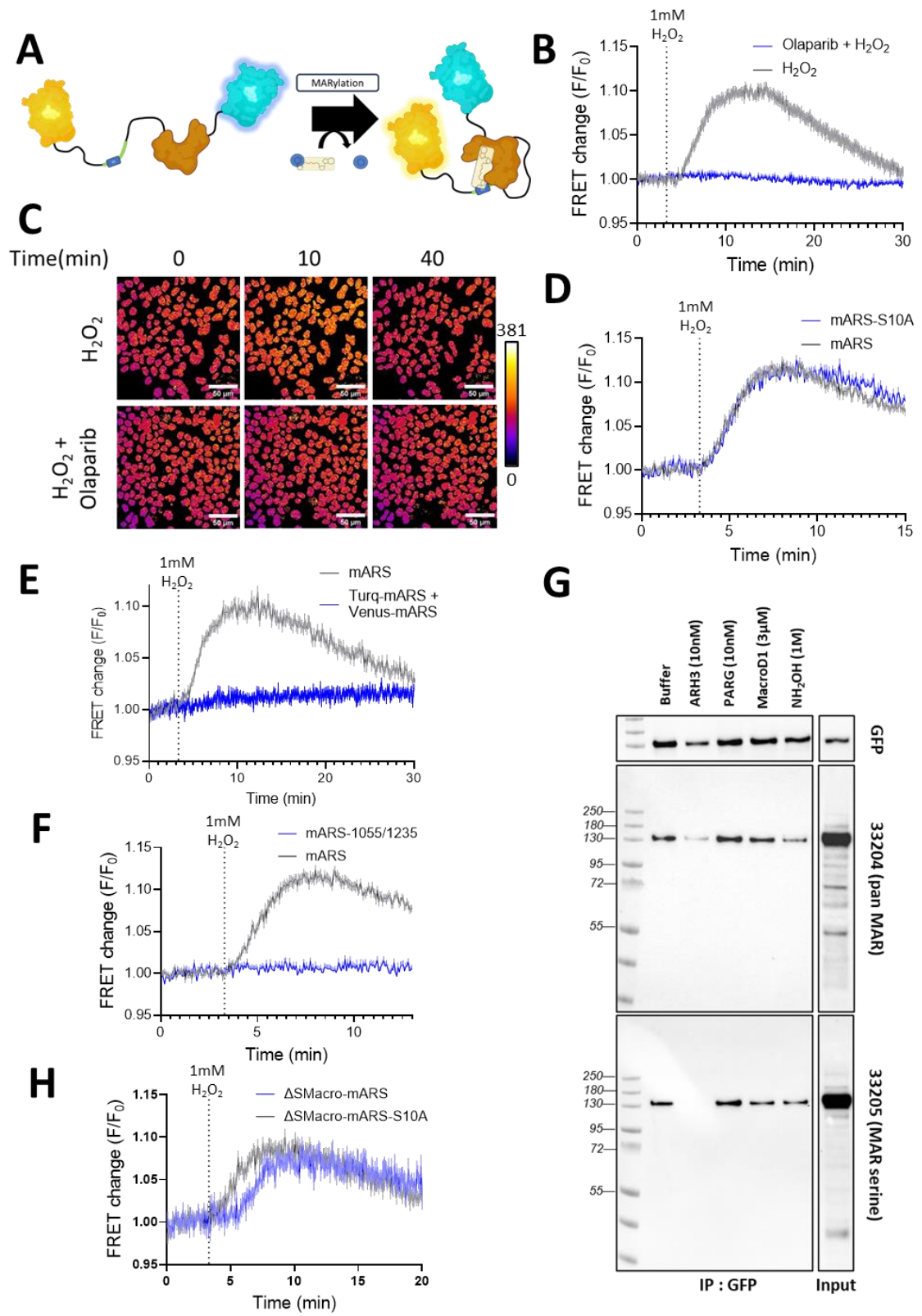


Figure 2-7. A. Sensor design of mARS. Generated using BioRender **B.** Average 35 and 70 HeLa cell traces showing FRET changes of mARS after treatment with 1 mM H₂O₂, with or without pretreatment with Olaparib. **C.** FRET ratio (CFP/YFP) of HeLa cells transfected with mARS at different time points after treatment with 1 mM H₂O₂ with or without PARP1 inhibitor Olaparib. Colors are representative of the CFP/YFP ratio of pixel intensities. **D.** FRET changes of mARS in 65 cells or the mARS-S10A sensor in 77 cells after treatment with 1 mM H₂O₂. **E.** FRET changes of mARS in 67 cells or the co-transfected Turq-mARS and Venus-mARS sensors in 59 cells after treatment with 1 mM H₂O₂. **F.** FRET changes of mARS in 65 cells or the mARS-1055/1235 sensor in 62 cells after treatment with 1 mM H₂O₂. **G.** Immunoprecipitated mARS with GFP-trap beads and treated with ADPr hydrolases or chemical, followed by Western blotting (N=2 biological replicates). **H.** FRET changes of ΔSMacro-mARS in 24 cells or the ΔSMacro-mARS-S10A sensor in 29 cells after treatment with 1 mM H₂O₂. Data is shown as Mean ± SEM of three (B,D,E) or two (F,H) independent experiments (biological replicates).

As expected, in cells not transfected with mCherry-PARP1, H₂O₂ treatment did not elicit an increase in ADP-ribosylation. In cells transfected with mCherry-PARP1, we observed a light smeared band after 10 min of H₂O₂ treatment and a large increase in signal after treatment with the PARG inhibitor PDD, most likely corresponding to PARP1 elongation activity. In cells transfected with mCherry-PARP1-E988Q, H₂O₂ treatment resulted in no apparent signal with or without PDD. This reflects the decrease in elongation activity of the E988Q mutant, however it will be important to repeat this experiment to confirm residual MARYlating activity of the PARP1-E988Q mutant. Taken together, our results suggest that mARS FRET increase in response to DNA damage is dependent on PARP1 MARYlating activity. Previously, we have shown that in cells expressing pARS, pretreatment with PDD prevented the decay of the FRET signal. In cells expressing mARS and pretreated with PDD, we observed a faster decrease of the signal compared to untreated cells (Figure 2-8D). This is another line of evidence supporting the specificity of mARS towards sensing MARYlation. However, it also suggests a role for PARG in regulating the response monitored by mARS. ARH3 is the main remover of serine ADP-ribosylation(166, 237). To further explore mARS sensing specificity, we expressed the sensor in WT and ARH3KO Hek293 cells and induced DNA damage. In WT cells, we observed a sharp increase followed by a rapid decrease down to ~15% of the maximum signal. In ARH3KO cells, we saw a similar increase in signal which

then dropped to ~50% of the maximum signal (Figure 2-8E). This partial prevention of the decay aligns with the proportion of serine MARYlated, relative to the total MARYlation of mARS, given that ARH3 specifically cleaves MAR from serine residues (Figure 2-7G). Surprisingly, in ARH3KO cells, pre-treatment with PDD led to a total prevention of decay. Transfection of ARH3KO cells with recombinant ARH3 rescued this effect, potentiating the decay to a sub-basal level (Figure 2-8F).

Recent evidences have emerged that serine MARYlation constitutes a second wave of PARP1 signaling following a first wave of PARylation(171). We tried to reproduce this observation by comparing pARS and mARS dynamics in HeLa cells. pARS achieved its peak FRET 2.5 min post-H₂O₂, compared to 7 min for mARS. This is in close alignment with previous experiments looking at PARP1 dependent ADP-ribosylation dynamics(171).

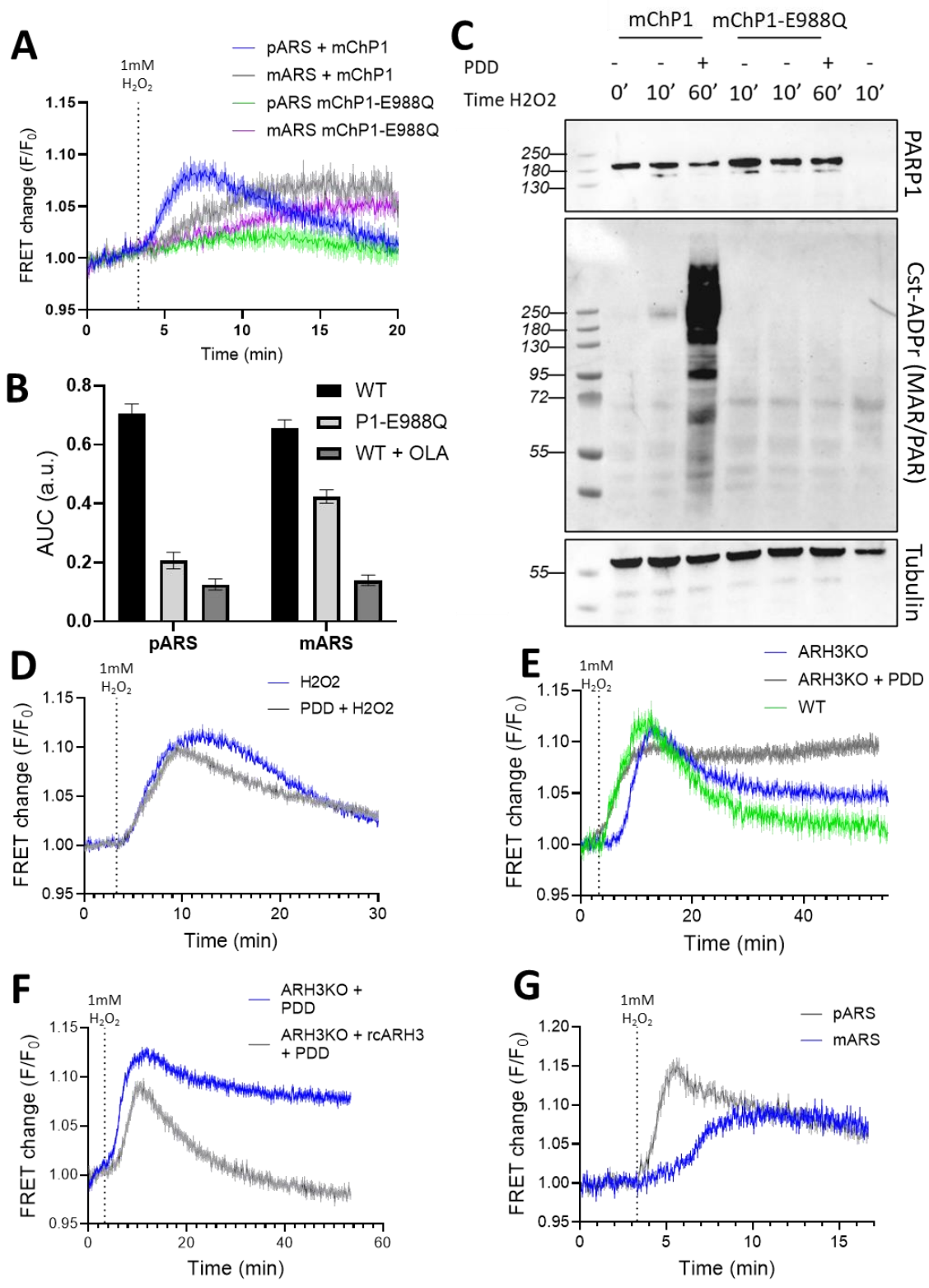


Figure 2-8. mARS characterization **A.** Average of 30 and 27 PARP1KO U2OS cells co-transfected with mCherry-PARP1 (mChP1) and pARS or mARS. Average of 36 and 38 PARP1KO U2OS cells co-transfected with mCherry-PARP1-E988Q and pARS or mARS. All cells were treated with 1mM H₂O₂. **B.** Bar graph representing the area under the curve (AUC) of each trace in (A) between 3.2 and 20 min. **C.** PARP1KO U2OS cells transfected with mCherry-PARP1 or mCherry-PARP1-E988Q were treated with 1mM H₂O₂ with or without pre-treatment with 10μM PDD, followed by Western blotting and probing for poly/mono ADPr, PARP1 and tubulin. **D.** Average of 66 and 62 HeLa cells treated with 1mM H₂O₂ with or without 10μM PDD. **E.** Average of 25 Hek293 cells, 24 ARH3KO Hek293 cells and 30 ARH3KO Hek293 cells pre-treated with 10μM PDD. All cells were treated with 1mM H₂O₂. **F.** Average of 40 ARH3KO Hek293 cells and 40 ARH3KO cells transfected with recombinant ARH3, treated with 10μM PDD and 1mM H₂O₂. **G.** Average of 46 and 18 HeLa cells transfected with mARS or pARS. Cells were treated with 1mM H₂O₂. Data is shown as Mean ± SEM of three (D,E,F) or two (A,C,G) independent experiments (biological replicates).

DISCUSSION

In summary, by utilizing intermolecular FRET, pARS efficiently detects PARP1-mediated PARylation, enabling semi-quantitative measurements *in vitro* and in live cells. This novel approach allows the characterization of PARP1 auto-PARylation kinetics at unprecedented second-scale resolution, potentially advancing our understanding of PARP1 modulation by cofactors and inhibitors. For the first time, our intramolecular FRET sensor mARS enabled semi-quantitative measurements of PARP1-mediated PARylation. While more work is necessary to fully characterize the residues modified on the sensor, we believe mARS, together with pARS, can help dissect the complexity of the regulatory mechanisms governing PARP1(261, 262).

By monitoring PARP1 auto-PARylation in real-time *in vitro*, we unveiled intriguingly delayed kinetics. We believe this is due to PAR acting as an allosteric activator, consistent with recent studies(263). Structural studies have demonstrated that PARP1 activity is influenced by the type of DNA breaks, shifting it from cis to trans-autoPARylation(252, 264-266). In the presence of DNA duplex, acting as mimics of DNA double-strand breaks, two PARP1 monomers can bind in close proximity to both ends of the DNA leading to trans-autoPARylation. However, automodifications occurs predominantly in cis when PARP1 is

bound to single strand breaks (SSB)(265). Additionally, it was shown that PARP1 and PARP2 have preferential SSB DNA structures for activation(252). The nature of the DNA breaks could contribute to our observed kinetics *in vitro*. We believe that pARS, thanks to its improved time resolution and throughput compared to streptavidin-biotin methods or FTIR spectroscopy, could help un-tangle the different kinetics of PARP1 under various conditions. The development of PARP1 inhibitors (PARPi) have proven to be a successful avenue in the treatment of cancer via a mechanism known as synthetic lethality(267, 268). The vast majority of PARPi bind with high affinity ranging from 10 pM to 1 nM(269). This can be driven by either a fast rate of association (k_{on}) or slow rate of dissociation (k_{off}). PARP1 is highly abundant in cells, with a nuclear concentration in the μ M range, yet most cellular potency reported for PARP1 fall under the μ M range. Conflicting reports on the cellular efficacy of inhibitors can be explained by the inhibitors concentrating in the nucleus, owing to their tight binding to PARP1. Interestingly, it was recently shown that the k_{off} of PARPi correlates best with their potency in cell assays(270, 271). Leveraging the dynamic range of the pARS sensor, we established a novel live-cell method for quantitative measurement of PARP1-dependent PARylation. This approach enabled precise IC_{50} determination for PARP inhibitors and promises to facilitate the assessment of their dissociation constants (k_{off}) in live cells, a critical factor for determining pre-clinical efficacy(270). This offers significant advancement over previously published qualitative probes(172, 239).

The interplay between PARylation and MARYlation-mediated by PARP1 is considered pivotal for developing next-generation inhibitors. For years, PARP1 inhibitor toxicity has been exclusively associated with the trapping of PARP1 onto chromatin by interfering with PAR chain elongation on glutamate and aspartate, preventing the necessary electrostatic

interference for PARP1 to detach from DNA. HPF1-dependent serine-ADP-ribosylation is now accepted as the main physiological modification catalyzed by PARP1. It is controversial whether the main role of serine MARYlation is as an initiator for PARylation or if it serves direct cellular roles, specifically through the modification of dedicated histone sites. In any case, it is clear that understanding the balance in activity of PARP1 between MARYlation and PARylation will help design a new generation of PARP1/2 inhibitor for the clinic. Our novel genetically encoded biosensor mARS, capable of quantifying MARYlation alongside pARS, could revolutionize our understanding of PARP1's regulatory mechanisms(171). We have shown that mARS is specific to PARP1-dependent MARYlation and is ADP-ribosylated, seemingly exclusively with mono-ADPr. We initially expected that only the serine residue on the histone H3 peptide would be modified upon DNA damage, but we found that many other residues were also targeted, predominantly serines, along with a smaller proportion of glutamate and aspartate residues. Further characterization is necessary to identify the specific residues that are modified and responsible for the observed FRET change upon PARP1 activity. This could enable, through point mutation, the creation of new mARS variants, modified by PARP1 exclusively either at serine or acidic residues. Such sensors would be valuable for understanding the dynamics of MARYlation in cells and could be further adapted to detect other types of ADP-ribosylation relevant to the PARP field.

A recent study generated, by combining the SpyTag technology and a recombinant antibody, a fluorescent probe specific for serine MARYlation which the authors applied in live cell imaging experiments(171). Using this tool, they were able to identify two distinct 'waves' of ADP-ribosylation: the first wave being PARylation and the second serine MARYlation.

Notably, our combined pARS and mARS sensors accurately recapitulated these observed kinetics, highlighting the potential utility of multiplexing both probes in the future.

OUTLOOK AND FUTURE WORK

We have demonstrated that our new pARS can measure dynamic changes in PARP1-dependent PARylation in live cells using relatively mild UV irradiation. This represents a novel approach for assessing PARP1 inhibition and could assist in the future design of PARP1 inhibitors. However, as mentioned in the introduction, the primary advantage of developing dynamic sensors for live cells is the ability to detect physiological, low, transient increases in PARP1 activity during DNA replication. To achieve this, further optimization of pARS will be necessary to enhance its sensitivity.

Our MARylation sensor mARS, while showing promise, needs to be further characterized. More evidence is needed to establish its specificity to PARP1 MARylation activity. This will involve identifying the specific residues ADP-ribosylated by PARP1. An alternative sensor design could also be considered.

Sensor optimization

A first limiting aspect of pARS is the relatively high basal FRET of the sensor (Figure 2-2A). In the present design of the sensor, the linker between CFP and WWE is four amino acids long, while the linker between YFP and WWE is 100 amino acids long and flexible. We hoped that the long linker would decrease basal FRET, the major limiting factor when designing FRET sensors with both pair of FPs linked together(36). Redesigning the long linker could substantially reduce basal FRET. In most proteins or protein domains, the N-terminus and C-terminus are close and oriented toward each other. This causes both FPs to

face the same direction, potentially leading to unwanted intramolecular FRET between CFP and YFP within the same protein, while also possibly reducing desired intermolecular FRET by orienting the FPs away from each other. (Figure 2-9).

Another approach to increase the dynamic range of the sensor would be to replace the FP pair. It was recently demonstrated that switching the donor CFP with a GFP and the acceptor YFP with a HaLo-tag labeled with a far-red silico-rhodamine led to a significant increase in FRET efficiency between the donor and acceptor(74). This new pair could be rapidly implemented into both pARS and mARS.

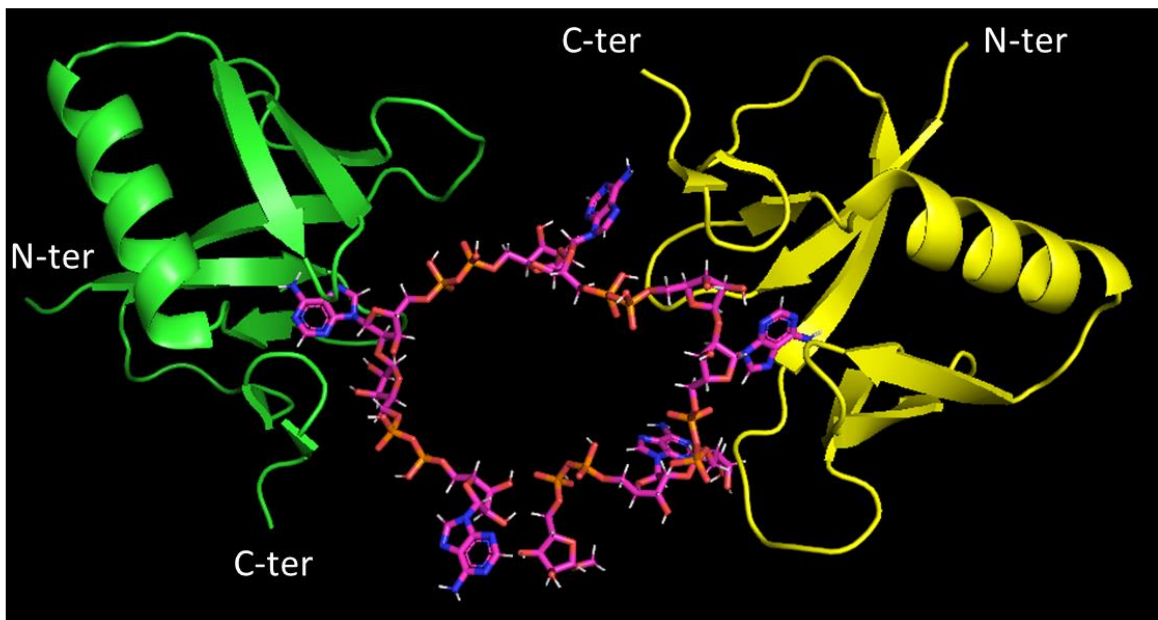


Figure 2-9. Tentative representation of WWE domains (PDB 3V31) bond to poly-ADP-ribose (PAR). The PAR chain was generated using Chem3D energy minimization (MMFF94 force field) and imported to PyMol. The WWE domains were “docked” to PAR by hand following crystal structure of WWE bond to isoADPr(243).

Alternative design for mARS

A significant challenge in studying PARP1 function lies in the diversity of the substrate proteins it modifies. Although advances in mass spectrometry (MS) have improved the identification of these substrates, this variety complicates the design of sensors that rely on the modification of a specific substrate, as the dynamics of modification can vary greatly between them. We selected the tail of histone H3 as our substrate because it is one of the most well-characterized targets for serine-linked MARylation by PARP1 during DNA damage. However, the exact mechanism by which the sensor is modified remains unclear. It is known that PARP1 undergoes auto-MARylation on four different serine residues upon activation. It is possible that the sensor first binds to auto-MARylated PARP1, positioning the histone H3 peptide close enough to be modified by PARP1. This could be a limitation of the sensor, as the increase in FRET would depend on three sequential events: PARP1 auto-MARylation, the binding of the sensor to PARP1, and the MARylation of the substrate peptide. These kinetics might differ significantly from the kinetics of MARylation of histones.

One way to address this issue is by anchoring the sensor directly to the histone. Previous attempts to design sensors anchored on histone tails to monitor post-translational modifications (PTMs) have been successful(35), indicating that anchoring mARS to histone tails could be a promising approach. In this design, CFP could be directly inserted at the end of the histone H3 tail, followed by a long flexible linker with the MAR recognition domain and YFP at the end. MARylation of the histone tail would cause the recognition domain to bind to the tail, bringing YFP closer to CFP and increasing FRET.

Multiplexing for study of PARP1 function in DNA repair.

The simultaneous detection of PAR and/or MAR formation and DNA replication would be useful for studying the role of PARP1 in the DNA repair pathway. Particularly, recent work has shown that PARP1 could be activated during the S phase by unligated Okazaki fragment, helping in their repair by recruiting the single-strand break repair protein XRCC1(148).

One drawback of FRET sensors is their broad spectral occupancy, which can limit multiplexing by spectral overlap. Replacing one of the sensor CFP/YFP FRET pair with the suggested GFP/HaLo-siRhodamine could allow multiplexing of both sensor but would limit the addition of a DNA replication indicator. One possible approach is by replacing the acceptor protein with a non-fluorescent protein or dye as a quencher. The sensor could then be used as an intensimetric sensor on a standard microscope, or potentially could be used for fluorescence lifetime imaging.

Chapter 3: Cannabinoid Receptor Signaling is Dependent on Sub-Cellular Location

Portions of this chapter are adapted from: Alix Thomas, Braden T Lobingier, Carsten Schultz & Aurélien Laguerre

bioRxiv 2024.03.21.586146; doi: <https://doi.org/10.1101/2024.03.21.586146>

ACKNOWLEDGMENT STATEMENT: Thanks to Braden Lobingier for providing input on experiment design and editing the manuscript, Carsten Schultz for contributing to the experimental design, analyzing the data, interpreting the results and editing the manuscript and Aurelien Laguerre for performing calcium imaging experiments, analyzing the data, interpreting the results and editing the manuscript.

ABSTRACT

G protein-coupled receptors (GPCRs) are membrane bound signaling molecules that regulate many aspects of human physiology. Recent advances have demonstrated that GPCR signaling can occur both at the cell surface and internal cellular membranes. Our findings suggest that cannabinoid receptor 1 (CB1) signaling is highly dependent on its subcellular location. We show that the subcellular location of CB1, and its signaling, is contingent on the choice of promoters and receptor tags. Heterologous expression with a strong promoter or N-terminal tag resulted in CB1 predominantly localizing to the plasma membrane and increases in cAMP levels after stimulation. Conversely, CB1 driven by low expressing promoters and lacking N-terminal genetic tags largely localized to internal membranes and agonist-binding negatively regulated cAMP levels. Because receptor location is frequently

altered by adding N-terminal tags, we demonstrated that genetically encodable non-canonical amino acids (ncAA) and fluorescent labeling by click chemistry offer a solution to this problem. We identified sites in CB1 and CB2 which can be tagged without disrupting CB signaling or trafficking after attaching fluorophores in live cells. Together, our data showcases one potential origin of location bias in cannabinoid signaling which now can be experimentally controlled and tracked in living cells through promoters and novel cannabinoid receptor tagging strategies.

INTRODUCTION

G-protein coupled receptors (GPCRs) are essential for regulating human development and physiology, and their perturbation can have dramatic effects on onset and disease progression. As a result, 30% of FDA approved drugs target GPCRs(272). Although there are over 200 structurally distinct GPCRs, they all signal via a few G-proteins. Recently, our understanding of how signal specificity is achieved by GPCRs and how it can be translated to therapeutic intervention has greatly increased(44, 173). Among other significant advancements, the concept of functional selectivity acknowledges that the same receptor can produce different cellular outcomes by modulating the specificity and timing of downstream events(273). This functional selectivity is thought to occur either through biased agonism (i.e ,the ability of a GPCR to adopt different receptor and scaffold conformation based on its ligand)(176, 274), or through location bias (i.e, the ability to signal from different subcellular localizations)(275-277). Emerging data are giving rise to a new signaling model where ligands bind and activate GPCR both at the cell surface and at internal membranes. For example, the B1 adrenergic receptor can stimulate an intracellular *Gas*-mediated cAMP signal from the Golgi apparatus, thereby significantly contributing to the increase in cAMP

levels (278), while the opioid receptors mu and delta can also couple to G α i/o at the Golgi apparatus(182). This location bias can dramatically modulate the activity of therapeutics as it requires the drug to either be actively transported or passively diffusing to the receptor's sub-localization.

Cannabinoid receptor 1, a rhodopsin-like G protein coupled receptor, is generally described as a G α i/o coupled receptor although its specificity for G α i/o was challenged years ago with evidence that the receptor is able to couple to numerous G proteins in different cell types(190, 279). It was shown by Diez-Alarcia *et al* that the cannabinoids Δ^9 -THC, WIN55 and ACEA can stimulate not only the G α i/o pathway but also G α s, G α q and G α 12/13 in a ligand dependent fashion(280). These findings align with reports that stimulation of CB1 in different areas of the brain or in peripheral tissues yields diverse outcomes(281). In addition to the diversity of CB1 coupling to G proteins, there is also heterogeneity in its expression and subcellular location. The expression level of CB1 is very high in the brain(282), but varies widely across other cell types (283, 284). This fluctuating expression level was shown to have implication in the receptor ligand binding and G protein activation(285), with Finlay *et al* and others demonstrating that treatment with CB1 agonists stimulates cAMP in HEK cells highly expressing CB1(286, 287), yet the reasons for this shift from inhibitory to stimulatory signaling remains unclear. CB1 has been described to reside and signal from intracellular compartments(281) such as late endo-lysosomes(200) and mitochondria. Here, it was shown to modulate mitochondrial respiration, intra-mitochondrial cAMP levels and PKA activity(288). To date it remains unclear if this differential coupling of the CB1 to G proteins originates from cell type-specific fluctuations in its expression level or represents a general principle in which signaling is influenced by location bias. Given the recent

appreciation for location bias in GPCR signaling, we hypothesized that the expression level and sub-cellular localization of the CB1 plays a critical role in determining its affinity and interaction profile of G-proteins.

To evaluate the impact of both expression level and location bias of CB1 on downstream signaling, we leveraged approaches commonly employed in GPCR molecular pharmacology. We used higher (CMV) and lower (UBC) expressing promoters to heterologously drive CB1 expression in HeLa cells. We also examined the effects of the commonly utilized N-terminal signal sequence FLAG (SSF) tag for monitoring GPCR expression and trafficking (289). We selected HeLa cells as a model because they lack endogenous CB1 yet possess the necessary downstream effectors for CB1 signaling. We found that lower expression levels predominantly localized CB1 within internal organelles and signaled via *G_{ai}*, contrasting with the prevalent plasma membrane localization and cAMP stimulation at higher expression levels. Furthermore, utilizing the SSF tag in conjunction with low CB1 expression mimicked the receptor's predominant plasma membrane localization previously observed at higher expression levels. This model suggests that the plasma membrane pool of CB1 stimulates cAMP production, whereas the endo-membrane pool reduces cAMP levels through canonical *G_{ai/o}* signaling. To visualize CB1 without interfering with its localization, we incorporated a single non-canonical amino acids in CB1 (*trans*-cyclooctene lysine (TCO*A)) and attached fluorophores by ultrafast copper-free click chemistry in live cells(290).

MATERIAL AND METHODS

This study did not generate new unique reagents.

Data and Code Availability

This study did not generate any unique datasets or code.

EXPERIMENTAL MODEL AND SUBJECT DETAILS

The HeLa Kyoto cell line (RRID:CVCL_1922, female) was kindly provided by R. Pepperkok (European Molecular Biology Laboratory, Germany). HeLa Kyoto (passage 15-35) were grown in 4.5g/L glucose DMEM (Life Technologies, 41965-039) supplied with 10 % fetal bovine serum (Life Technologies, 10270098).

METHOD DETAILS

General.

All chemicals were obtained from commercial sources (Acros, Sigma-Aldrich, Tocris, TCI, Cayman, Alfa Aesar, Atto-tec or Merck) and were used without further purification unless otherwise specified. Rimonabant (5-(4-chlorophenyl)-1-(2,4-dichlorophenyl)-4-methyl-N-(piperidin-1-yl)-1H-pyrazole-3-carboxamide), AM630 ((6-iodo-2-methyl-1-(2-morpholinoethyl)-1H-indol-3-yl)(4-methoxyphenyl) methanone, Forskolin (5-(acetyloxy)-3-ethenyldodecahydro-6,10,10b-trihydroxy-3,4a,7,7,10a-pentamethyl-(3R,4aR,5S,6S,6aS,10S,10aR,10bS)-1H-naphtho[2,1-b]pyran-1-one), Xestospongine C ([1R-(1R,4aR,11R,12aS,13S,16aS,23R,24aS)]-eicosahydro-5H,17H-1,23:11,13-diethano-2H,14H-[1,11]dioxacycloeicosino[2,3-b:12,13-b1]dipyridine) and WIN55, 212-2 ([11R)-2-methyl-11-(morpholin-4-ylmethyl)-9-oxa1-azatricyclo[6.3.1.0⁴,12]dodeca-2,4(12),5,7-tetraen-3-yl]-naphthalen-1-ylmethanone) from Cayman Chemical were dissolved in

dimethylsulfoxide (DMSO) to a stock concentration of 10 mM. Thapsigargin ((3S,3aS,4R,6R,7S,8R)-6-acetoxy-4-(butyryloxy)-3,3a-dihydroxy-3,6,9-trimethyl-8-(((Z)-2-methylbut-2-enoyl)oxy)-2-oxo-2,3,3a,4,5,6,6a,7,8,9b-decahydro-1H-cyclopenta[e]azulen-7-yl octanoate) from Sigma was dissolved in DMSO to a stock concentration of 5 mM. ATP (adenosine 5'-triphosphate disodium salt hydrate) from TCI was freshly dissolved in DMSO to a concentration of 10 mM. Atto488 Me-Tetrazine from Atto-Tec was dissolved in DMSO to a stock concentration of 1 mM. cg2-AG was synthesized, purified and chemically characterized following the methods previously reported in the literature (for details, see Laguerre A, Hauke S, Qiu J, Kelly MJ, Schultz C. Photorelease of 2-Arachidonoylglycerol in Live Cells. *J Am Chem Soc.* **2019**;141(42):16544–16547. doi:10.1021/jacs.9b05978). All chemicals were administrated to cells with a DMSO concentration lower or equal to 0.1 %.

Amplex intact cell assay.

Cells were seeded in a 6 well plates. After 24 h, CB1-APEX constructs were transfected according to the Lipofectamine 2000 (Life Technologies, 11668030) manufacturer protocol. After overnight incubation the transfection medium was replaced with fresh full growth medium. 24 h post transfection cells were lifted and resuspended in PBS. AUR (Amplex UltraRed, Thermo, A36006) was added to cells from a 10 mM stock to a 2 μ M final concentration and incubated at RT for 5 min followed by 10 min at 4°C (from there all steps were performed at 4°C). Cells were then incubated in PBS supplemented with 2% BSA and 50 μ M H₂O₂ for 1 min. The reaction was quenched with 1 mM sodium azide, the cells were spined down and washed with PBS + 2% BSA. Immediately after cells were imaged on a

FACS. The AUR fluorescent reaction product was detected with a Beckman Coulter Cytoflex S (excitation 633, emission 670/30).

Immunostaining of HeLa cells.

After incubation with transfection mix or microscopy, cells were fixed with 4% paraformaldehyde for 15 min, washed twice in PBS, permeabilized in 0.1% Triton X-100 for 2 min and immunostained with primary antibodies overnight. The cells were then washed four times in PBS and incubated with a secondary antibody for 1 h. Cells were then washed four times with PBS and imaged on a dual scanner confocal microscope Olympus Fluoview 1200, using a 63x (oil) objectives.

Genetic code expansion and SPIEDAC tagging.

Cells were seeded in eight-well Lab-Tek microscope dishes for 24 h (to reach 60-70 % confluence) before transfection. After 24 h, 200 ng of hMbPylRS-4xU6M15 (Addgene, #105830) and 200 ng of the respective amber construct were premixed in 20 μ L of DMEM. 0.3 μ L of Lipofectamine 2000 (Life Technologies, 11668030) in 20 μ L of DMEM was then added to the DNA premix and incubated for 20 min at RT before being added to the wells. Shortly after the transfection mixture was added to cells, 100 μ M of the ncAA TCOA *K was added from a 100 mM stock solution in 0.1 M NaOH. After overnight incubation, the transfection medium was replaced with fresh full growth medium. 30 min before imaging, cells were washed two times with DMEM (without FBS) and incubated for 20 min with 1 μ M of Me-Tet Atto488 from a 1 mM stock solution in DMSO. After 20 min cells were washed with imaging medium (Invitrogen, A14291DJ) four times before imaging.

Ca²⁺ imaging experiments.

Cells were seeded in eight-well Lab-Tek microscope dishes for 24 h (to reach 60-70 % confluence) before transfection. For imaging of CB1-GFP transfected cells, 100 ng of CB1-GFP and 100 ng of R-GECO (Addgene #32444) were mixed with 0.2 μ L of lipofectamine 2000 transfection reagent. For imaging of cells transfected with CB1-F180 or CB2-S29, the experimental protocol described in the genetic code expansion section was followed with an addition of 200 ng of R-GECO. For all of the above mixes, DNAs and lipofectamine were separately premixed in 20 μ L of DMEM then mixed together and incubated for 20 min before being added to each well of the eight well Lab-Tek containing 200 μ L of DMEM 4.5g/L glucose supplemented with 10% FBS. Cells were imaged at 37°C in imaging buffer. Imaging was performed on a dual scanner confocal microscope Olympus Fluoview 1200, using a 63x (oil) objective. The R-GECO sensor was imaged using a 559 nm laser (at a laser power of 1.0%) and a 643/50 emission filter. Fluctuations of $[Ca^{2+}]_i$ were monitored through excitation at 559 nm and emission above 600 nm (F/F_0) on the confocal microscope.

Trafficking experiments.

Cells were seeded in eight-well Lab-Tek microscope dishes for 24 h before transfection. 100 ng of CB1-GFP and 100 ng of Rab5-BFP (Addgene #49147) were mixed with 0.2 μ L of lipofectamine 2000 following transfection method previously described then added to the wells. 48 h after the transfection, cells were incubated with 10 μ M of WIN55,212-22 or 10 μ M of rimonabant for 3 h. Cells were imaged at 37°C in imaging buffer. Imaging was performed on a dual scanner confocal microscope Olympus Fluoview 1200, using a 63x (oil) objectives.

EPAC-based sensor imaging experiments.

Cells were seeded in eight-well Lab-Tek microscope dishes for 24 h (to reach 60-70 % confluence) before transfection. 100 ng of the EPAC sensor (Addgene #61622)(291) were mixed with 0.2 μ L of lipofectamine 2000 following the transfection method previously described. After overnight incubation the transfection medium was replaced with fresh full growth medium. 24 h after the first transfection, CB1 (100 ng) or CB2R (100 ng) were mixed with 0.2 μ L of lipofectamine 2000 and added to cells. For CB1-F180 or CB2-S29, the experimental protocol described in the genetic code expansion section was used after the cells were first transfected with the EPAC sensor. Cells were imaged at 37°C in imaging buffer. Imaging was performed on a dual scanner confocal microscope Olympus Fluoview 1200, using a 63x (oil) objective. The EPAC FRET sensor was imaged using a 440 nm laser (at a laser power of 1.0%) and the signal was collected in the CFP/YFP emission channels.

To sort between cells expressing CB1 at the plasma membrane from cells expressing CB1 in endomembrane, the exact field of view during the live cell experiment was saved and the cells removed from the microscope stage and fixed in 4% PFA for 15 min at RT. The cells were then immunostained following the protocol described above. After immunostaining the cells were reset on the microscope stage and using the saved coordinate, re-imaged using an identical field of view and sorted by hand using ImageJ.

siRNA knockdown assay.

siRNA (20 μ M) was mixed with dharmafect according to the manufacturer protocol recommendation for HeLa Kyoto cells. Cells were seeded at 10% confluence in the presence of the transfection mix. After overnight incubation, the transfection medium was replaced with fresh full growth medium. For microscopy, the EPAC-based sensor imaging protocol was performed 48 h after cell seeding. For blotting, cells were lysed 80 h post seeding in

RIPA buffer (Thermo, 89901) containing cOmplete EDTA-free protease inhibitor cocktail (Roche). Lysate were centrifuged at 15000 rpm for 15 min. Total protein was quantified with a BCA assay (Thermo, 23225), normalized, denatured in sample buffer by boiling for 5 min at 95 °C and resolved in a 4-12% gradient gel Bis-Tris gel (Thermo, NP0321BOX). The proteins were then transfer to a PVDF membrane using Trans-Blot Turbo Transfer system (Bio-Rad), blocked in 3% milk PBST and incubated overnight at 4°C with primary antibodies. Blots were washed with PBST 4x5min and incubated with secondary HRP conjugated antibodies for one hour and washed 4x5min. Developing was done with SuperSignal West Femto Maximum Sensitivity Substrate (Thermo, 34095) and imaged on a ChemiDoc (BioRad).

Images analysis.

All Images were analyzed on the FIJI software using the pipeline summarized in Figure S1B. Primarily, multi-channel images were separated into single channels and converted to 8-bit for Ca^{2+} imaging or 32-bit for EPAC experiments. The time course experiment was duplicated and stacked using the Z project function (RFP channel for calcium imaging and CFP channel for EPAC imaging). Using the paintbrush tool set at 0, cells were manually delimited to achieve robust single cell segmentation. A mask of regions of interest was generated using the combination of the threshold and analyze particles tools (as depicted in Figure S1B). This ROI mask was then superimposed to the time course experiment and the multi-measure function was applied to it. From this stack, we extracted mean single cell values from the time course experiment. Those values were then exported to an excel files for further analysis.

Statistical analysis.

All statistical comparisons were performed using One way ANOVA by Prism or Excel. Statistical details of each experiment can be found in the figures and figure legends. For all experiments, the number of cells and error bars (SEM) can be found in the results section and the respective figure legends. All imaging experiments were performed at least in biological triplicates, n indicating the total number of cells.

Key resource table

REAGENT or RESOURCE	SOURCE	IDENTIFIER
Antibodies		
Rabbit polyclonal Cannabinoid Receptor I antibody	Abcam	Cat# ab3561
Rabbit polyclonal Cannabinoid Receptor II antibody	Abcam	Cat# ab3561
Goat anti-Rabbit IgG (H+L) Highly Cross-Adsorbed Secondary Antibody, Alexa Fluor Plus 488	Invitrogen	Cat# A32731
Mouse monoclonal Anti-GNAS antibody	Abcam	Cat# ab21612
Rabbit monoclonal recombinant GNAI2 antibody	Abcam	Cat# ab15720
Rabbit GM130 antibody	CellSignaling	Cat# 12480
Rabbit Calreticulin antibody	CellSignaling	Cat# 12238
Rabbit EEA1 antibody	CellSignaling	Cat# 2411
Recombinant proteins		
hMbPyIRS-4xU6M15	Addgene (Serfling et al,2017)	Cat# 105830
CB1-GFP	Farrens Lab, OHSU	N/A
R-GECO	Addgene (Zhao et al, 2011)	Cat# 32444
CB1	Farrens Lab, OHSU	N/A
CB1-F180	This study	N/A
CB2	UMR cDNA RC (U Missouri)	Cat# AY2421
CB2-S29	This study	N/A
EPAC	Addgene (Dipilato et al, 2009)	Cat# 61622
RAB5-BFP	Addgene (Friedman et al, 2013)	Cat# 49147
^{Ub} C CB1	This study	N/A
^{Ub} C CB1-APEX	This study	N/A
^{Ub} C SSFCB1	This study	N/A
^{Ub} C SSFCB1-APEX	This study	N/A
^{CMV} CB1	This study	N/A
^{CMV} CB1-APEX	This study	N/A
^{CMV} SSFCB1-F180	This study	N/A
Chemicals, Peptides, and Recombinant Proteins		
Rimonabant	Cayman Chemical	Cat# 900048
AM630	Cayman Chemical	Cat# 100069
WIN55,212-2	Cayman Chemical	Cat# 100090
Forskolin	Cayman Chemical	Cat# 11018
Xestospongins C	Cayman Chemical	Cat# 64950
Thapsigargin	Sigma	Cat# T9033
ATP	TCI	Cat# A0157

RESULTS

Expression level and N-terminal tagging direct the sub-cellular localization of CB1.

Immunofluorescence analysis revealed the absence of endogenous cannabinoid receptor 1

(CB1) expression within our HeLa cell line

(Figure 3-1). We established two distinct

expression systems: CMV_{CB1} and Ubc_{CB1} ,

driven by the stronger CMV and weaker Ubc

promoters, respectively(292). Confocal

microscopy imaging delineated disparate

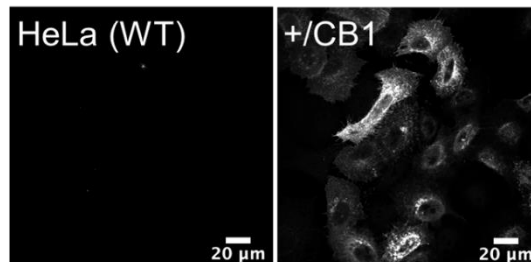


Figure 3-1. Immunofluorescence experiment comparing CB1 expression between untransfected (WT) or CMV_{CB1} (+/CB1) HeLa cells.

subcellular localization patterns between the two expression systems. Ubc_{CB1} primarily

localized within endomembranes, notably the endoplasmic reticulum (ER), Golgi apparatus,

as well as a minor fraction at the plasma membrane. Conversely, CMV_{CB1} predominantly

localized to the plasma membrane, with a residual presence observed at the Golgi apparatus

and ER (Figure 3-2A, 3-3A,B,C). Thus, in our heterologous expression system, subcellular

localization of CB1 was largely controlled by promoter strength.

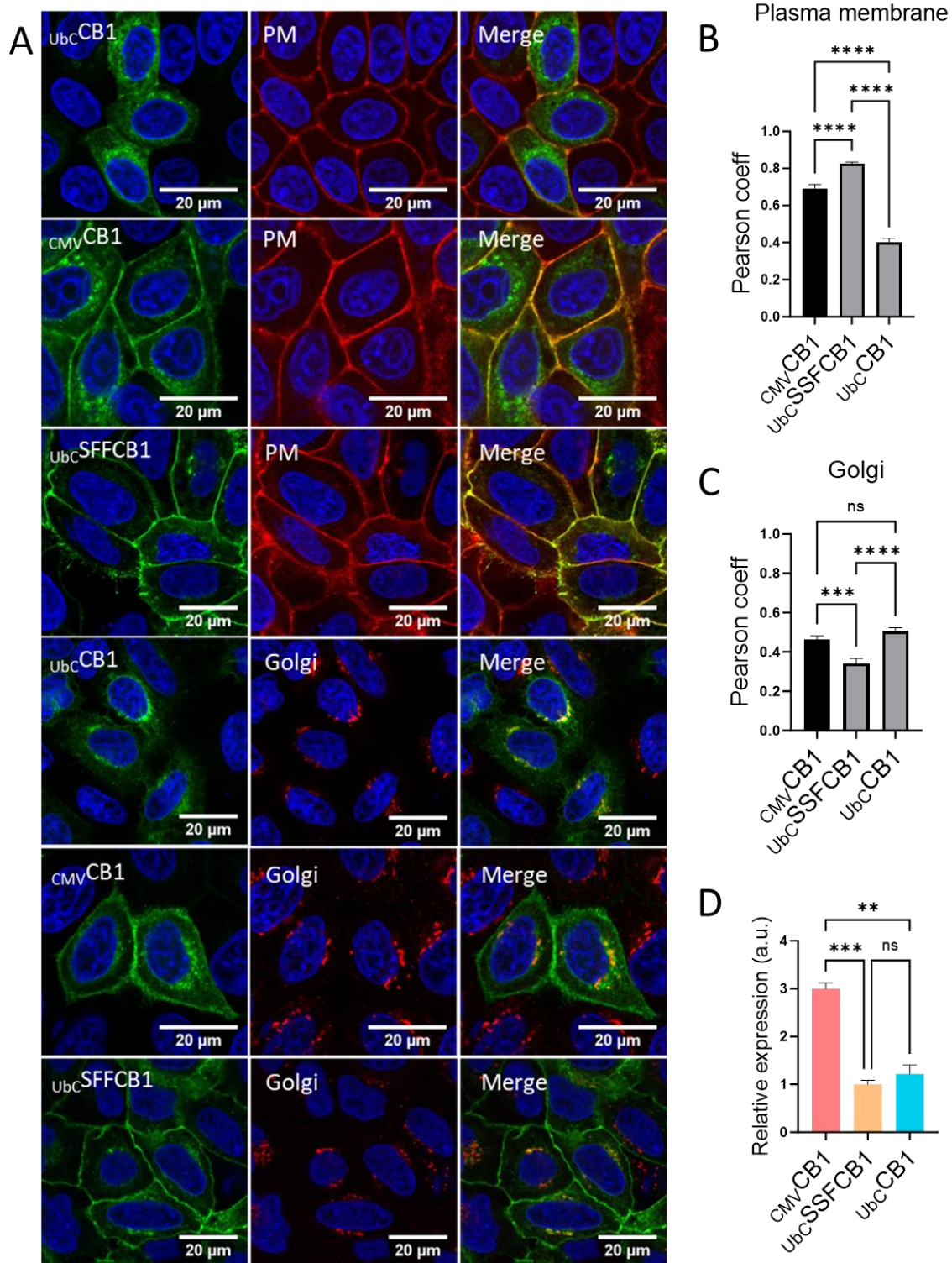


Figure 3-2. Expression level and N-terminal modification direct CB1's sub-cellular localization and impact downstream cAMP signaling. A. Confocal micrographs showing HeLa Kyoto cells transfected with UbCCB1, CMV-CB1 or UbCSSFCB1. Cells were fixed, permeabilized and co-immuno-stained with a CB1 antibody (left), and respective PM and Golgi organelle marker CellBrite and GM130 antibody (middle). B. Colocalization measurement in HeLa cells using Pearson coefficient of immunolabeled UbCCB1, CMV-CB1

or UbCSSFCB1 with the plasma membrane stain CellBrite. C. Colocalization measurement in HeLa cells using Pearson coefficient of immunolabeled UbCCB1, CMVCB1 or UbCSSFCB1 with the immunolabeled Golgi apparatus. D. Bar graphs showing n=3 replicates of expression levels of UbCSSFCB1-APEX, UbCCB1-APEX and CMVCB1-APEX. CMVCB1-APEX / SSFCB1-APEX $p < 0.005$. CMVCB1-APEX / UbCCB1-APEX $p < 0.01$. SSFCB1-APEX / UbCCB1-APEX was non-significantly different.

We next wanted to employ tagging methods to monitor CB1 expression and agonist-induced trafficking. We tagged CB1 at its N-terminus with the signal sequence FLAG (SSF) tag as antibody epitope tags like SSF are a common approach in the molecular pharmacology field to monitor GPCR expression, trafficking, and improve delivery to the cell surface(289, 293, 294). We introduced a modified construct called U_{bc} SSF-CB1, where a signal sequence flag (SSF) tag was added to the N-terminus of CB1. We found that the SSF tag caused U_{bc} SSF-CB1 to largely be localized to the plasma membrane and mostly excluded from endomembranes (Figure 3-2A,B,C, 3-3A,D). To ensure that the SSF tag's effect on localization was not due to higher expression levels relative to U_{bc} CB1, we used a CB1-APEX2 fusion protein to quantify whole cell receptor expression(295). We found that the expression level of U_{bc} SSF-CB1 was comparable to that of U_{bc} CB1, while CMV CB1 showed a three-fold increase in expression compared to when the SSF tag was present (Figure 3-2D, 3-3E). It is unclear how the SSF tag directs CB1 to the plasma membrane, the original goal of the tag was to enhance cell surface delivery of GPCRs by introducing a non-native and cleavable signal sequence from influenza hemagglutinin(294). We found that the SSF tag can be cleaved in live cells by trypsin, possibly due to the uniquely long N-terminal tail of CB1 (Figure 3-3F). This supports the hypothesis that the N-terminal tail plays a significant role in CB1 trafficking and expression regulation, as was postulated before (195). In conclusion, our results demonstrate that the localization of CB1 is highly dependent on expression level and N-terminal tagging.

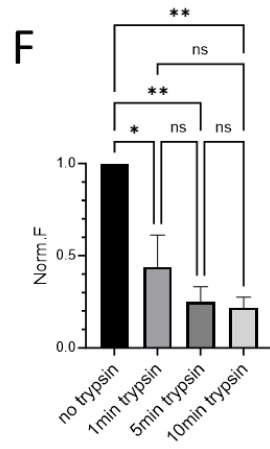
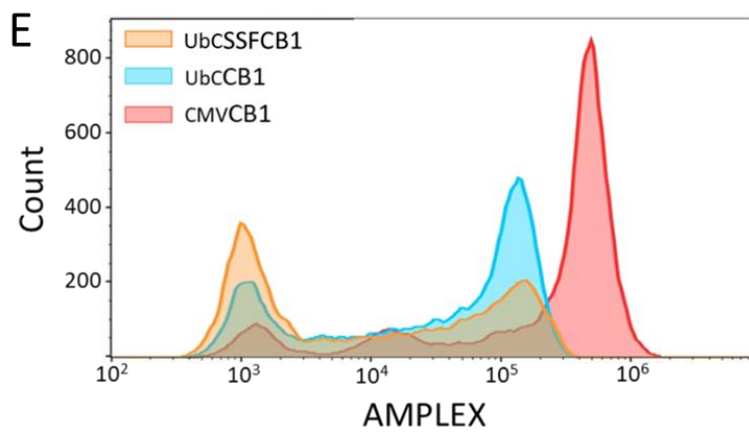
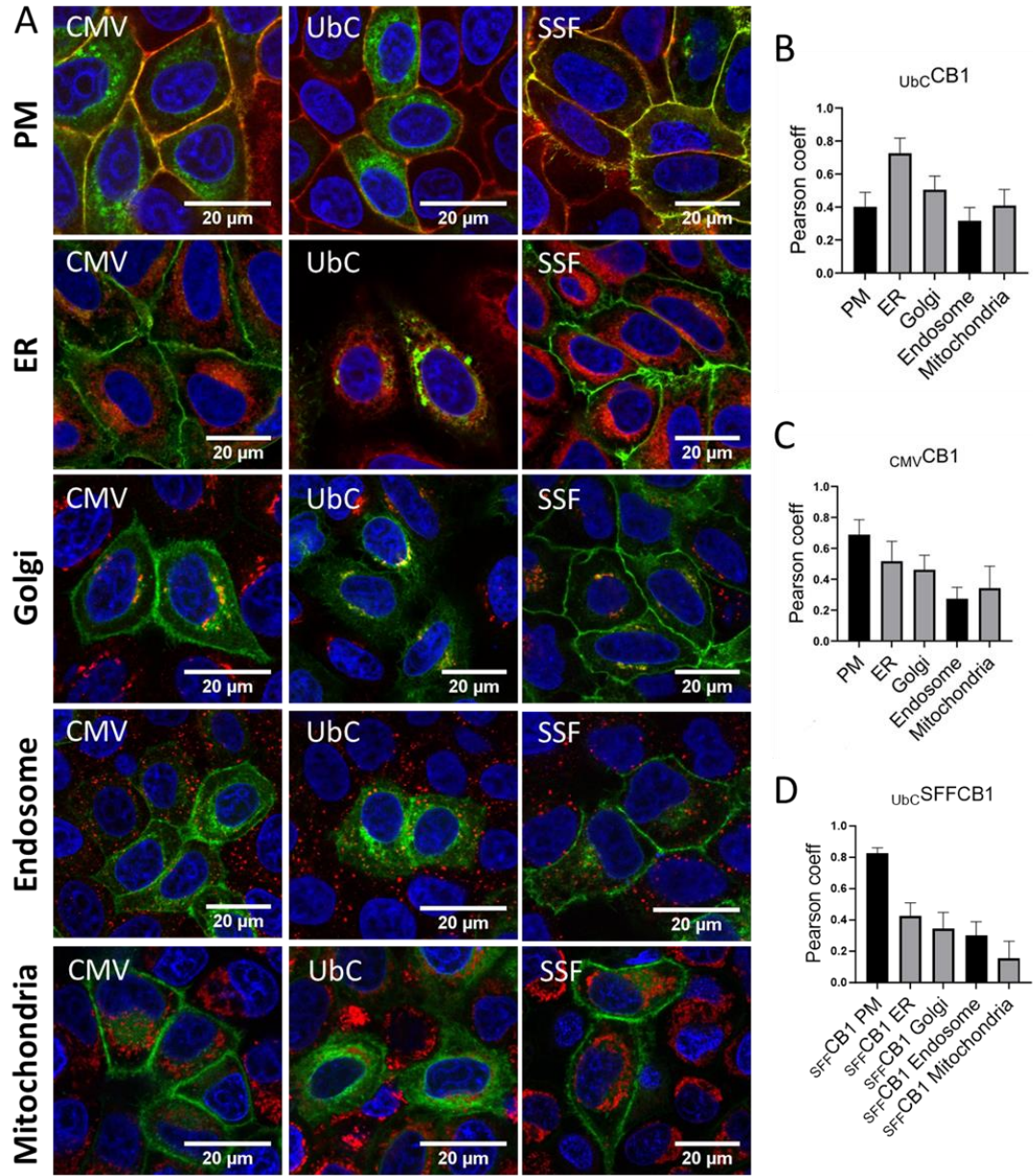


Figure 3-3 Quantification of CB1 expression constructs **A.** Confocal micrographs showing HeLa Kyoto cells transfected with U_{bc} CB1, CMV CB1 or U_{bc} SSFCB1. Cells were fixed, permeabilized and c-immunostained with a CB1 antibody and the PM, ER, Golgi, endosome and mitochondria organelle markers cellBrite, Calreticulin, GM130, EEA1 and MitoTracker, respectively. Co-localization measurement in HeLa cells using Pearson coefficient of immunolabeled U_{bc} CB1 (**B**), of immunolabeled CMV CB1 (**C**) or immunolabeled U_{bc} SSFCB1 (**D**) with respective organelle markers. **E.** Single cell analysis of APEX2/AUR intact assay following transient transfection of either CMV CB1-APEX2, U_{bc} CB1-APEX2 or U_{bc} SSFCB1-APEX2. The fluorescence reaction product of the APEX2 reaction with AUR was detected with a Beckman Coulter Cytoflex S. **F.** Time course bar graph of U_{bc} SSFCB1 as assayed by loss of cell surface immunoreactivity and measured by flow cytometry comparing non-trypsinized U_{bc} SSFCB1-expressing cells with trypsinized U_{bc} SSFCB1 cells. (0,1,5,10 min time points).

Sub-cellular localization of CB1 impacts downstream signaling via cAMP. Our investigation aimed to discern how CB1's subcellular localization might affect cell signaling. CB1 is well known to predominantly signal via $G_{\alpha i/o}$ proteins at the plasma membrane but has also been reported to couple to $G_{\alpha s}$ and $G_{\alpha q}$ (280, 287). These interactions lead to alterations in cAMP and calcium levels, respectively. Recent studies have suggested that the intracellular pool of CB1 may play a role in cell signaling, prompting an exploration into the potential signaling processes originating from intracellular membranes (283). To measure changes in cAMP levels upon CB1 activation, we employed a genetically encoded EPAC-based FRET sensor(32, 296). Cells were co-transfected with different CB1 constructs (CMV CB1, U_{bc} CB1, and U_{bc} SSF-CB1) and pretreated with forskolin (50 μ M) before treating with the CB1 full agonist WIN55,212 (10 μ M). Cells expressing U_{bc} CB1, which predominantly localizes CB1 to endo-membranes, exhibited a decrease in cAMP levels after WIN55,212 treatment, indicating $G_{\alpha i/o}$ coupling. In contrast, cells expressing CMV CB1, mainly located at the plasma membrane, showed an increase in cAMP levels, suggestive of $G_{\alpha s}$ coupling (Figure 3-4A,D).

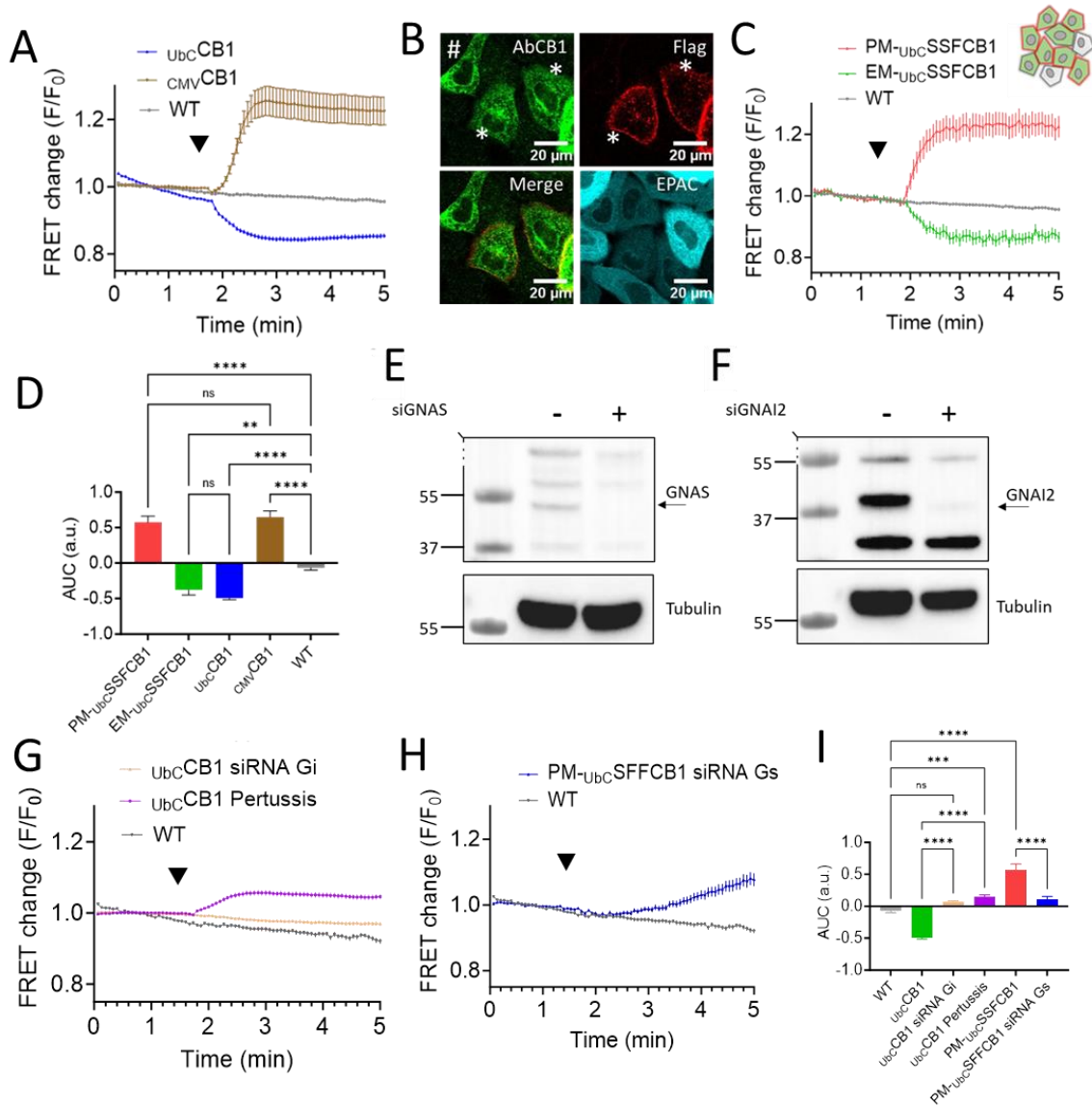


Figure 3-4. Location bias drives emCB1 to couple to *Gai/o* and pmCB1 to couple to *Gas*. **A.** Average of 111, 63, and 57 traces showing FRET changes of the EPAC-based FRET sensor in *UbcCB1*-expressing, *CMVCB1*-expressing or non-expressing (WT) HeLa cells, respectively. **B.** Confocal micrographs showing HeLa Kyoto cells transfected with *UbCSSFCB1*. Receptors were labelled with a functionalized 647Alexa-M1-FLAG antibody for 20 min in live cells (top right), then fixed, permeabilized and immuno-stained with a CB1 C. Average of 67, 46 and 57 traces showing FRET changes of the EPAC-based FRET sensor in *SSF_{UbcCB1}*-transfected HeLa cells with (PM) or without (EM) tagging with the Flag antibody or not transfected (WT), respectively, after treatment with the agonist WIN55,212-2 (10 μ M). **D.** Bar graphs showing area under the curve of the EPAC-based FRET sensor after WIN55,212-2 stimulation (10uM) in *PM-SSF_{UbcCB1}* expressing cells, *EM-UbcSSFCB1*, *UbcCB1* expressing cells and WT non-expressing cells. *PM-UbcSSFCB1* / WT $p < 0.001$, *EM-UbcSSFCB1* / WT $p < 0.001$, *UbcCB1* / WT $p < 0.001$. **E.F.** Immunoblot analysis of HeLa Kyoto cells upon **E.** *G α s* (GNAS) knockdown and **F.** *G α i* (GNAI2) knockdown. Arrows indicate the corresponding molecular weight of GNAS and GNAI2. (N=2). Dash lines indicate cropping of blot. **G.** Average of 179, 176 and 84 traces showing FRET changes of the EPAC-based FRET sensor in *UbcCB1*-expressing HeLa, pre-treated with pertussis toxin 24h prior to the experiment, pre-transfected with *Gai/o* siRNA 72h prior to the experiment or WT-(not expressing CB1) HeLa respectively, after treatment

with the agonist WIN55,212-2 (10 μ M). **H.** Average of 116 and 84 traces showing FRET changes of the EPAC-based FRET sensor in SSFCB1-transfected HeLa cells tagged (PM) with the Flag antibody, pre-transfected with *Gas* siRNA 72 h prior to the experiment or WT-not expressing HeLa, respectively, after treatment with the agonist WIN55,212-2 (10 μ M). Cells in all experiments were pre-treated with forskolin (50 μ M). **I.** Bar graphs showing area under the curve of the EPAC-based FRET sensor after WIN55,212-2 stimulation (10 μ M) in WT non-expressing cells, PM- U_{bc} SSFCB1-expressing cells pre-transfected with *Gas* siRNA and, U_{bc} CB1-expressing cells pre-transfected with *Gai/o* siRNA. PM- U_{bc} SSFCB1 siRNA *Gas* and U_{bc} CB1 siRNA *Gai/o* versus WT were not significant. Cells in **A** to **F** were pre-treated with forskolin (50 μ M).

We next sought to take advantage of the fact that our U_{bc} SSF-CB1 resulted in a mixed population in which most cells had CB1 at the plasma membrane but a subset retained CB1 internally (Figure 3-4 B). We labeled U_{bc} SSF-CB1 receptors with a non-cell-permeant 647Alexa-M1-FLAG antibody prior to the experiment for sub-cellular localization analysis. Using the flag tag to identify plasma membrane CB1 in live cell, and immunostaining post cell-fixation to identify all CB1, we differentiated cells expressing CB1 predominantly at the plasma membrane (PM- U_{bc} SSF-CB1) from those at endo-membranes (EM- U_{bc} SSF-CB1). Cells with plasma membrane stains prior to the imaging experiment were first identified and categorized as PM- U_{bc} SSF-CB1, then cross-referenced after fixation and immunostaining. Every cell appearing positive to the immunostaining which was not pre-identified as PM- U_{bc} SSF-CB1, was categorized as EM- U_{bc} SSF-CB1. To avoid bias in the selection process, the categorization of the two different populations of cells was performed prior to cAMP analysis. This allowed us to separate both populations post-imaging by cell sorting and to separate their unique cAMP responses. In the PM- U_{bc} SSF-CB1 population, we observed an increase in cAMP levels after WIN55,212 treatment and a decrease of cAMP in the EM- U_{bc} SSF-CB1 population (Figure 3-4C,D). These findings underscore that the sub-cellular localization of CB1 significantly dictates its downstream signaling, particularly its impact on cAMP levels. Our findings suggest that agonist-bound CB1 positioned at the plasma

membrane increases cAMP levels, whereas localization in endo-membranes results in decreased cAMP levels analogous to the canonical inhibitory signaling. (Table 1).

promoter	N-ter tag	predominant localization	cAMP signaling
CMV	WT	PM	increase cAMP
UbC	WT	EM	decrease cAMP
	SSF	PM	increase cAMP
		EM	decrease cAMP

Table 1: Location bias of CB1 leads to differences in cAMP signaling

Next, we investigated whether these effects were mediated by G-protein coupling or through alternative mechanistic pathways. Heterotrimeric G proteins and adenylylated cyclase have been observed not only associated to the plasma membrane but also to intracellular compartments such as endosomes or the Golgi, supporting the concept of endo-membrane based G-protein signaling(182, 205, 278, 297). Recently, it has been demonstrated that the β 1-adrenergic receptor and the opioid receptor mu can both localize at the Golgi and activate $G_{\alpha s}$ and $G_{\alpha i}$ respectively (182, 278). To assess the role of G proteins in CB1-mediated cAMP signaling, we generated siRNA-based knockdowns of specific G proteins in our cell model (Figure 3-4 E,F). We first performed a $G_{\alpha s}$ knockdown and co-expressed the EPAC sensor with $U_{bc}SSF$ -CB1, the receptor construct which expresses at low levels but is primarily at the cell surface due to the non-native signal sequence (SS). This helped mitigating the possible contribution of receptor numbers in the cAMP response downstream of CB1 when comparing PM-CB1 and EM-CB1. After treatment with the CB1 agonist WIN55,212, we observed a delayed and significantly smaller increase in cAMP levels compared to non-pretreated cells (Table 1, Figure 3-4H,I), suggesting that PM-CB1 can activate $G_{\alpha s}$ for cAMP signaling although contributions of $G_{\beta\gamma}$ and $G_{\alpha i}$ cannot be excluded.

Subsequently, we generated a $G\alpha i$ knockdown and co-expressed the EPAC sensor with $UbcCB1$ (Figure 3-4 F). Consistent with our observations, knockdown of $G\alpha i$ blocked all effects of WIN55,212 treatment in the endo-membrane localized $UbcCB1$ cells (Figure 3-4G,I). To further confirm this finding, we treated cells with Pertussis toxin for 24h, a treatment known to induce ADP-ribosylation and subsequent degradation of $G\alpha i/o$. Interestingly, in Pertussis toxin-treated cells expressing $UbcCB1$, we observed an increase in cAMP levels after WIN55,212 treatment (Figure 3-4G,I), consistent with previous observations(286). This increase could be driven by the small fraction of CB1 at the plasma membrane still presenting $UbcCB1$ expressing cells or the increased availability of CB1 to couple with $G\alpha s$ after depletion of $G\alpha i$. The results from the $G\alpha s$ knockdown and Pertussis toxin experiments support the idea that PM-CB1 predominantly activates $G\alpha s$ for cAMP signaling. Correspondingly, knockdown of $G\alpha i/o$ blocked CB1 effects on cAMP in cells in which CB1 was largely retained at endomembranes. In our model system in which we can control CB1 localization with the SSF tag without measurably affecting expression levels, our findings indicate that the sub-cellular localization of CB1 plays a crucial role in determining its downstream G protein-coupled signaling.

Minimally invasive labeling of CB1 by a non-canonical amino acid as an alternative method to distinguish EM-CB1 to PM-CB1.

We found that a standard tag used for monitoring GPCR expression and trafficking, SSF, affected CB1 localization and signaling. However, the simple solution to this problem -- removing SSF tag -- would make it highly challenging to monitoring CB1 trafficking in living cells. We therefore aimed to develop a novel approach for monitoring CB1 expression

and trafficking by using the smallest possible tagging technique while maintaining the ability to distinguish between cells with CB1 predominantly at the plasma membrane or in intracellular compartments. We sought to achieve this goal without interfering with cannabinoid receptor signaling or trafficking. To accomplish this, we used genetic code expansion to incorporate a *trans*-cyclooct-2-en-L-lysine (TCO**A*) for catalyst-free ultrafast labeling of the receptor, a technique previously employed for other membrane proteins.(298) We utilized an orthogonal tRNA/tRNA synthetase pair (tRNA/RS) from *Methanosarcina mazei* to introduce TCO**A* lysine into the first extracellular loops of CB1 (Figure 3-5A). We used a CB1-GFP construct to screen several positions for the most receptor expression and efficient TCO**A* incorporation, and the most successful site was found to be by replacing the phenylalanine at position 180 in CB1 ($_{CMV}CB1-F180$)(Figure 3-5A,B). We also added an SSF tag at the N-terminus of $_{CMV}CB1-F180$ to assess its functionality, specifically looking at the kinetics of internalization after treatment with WIN55,212 (10 μ M). For labeling CB1 before agonist treatment, we utilized the non-cell-permeable dye methyl tetrazine ATTO 647 (ATTO 647 MeTet). The functionality of $_{CMV}CB1-F180$ was assessed by examining its internalization kinetics compared to $_{CMV}SSFCB1$ (wild-type CB1 with an SSF tag) after treatment with WIN55,212. Both $_{CMV}SSFCB1$ and $_{CMV}SSFCB1-F180$ showed similar levels of receptor internalization (approximately 75% and 70%, respectively) during 3 hours of treatment (Figure 3-5C,D,K). This suggest that the F180 tag minimally perturbed CB1 functionality. To further confirm the functional integrity of $_{CMV}CB1-F180$, we activated the receptor by uncaging caged-2AG, which has previously been shown to transiently increase intracellular calcium levels ($[Ca^{2+}]_i$) (227). Uncaging showed a response at the same order of magnitude as through wild-type CB1 expression (Figure 3-5E). Notably, the response to

2AG was completely abolished by the CB1 inverse agonist rimonabant, validating the specificity of CMV-CB1-F180 (Figure 3-5E,F,G).

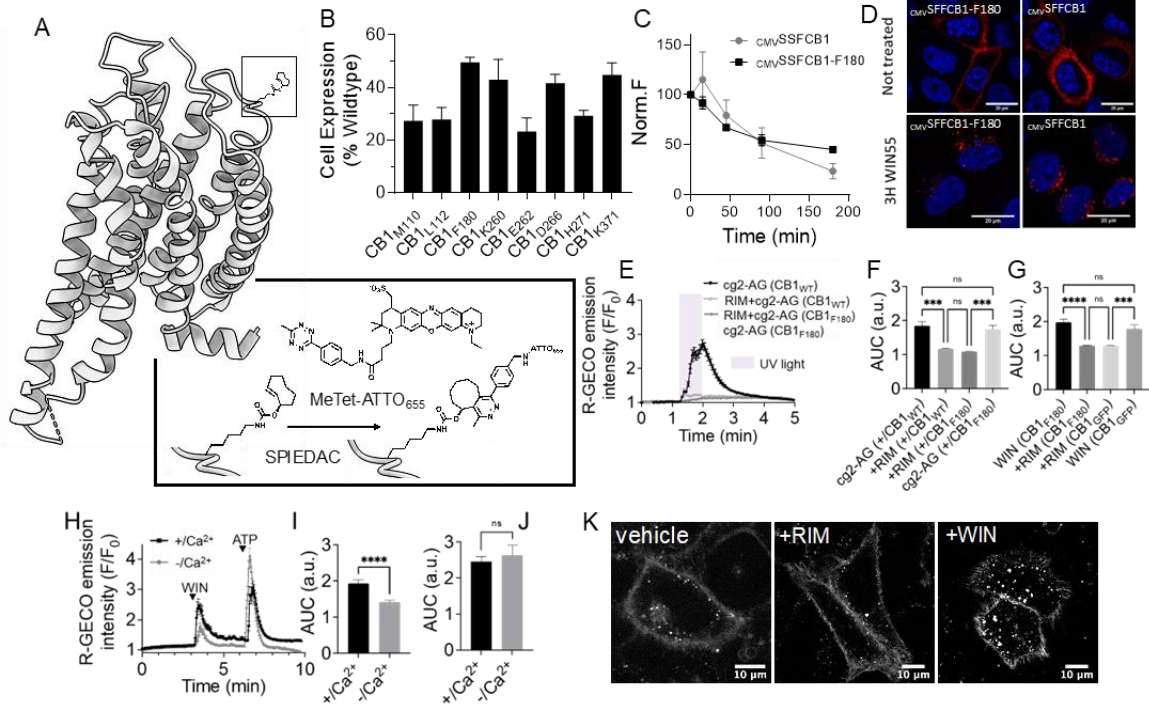


Figure 3-5. Introducing a clickable TCO*A in CB1 without interfering with signaling or trafficking provides an alternative method to distinguish EM-CB1 to PM-CB1. **A.** Structural model of CB1 having the unnatural amino acid TCO*A incorporated before and after SPIEDAC reaction with the methyl tetrazine dye Me-Tet-ATTO₆₅₅. **B.** Single cell analysis of GFP fluorescence following transient transfection of CB1-GFP that contained TCO*A at the position indicated. Data represent the mean \pm SD of biological triplicate. The fluorescence was detected with a Beckman Coulter Cytoflex S. **C.** Time course of WIN55,212-2 (10 μ M) stimulated receptor internalization as assayed by loss of cell surface immunoreactivity and measured by flow cytometry comparing un-modified CMVSSFCB1 with the CMVSSFCB1-F180. (10 μ M WIN55, 0,15,45,90 and 180 min after stimulation). **D.** Confocal micrographs showing live HeLa Kyoto cells transfected with CMVSSFCB1 or CMVSSFCB1-F180. Cells were immuno-labeled with a functionalized Flag antibody and treated for 3 h with WIN55. **E.** Fluctuations of [Ca²⁺]_i measured by R-GECO in CB1-WT or CB1-F180-transfected HeLa Kyoto subjected to treatment with the CB1 agonist cg2-AG (10 μ M) and illuminated by 375nm UV light, pretreated or not with the antagonist rimonabant. **F,G.** Comparison of area under the curve fluorescence of R-GECO in CB1-WT or CB1-F180-transfected HeLa Kyoto after uncaging cg2-AG (10 μ M) under different experimental conditions. **H.** Fluctuations of [Ca²⁺]_i in CB1-transfected HeLa Kyoto upon treatment with WIN55,212-2 (10 μ M) and with ATP (50 μ M), pre-incubated or not in nominally Ca²⁺-free media. **I.** Comparison of area under the curve fluorescence of R-GECO in CB1-transfected cells after treatment with WIN55,212-2 (10 μ M). **J.** Comparison of area under the curve fluorescence of R-GECO in CB1-transfected cells after treatment with ATP (50 μ M). **K.** Confocal micrographs showing HeLa Kyoto cells transfected with CB1-F180, tagged with MeTet-ATTO655 and treated with the CB1 antagonist rimonabant (10 μ M) or the agonist WIN55,212-2 (10 μ M).

Our alternative method for tagging CB1 model by incorporating the TCO*A label at position 180 in CB1 enabled efficient and catalyst-free ultrafast labeling of the receptor exclusively at the plasma membrane, allowing discrimination from intracellular compartment localization. Importantly, functional assessment demonstrated minimal perturbation of CB1 by the F180 tag, as evidenced by normal internalization kinetics and intact calcium signaling responses to 2AG.

Effects of CB1 expression and activation on calcium levels and receptor internalization

To control for potential contributions of intracellular calcium levels to cannabinoid signaling, we employed a classical approach and expressed a GFP-fused version of CB1 with an unmodified N-terminus under the CMV promoter along with the calcium sensor R-GECO to monitor changes in intracellular calcium concentrations ($[Ca^{2+}]_i$) upon CB1 activation. WIN55,212-2 triggered a transient increase in $[Ca^{2+}]_i$ ($F/F_0=2.545\pm 0.128$, $n=80$, Figure 3-6A,B). This response was completely abolished by pre-treating cells with the inverse agonist rimonabant ($F/F_0=1.267\pm 0.003$, $n=170$, Figure 3-6A,B). In control experiments, ATP addition induced a major calcium transient ($F/F_0=3.339\pm 0.119$, $n=89$), likely through Gq/11-coupled P2Y receptors (Figure 3-6A,B)(299). Intracellular calcium stores are known to be involved in the CB1-mediated increase in cytoplasmic calcium levels in different cellular models(190, 300, 301). This was confirmed by a short incubation with thapsigargin, a non-competitive inhibitor of the sarco/endoplasmic reticulum Ca^{2+} ATPase (SERCA) ($F/F_0=1.761\pm 0.131$, $n=80$), or Xestospongin C (an IP_3 receptor antagonist) respectively, which reduced the calcium response to WIN55,212-2 (Figure 3-6C,D). This result suggests that CB1-mediated calcium increase partially relies on the release of calcium from internal stores mediated by IP_3 and IP_3 receptors. As expected, both thapsigargin and xestospongin C

also dramatically decreased the cytosolic increase in calcium after addition of ATP (Figure 3-6C,E). To explore if extracellular calcium intake via GIRK channels is a primary pathway after CB1 activation, we incubated cells in Ca^{2+} -depleted media supplemented with EGTA for 5 min. The reduction in calcium response after WIN55,212 addition in calcium-depleted media suggested that both extracellular intake and release from intracellular stores contributed to the cytosolic increase in calcium levels (Figure 3-6H,I). Importantly, the extracellular depletion of calcium had no impact on the cytosolic increase in calcium after addition of ATP (Figure 3-6H,J).

We also observed that prolonged activation of CB1 triggered receptor internalization and co-localization with Rab5 in early endosomes. Desensitization of the receptor upon internalization was indicated by the inability of a second dose of the agonist to provide another transient calcium response ($F/F_0=1.107\pm 0.008$, $n=80$, Figure 3-6K,L). In contrast, inactivation of CB1 with the reverse agonist rimonabant led to the accumulation of the receptor at the plasma membrane (Figure 3-6F,I,J). In summary, CB1 activation induced calcium release from intracellular stores, likely through IP_3 receptors, and extracellular calcium influx. The desensitization of CB1 upon prolonged activation highlights the

receptor's critical regulatory role in maintaining cellular responses.

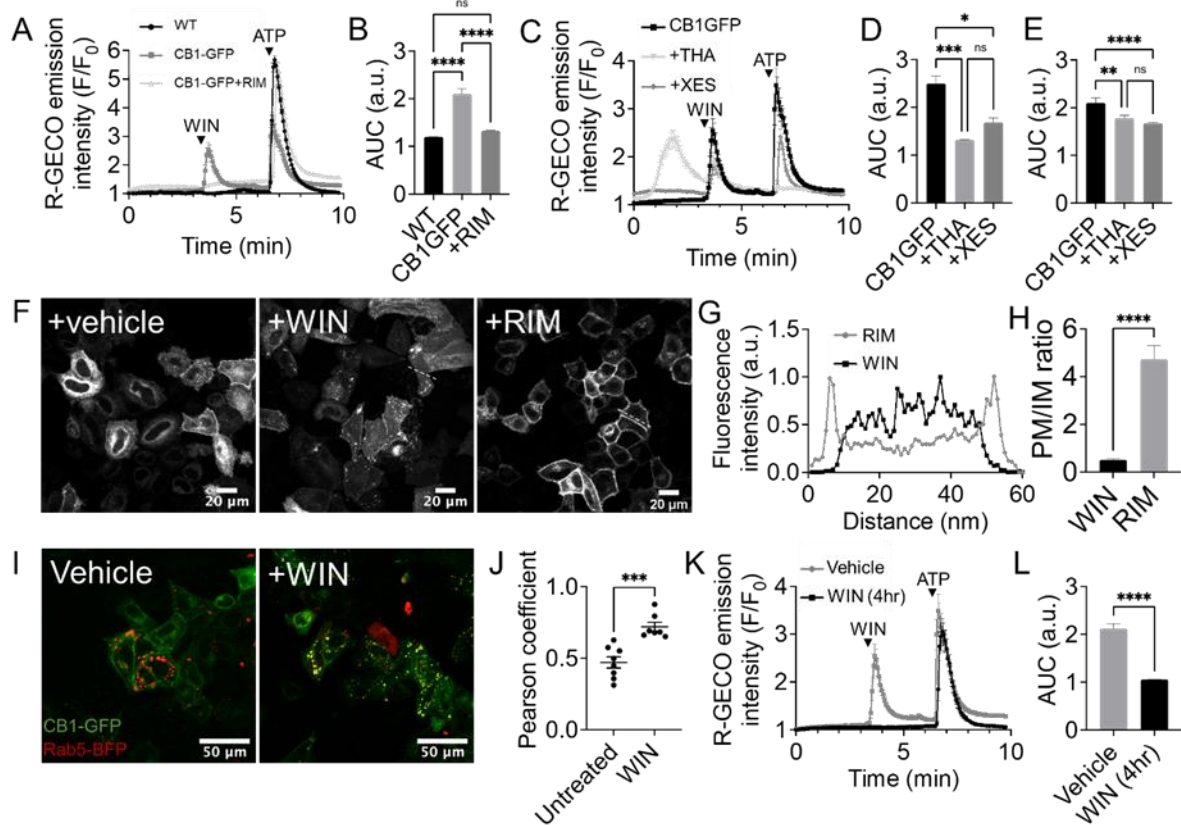


Figure 3-6. CB1 activation leads to a transient increase in calcium levels via influx of extracellular calcium and intracellular release. **A.** Fluctuations of $[Ca^{2+}]_i$ in CB1-GFP transfected HeLa Kyoto upon treatment with WIN55,212-2 ($10\mu M$) and with ATP ($50\mu M$) pre-treated or not with the antagonist rimonabant. **B.** Comparison of area under the curve fluorescence of R-GECO in CB1-GFP transfected HeLa Kyoto after treatment with WIN55,212-2 ($10\mu M$) under different experimental conditions. **C.** Fluctuations of $[Ca^{2+}]_i$ in CB1-GFP transfected HeLa Kyoto upon treatment with WIN55,212-2 ($10\mu M$) and with ATP ($50\mu M$) pre-treated or not with Thapsigargin ($10\mu M$) or Xestospongin C ($10\mu M$). **D.E.** Comparison of area under the curve fluorescence of R-GECO in CB1-GFP transfected HeLa Kyoto after treatment with WIN55,212-2 ($10\mu M$) and with ATP ($50\mu M$) pre-treated or not with Thapsigargin ($10\mu M$) or Xestospongin C ($10\mu M$). **F.** Confocal micrographs (20x) showing CB1-GFP transfected cells after 3 h treatment with $10\mu M$ of WIN55,212-2 or with $10\mu M$ of rimonabant. **G.H.** To quantify the ratio of CB1-GFP at the plasma membrane to the endomembrane after different treatments a line was drawn across each cell and the fluorescence across the line was measured. **I.** Confocal micrographs showing the relative subcellular locations of CB1-GFP and Rab5-BFP with vehicle or with WIN55,212-2 ($10\mu M$) for 3 hr. **J.** Colocalization measurement in HeLa cells using Pearson coefficient of CB1-GFP and Rab5-BFP. **K.** Fluctuations of $[Ca^{2+}]_i$ in CB1-GFP transfected HeLa Kyoto upon treatment with WIN55,212-2 ($10\mu M$) and with ATP ($50\mu M$) pre-treated or not for 4 hours with WIN55,212-2 ($10\mu M$). **L.** Comparison of area under the curve fluorescence of R-GECO.

Cannabinoid receptor constructs regulate adenylate cyclase activity and trigger distinct signaling pathways.

Next, we aimed to investigate how the newly developed CMV CB1-F180 construct regulates adenylate cyclase (AC) activity and to compare its signaling to the unmodified CMV CB1 receptor. To assess adenylate cyclase (AC) activity, we co-transfected CMV CB1-F180 or CMV CB1 with the EPAC-based sensor and measured cAMP levels after stimulation with WIN55,212 (10 μ M) followed by forskolin (50 μ M) (Figure 3-8 A,B,C). Both CMV CB1-F180 and CMV CB1 expressing cells showed a comparable moderate increase in intracellular cAMP levels after WIN55,212 stimulation. However, the difference in cAMP levels between CMV CB1-F180 and CMV CB1 was more pronounced after forskolin stimulation, with CMV CB1-F180 expressing cells displaying moderately higher cAMP levels than wild type cells. These results indicate that CMV CB1-F180-mediated signaling is comparable to the unmodified receptor and that CMV CB1-F180 couples to Gas proteins (Figure 3-8B,C). Furthermore, the CMV CB1-F180 construct showed approximately 50% expression level relative to unmodified CMV CB1 (Figure 3-5B). This led us to hypothesize that two populations exist in CMV CB1-F180 transfected cells: one with lower

expression level and CB1 predominantly at endo-membranes and another with higher expression level and CB1 present in both plasma and endo-membranes. By post-translationally labeling CMV CB1-F180 before

experiments with the non-cell-permeant dye methyl tetrazine ATTO 647 (ATTO 647 MeTet) and tagging of all CB1 receptors post fixation with a CB1-specific antibody, we distinguished between cells with CB1

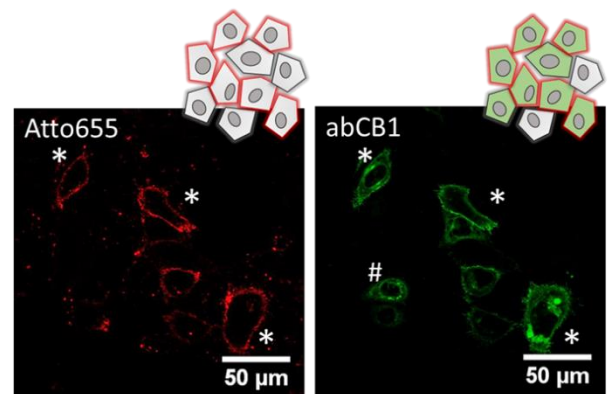


Figure 3-7. Confocal micrographs showing HeLa Kyoto cells transfected with CB1-F180. Receptors were labelled with Me-Tet-ATTO655 (1 μ M) for 20 min (left panel) then fixed and immuno-stained with a CB1 antibody. Note that cells marked with a (#) are labeled exclusively by the antibody while cells marked with a (*) are labeled with both antibody and Me-Tet-ATTO655. This experiment is representative of three biological repeats.

predominantly at the plasma and endo-membranes (PM-_{CMV}CB1-F180) and exclusively in endo-membranes (EM-_{CMV}CB1-F180)(Figure 3-7). After CB1 activation, PM-_{CMV}CB1-F180 cells showed an increase, while EM-_{CMV}CB1-F180 cells displayed a canonical decrease in cAMP levels(Figure 3-8D,E). These data provide a parallel line of evidence that subcellular localization of CB1 drives the cAMP response after agonist treatment.

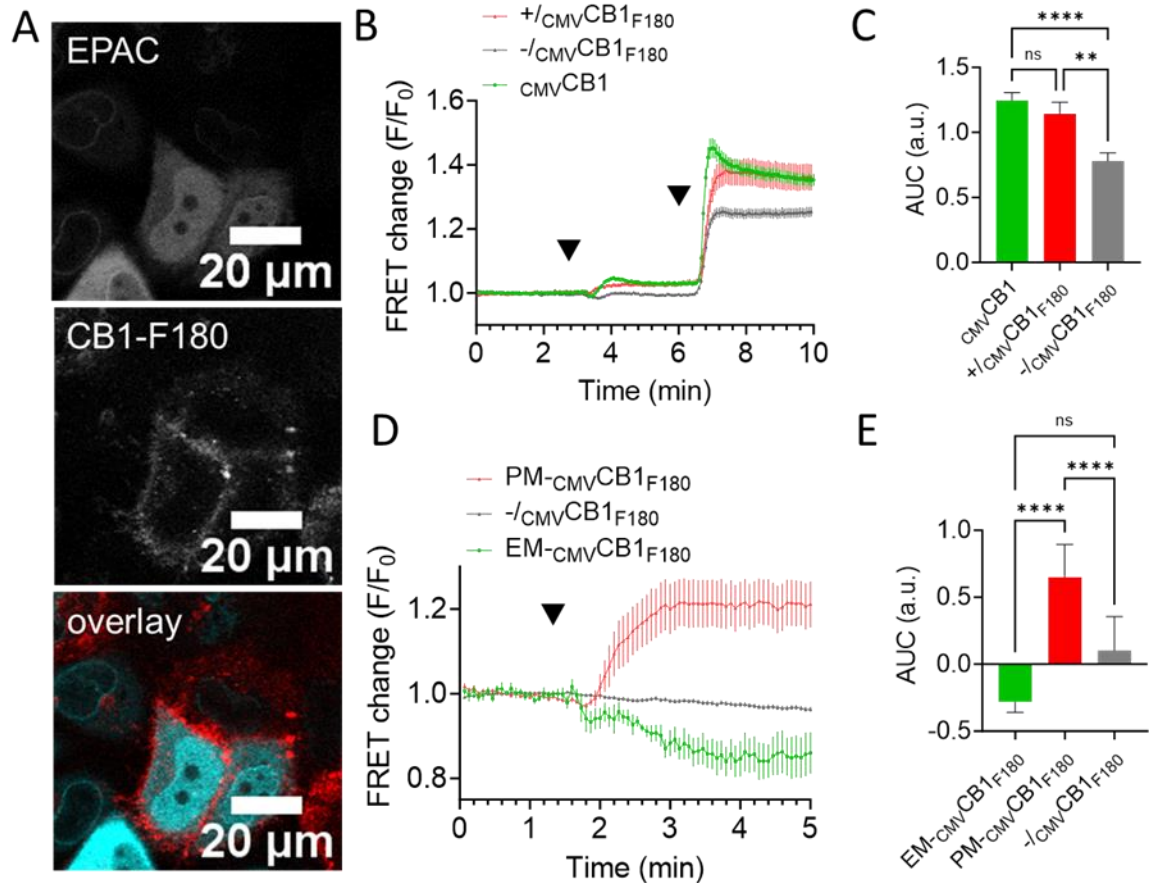


Figure 3-8. Additional evidence from CB1-F180 post-translational labeling and change in [cAMP] levels shows that CB1 localization in endo-membrane affects G-protein coupling. **A.** Confocal micrographs showing _{CMV}CB1-F180 and EPAC FRET sensor co-transfected HeLa Kyoto cells after receptor labelling with Me-Tet-ATTO655 (1 μM) for 20 min. **B.** Average of 45, 178 and 76 cell traces showing FRET changes of the EPAC-based FRET sensor in _{CMV}CB1-F180-transfected HeLa (+), (-) and wt _{CMV}CB1 respectively, after treatment with WIN55,212-2 (10 μM) followed by forskolin (FSK, 50 μM). **C.** Bar graphs showing FRET changes of the EPAC-based FRET sensor after forskolin stimulation (50 μM) in -/_{CMV}CB1-F180 (WT) versus +/_{CMV}CB1-F180 $p < 0.005$, _{CMV}CB1 versus +/_{CMV}CB1-F180 non-significant or _{CMV}CB1 versus -/_{CMV}CB1-F180 $p < 0.001$ expressing cells. **D.** Average of 14, 6 and 82 cell traces showing FRET changes of the EPAC-based FRET sensor in _{CMV}CB1-F180-expressing cells tagged with Me-Tet-ATTO655 (+PM-_{CMV}CB1-F180), _{CMV}CB1-F180-expressing cells without me-Tet-ATTO655 (EM-_{CMV}CB1-F180) and non-expressing cells (-/_{CMV}CB1-F180) respectively, after treatment with WIN55,212-2 (10 μM). **E.** Bar

graphs showing area under the curve of the EPAC-based FRET sensor after WIN55,212-2 stimulation (10 μ M) in $-/_{CMV}CB1-F180$ non-expressing cells, $PM-CMVCB1-F180$ or $EM-CMVCB1-F180$ expressing cells. $EM-CMVCB1-F180$ versus $PM-CMVCB1-F180$ $p < 0.005$, $PM-CMVCB1-F180$ versus $-/_{CMV}CB1-F180$ $p < 0.005$, $EM-CMVCB1-F180$ versus $-/_{CMV}CB1-F180$ was non-significant.

As a control, we also incorporated TCO*A lysine in the N-terminus of the CB2 receptor (CB2R) at serine 29, termed CB2-S29, to explore its G-protein coupling and signaling characteristics (Appendix 3-1). CB2 is a class A GPCR sharing 44% homology with CB1 and can be activated by WIN55,212 as a full agonist. It predominantly couples to *Gai/o* proteins and unlike CB1, has shown little promiscuity for other G proteins. We observed no changes in cAMP levels after WIN55,212 stimulation in CB2-S29 expressing cells compared to non-transfected cells (Appendix 3-1 B,C). However, after forskolin treatment, CB2-S29 cells showed lower cAMP levels, suggesting predominantly *Gai/o* coupling, consistent with CB2 being a *Gai/o*-coupled receptor. When treated with the CB2-inverse agonist AM630, CB2-S29 showed significantly higher level of $[cAMP]_i$ after forskolin stimulation compared to non-transfected cells (Appendix 3-1 B,D) suggesting a strong *Gai/o* interaction (Appendix 3-1 B,C). Our study provides

valuable insights into the signaling characteristics of $CMVCB1-F180$ and CB2-S29 receptors. $CMVCB1-F180$ retains its ability to signal predominantly via *G α s* coupling, while CB2-S29 exhibits *Gai/o* coupling.

Additionally, our results support the idea that CB1 can signal from endo-membranes and modulate its G-protein coupling based on its subcellular localization.

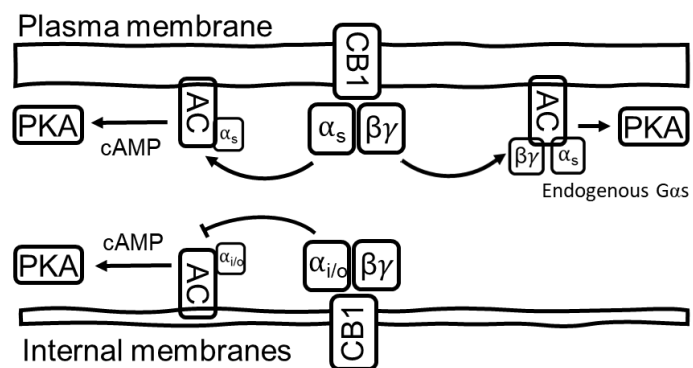


Figure 3-9. Tentative representation of the contradictory effect of activated CB1 on cAMP levels depending on receptor location.

DISCUSSION

We set out to examine how CB1 signaling is dependent on subcellular location and how spatial bias could contribute to cannabinoid activity. Our data indicate that CB1 located to internal membranes might predominantly couple to G α i/o while CB1 at the cell surface appears to prefer coupling to G α s. This indicates a location bias in cannabinoid receptor function (Figure 3-9). A critical step in our finding was developing methods to control, and deconvolve, subcellular CB1 localization. We have demonstrated that CB1 trafficking and location can be highly dependent on its expression level and modification of the CB1 N-terminal tail with a non-native epitope tag (SSF). This allows for control of CB1 localization. Importantly, we provide an alternative solution to the commonly used SSF for tracking cannabinoid receptor trafficking by developing methods for single site incorporation of *trans*-cyclooctene lysine (TCO*A) into the extracellular loops of CB1 or CB2.

Subcellular localization of CB1. The subcellular localization of CB1 has been a point of controversy. It is mostly believed that functional CB1 receptors are present at the plasma membrane and ligand binding there is fully responsible for its signaling activity (302, 303). Some studies have shown that the internal pool is a result of CB1 internalization from the plasma membrane and trafficking to internal membranes (304, 305). It is believed that CB1 is cycling back to the plasma membrane after inverse-agonist treatment (306). This view has been challenged by other studies demonstrating that internalized CB1 is mostly degraded in the endolysosomal pathway and that the internal pool does not contribute to the plasma membrane CB1 population (199). We found in this study that CB1, at relative low expression levels, resides predominantly in internal membranes with very low plasma

membrane expression. While we did not characterize the mode of trafficking, our findings suggest that the internal pool of CB1 in proximity to the Golgi was never trafficked to the plasma membrane. This aligns with the studies describing internal CB1 as an independently operating receptor pool(201). In our model, expression levels are the main driver of basal sub-cellular localization suggesting that the formation of the CB1 intracellular pool is potentially a result of retention by an adaptor protein preventing CB1 to enter trafficking vesicles and to reach the plasma membrane, and such a mechanism has been described for several other GPCRs (307, 308).

Location bias in CB1 signaling. We demonstrate, using different expression and tagging systems, that CB1 signaling is highly influenced by its subcellular localization: plasma membrane CB1 promotes cAMP accumulation while intracellular CB1 shows reduced cAMP production. Measurements of intracellular cAMP levels in combination with a predominant location of CB1 at internal membranes through a weak promoter suggest that CB1 can signal from internal membranes and is subject to location bias. This result has major implications on the pharmacology of CB1 stimulation. Specifically, the lipophilicity of a ligand, or its synthesis location in the case of endocannabinoids, will influence its preferential binding to either the plasma membrane or endomembrane population of the receptor. Our observations raise the question, how does CB1 regulates cAMP positively when signaling from the cell surface and negatively when signaling from the endomembranes? Recent studies have suggested that the membrane itself plays a key role in GPCR coupling to G proteins. Specifically, anionic phospholipids at the plasma membrane like PI(4,5)P₂ have been shown to control coupling of the β 2-adrenergic receptor (β 2AR) to G proteins through charge-based suppression of the receptor interaction

with *G α i* (309). Building on this finding, recent studies show that this lipid-based regulation can give rise to location bias in β 2AR signaling as the Golgi is not enriched in PI(4,5)P₂ (310), abolishing the β 2AR coupling to *G α i* in this organelle. Thus, we speculate that one of the possible underlying mechanisms for our observation of location bias in CB1 signaling is the modulation of the G protein coupling of CB1 by differential phospholipids enrichment at endomembranes compared to the cell surface. By sequentially knocking down *G α s* and *G α i*, our experiments suggest that plasma membrane CB1 could preferentially couple to *G α s* while CB1 located in internal membranes couples to *G α i*. Overexpressed CB1 has been previously shown to couple not only to *G α i/o* but also to *G α s* (287). It was argued that the presence of a “receptor reserve” amplifies GPCR signaling and makes low affinity binding of *G α s* appear as the main response(311). We cannot exclude that the CB1 coupling to *G α s* is a product of this phenomena. Additionnaly, *G β γ* has been recently described to activate the adenylyl cyclase 5 in the presence of *G α s* or forskolin. This mechanism could also play a role in our observed accumulation of cAMP after CB1 activation (312). It will be important in the future to use methods to restrict CB1 activation or visualization locally to clearly identify CB1 signaling, effector activation and ligand accessibility(297, 313).

Role of CB1 N-terminus in its subcellular localization. The CB1 N-terminal tail is uniquely long within the rhodopsin receptor family and has been suggested to play a role in its expression, trafficking and signaling(196). However, the function of the N-terminus is still poorly understood. As was already shown previously(195, 305), we demonstrated that modifying the N-terminal portion even by only adding an SSF tag dramatically affects

CB1's sub-cellular localization. This turned out to be an effective tool in allowing for deconvolving the role of subcellular localization in CB1 signaling.

CB1 signaling via calcium. The signaling picture is not complete without accounting for CB1-induced calcium transients. Our results show that there is a component of WIN-induced calcium peaks that is driven by calcium influx which could be triggered by $G\beta\gamma$ at the plasma membrane. However, there is a second component that is sensitive to thapsigargin and therefore originates likely from intracellular calcium stores. Whether this is induced by $G\alpha_q(190)$ or through calcium-induced calcium release remains unclear.

Minimally perturbative methods for monitoring cannabinoid receptor trafficking. We have demonstrated that tags commonly used for monitoring GPCR expression and trafficking, like SSF, perturb the subcellular localization of CB1. To provide a solution to this issue, we have developed an alternative method for live cell tagging and tracking of CB receptors. We used genetic code expansion in combination with strain-promoted inverse electron-demand Diels-Alder chemistry (SPIEDAC) which provides a minimal alteration and changes the labeling from the N-terminus to the first extracellular loop. This proved to be an efficient method for tagging the receptor at the plasma membrane while having little impact on CB1 signaling and trafficking, and we identified sites for efficient incorporation into both CB1 and CB2. Previously, other groups have employed genetic code expansion to study GPCRs and other membrane receptors in a variety of settings (298, 314). We believe our SPIEDAC incorporation site will allow for high flexibility in the choice of dye and will hence provide a valuable tool for future studies of CB1 in intact cells.

In summary, we demonstrated that expression level and N-terminal modification of CB1 can lead to disruption in the receptor location and function. We identified a modulatory signal transduction of CB1 dependent on the receptor's cellular location, indicative of location bias. Consequently, the synthesis of agonists and antagonists with cell-permeable or impermeable properties, designed to target intracellular organelles or to bind receptors exclusively at the cellular surface, respectively, may be instrumental in leveraging the functional selectivity of the CB1

OUTLOOK AND FUTURE WORK

Probing for the functional state of intracellular CB1

We show in our study differences in cAMP regulation dependent on the apparent localization of the CB1 receptor. We proposed that these changes are connected to differential G protein coupling between the receptor pool at the plasma membrane and the pool in internal membranes. However, it will be necessary to probe directly at the active conformation state of both pool of receptor in order to demonstrate their functional duality in regard to G protein coupling.

One of the pivotal studies demonstrating intracellular GPCR signaling utilized a conformational sensitive nanobody(205). Such nanobody do not exist yet for CB1 but alternative approaches, such as mini-G proteins (mG), could be helpful in probing for active conformation of CB1 in internal membranes. A recent study has shown that mG proteins fused to a mVenus and co-expressed with A₁-adenosine receptors in Hek293 cells were first localized in the cytosol but translocated to the plasma membrane and Golgi upon activation of the receptor with adenosine(315). Perhaps this methodology could be adapted to the CB1.

Generation of cell impermeable CB1 ligands

Most endocannabinoid ligands are characterized by a high lipophilicity. This means that the ligands are readily able to access the under-studied intracellular pool of CB1. Generating cell impermeable ligands for CB1 would enable to independently activate the pool of receptor at the plasma membrane or at the intra-organelles. A recent study developed a cell impermeable β 1AR antagonist by conjugating a pharmacophore to a sulfonate-containing fluorophore. The sulfonated fluorophore prevents the pharmacophore to enter the cells hence enabling compartmentalized of β 1AR signaling(316). The advantage of such a strategy is that it could allow rapid screening of potential cell types or conditions where intracellular CB1 is functional by inactivating the plasma membrane pool of CB1 with a receptor specific cell impermeable antagonist.

Improvement of ncAA incorporation in CB1

While we successfully incorporated a TCO*Lys in the ECL1 of CB1, this method of tagging is far from being without any drawbacks. The expression of the orthogonal suppressor RS together with its cognate suppressor tRNA led to non negligible cell toxicity. Additionally, modification of nontargeted host proteins through amber stop suppression (data not shown) can make alternative experiment, such as crosslinking of the receptor using photo-crosslinkable ncAA, challenging. Methods such as membraneless organelles(137) or generation of stable cell lines(317) could help mitigate some of these drawbacks and expand potential applications(318).

Chapter 4: Trifunctional fatty acid derivatives: PE's mitochondrial interactome

Alix Thomas, Rainer Mueller, Scotland Farley, Ana Kojic, Frank Stein, Per Haberkant,
Carsten Schultz

ACKNOWLEDGMENT STATEMENT: Thanks to Rainer Müller for synthesizing the trifunctional lipids used in this study, Scotland Farley for providing codes for the analysis of the proteomic data, Ana Kojic for contributing to the sample collection of the proteomic experiment, Frank Stein and Per Haberkant for the processing and primary analysis of the proteomic experiment and Carsten Schultz for contributing to the experimental design, analyzing the data, and editing the manuscript.

ABSTRACT

Phosphatidylethanolamine (PE) is a ubiquitous lipid species in higher eukaryotes which resides preferentially in mitochondria. Here, we synthesized a multifunctionalized PE derivative (TF-PE ; 1) designed to identify PE-binding proteins in intact cells through photo-crosslinking and subsequent isolation and proteomic analysis of the PE-protein conjugates. Due to its aromatic caging group, 1 is initially concentrated in perinuclear membranes. After uncaging, rapid translocation to mitochondria was observed. Hence, the tool is useful for tracking PE location and for determining the PE interactome. A trifunctional phosphatidic acid derivative in comparison was rapidly metabolized and is hence more limited in its use.

INTRODUCTION

Phosphatidylethanolamine (PE) is highly abundant in mammalian cells where it makes up to 25% of all phospholipids(319). PE is also the most common phospholipid in bacteria. Its

biosynthesis is well described. In the endoplasmic reticulum (ER), CDP-ethanolamine is coupled preferentially to mono- and di-unsaturated diacylglycerol (DAG) via the CDP-ethanolamine pathway. In mitochondria, more highly unsaturated PE is mainly produced by decarboxylation of phosphatidylserine (PS)(320) by PS decarboxylase located on the inner mitochondrial membrane(321). Importantly, each biosynthetic pathway aforementioned are required for mammalian development, highlighting the functional differences between PE species(322, 323). The knock-out of PS decarboxylase causes embryonic lethality due to mitochondrial defects, demonstrating that the CDP-ethanolamine pathway cannot compensate for the absence of PS decarboxylase during development(323). Unsaturated PE in the mitochondria play a crucial role in oxidative phosphorylation and the membrane fluidity and dynamics(324, 325). PS is swiftly transported from the ER to the mitochondria, presumably facilitated by the ER-membrane protein complex EMC(326) at the MAM contact site(327), while robust levels of PE in the ER limits PE export from the mitochondria as this process may be more energetically unfavorable, with unsaturated PE species largely retained in the mitochondria(320). This leads to a concentration of unsaturated PE in the mitochondria. Overall, the mechanisms of PS and PE transport between the ER and mitochondria in mammals is still presently unclear.

Despite its prominent distribution in endomembranes, few functions of PE have been established. Clearly, mitochondria deprived of PE are not functional(323). This has in part been attributed to PE's role in allowing membrane curvature. PE promote the formation of hexagonal phase structures which induce membranes bending events and conformational changes within membrane proteins(328). In mammals, PE depletion in the mitochondria impair the formation of the complex IV of the respiratory chain(324), possibly because of its presence at the dimer interface of the complex(329). Metabolically, it is the precursor for

phosphatidylcholine and the cannabinoid anandamide. Prominently, PE accumulates in the cytokinetic furrow during the last stages of mitosis(330).

Considering the abundance of physiological roles of PE —such as its involvement in membrane fusion during the final stages of cell division(330), mitochondrial function(325), autophagy(331), and serving as a precursor for other lipids(319)—little is known about PE-binding proteins outside of lipid metabolism and transport. This is partly due to a lack of tools to systematically determine the PE interactome in intact cells and cell lysates and to visualize the location of PE in a cell as most evidence gathered on PE physiological roles have been obtained by disrupting PE metabolic pathways. For PE visualization, fluorescently tagged PE derivatives are potentially less feasible because many lipid derivatives with aromatic groups seem to locate to endomembranes(119). This is also evident for photo-releasable (caged) PE derivatives as is shown below. However, due to the unusual location of caged lipid derivatives, transport from endomembranes to preferred membranes for a given lipid can be followed with multifunctional lipid derivatives. In brief, removal of the aromatic cage group by a flash of light permits transport by lipid transport proteins or diffusion out of endomembranes.

For instance, after uncaging phosphatidylinositol(229), PI(3,4)P₂, and PI(3,4,5)P₃ rapidly translocated to the plasma membrane(332). The location is visualized by photo-crosslinking the lipid derivatives with 350 nm UV-light in defined intervals after uncaging. Cell fixation with methanol will remove all lipid derivatives not crosslinked to proteins and subsequent click chemistry will add a fluorescent label to the lipid-protein conjugate. This powerful technique may lead to significant discoveries. For instance, co-staining with an antibody for double-stranded RNA revealed that sphinganine co-localizes with viral particles in COVID-infected cells(231).

In this work, we intended to identify PE binding proteins through a multifunctionalized PE derivative (TF-PE, **1**). Functional units added to the parent lipid are an alkyne group for bioorthogonal labeling, a diazirine for photo-crosslinking and a light-removable coumarin (cage) similar to the above named lipids, sphingosine and diacylglycerols(228). As a control lipid, Rainer Müller synthesized trifunctional phosphatidic acid (TF-PA, **2**). Both caged lipid derivatives, TF-PE and TF-PA accumulate in endomembranes, but change location once the caging group is removed by a flash of light. Uncaged PE heads towards mitochondria while uncaged PA seems to be metabolized rapidly. The mitochondrial location of PE was then used to determine the mitochondrial interactome of PE.

MATERIALS AND METHODS

Cell Culture

The HeLa Kyoto cell line (female) was kindly provided by R. Pepperkok (European Molecular Biology Laboratory, Germany). HeLa Kyoto (passage 15-35) were grown in high glucose DMEM (41965-039, Life Technologies) supplied with 10% fetal bovine serum (10270098, Life Technologies) at 37 °C and 5% CO₂.

Antibodies, Chemicals and Reagents

Anti-calreticulin, rabbit (Invitrogen 3501S)

Anti-Tom20, mouse (Santa Cruz, sc-17764)

Anti-GM130, rabbit (Cell Signaling, D6B1)

Goat anti-Rabbit IgG (H+L) Highly Cross-Adsorbed secondary antibody, Alexa Fluor Plus 488 (Invitrogen, A32731)

Goat anti-Mouse IgG (H+L) Highly Cross-Adsorbed secondary antibody, Alexa Fluor Plus 647 (Invitrogen A32728)

For proteomics, the kit Click Chemistry Tools (Cat No 1235) was used following the standard manufacturer's protocol.

For microscopy, the kit Click-&-Go® Plus 568 Imaging Kit (Vector Labs, CCT-1318) was used following the standard manufacturer's protocol

Cell-based Experiments

Live cell uncaging of TF-probes

HeLa cells were grown to 70% density in an 8-well Labtek dish. Each well was washed two times with DMEM free of FBS and loaded with 250 μ L of a 5 μ M caged lipid solution. Fluorescence images of the coumarin were captured on an inverted dual scanner confocal laser scanning microscope (Olympus Fluoview 1200) with a 63 \times oil objective using excitation at 405 nm for coumarin imaging and simultaneous excitation at 375 nm for uncaging.

Analysis of Trifunctional Lipids by Thin-Layer Chromatography

HeLa cells were seeded in 6 cm dishes and grown to confluence. The cells were loaded with the lipid derivatives (10 μ M) in FBS free media and allowed to sit on cells for 30 min at 37 $^{\circ}$ C prior to uncaging. After the probe media was removed and replaced with normal complete media, dishes were exposed to 400 nm light (Narrow band 400 nm NailStar LED lamp, Amazon, ASIN B01286DTFQ) to uncage the probe and either immediately processed or returned to the incubator for the indicated amount of time to allow metabolism. For the lipid extraction, dishes were rinsed with ice-cold PBS, and scraped in 300 μ L of ice-cold PBS. The scraped cells were transferred into a glass tube to which 600 μ L of methanol was added at room temperature. Samples were vortexed for 10 seconds and then 150 μ L of chloroform was added and samples were vortexed for 10 seconds again. Samples were centrifuged at 3000 x g for 10 min. The supernatants were transferred to fresh tubes, to which 300 μ L of chloroform and 600 μ L of 0.1% (v/v) aqueous acetic acid were successively added. Following vortex mixing, samples were left at -20 $^{\circ}$ C over-night to allow for phase separation. The next day the lower phases were transferred into fresh tubes and dried under a stream of nitrogen.

Lipids were labeled with the fluorogenic 3-azido-7-hydroxycoumarin dye prior to TLC analysis. The dried lipid extracts were re-dissolved in 8 μ L chloroform, to which 30 μ L was added from a copper-click master mix containing 5 μ L of 10 mM 3-azido-7-hydroxycoumarin in acetonitrile, 100 μ L of 10 mM tetrakis(acetonitrile)copper(I) tetrafluoroborate in acetonitrile, and 400 μ L of ethanol. The reaction was allowed to proceed for 3 hours at 37 $^{\circ}$ C, and then extracts were once more dried under a stream of nitrogen. Extracted lipids were redissolved in 10 μ L chloroform and plated on 10 \times 10 cm HPTLC silica 60 glass plates (Merck, Cat No 105631) without F254 fluorophore. Lipids were

resolved by a two-step system: first using chloroform/methanol/water/acetic acid 65:25:4:1 for 6 cm, then drying, and finally using hexane/ethyl acetate 1:1 for 9 cm. Fluorescently labeled lipids were visualized by using the SYBR Green channel of a BioRad Chemidoc Touch Imaging System. *TLC/CMS* bands with enough signal intensity (PE) were subjected to analysis by TLC-MS using an Advion Plate Express Compact Mass Spectrometer.

Subcellular Visualization of Lipids by Confocal Microscopy

HeLa cells were seeded on coverslips in 24-well plates and grown to 60-80% confluence. The cells were washed with DMEM and loaded with the lipid derivatives (5 μ M) in FBS free media and allowed to sit on cells for 30 min at 37 °C prior to uncaging. Dishes were exposed to 400 nm light (Narrow band 400 nm NailStar LED lamp, Amazon, ASIN B01286DTFQ) to uncage the probe and returned to the incubator for varying amounts of time to allow for metabolism. Then, they were exposed to 350 nm to photocross-link using a lamp with narrow band 350 nm (NailStar 36 W UV lamp, Amazon, ASIN B00R4M0TI0), and immediately fixed by washing twice with PBS, then left in methanol for 20 min (for further analysis using the automated CellProfiler pipeline, cells were washed 4 times with ice-cold PBS after photocross-linking and incubated with CellBrite for 15 min at 4°C and washed 4 more time with ice cold PBS prior to fixation). To remove non-crosslinked probes, cells were washed once with chloroform/methanol/ammonium hydroxide (10:55:0.75) and then the coverslips were transferred to a new 24-well plates and washed three times with PBS to remove organic solvent. 250 μ L of a click mix was added in each well (Click-&-Go Plus 568 Imaging Kit).

The reaction was allowed to proceed for 30 min in the dark. Click mix was removed, cells were washed twice with PBS, and blocking buffer (3% BSA in PBS) was added. Cells were blocked for 1 h before the addition of primary antibodies. All primary antibodies were diluted 1:250 in blocking buffer and left on cells, with rocking, overnight at 4 °C. The next day, primary antibodies were removed, cells were washed four times with PBS, and fluorescently tagged secondary antibodies were added, either A488 antirabbit or A647 antimouse, 1:1000 dilution in blocking buffer, for 1 h at RT, with rocking. Secondary antibodies were removed, cells were washed four times with PBS, and DAPI (1:1000) was added for 5 min.

Cells were imaged on a dual scanner confocal microscope Olympus Fluoview 1200, using a 63x (oil) objective or a Zeiss LSM 980 airyscan equipped with a 63x objective. Image resolution was improved down to 0.1 um using joint deconvolution algorithm from the Zeiss software. Pearson's correlation and Manders' coefficient between the lipid signal and the signal for each organelle marker were calculated using an ImageJ(1.53T)(242) pipeline running the plugin JaCoP(333). Each image was cropped to exclude any extracellular space or the nucleus. For each channel, the thresholding algorithm IsoData was used to generate mask in order to remove background pixels (Appendix 4-1). Individual cells were selected based on regions of intensity of the lipid signal, and coefficients were calculated within each cell.

Cell profiler Pipeline

Hoechst was used for staining the nuclei and CellBrite Fix (Biotium) for covalently staining the plasma membranes of fixed cells. The nuclear stain allowed us to identify a primary set of objects, each corresponding to a single cell. The plasma membrane stain CellBrite allowed the identification of a secondary set of objects derived from the first set, each object corresponding to a full single cell body. For this, watershed and global minimum cross entropy thresholding were used permitting efficient single cell segmentation. For defining the PM ROI, we shrank the secondary objects (segmented cell objects) by two pixels and then subtracted the outcome from the original secondary objects, generating a two pixels wide single cell plasma membrane mask. The plasma membrane mask was used to determine the increase in fluorescence intensity after uncaging at the plasma membrane. This intensity was normalized to the intensity of the cell body ROI (Intra, shrunk secondary objects). Values of at least 20 cells per well were compared for each condition.

Isolation of Protein–Lipid Complexes

HeLa cells were seeded in three 10 cm dishes per condition and grown to confluency. Cells were loaded with 10 μ M of the lipid probes in DMEM overnight. The cells were subjected to photocross-linking directly after uncaging. After photo-cross-linking, cells were washed with PBS and scraped into PBS. Cells were pelleted by centrifugation (500g for 5 min) and the supernatant was discarded.

Cells fractions were then isolated using the MinElute plasma membrane protein isolation kit (Invent Biotechnologies, Cat No SM-005). The total membrane fraction (resuspended in

PBS:0.5% Triton X-100) for each sample were incubated with 200 μ l prewashed picolylazide agarose beads (Click Chemistry Tools, Cat No 1235, Component A) in presence of 1 mM final CuSO_4 , 100 μ M BTTAA and 1 mM sodium ascorbate to catalyze the click reaction (RT for 1 h agitating). The beads were then extensively washed in disposable PD-10 columns (full column volume of each buffer): 3x with PBS, 3x with 50mM ammonium-bicarbonate, 3x 50 mM ammonium-bicarbonate 3M urea and 3x with 50 mM ammonium-bicarbonate to remove unspecific binders. The beads were then transferred to a clean Eppendorf tube, spun down and resuspended in 500 μ L 50 mM ammonium-bicarbonate/3 M urea. Bound proteins were reduced via the addition of 5 mM final TCEP and incubated at 55°C with orbital shaking for 30 min. Proteins were then alkylated with 10 mM iodoacetamide (final concentration) for 20 min, incubated at RT in the dark, followed by the addition of 20 mM final DTT for 10 min at RT with shaking. The beads were precipitated via centrifugation and the supernatant was removed from the beads. The beads were resuspended in 150 μ l 50 mM ammonium-bicarbonate/2M urea. 3 μ g of MS grade trypsin (VWR, PI90057) was added and incubated overnight at 37°C with vigorous shaking to prevent the beads from settling. In the morning 1 μ g fresh trypsin was added and incubated for additional 2h. The supernatant was saved and beads washed once with 250 μ l 50 mM ammonium-bicarbonate/2M urea that was added to the previous supernatant containing digested peptides. The total supernatant containing the digested peptides was acidified with 0.5% TFA (final concentration). The peptides were purified on a C18 desalting column, and dried.

Each experiments were performed in two biological replicates.

Identification of Proteins by LC-MS/MS

Dried peptides were shipped to the EMBL proteomics core facility, where they were TMT-labeled using the TMT-16-plex system and analyzed by LC-MS/MS on an Orbitrap Fusion Lumos mass spectrometer (Thermo Scientific). Peptides were separated using an Ultimate 3000 nano RSLC system (Dionex) equipped with a trapping cartridge (Precolumn C18 PepMap100, 5 mm, 300 μm i.d., 5 μm , 100 \AA) and an analytical column (Acclaim PepMap 100. 75 \times 50 cm C18, 3 mm, 100 \AA) connected to a nanospray-Flex ion source. The peptides were loaded onto the trap column at 30 μL per min using solvent A (0.1% formic acid) and eluted using a gradient from 2 to 80% Solvent B (0.1% formic acid in acetonitrile) over 2 h at 0.3 μL per min (all solvents were of LC-MS grade). The Orbitrap Fusion Lumos was operated in positive ion mode with a spray voltage of 2.2 kV and capillary temperature of 275 $^{\circ}\text{C}$. Full scan MS spectra with a mass range of 375–1500 m/z were acquired in profile mode using a resolution of 120,000 with a maximum injection time of 50 ms, AGC operated in standard mode, and an RF lens setting of 30%. Fragmentation was triggered for 3 s cycle time for peptide-like features with charge states of 2–7 on the MS scan (data-dependent acquisition). Precursors were isolated using the quadrupole with a window of 0.7 m/z and fragmented with a normalized collision energy of 34%. Fragment mass spectra were acquired in profile mode and a resolution of 30,000. The maximum injection time was set to 94 ms and AGC target to custom. The dynamic exclusion was set to 60 s.

MS Data Analysis

Acquired data were analyzed using IsobarQuant (334) and Mascot V2.4 (Matrix Science) using a reverse UniProt FASTA Homo sapiens database (UP000005640 from May 2016) including common contaminants. The following modifications were taken into account: Carbamidomethyl (C, fixed), TMT16plex (K, fixed), Acetyl (N-term, variable), Oxidation (M, variable) and TMT16plex (N-term, variable). The mass error tolerance for full scan MS spectra was set to 10 ppm and for MS/MS spectra to 0.02 Da. A maximum of 2 missed cleavages were allowed. A minimum of 2 unique peptides with a peptide length of at least seven amino acids and a false discovery rate below 0.01 were required on the peptide and protein level(335). Only proteins which were identified in two out of two mass spec runs were kept. Log2 transformed raw TMT reporter ion intensities ('signal_sum' columns) were first cleaned for batch effects using limma(335) and further normalized using vsn (variance stabilization normalization(336)). Different normalization coefficients were estimated for +UV and -UV conditions in order to maintain for the abundance difference. Proteins were tested for differential expression using the limma package. The replicate information was added as a factor in the design matrix given as an argument to the 'lmFit' function of limma. A protein was annotated as a hit with a false discovery rate (fdr) smaller 5 % and a fold-change of at least 100 % and as a candidate with a fdr below 20 % and a fold-change of at least 50 %.

RESULTS

Rainer Müller synthesized the TF-PE (**1**) (Scheme 4-1) The synthesis started from the previously described diacylglycerol derivative **3**

which already provided a fatty acid featuring a terminal alkyne and a diazirine at the C11 position of the fatty acid in the *sn1* position(228).

For the *sn2* ester, Rainer Müller used arachidonic acid to maintain solubility. From the previously synthesized bis(*diisopropylamino*)phosphorous methylenocoumarinyl ester **4**,(337) Rainer prepared P(III) reagent **5** containing the Boc-protected ethanolamine group. Deprotection

gave the desired trifunctional PS derivative **1**.

The synthesis of the trifunctional phosphatidic

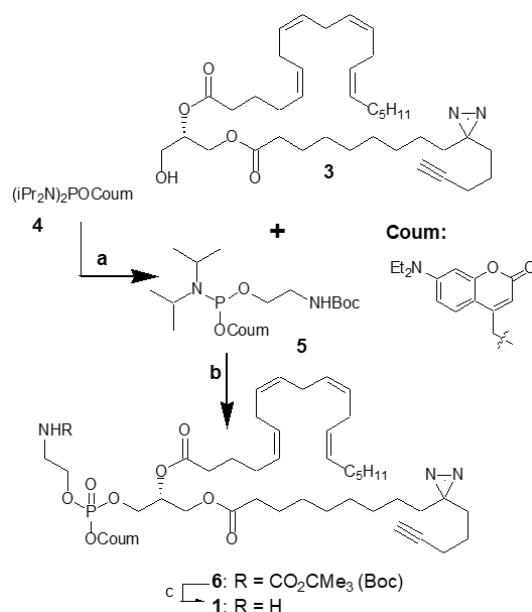
acid derivative **2** followed a similar path (Scheme 4-2). In this case, the phosphoramidate reagent (338, 339) provided the coumarin cage as well as

a fluorenylmethyl protecting group that is gently removable in the presence of the coumarinylmethylene

ester(226). After deprotection of compound **7** with dimethylethylamine, phosphate **8** was alkylated with

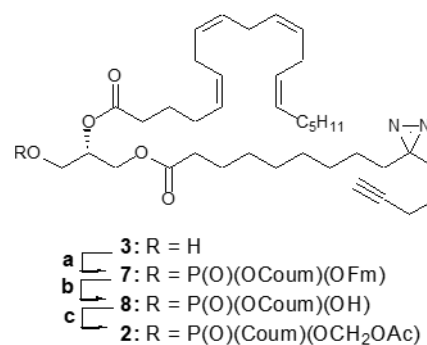
acetoxymethyl bromide to yield the non-charged TF-

PA derivative **2**. Acetoxymethyl (AM) esters of phosphates have been widely used to mask negative



Scheme 4-1. Synthesis of trifunctional PE.

Diacylglycerol derivative **3** was prepared as described by our group previously. Reaction conditions and reagents: a) BocHNCH₂CH₂OH, 1H-tetrazole, DCM, 24°C, 1h, 89%; b) 1.) 1H-tetrazole, DCM, 24°C, 1h; 2.) AcO₂H/AcOH, DCM, -78 to 24°C, 1h, 69% over 2 steps; c) CF₃COOH, DCM, 24°C, 1h, 99% **Compounds were synthesized by Rainer Müller.**



Scheme 4-2 Synthesis of trifunctional PA. Reaction conditions and reagents: a) *iPr*₂N-P(O)(OCoup)-(OFm), 1H-tetrazole, DCM, 24°C, 1h; b) trimethylamine, DCM, 24°C, 12h; c) AcOCH₂Br, DIEA, AcCN, 24°C, 12h. **Compounds were synthesized by Rainer Müller**

charges and permit cell membrane penetration. Once inside cells, AM esters are readily cleaved by endogenous hydrolases, especially when situated on a phosphate(340).

To test whether the lipids can be efficiently uncaged, we irradiated the lipids with a 400 nm UV lamp in chloroform and performed TLC (Figure 4-1A). We did not observe any free 7-Diethylamino-coumarin prior to irradiation for TF-PE, TF-PA and TF-PS (synthesis not shown), indicating a good stability of the cage for all three lipids. After light irradiation, we observed an increase in free 7-diethylamino-coumarin for TF-PE and TF-PA by TLC, demonstrating robust uncaging of the probes while no change was observed for TF-PS. As suspected with TF-PG (synthesis not shown), high level of free 7-diethylamino-coumarin were already present prior to irradiation, with no apparent changes after irradiation. We believe this is because of an intramolecular transesterification from the glycerol attacking the phosphoester, releasing the coumarin cage, hence the lower stability of this probe. Because TF-PE and TF-PA appeared to be stable and have high uncaging efficiency, we decided to further characterize these two probes.

A key consideration when developing trifunctional lipid probes is to ensure that the probes are capable of entering cells and are released by light. We treated live HeLa cells with 5 μ M of TF-PE or TF-PA and observed a rapid increase in the coumarin fluorescence within cells. Maximum fluorescence levels were reached after 10 min with TF-PE and 20 min with TF-PA (Figure 4-1B-C). Illumination with a 375 nm laser on the microscope stage led to a transient increase of the coumarin fluorescence indicative of successful uncaging, as free coumarin is known to be brighter than its phosphate ester counterpart(337).

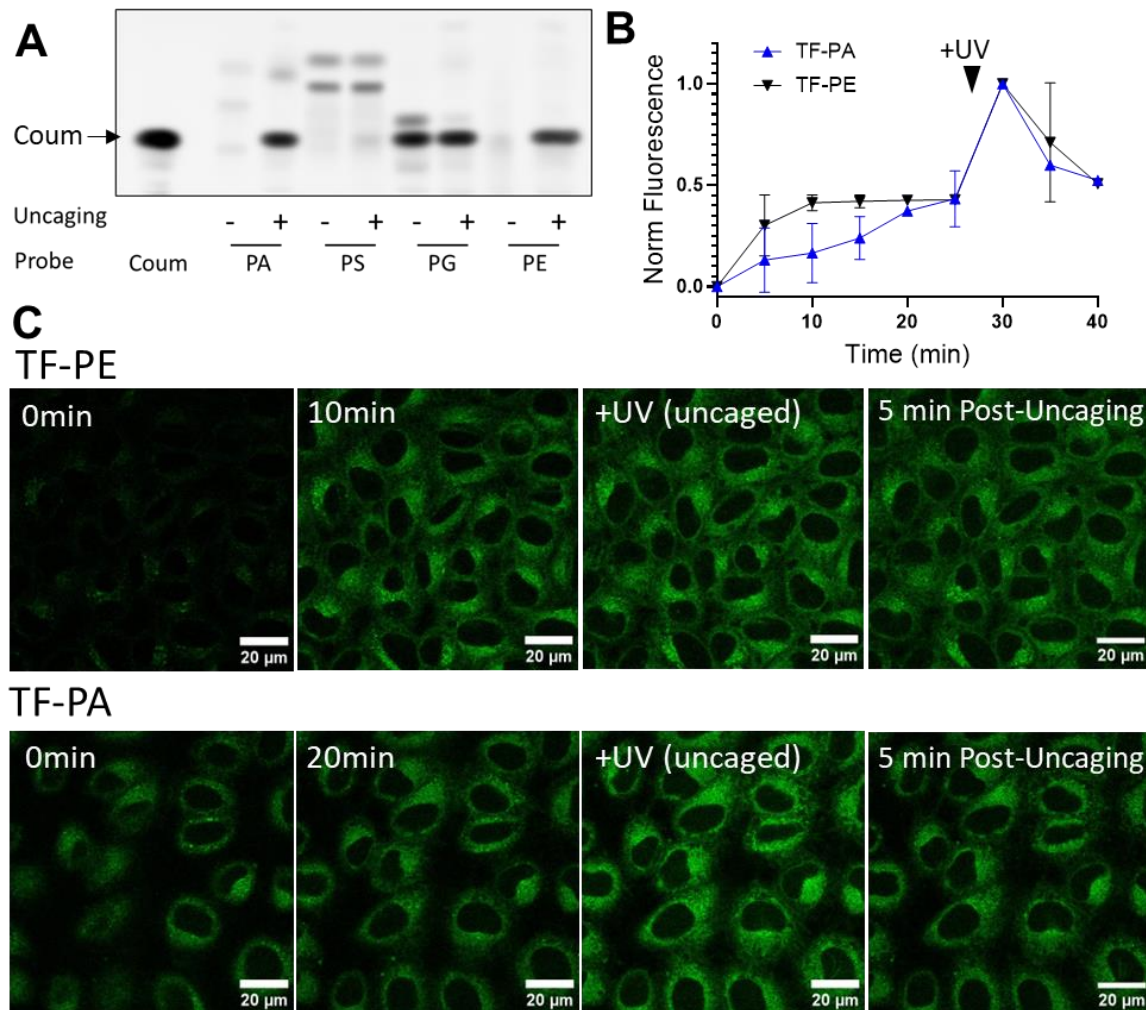


Figure 4-1 TF-lipid loading. **A.** Thin layer chromatography of the TF-lipids probes illuminated or not with 405nm light. The coumarin was imaged using a Biorad imager. Eluent: chloroform:methanol:water:acetic acid (65:25:4:1) for 6 cm, then cyclohexane:ethyl acetate (1:1) for 9 cm. **B.** Coumarin mean emission values of three replicates were normalized to the minimum observed fluorescence intensity. Cells were irradiated with 405nm light 20 sec prior to the 30 min imaging time point. Error bars represent standard error. **C.** Confocal micrograph showing loading of TF-PE (5 μ M) and TF-PA (5 μ M) derivative into HeLa cells. Illumination of cells with 405 nm laser light (uncaging) led to a rapid increase of emission intensity due to the higher quantum yield of the released 7-diethylamino-4-hydroxymethyl-coumarin.

To further test proper cell entry and uncaging of the TF-lipid probes, we treated HeLa cells with the trifunctional derivatives, washed the cells, extracted the lipids and labeled with the fluoro-genic 3-azido-7-hydroxy-coumarin via copper-catalyzed click chemistry. TLC analysis showed robust uncaging of both TF-PE and TF-PA after >400 nm irradiation. We did not observe any significant decrease of the TF-PE lipid after uncaging within 2 hours

(Figure 4-2A-B), in contrast to a marked drop in the TF-PA level, starting as soon as 30 seconds post uncaging with most of the uncaged probe being metabolized after 20 min (Figure 4-2C). The bulk of the PA derivatives appears to be incorporated into phosphatidylcholine (PC), likely through dephosphorylation into diacylglycerol, a precursor for the formation of PC via the Kennedy pathway(341)(Figure 4-2D).

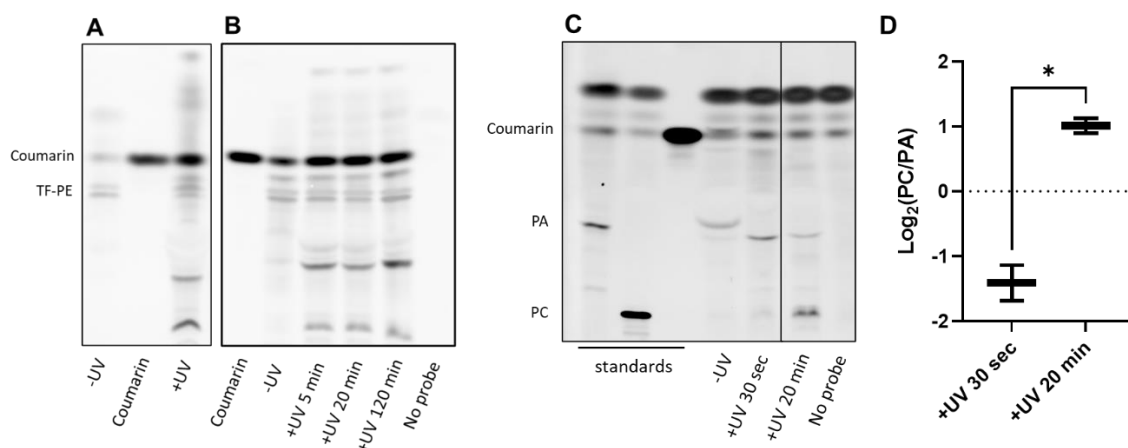


Figure 4-2 TF-lipid TLC A.B.C. TLC of caged and uncaged TF-PE and TF-PA derivatives on HPTLC silica 60. Lipids were labeled with 3-azido-7-hydroxy-coumarin prior to TLC. 65:25:4 chloroform : methanol : water, for 6 cm, followed by 1:1 hexanes : ethyl acetate for 9 cm (A,B) or 65:25:4:1 chloroform : methanol : water, acetic acid for 6 cm, followed by 1:1 hexanes : ethyl acetate for 9 cm (C). . **A.** 7-Diethylamino-coumarin and TF-PE with and without UV irradiation. **B.** Extracts from HeLa cells initially treated with 10 μM TF-PE with or without subsequent UV light irradiation and metabolization for the time indicated. **C.** TLC (HPTLC silica 60) of the standards TF-PA (uncaged), alkyne PC and 7-(Diethylamino)coumarin in the first three lanes followed by lipid extracts from HeLa cells initially treated with 10 μM of TF-PA derivative with and without subsequent UV light irradiation and metabolization for the time indicated. **D.** Integrated densities following background subtraction of lipid spots corresponding to PA and PC 30 sec or 20 min after light irradiation (from figure 2C). Two biological replicates.

Next, we examined the subcellular localization of both trifunctional lipid derivatives before and after uncaging by 405 nm light. PE is described as the most abundant phospholipid after PC(319). It is enriched in the inner leaflet of the plasma membrane and the inner membrane of the mitochondria but is found in most cellular membranes. On the other end, PA has low abundance in cells (1-2% of total phospholipids) and is mostly known as a precursor in the ER, where it is rapidly metabolized into diacylglycerol. PE

has been shown to be imported from the ER into mitochondria. We performed a short time course in HeLa cells, crosslinking each lipid probe while still caged as well as 5 and 20 min post uncaging (Figure 4-3). Prior to uncaging, TF-PE appeared to localized exclusively in internal membranes, consistent with our imaging of caged TF-PE in live cell (Figure 4-1) and it remained localized exclusively in internal membranes 5 min and 20 min after uncaging (Figure 4-3). TF-PA was found predominantly in internal membranes, with an additional fraction of the lipid localizing at the plasma membrane (Figure 4-3). This diverged from our live cell experiments where the coumarin signal did not appear at the plasma membrane. Additionally, coumarin-caged lipids preferentially localize to the ER and Golgi(216). We cannot exclude that during the photo-crosslinking step, a portion of the lipid is uncaged and rapidly transported to the plasma membrane before being crosslinked. The initial fraction at the plasma membrane visibly decreased over time following uncaging. The re-distribution of the probe 20 min after uncaging is consistent with the rapid metabolism of PA into PC observed in our previous experiment, as PC is homogeneously distributed across cellular organelles.

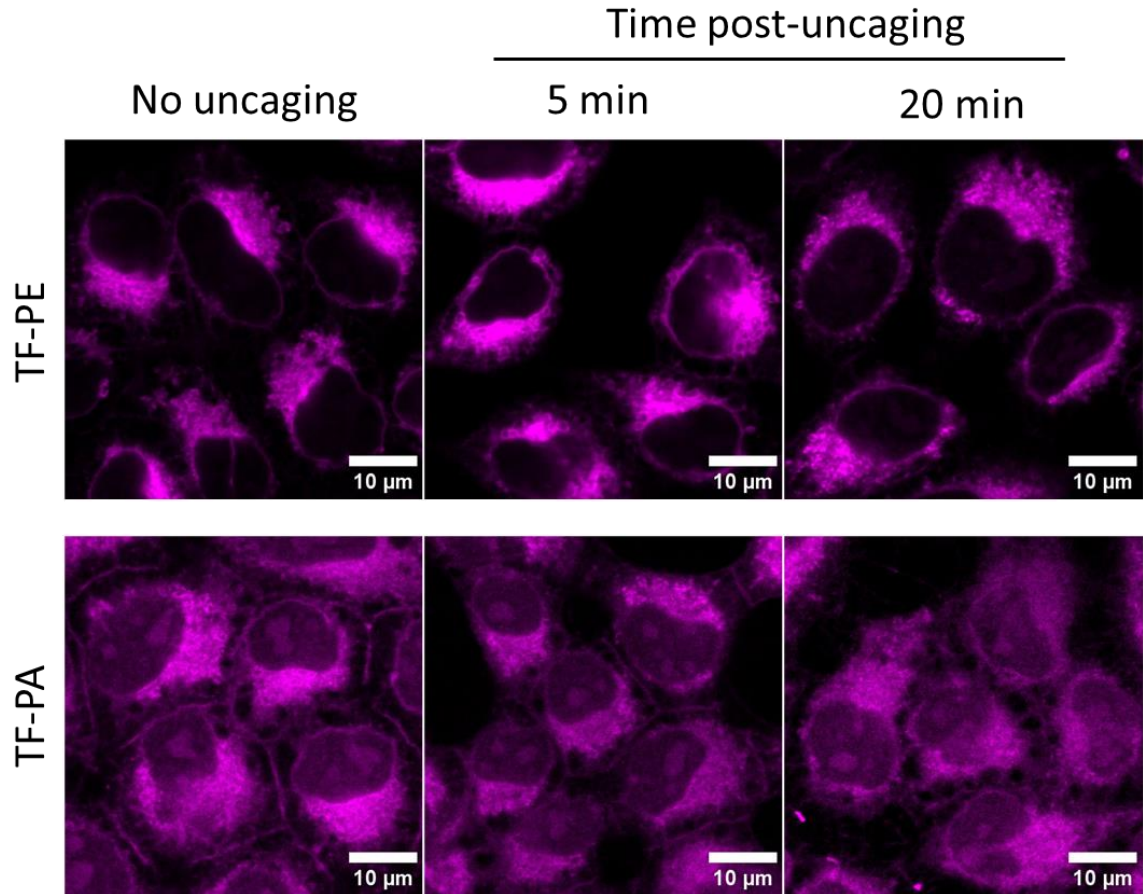


Figure 4-3 TF-lipid microscopy. Confocal micrograph showing subcellular localization of lipid probes. HeLa cells were treated with 5 μ M of TF-PE or TF-PA, exposed to 400nm light to uncage the probe, and allowed to metabolized for 5 or 20 min. The lipids were photo-crosslinked to proteins using 350 nm light, fixed, subjected to click reactions with a fluorescent azide, and immuno-stained with organelle markers. Images are representative of three independent experiments.

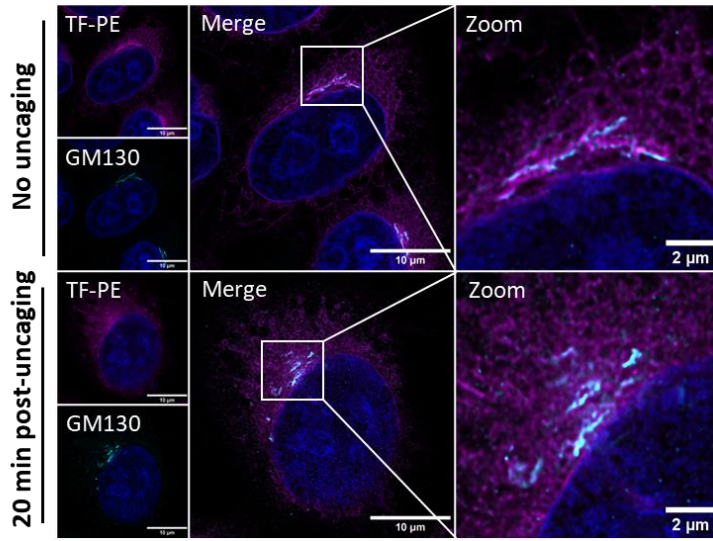
To further study the localization of TF-PE when caged and 20 min after uncaging, the cells were co-stained with antibodies for the ER, mitochondria and Golgi, and imaged at a resolution of about 0.1 μ m. The colocalization between the organelle markers and the lipid was calculated using Pearson's correlation coefficients (Figure 4-4A-B) and Manders' coefficients (Appendix 4-2). Caged TF-PE appeared to moderately colocalize with the Golgi organelle marker golgi matrix protein GM130 (Pearson's coefficient = 0.49) (Figure 4-4 A,B). This demonstrates the presence of our caged lipid in the Golgi prior to uncaging. Additionally, we observed a similar signal from TF-PE in close proximity but not

overlapping with the GM130 marker. This could correspond to the trans-Golgi network, as the protein GM130 predominantly localizes in the cis-Golgi(342). The caged lipid weakly colocalized with the mitochondrial marker Tom20 (Pearson's coefficient = 0.3) and the ER marker calreticulin (Pearson's coefficient = 0.29) (Figure 4-4, C-F). Twenty minutes after uncaging, TF-PE colocalization with GM130 and Calreticulin decreased by 13% and 57%, respectively, while we observed no significant changes between TF-PE and Tom20 (Figure 4-4, B,D,F). To rule out potential artifacts in the Pearson's coefficient measurements, the TF-PE channel (prior to uncaging) was rotated by 90°, followed by repeated measurements for each marker. Control experiments demonstrated no colocalization for GM130 and calreticulin, and a slight exclusion with Tom20 (Appendix 4-2 A).

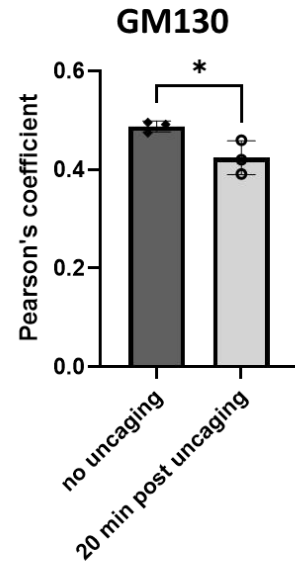
Analysis using the Manders' coefficient, which quantify the overlap between channels independently of the pixel intensity, showed no difference in colocalization before and after uncaging between TF-PE and the GM130 or Tom20 markers and a 53% decrease in the TF-PE area overlapping with the Calreticulin marker (Appendix 4-2 B-D). The Mander's coefficient showed overall similar trend as with the Pearson's coefficient except for the overlap between TF-PE and GM130. This is likely due to the inability of the Mander method to detect discreet changes in pixel intensity. It is important to note that, while generalized here as mitochondrial and ER markers, Tom20 is restricted to the outer mitochondrial membrane, while calreticulin predominantly localizes within the smooth ER. This specific localization may influence the extent of overlap quantified in this study. The Manders' coefficient analysis supports this, with the total overlap between TF-PE and the three markers summing to 0.49, indicating that approximately half of TF-PE does not

colocalize with the combined three markers. This is under the assumption that other organelles, such as autophagosomes or lysosomes, contribute minimally to the overall inter-membrane pool of the cell under the experiment conditions.

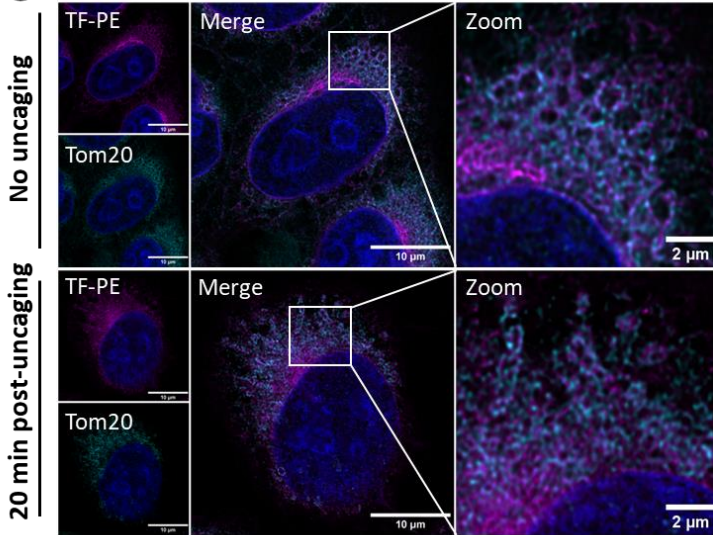
A TF-PE : GM130



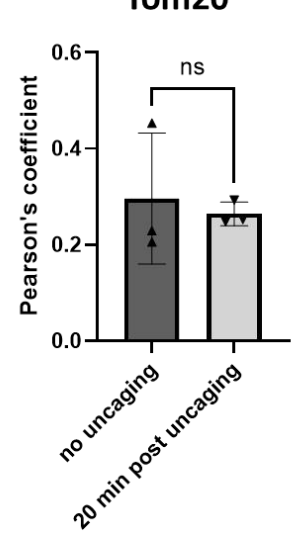
B



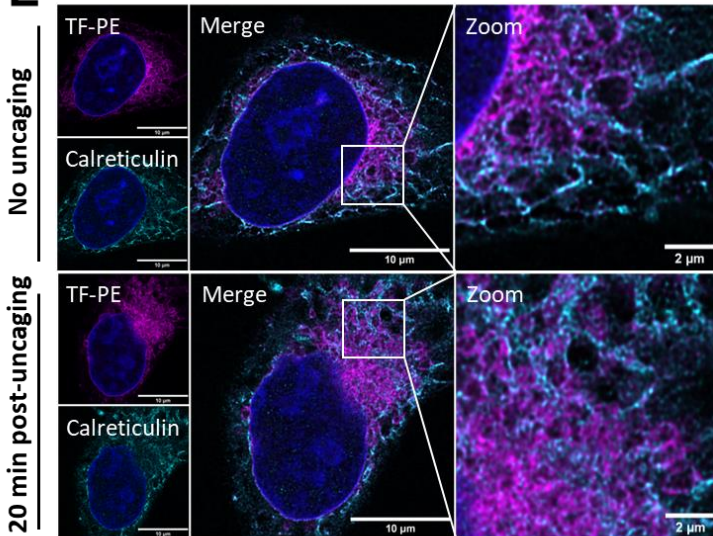
C TF-PE : Tom20



D



E TF-PE : Calreticulin



F

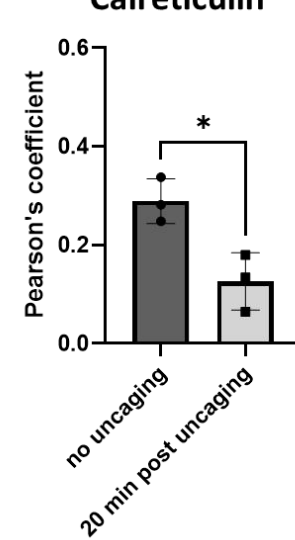


Figure 4-4 A,C,E Confocal micrograph showing subcellular localization of lipid probes. HeLa cells were treated with 5 μ M of TF-PE and either immediately photo-crosslinked with 350 nm light or uncaged with 400 nm light and allowed to metabolized for 20 min prior to photo-crosslinking. The cells were then fixed, subjected to click reactions with a fluorescent azide, and immuno-stained with the organelle markers (A) GM130 (Golgi), (B) Tom20 (Mitochondria), and (C) Calreticulin (ER). Images are representative of three independent experiments. **B,D,F.** Colocalization measurement using Pearson's coefficient between TF-PE and (B) GM130 (Golgi), (D) Tom20 (Mitochondria), and (F) Calreticulin (ER). Pearson's correlation coefficients were calculated using an ImageJ pipeline. Each experiment was performed in biological triplicates and 7 cells from different field of views were analyzed with Pearson per replicates. * $p < 0.05$, ** $p < 0.01$, *** $p < 0.005$, **** $p < 0.001$ (Unpaired t-test).

Previous work with trifunctional PI, PI(3,4)P2 and PI(3,4,5)P3 has shown that our probes can translocate from internal membranes to the plasma membrane within minutes after uncaging and demonstrated that the PI lipids are actively transported by lipid transport proteins(229). The observations in those studies were purely qualitative. In order to be able to robustly quantify the fraction of the probe translocating to the plasma membrane, we developed a method enabling un-biased quantification of fluorescence signal of our clicked probe at the plasma membrane. Using a plasma membrane stain in combination with a fully automated CellProfiler image analysis pipeline (Appendix 4-3A), we were capable of quantifying the fraction of our probe at the plasma membrane at different time point with TF-PIP3 and TF-PI(3,4)P2 (Appendix 4-3 B-E). We observed a rapid increase of each probe signal at the PM just 30 sec after uncaging. TF-PI(3,4)P2 shown an increase at the PM until 2 min with the signal dropping after 10 min (Appendix 4-3 B-E). We hope that this enable future studies comparing lipid transport between disease model or partially impaired lipid transport where a yes/no answer is not enough.

Having established the metabolism and localization of each probe, we proceeded to utilize the photo-crosslinking capability of the trifunctional lipid derivatives to compare their respective protein interactomes. HeLa cells were treated with TF-PE or TF-PA, each in two biological replicates. We photo-crosslinked both probes 15 min after uncaging (+UV). Additionally, two biological replicates where cells were not exposed to 350 nm light for crosslinking (-UV) were included as negative controls for each probe. Cells were lysed and the membrane and cytosolic fractions isolated. For the membrane fraction, we used azide-agarose beads and click chemistry to enrich proteins and analyzed them by LC-MS/MS, as previously described(337) (Figure 4-5A). Raw signal intensities for each channel were normalized based on variance stabilization(336), and 1113 proteins were identified and quantified. The intensity ratio of each protein under +UV conditions versus -UV conditions was calculated. To identify the most robust interacting proteins for each probe, the normalized signal intensities were subjected to Limma analysis to calculate fold changes and p-values of the intensity in the +UV over the -UV samples. Proteins with fold change greater than 2 and false discovery rate below 0.05 were categorized as “hit” and proteins with fold change above 1.5 and false discovery rate less than 0.2 were categorized as “candidate” (Figure 4-5B-C).

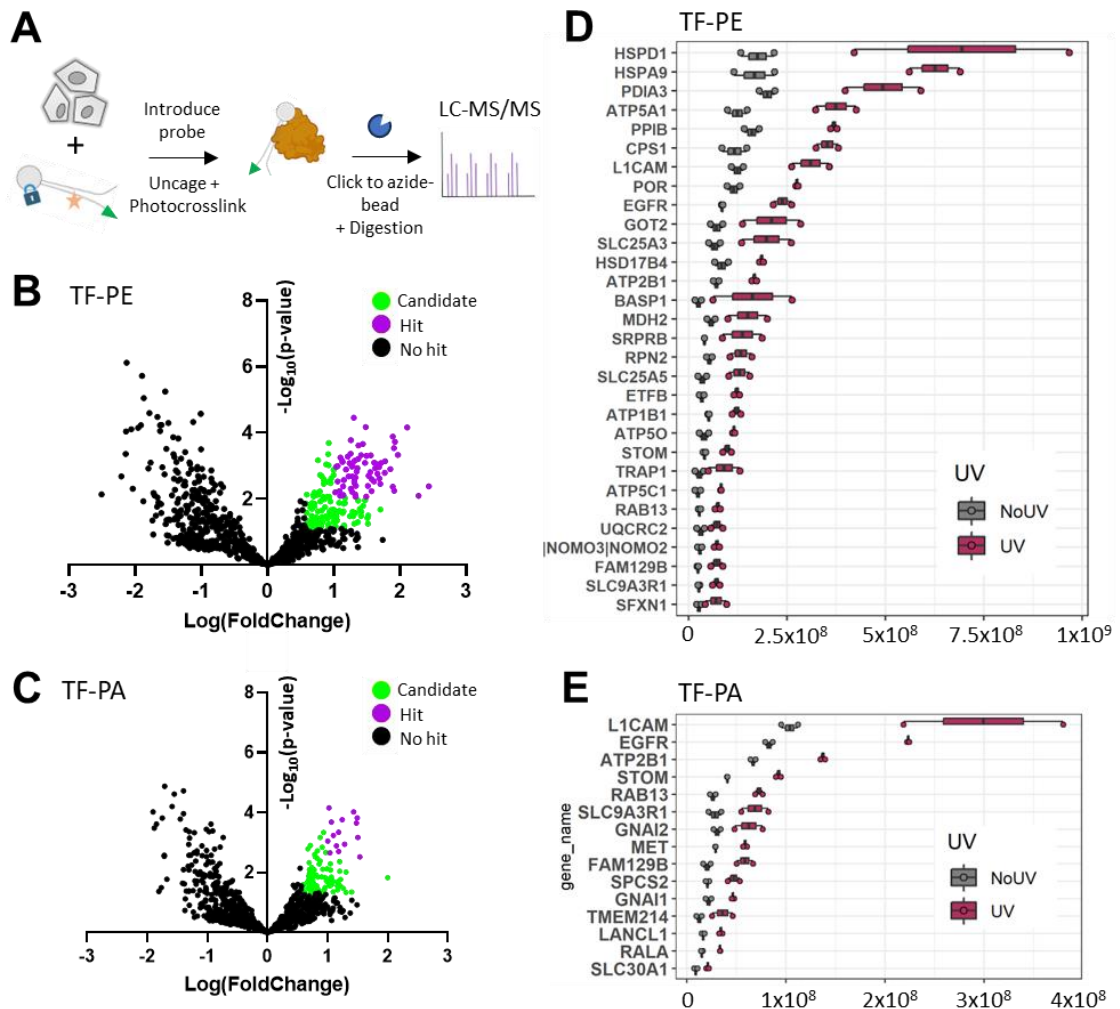


Figure 4-5. Proteomic analysis **A.** Experimental design pipeline. **B-C.** Volcano plots of identified hit proteins for each probe, by Limma analysis. “Hits” are defined as proteins with a false discovery rate less than 0.05 and a fold change of at least 2-fold in the +UV over the -UV. “Candidates” are defined as proteins with a false discovery rate less than 0.2 and a fold change of at least 1.5-fold. **D-E.** Normalized intensities of proteins identified as hits by the Limma analysis for (E) TF-PE; (F) TF-PA.

We identified 68 hits and 105 candidates for TF-PE and 15 hits and 85 candidates for TF-PA, revealing a major gap between potential interactors pull-downed by the PE probe compared to the PA probe. The normalized signal intensities for +UV and -UV of the top hits for TF-PE and TF-PA are displayed in Figure 4-5D-E. Many known lipid binders were identified for each probe. The fatty acid catabolic enzymes ECH1 and ECHS1, which were

identified in a previous screen(230), were significantly enriched with both probes. Several other enzymes involved in fatty acid metabolism were identified for both probes such as ACSL3 and ECI1. The mitochondrial phospholipid scramblases VDAC1 and 2(343) were enriched for both TF-PE and TF-PA, although not sufficiently to be categorized as hits. Similarly, the P4-ATPase ATP11C, an aminophospholipid translocase which has been shown to have substrate specificity for PS and PE(344), was weakly enriched for both TF-PE and TF-PA. The other P4-ATPase aminophospholipid translocase ATP11A and ATP11B expressed in HeLa cells and shown to have affinity for PE did not appear in our screen. TF-PE was significantly enriched with other known PE binders, such as the cytochrome c oxidase subunit NDUFA4(345) and, to a lower extent, the phospholipid remodeling enzyme (LPCAT3) which is involved in PE biosynthesis(346, 347). Surprisingly, Phosphatidylethanolamine-Binding Protein 1 (PEBP1), which specifically binds PE(348), was enriched in the -UV condition. Other well-known binders of PE, such as Atg3 and GABARAP, with autophagy-related functions(349), were absent from the screen, as well as the Phosphatidylethanolamine N-Methyltransferase (PEMT), which catalyzes the methylation of PE to form phosphatidylcholine(350).

To assess the quality of our biological replicates, we analyzed the variances among them using principal component analysis (PCA) (Appendix 4-4). The PCA analysis demonstrated high similarity for both +UV and -UV replicates for TF-PA. However, inconsistencies were observed in the TF-PE replicates, with significant differences in the second principal component (PC2), accounting for 15.7% of the variance, in both the -UV and +UV conditions. The addition of a third biological replicate could help reduce the potential false positives originating from this inconsistency.

We confirmed that TF-PA undergoes rapid metabolism, in contrast to the more stable TF-PE. We hypothesized that the rapid turnover of PA limits its utility in identifying reliable PA protein interactors using our probe, whereas the stability of PE favors this approach. To confirm this, we analyzed the overlap between the hits and candidates observed for each probe. We found that most hits and candidates from TF-PA appeared in near equal proportion for both lipids, suggesting nonspecific binding or binding with a metabolite product common to both probes, such as PC. In contrast, the hits for TF-PE had a +UV/-UV ratio markedly higher compared to TF-PA, increasing our confidence that these hits are specific to TF-PE (Figure 4-6).

To further compare between the TF-PE and TF-PA pool of identified hits and candidates, we analyzed the subcellular localization of each protein (Figure 4-7A). Strikingly, we observed a significant enrichment of mitochondrial proteins for TF-PE, in stark contrast to the near absence of mitochondrial proteins for TF-PA. This partitioning was also observed for ER-localized proteins, albeit much less pronounced. This was not unexpected as PE has been shown to be highly enriched in mitochondria and to be important for many mitochondrial functions(323), such as mitochondrial fusion(351) and oxidative phosphorylation(324) (Figure 4-7B).

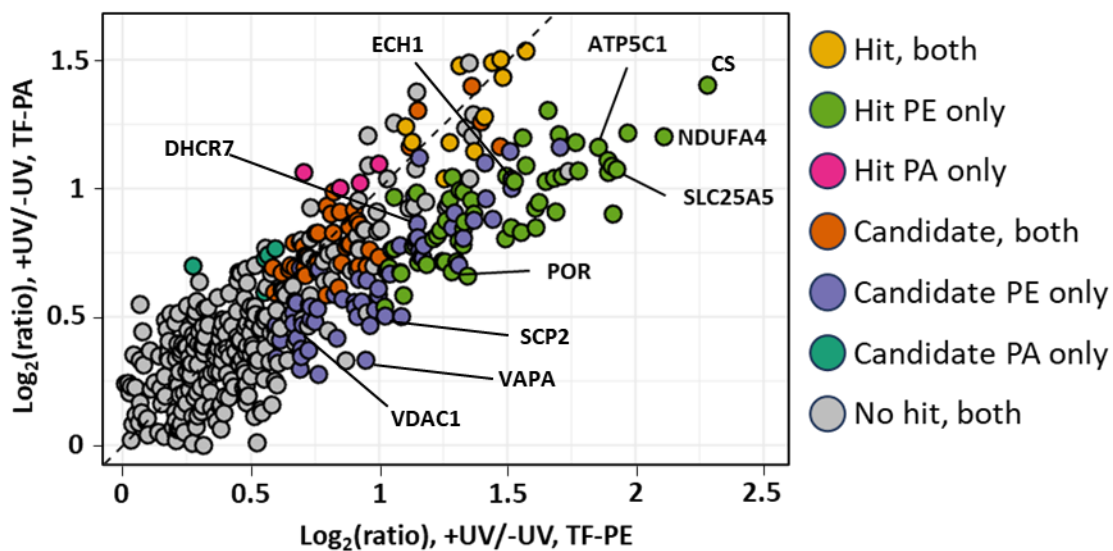


Figure 4-6. Comparison of PE and PA. Proteins pull down by TF-PA and TF-PE, colored by the degree of enrichment in the (+) UV condition over the (-) UV condition.

Notably, cytochrome c oxidase subunit NDUFA4 was identified as one of the strongest hits of the screen. The subunits UQCRC1 and 2 of cytochrome b-c1 complex were also highly enriched as well as the inorganic ion transport SLC25A3 and the nucleotide transporter SLC25A5 and 6, belonging to the larger SLC25A mitochondrial carrier family. Several hits highly enriched in PE over PA samples reside in the ER. Interestingly, the NADPH cytochrome p450 oxidoreductases (POR), which was demonstrated to regulate ferroptosis(352), a biological process thought to be specific to PE lipids(353), was one of the hits in our screen. Additionally, DHCR7, involved in ferroptosis regulation through the metabolic breakdown of the cholesterol precursor 7-DHC(354), was significantly enriched for TF-PE; however, it was also enriched for TF-PA.

Lastly, two proteins known to be involved in lipid transport were significantly enriched for TF-PE: SCP2, a lipid transport protein involved in cholesterol and fatty acid transport(355), and VAPA, known to interact with the

phosphatidylinositol/phosphatidylcholine transfer proteins Nir2 and Nir3 (also known as PITPNM1 and 2)(356). Interestingly, although Nir2 has been shown to transfer PA from the ER to the PM(357), VAPA was only marginally enriched for TF-PA, and Nir2 was not identified in the screen.

The lipid probes TF-PS, TF-PG, TF-PI3P, TF-PI4P, TF-PI(3,4)P2, and TF-PI(4,5)P2 (synthesized by Rainer Müller) were included in this screen following an identical workflow and will be briefly discussed here. We observed a distinct pattern of subcellular localization for the enriched proteins for each lipid probe (Appendix 4-5 A). Notably, TF-PI(3,4)P2 exhibited the highest enrichment in protein from the plasma membrane, whereas TF-PI(4,5)P2 showed the greatest enrichment for endoplasmic reticulum (ER) proteins. The identity of each enriched protein was significantly heterogeneous across each probe, increasing confidence in the specificity of each lipid for the proteins they pulled down (Appendix 4-5 A). We compared the proteomic results between each probe using principal component analysis on the Log₂(FC) enrichment of each protein (Appendix 4-5 B). Consistent with our previous observation, TF-PE, TF-PI(3,4)P2 and TF-PI(4,5)P2 showed the most variance with TF-PA, TF-PG, TF-PI3P and TF-PI4P clustering close together. While this does not necessarily reflect similarities in their biological functions, it can help in identifying probes with unique hit patterns.

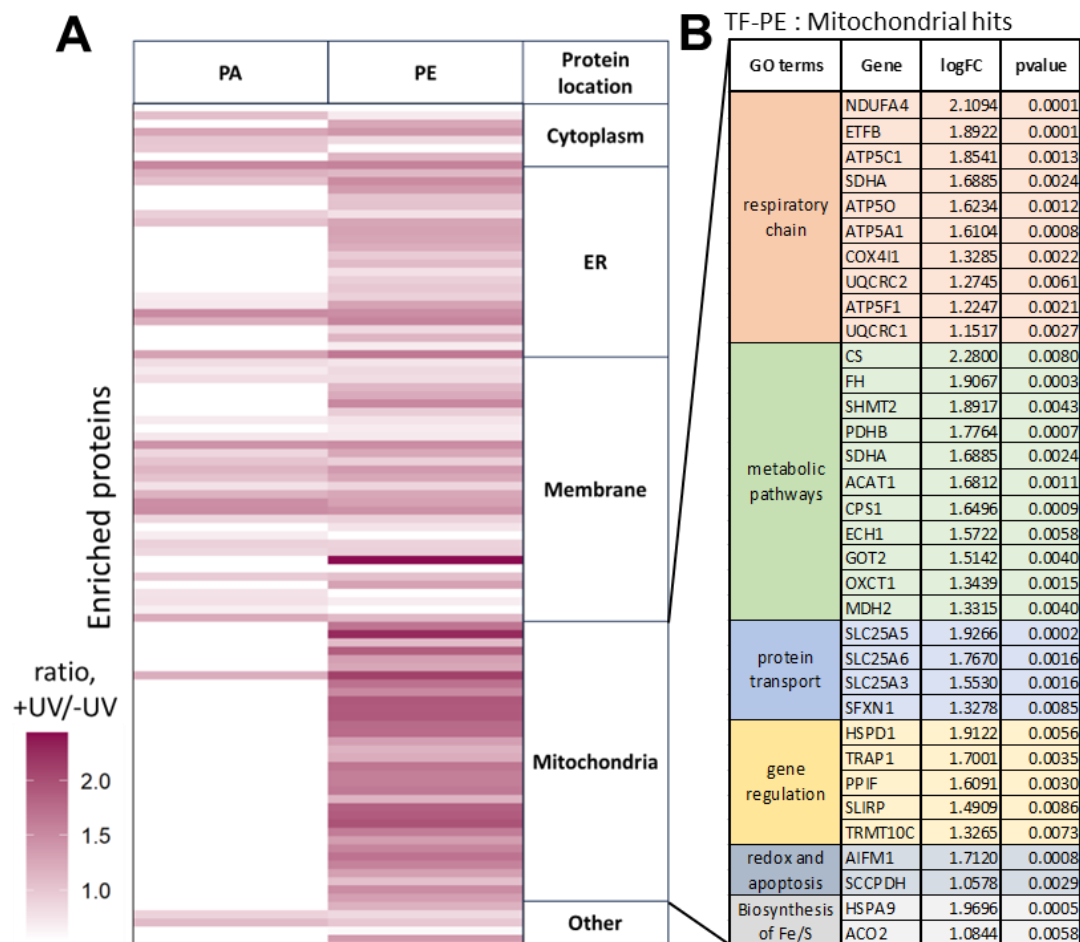


Figure 4-7 PE protein hits. **A.** Analysis of PE and PA binding proteins. Go-term enrichment of proteins identified as hits for each probe. The $\text{Log}_2(\text{FC})$ for the UV condition over the -UV condition for each probe is shown in each cellular compartment. **B.** Table summarizing mitochondrial proteins identified as enriched hits for TF-PE. Proteins are ordered by logFC values within each of the color-coded GO mitochondrial biological process categories.

DISCUSSION

We present the synthesis of two novel multifunctionalized lipid probes to profile their interactomes and to determine the lipid location after uncaging. The TF-PE derivative, after uncaging, translocated to mitochondria with no apparent metabolization, demonstrating its utility in determining the PE interactome. In contrast, the TF-PA derivative exhibited rapid metabolism, limiting its use in interactome studies to very short periods after uncaging. The

proteomic analysis revealed important enrichment of mitochondrial proteins associated with TF-PE, with key proteins involved in the respiratory chain and mitochondrial transport, and ferroptosis, underscoring PE's critical role in mitochondrial function.

Lipid metabolism

PA is produced by four different biosynthetic routes and its level can transiently rise downstream of receptor for specific signaling events(358, 359). As a signaling lipid, PA levels are tightly regulated in cells and it is rapidly metabolized into various phospholipids. Consistent with this, we observed a rapid conversion of TF-PA into PC, likely through the Kennedy pathway in the ER. After 30 sec of uncaging, 25% of the probe was already converted into PC, increasing to 66% of the probe after 20 min. Due to this rapid conversion, using the trifunctional probe to study the PA protein interactome is challenging. On the other hand, our PE probe after uncaging was stable with little apparent conversion even 2 hours post uncaging. However, we were surprised to see two bands corresponding to the uncaged "clicked" PE probe on the TLC as opposed to a single band. We confirmed by mass spectrometry that both extracted bands corresponded to our uncaged probe clicked with azido coumarin. Despite a clear characterization of the two bands, the apparent stability of our PE probe render it well adapted for screening protein interactors.

Following lipid transport in cells

Inter-organelle lipid trafficking is mediated via various mechanisms separated in two major categories, vesicular and nonvesicular transport mediated by lipid transport proteins (LTPs)(360). Identifying LTPs is challenging and many innovative biochemical techniques have allowed to expand the repertoire of LTP in the recent years(343, 361, 362). Our TF-

probes permit to reliably follow inter-organelle lipid transport in a time-controlled manner(229, 337). PE is synthesized in the ER and mitochondria and can be found in every organelle. It has been shown to shuttle in and out of mitochondria and the ER(363) yet its mode of transport is still poorly characterized. In our microscopy assay, we found that caged TF-PE is present in the Golgi, ER, and mitochondria. After uncaging, the probe level decreased by a two-fold factor in the ER, marginally dropped in the Golgi, while no significant changes were observed in the mitochondria. Our ER marker, calreticulin, is predominantly expressed in the smooth ER, suggesting that the observed decrease reflects the probe's level in this specific region. This is interesting, as most ER-mitochondria contact sites are primarily formed by the smooth ER(364), from which PE is most likely to shuttle between the ER and mitochondria(365). This could explain the depletion observed in our assay, although we did not observe an increase in colocalization of our probe with the mitochondria marker Tom20. Additionally, it has been suggested that ER-mitochondria contact sites are one of the key location of autophagosome formation(366, 367), in which PE plays a central role by being connected to ATG3, facilitating the fusion and closure of the phagophore(331, 368). While autophagy in the absence of starvation is downregulated, this process could also contribute to the decrease in TF-PE at the ER observed in our assay. It will be interesting to investigate the colocalization between TF-PE and LC3, and to determine how uncaging affects autophagosome formation, as increased PE levels are known to enhance autophagic flux(369).

While our results suggest the potential applicability of our trifunctional probe to study active and passive transport of PE, the assay will have to be improved to reliably determine PE trafficking in cells. Particularly, our Manders' coefficient analysis showed that half of the

TF-PE did not colocalize with either of our three markers. We believe that improvements in the markers used to identify the Golgi, ER, and mitochondria, as well as markers for additional organelles, will help increase the reliability of our assay and its application to characterize PE transporters in cells.

The lab previously demonstrated rapid transport from the internal membrane to the plasma membrane using our trifunctional phosphatidylinositol, suggesting active transport(229, 337). Despite the relative abundance and numerous physiological roles played by PE at the plasma membrane(370), we did not observe any detectable TF-PE localizing at the plasma membrane 20 min after uncaging. This contrasts with the TF-PI probes that showed transport to the plasma membrane in as little as 30 sec after uncaging and suggests a much slower, passive transport of PE from internal membranes to the plasma membrane.

Interestingly, our TF-PA probe appeared to localize at the plasma membrane while still caged. This is unusual for caged probes as the aromatic coumarin typically direct the lipids exclusively in internal membranes. After uncaging, the probe leaves the plasma membrane rapidly. This could be attributed to active transport of PA out of the plasma membrane or transport following metabolism into different lipid species.

Lipid-protein interactions

In average, proteins pulled down by TF-PA exhibited enrichment levels very similar to those of proteins pulled down by TF-PE. However, most of the major hits from TF-PE displayed significantly higher enrichment levels compared to TF-PA. We have shown that both probes, 20 minutes post uncaging, localize to similar cell compartments, and the majority of TF-PA has been metabolized into PC. Many of those common hits are relatively abundant

transmembrane proteins (EGFR, NHERF1, L1CAM) or protein known to be lipidated (GNAIs, GNAS), which could explain their presence in our screen. Additionally, the number of hits for TF-PA was markedly lower than for TF-PE, likely due to the rapid metabolism of TF-PA into various lipid species, which reduces its potential for specific protein enrichment. It is noteworthy that the majority of overlapping proteins between TF-PA and TF-PE are associated with the plasma membrane or cytosol, compartments in which PE does not typically dominate, suggesting non-specific protein enrichment.

We identified several proteins that overlap with the known biological functions of PE in the mitochondria. PE is critical for the function of cytochrome c and has been shown to reside at the interface where complex IV dimerizes(345). When mitochondrial PE production is decreased, complex I and IV are reduced and ATP production is impaired(324). Strikingly, four different subunits of ATP5 (complex V) were identified as hits as well as NDUFA4 and the subunits UQCRC1 and 2 of cytochrome b-c1 complex. These results may indicate that PE is involved in the regulation of complex assembly for not only complexes I and IV but also complex V. The inorganic ion transport SLC25A3 and the nucleotide transporter SLC25A5 and 6, belonging to the larger SLC25A mitochondrial carrier family, were identified as hits and might be implicated in PE transport to the inner membrane of the mitochondria(371). Another mitochondrial protein that has been proposed as a potential PE transporter from the ER to the mitochondria at mitochondria-associated membrane (MAM) contact sites is SLC25A46(372).

We identified two proteins known to be involved in lipid transport that were significantly enriched exclusively with the TF-PE probe. SCP2 is a well-characterized lipid binder that plays a critical role in the transport of cholesterol and fatty acids. Remarkably, several studies

have shown that it can mediate the transfer of lipids from the IMM to the OMM and the transfer of phospholipid-derived hydroperoxides(373, 374). This places SCP2 as a promising putative PE transporter. The other protein involved in lipid transport and enriched with the TF-PE probe is VAPA. It mediates, together with the lipid-binding protein Nir2, PA and PC transport at membrane contact sites between the ER and both the Golgi(356) and the plasma membrane(357). Its well-characterized function as a phospholipid transporter makes it an interesting candidate for PE transport. Notably, the aminophospholipid translocases ATP11C, while only marginally enriched with the TF-PE probe, was identified in our screen and is a known PS flippase with lower affinity for PE(344). In a previous study in our lab, the closely related ATP11A, a PS and PE scramblase, was identified as a putative PI(3,4,5)P₃ transporter(337).

Ferroptosis, a death program triggered by dysregulation of the redox system, produces oxygenated lipids that serve as direct signals for cell death(375). This is catalyzed by iron containing enzymes and is thought to occur predominantly on PEs and is specific to the two fatty acyls-arachidonoyl and adrenoyl(353). Additionally, one major enzyme believed to catalyze the lipid oxidation of several phospholipids, such as PC, PE, PI, or PS, is the NADPH-cytochrome P450 reductase (POR)(352). POR was highly enriched in our screen with the TF-PE probe. This is the first example of POR possibly directly interacting with PE. Additionally, several other proteins enriched with TF-PE in our screen are directly involved in regulating ferroptosis. DHCR7 was enriched with TF-PE and TF-PA and has been shown to have a proferroptotic role by consuming its substrate 7-dehydrocholesterol, which has a prosurvival function in cancer cells(354). Ferroptosis is dependent on the enrichment in polyunsaturated fatty acids (PUFA). This high PUFA state is regulated by the activity of the

enzyme acyl-CoA-synthetase long-chain family 4 (ACSL4)(376) which was enriched in one of the biological replicates of TF-PE. Interestingly, the enzyme ACSL3, which generates monounsaturated fatty acids, was significantly enriched with TF-PE. Finally, SCP2 was demonstrated to transport lipid hydroperoxides to the mitochondria in chondrocytes induced to undergo ferroptosis. SCP2 activity leads to mitochondrial membrane damage and release of oxygen species, promoting ferroptosis(377). Given the known involvement of polyunsaturated PE in ferroptosis, it is unsurprising that our TF-PE screen identified numerous proteins related to this process. Nevertheless, it is exciting to gather evidence of PE's interaction with those proteins, and its potential regulatory role in the ferroptotic process, beyond only serving as a substrate. It will be interesting to further probe and confirm PE interaction with those proteins.

This innovative approach contributes to our understanding of regulatory functions of PE and paves the way for further exploration of PE interactomes, especially when healthy and diseased cells are compared. Further validation of hits will be needed and implementation into disease models related to PE functions.

OUTLOOK AND FUTURE WORK

PE transport assay

The mechanism of PE transport between the ER and mitochondria is still unclear. A study has shown that PE synthesized by the ER-localized Kennedy pathway can access the inner mitochondrial membrane (IMM), but cannot rescue mitochondrial PE content and functions in the absence of PE made in the IMM by Psd1(378). Importantly, by expressing Psd1 in the outer mitochondrial membrane (OMM), it was shown that the limiting step in the transport

of PE is from the OMM to the IMM. Moreover, PE produced by Psd1 can either stay in the mitochondria or be exported to contribute to the global cellular pool of PE(363). Both shuttling of PE from the ER to the IMM and vice versa are processes that remain poorly characterized. The ability to track PE trafficking from the ER to the IMM could, in the future, serve as an assay to discover and characterize PE transport proteins. The IMM and OMM are separated by approximately 10 to 20 nanometers, which is too close to be distinguished with the current super-resolution fluorescent microscopy techniques. Adapting our microscopy assay to electron microscopy could potentially enable an assay to track PE trafficking between the IMM and OMM.

The current protocol for sample preparation for microscopy relies on methanol fixation and further lipid extraction prior to clicking of an azide dye to the probe. Methanol fixation can cause distortion of the membrane of organelles leading to lower quality of samples when trying to distinguish each organelle in the cell. This can affect the reliability and applicability of our microscopy assay when following TF-PE transport. Aldehyde-based fixation methods preserve membrane morphology more effectively than methanol. Additionally, aldehyde fixation is compatible with organelle-selective dyes, which typically outperform antibody staining for visualizing organelle structures. However, paraformaldehyde fixation has proven challenging to use in combination with our trifunctional probes, although it should be compatible with click chemistry as demonstrated in other studies.(379). Developing a new paraformaldehyde (PFA)-compatible method with organelle dyes would significantly improve sample quality and enable to tracking of TF-PE transport between the outer and inner mitochondria membranes using EM. This could be achieve by clicking gold

nanoparticles carrying an azide group and a fluorescent dye to the lipid probe, facilitating correlative light and electron microscopy.

Finally, in our current microscopy assay, we have not examined time points beyond 20 minutes, and the change in localization is modest. It would be interesting to observe the PE probe localization several hours or even a full day after uncaging to determine if the discrete trafficking observed becomes more pronounced. In parallel, extracting the lipid from cells at corresponding time points for analysis on TLC would provide information on the fate of the lipid.

Validation of PE potential interactors

The large amount of potential lipid-protein interactions identified with our PE probe opens many possible future directions.

To validate protein-lipid interactions, recombinant FLAG-tagged proteins of interest can be transfected into cells. After treating the cells with the TF probe and subjecting them to UV irradiation, the proteins can be enriched via pull-down using azide beads and subsequently analyzed by SDS-PAGE and Western Blotting. Alternatively, a fluorescent dye can be clicked on the probe in the cell lysate, followed by in-gel fluorescence imaging and Western blotting. This approach allows for the identification of protein interactors through the co-localization of fluorescence signals and Western blot bands within the gel. An additional assay to assess the specificity of the lipid-protein interaction involves competition experiments in which cells are treated with an excess of the native lipid to out-compete the probe's binding. Membrane-permeable PE can be synthesized by adding an AM-ester to the phosphate group,

which is rapidly cleaved by intracellular esterases. This modification masks the negative charge, facilitating cellular entry. To assess which concentration of PE to use in the competitive assay, the protein LC3 could be used. Upon induction of autophagy (by starvation for example), LC3(I) form a complex with ATG3 leading to the conjugation of LC3(I) and PE. The conjugation results in the formation of LC3(II), which serves as an indicator of autophagic activity. The ratio of LC3(I) and LC3(II) can be easily quantified on a Western Blot. Using in-gel fluorescence should allow to quantify the amount of the TF-PE probe conjugated to LC3(II), and hence determine a working concentration of PE to use for the competition assay.

We identified SCP2 and VAPA as proteins potentially involved in PE transport within cells. Several lipid transport assays could be used to explore this possibility. SCP2 is a soluble protein which has been shown to transport phospholipids from the ER to the plasma membrane. Since it is soluble, it can be recombinantly expressed, purified, and its affinity for PE can be assessed using relatively straightforward methods, such as lipid dot blots and isothermal calorimetry.. To test SCP2's ability to transport PE between membranes, a liposome assay utilizing a fluorescently labeled NBD-PE probe can be employed. This approach involves incorporating a small percentage of fluorescent lipid along with a quencher into donor liposomes, which are then mixed with acceptor liposomes and SCP2. An increase in fluorescence would indicate active transport of the tagged lipid by SCP2. Finally, if reliable enough, our microscopy assay using the trifunctional probes could be used to quantify lipid transport from one organelle to another in WT cells or in cells engineered with knockouts of specific putative transporters.

As discussed above, PE is directly tied to ferroptosis as one of the main substrate for oxidation of polyunsaturated fatty acids. Ferroptosis holds significant therapeutics potential to treat cancer which makes targeting pathways regulating PE metabolism and lipid peroxidation promising treatment avenue. Ferroptosis can be induced with the widely used small molecule Erastin(380, 381). It would be interesting to see how induction of ferroptosis modulates the interactome of our TF-PE probe and vice versa how uncaging of TF-PE affects ferroptosis. The interaction between POR and PE could be rapidly confirmed by a pulldown assay comparing healthy cells and ferroptosis-induced cells. If this interaction is confirmed, our probe could help further investigate the strength, binding site, and potential regulatory role of PE in ferroptosis and POR activity.

Adjustment to TF-PA's rapid metabolism rate

We have shown that the rapid metabolism rate of TF-PA after uncaging limited the interpretability of the lipid protein interactome screen. Decreasing the time of irradiation for uncaging and photo-crosslinking could help capture PA interactome. Additionally, CDP-diacylglycerol synthase, one of the main enzyme responsible for PA metabolism, can be inhibited by PI lipids, particularly PI(4,5)P₂(382). It would be interesting to measure the rate of metabolism of the TF-PA in cells with physiological or elevated level of PI(4,5)P₂. Our caged PI(4,5)P₂ derivative could be used for this purpose.

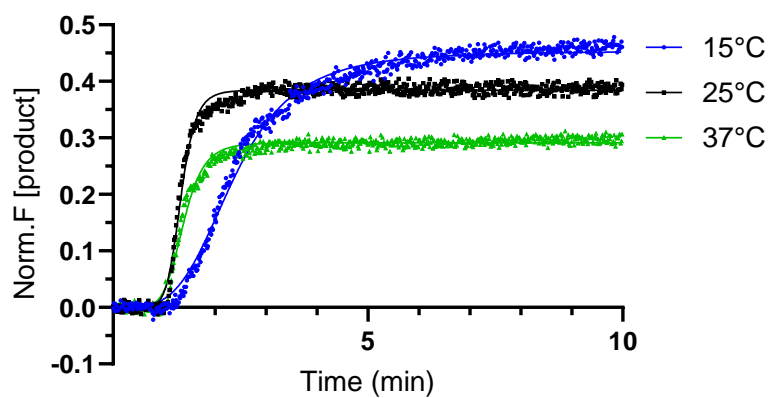
Concluding remarks

In this dissertation, I have described the development of two genetically encoded FRET sensors to dynamically monitor PARP1-dependent ADP-ribosylation, a methodology to investigate CB1 functional selectivity, and the application of trifunctional lipid derivatives to uncover novel lipid-protein interactions.

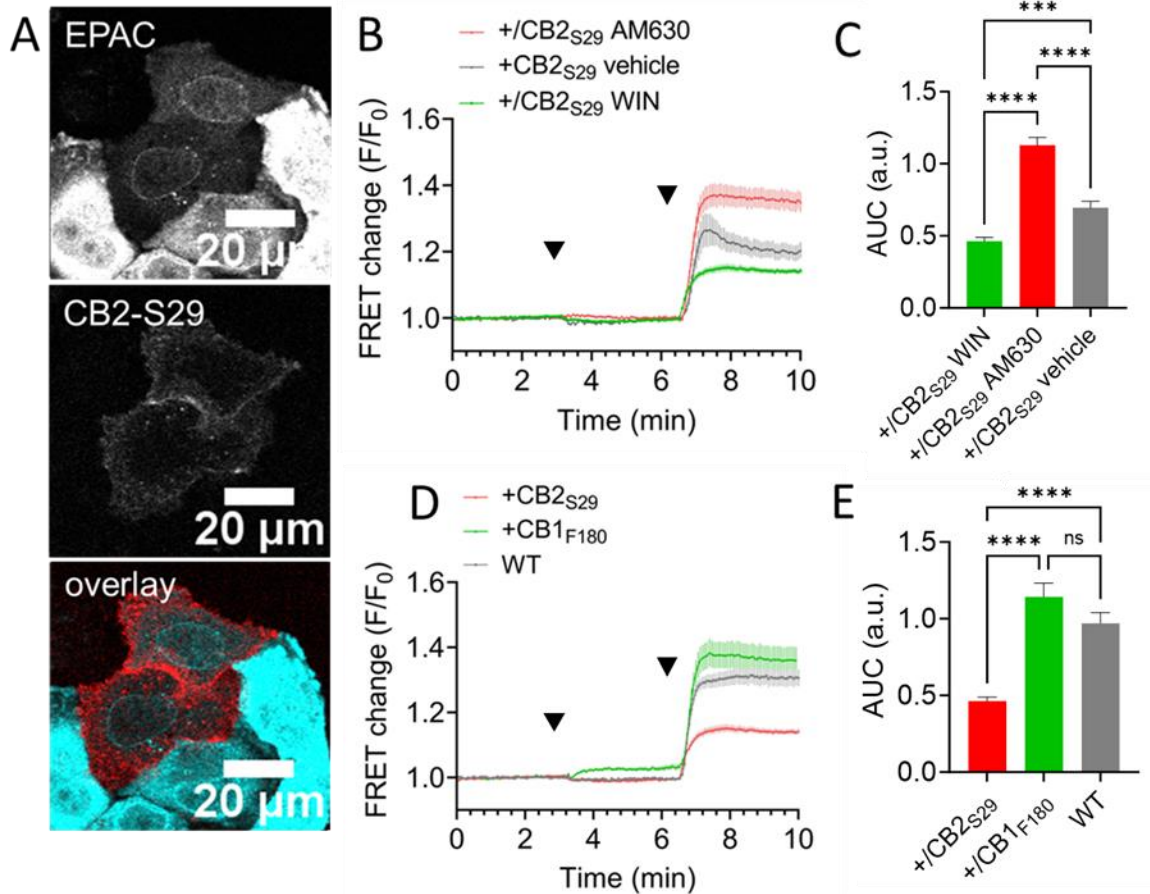
The tools developed through-out the projects outlined above vary in their design and utility. In chapter 2, our FRET sensors scaffolds are based on very well-established tools which should maximize their ease of utilization. We hope that our thorough characterization of their sensing mechanisms will lead to broad applicability in the field of ADP-ribosylation and pave the way for the development of new generations of sensors with improved sensing capabilities and diversity of functions. In chapter 3, we developed recombinant systems to dissect the functionality of different CB1 pools in cells. We showed that intracellular and plasma membrane CB1 can down-regulate and up-regulates cAMP, respectively. This suggests different biological functions for each pool of CB1. Moreover, we incorporated an unnatural amino acid in the extra cellular loop 1 of CB1 for visualization of the receptor in live cells with minimal perturbation. While enabling a wide array of application, this methodology still needs improvement for broader application. Lastly, in chapter 4, we characterized a set of trifunctional lipid derivatives. Studying lipid function, fate and interactors has been historically difficult. I and other in the lab before me have demonstrated the broad applicability of these new lipid probes. The standardization of protocol dedicated to those probes and the identification of new PE protein interactors will hopefully lead to more future discoveries.

Appendix

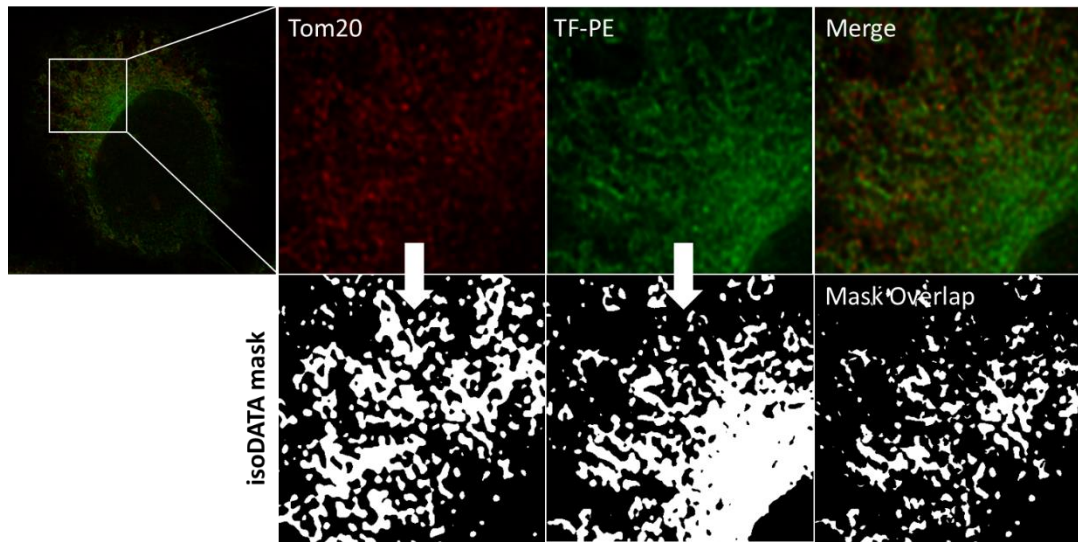
FIGURES



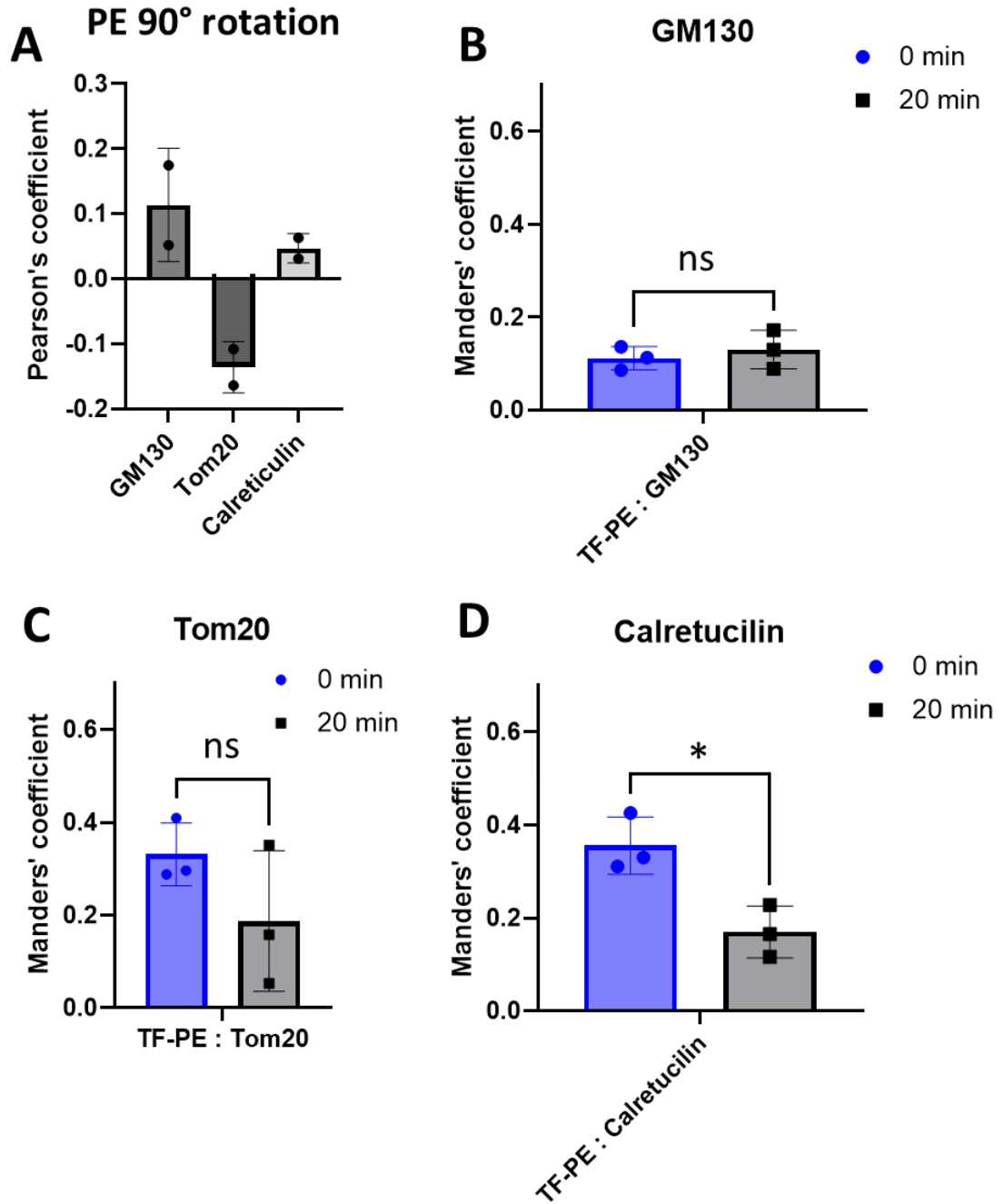
Appendix 2-1. PARP1 (5 nM) dependent PAR formation at 10 μ M NAD at 15, 25 or 37°C. Curve was fitted using an allosteric/sigmoidal non-linear regression model.



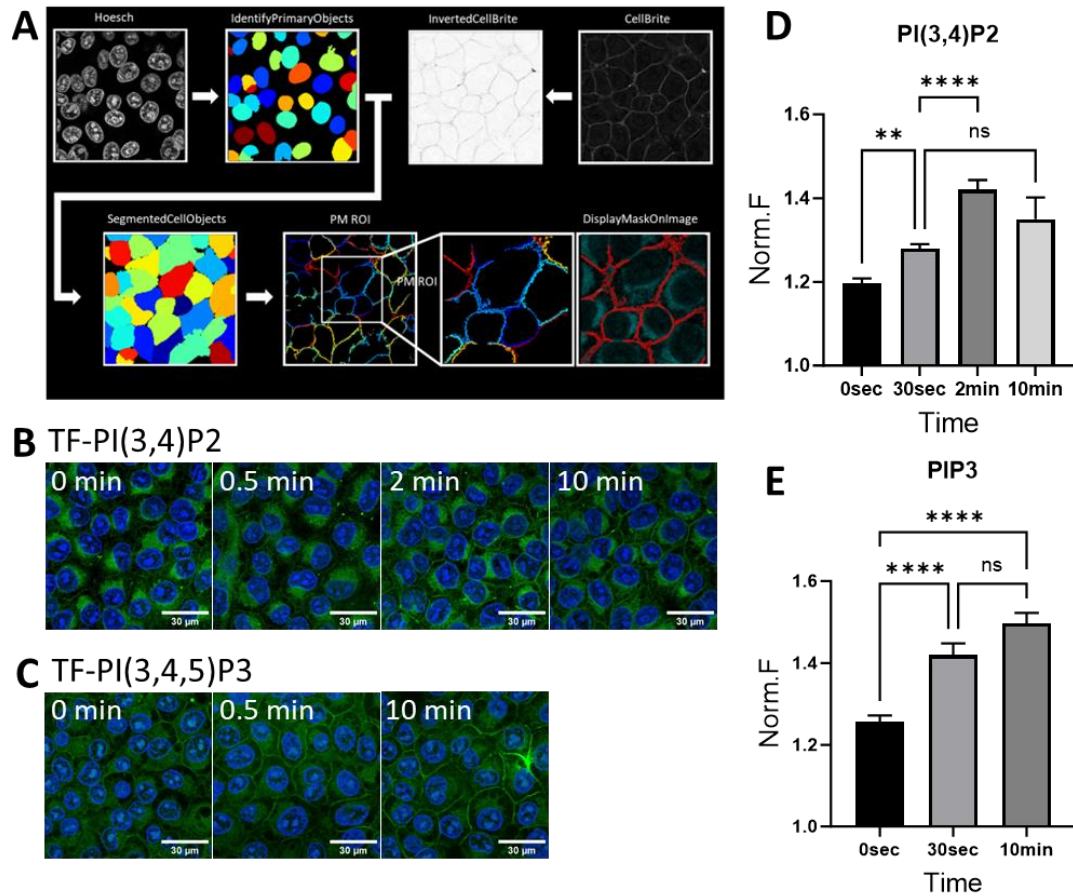
Appendix 3-1 CB1-F180 and CB2-S29 constructs regulate AC activity and demonstrate distinct signaling pathways. **A.** Confocal micrographs showing HeLa Kyoto cells co-transfected with CB2-S29 and the EPAC-based FRET sensor. Receptors were labelled with Me-Tet-ATTO655 (1 μ M) for 20 min. **B.** Average of 21, 16 and 27 cell traces showing FRET changes of the EPAC-based FRET sensor in CB2-S29-transfected HeLa, after treatment with the agonist WIN55,212-2 (10 μ M) or the inverse agonist AM630 (1 μ M), followed by forskolin (FSK, 50 μ M). **C.** Bar graphs showing FRET changes of the EPAC-based FRET sensor after forskolin stimulation (50 μ M) in CB2-S29 expressing cells tagged with Me-Tet-ATTO655 (+/CB2R). WIN - vehicle $p < 0.005$, WIN vs AM630 $p < 0.001$, AM630 vs vehicle $p < 0.001$. **D.** Average of 27, 45 and 70 cell traces showing FRET changes of the EPAC-based FRET sensor in CB2-S29 and CB1-F180-transfected HeLa, after treatment with the agonist WIN55,212-2 (10 μ M), followed by forskolin (FSK, 50 μ M). **E.** Bar graphs showing FRET changes of the EPAC-based FRET sensor after WIN55,212-2 and forskolin stimulation ((50 μ M) in wild type (WT) versus CB2-S29 expressing cells tagged with Me-Tet-ATTO655 (+/CB2-S29) and CB1-F180 expressing cells (+/CB1-F180). +/CB2R versus +/CB1 $p < 0.0001$, +/CB1 versus WT p -value non-significant.



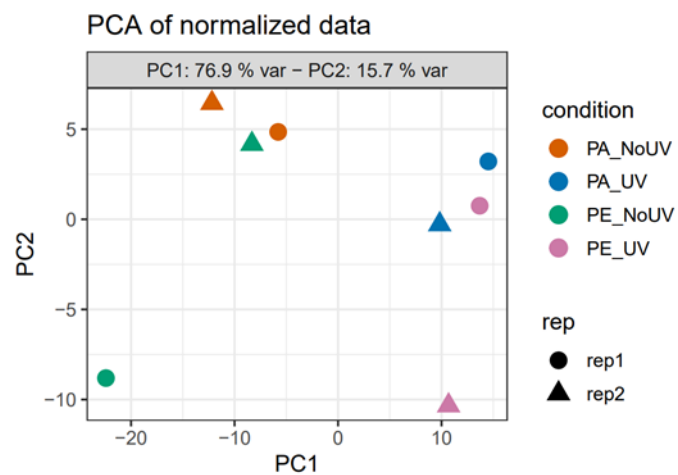
Appendix 4-1. Representative images of the ImageJ JaCoP pipeline for Pearson's correlation and Manders' coefficient analysis



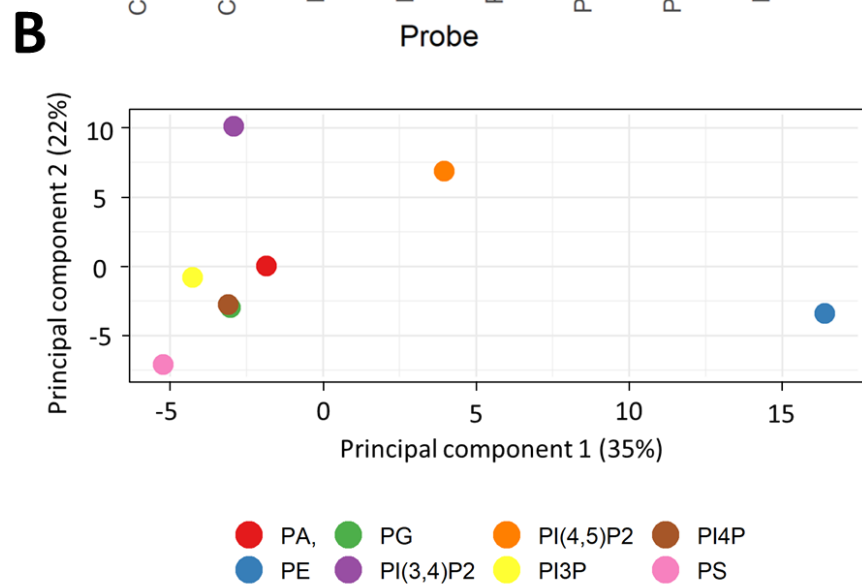
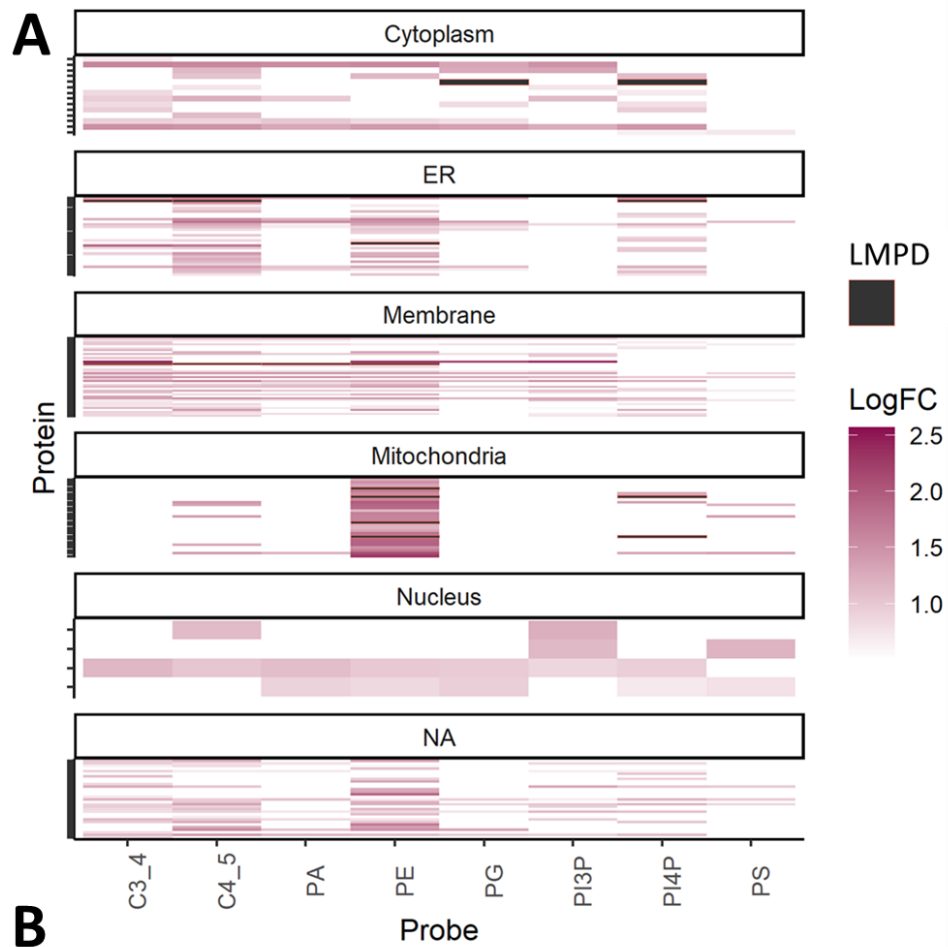
Appendix 4-2. A. Colocalization measurement using Pearson's coefficient between TF-PE after 90° rotation of the field of view and Calreticulin (ER), Tom20 (Mitochondria) or GM130 (Golgi). **B-D.** Colocalization measurement using Manders' coefficient between TF-PE and (B) GM130 (Golgi), (C) Tom20 (Mitochondria) and (D) Calreticulin (ER). Manders' correlation coefficients were calculated using an ImageJ pipeline. Each experiment was performed in biological triplicates and 7 cells were analyzed with Manders per replicates. * $p < 0.05$, ** $p < 0.01$, *** $p < 0.005$, **** $p < 0.001$ (Unpaired t-test).



Appendix 4-3 A. Representation of a automated cell profiler image analysis pipeline to quantify signal of a given trifunctional at the cell surface. Cell nucleus were imaged using Hoesch and the plasma membrane were imaged using the far red Cellbrite dye. **B.D.** Confocal micrograph showing subcellular localization of lipid probes. HeLa cells were treated with 10 μ M of PI(3,4)P2 (A) or TF-PIP3 (C), exposed to 400nm light to uncage the probe, and allowed to translocate for 0, 30 sec, 2 and 10min. The lipids were photo-crosslinked to proteins using 350 nm light, fixed, subjected to click reactions with a fluorescent azide. **C.E.** Quantification of plasma membrane translocation of the lipid probes TF-PI(3,4)P2 (B) and TF-PIP3 (D) using previously described Cell Profiler pipeline. See methods for details on normalization.



Appendix 4-4. PCA for quality control of lipid-protein interactome replicates. PCA was performed on the normalized protein abundance values. Each point represents a single replicate. The first two principal components account for 76.9% (PC1) and 15.7% (PC2) of the total variance.



Appendix 4-5 A. Analysis of lipid binding proteins. Go-term enrichment of proteins identified as hits for each probe. The $\text{Log}_2(\text{FC})$ for the UV condition over the -UV condition for each probe is shown in each cellular compartment. Protein hit present in the Lipid Maps Proteome Database (LMPD) **B.** Comparison of protein binder “fold enrichment” for each lipid using principal component analysis. A protein binder was defined as having a $\text{Log}_2\text{FC} > 0,5$ and $p\text{value} > 0,01$.

TABLE INTERACTOME

gene_name	logFC_PA	logFC_PE	pvalue_PA	pvalue_PE	hit_annotation_PA	hit_annotation_PE
MAP4	-1.7102873	-2.1282363	0.0000132	0.0000008	no hit	no hit
SEC24C	-1.3996266	-1.5440426	0.0000189	0.0000056	no hit	no hit
STRAP	-1.5509555	-1.8955412	0.0000240	0.0000019	no hit	no hit
PCBP1	-1.5867500	-1.8692164	0.0000622	0.0000089	no hit	no hit
MET	1.0225475	0.9244389	0.0000697	0.0002044	enriched hit	enriched candidate
TPT1	-1.9047844	-1.9563568	0.0000945	0.0000705	no hit	no hit
EGFR	1.4329414	1.4807718	0.0000951	0.0000662	enriched hit	enriched hit
ATXN10	-1.3980813	-1.4974015	0.0001086	0.0000509	no hit	no hit
RAB13	1.4903360	1.4399773	0.0001511	0.0002155	enriched hit	enriched hit
MAPRE1	-1.7511824	-1.9126243	0.0001529	0.0000587	no hit	no hit
FAM114A1	-1.4527281	-1.6007909	0.0001658	0.0000580	no hit	no hit
SLC30A1	1.2417693	1.1022616	0.0001735	0.0005614	enriched hit	enriched hit
LANCL1	1.0626288	0.7065839	0.0002058	0.0064983	enriched hit	enriched candidate
L1CAM	1.4784112	1.3140481	0.0002255	0.0007020	enriched hit	enriched hit
EEF1G	-1.8482329	-2.0576506	0.0002410	0.0000776	no hit	no hit
USO1	-0.9412429	-0.6719631	0.0002413	0.0044181	no hit	no hit
PDCD6	-1.8859665	-2.1370521	0.0003295	0.0000902	no hit	no hit
VPS29	-1.0191345	-0.7172935	0.0003607	0.0064704	no hit	no hit
SEC13	-1.3569496	-1.6202865	0.0003764	0.0000588	no hit	no hit
EIF4E	-0.9111330	-1.1200372	0.0004089	0.0000466	no hit	no hit
PCBP2	-1.3050835	-1.6614153	0.0004300	0.0000331	no hit	no hit
EIF2B1	-0.9708108	-1.0045364	0.0004362	0.0003131	no hit	no hit
SPCS2	1.1806362	1.1264986	0.0004516	0.0006998	enriched hit	enriched hit
SEC11A	0.9320441	0.7949083	0.0004619	0.0018796	enriched candidate	enriched candidate
NAA50	-1.2192150	-1.2449251	0.0004681	0.0003832	no hit	no hit
GNAI1	1.0962794	0.9991076	0.0005795	0.0013233	enriched hit	enriched candidate
TMEM214	1.5019694	1.4725462	0.0006800	0.0008135	enriched hit	enriched hit
COPE	-0.7396678	-1.0079993	0.0006801	0.0000264	no hit	no hit
EPHB4	0.8741008	0.9153067	0.0006809	0.0004426	enriched candidate	enriched candidate
ATXN2L	-1.2994512	-1.7866263	0.0007103	0.0000252	no hit	no hit
GNAI2	1.0018102	0.8476414	0.0008882	0.0034789	enriched hit	enriched candidate
SLC9A3R1	1.2805822	1.4100435	0.0011358	0.0004743	enriched hit	enriched hit
BZW1	-1.3116651	-1.3766574	0.0011635	0.0007590	no hit	no hit
ABCC1	0.7114526	0.7618172	0.0012429	0.0006783	enriched candidate	enriched candidate
PDCD6IP	-1.0900299	-0.8838015	0.0012865	0.0063745	no hit	no hit
RALA	1.1455485	1.3715065	0.0012948	0.0002427	enriched hit	enriched hit
ARF4	-0.7899130	-0.7036164	0.0014075	0.0035243	no hit	no hit
NPM1	0.9090801	0.8472015	0.0014406	0.0025504	enriched candidate	enriched candidate
RAB23	0.6729241	0.4513435	0.0016281	0.0232187	enriched candidate	no hit
PARVA	-0.8810579	-0.7908037	0.0016454	0.0038259	no hit	no hit
SEC23A	-1.0161021	-1.0629142	0.0018440	0.0012664	no hit	no hit
SEC31A	-1.1761229	-1.6216455	0.0018814	0.0000882	no hit	no hit
IGF1R	0.8272967	0.8199912	0.0019043	0.0020457	enriched candidate	enriched candidate
STOM	1.1804349	1.2737570	0.0019705	0.0010394	enriched hit	enriched hit
GNA13	0.9670985	1.0586222	0.0021405	0.0010034	enriched candidate	enriched hit
SYAP1	-1.2244537	-1.5291549	0.0022067	0.0003040	no hit	no hit

gene_name	logFC_PA	logFC_PE	pvalue_PA	pvalue_PE	hit_annotation_PA	hit_annotation_PE
ATP2B1	1.0384657	1.2540792	0.0022216	0.0004250	enriched hit	enriched hit
YWHAQ	-1.1744336	-1.4219177	0.0023217	0.0004374	no hit	no hit
ATP2B4	0.7835533	0.8851383	0.0025009	0.0009042	enriched candidate	enriched candidate
IPO5	-1.2780783	-1.3857587	0.0026504	0.0013759	no hit	no hit
ACO1	-0.9398386	-0.9656543	0.0026515	0.0021420	no hit	no hit
TARS	-1.3090394	-1.2452180	0.0026577	0.0038755	no hit	no hit
SORD	-1.7193752	-1.3600723	0.0026600	0.0131007	no hit	no hit
AARS	-1.0898991	-1.0073615	0.0027365	0.0048995	no hit	no hit
UBAP2L	-1.7198342	-2.1402332	0.0028668	0.0004357	no hit	no hit
IL1RAP	0.7931747	0.6907412	0.0029004	0.0077324	enriched candidate	enriched candidate
ARHGDI1A	-1.0157838	-1.4247269	0.0029327	0.0001345	no hit	no hit
FAM129B	1.5349159	1.5722074	0.0029940	0.0024871	enriched hit	enriched hit
RRAS2	0.8253033	0.7508358	0.0033333	0.0065344	enriched candidate	enriched candidate
SRI	-1.1956447	-1.2497933	0.0041415	0.0029779	no hit	no hit
ATP1B1	0.8745413	1.2597072	0.0041624	0.0001665	enriched candidate	enriched hit
PCNA	-1.1992113	-1.3561269	0.0041739	0.0016054	no hit	no hit
PPIA	-0.9861701	-1.0379672	0.0042413	0.0028967	no hit	no hit
CISD2	1.1989323	1.5598348	0.0043038	0.0004798	enriched candidate	enriched hit
PLIN4	-0.9154316	-1.3468834	0.0044788	0.0001483	no hit	no hit
SERPINB1	-0.9539765	-1.1727315	0.0045716	0.0008729	no hit	no hit
GNB1	0.6925947	0.5853194	0.0047082	0.0139438	enriched candidate	enriched candidate
IST1	-0.7949002	-0.5686618	0.0049541	0.0344595	no hit	no hit
PDIA3	1.0440225	1.2854647	0.0051192	0.0009913	enriched candidate	enriched hit
GNAS	0.8591344	0.9233122	0.0052333	0.0030950	enriched candidate	enriched candidate
PGLS	-1.0212386	-1.1916845	0.0054511	0.0016900	no hit	no hit
ANXA5	-1.2619308	-1.4111686	0.0056159	0.0024635	no hit	no hit
ANXA7	-1.3200992	-1.5553000	0.0061690	0.0018104	no hit	no hit
TSN	-0.8431285	-1.0572653	0.0061709	0.0010701	no hit	no hit
LYPD3	0.7343130	0.7199076	0.0067500	0.0076958	enriched candidate	enriched candidate
RHOG	0.5404821	0.4997986	0.0072035	0.0118088	no hit	no hit
TNPO1	-0.8815140	-1.0499972	0.0073774	0.0020571	no hit	no hit
JUP	0.9868617	0.8219394	0.0075067	0.0220077	enriched candidate	enriched candidate
RAC1	0.9171846	0.9021876	0.0077608	0.0086338	enriched candidate	enriched candidate
RCN1	0.7152582	1.3019973	0.0078572	0.0000349	enriched candidate	enriched hit
PDIA6	0.6981538	0.9202651	0.0079715	0.0009685	enriched candidate	enriched candidate
EEF1B2	-1.3968312	-1.7993297	0.0080297	0.0011948	no hit	no hit
EIF4G1	-1.3069674	-1.7655515	0.0080956	0.0007951	no hit	no hit
GNB4	0.7740150	0.7026174	0.0081284	0.0146772	enriched candidate	enriched candidate
HYOU1	1.0490048	1.4954338	0.0082523	0.0004974	enriched candidate	enriched hit
HSPB1	-0.8559313	-1.1778545	0.0090629	0.0007887	no hit	no hit
NDUFA4	1.2029840	2.1094055	0.0090763	0.0000690	enriched candidate	enriched hit
UBE2M	-1.2063453	-1.0476949	0.0092340	0.0209101	no hit	no hit
PRDX6	-1.1222757	-1.1227733	0.0094776	0.0094513	no hit	no hit
SRPRB	1.3048445	1.6576933	0.0096783	0.0017175	enriched candidate	enriched hit
CD55	0.7103563	0.8532823	0.0097561	0.0027128	enriched candidate	enriched candidate
GNA11	0.6994555	0.6551633	0.0104753	0.0154319	enriched candidate	enriched candidate
PHGDH	-0.8681374	-0.9620424	0.0107426	0.0054918	no hit	no hit
EIF4G2	-0.9535521	-1.4050036	0.0107689	0.0005427	no hit	no hit
PGM1	-1.1487993	-1.2298332	0.0109453	0.0070886	no hit	no hit
S100A4	-1.1564389	-1.5897264	0.0114301	0.0011082	no hit	no hit
DPP3	-1.0717803	-0.8187028	0.0115417	0.0456998	no hit	no hit
RABGGTB	-1.1020058	-1.3531511	0.0115516	0.0028302	no hit	no hit

gene_name	logFC_PA	logFC_PE	pvalue_PA	pvalue_PE	hit_annotation_PA	hit_annotation_PE
API5	-0.8858819	-0.5529997	0.0118380	0.0977886	no hit	no hit
PPIB	0.8054460	1.2116555	0.0118508	0.0005179	enriched candidate	enriched hit
CANX	0.7625202	0.9614163	0.0118849	0.0023895	enriched candidate	enriched candidate
YWHAZ	-0.8795410	-1.3062261	0.0120203	0.0005970	no hit	no hit
SFN	-1.0509365	-1.3210768	0.0121962	0.0025308	no hit	no hit
NARS	-1.0583062	-1.2664898	0.0125384	0.0038066	no hit	no hit
IPO7	-1.0332833	-1.0718186	0.0125476	0.0100435	no hit	no hit
CRTAP	0.7743448	1.1324719	0.0128594	0.0007623	enriched candidate	enriched hit
PRRC1	-0.8420595	-0.9514735	0.0128906	0.0059171	no hit	no hit
GNAQ	0.6864202	0.6472779	0.0130591	0.0182277	enriched candidate	enriched candidate
TAGLN2	-0.8251559	-1.1475567	0.0133704	0.0012577	no hit	no hit
SRM	-0.9561359	-1.0658276	0.0133937	0.0067780	no hit	no hit
LTA4H	-1.0575724	-0.8715713	0.0136723	0.0371187	no hit	no hit
HARS	-0.8074889	-1.0336960	0.0137303	0.0025679	no hit	no hit
CAND1	-0.9088526	-0.3867741	0.0137839	0.2612188	no hit	no hit
FDPS	-1.0565812	-1.1397483	0.0138986	0.0087567	no hit	no hit
GSTK1	0.9017188	1.3693811	0.0139953	0.0006165	enriched candidate	enriched hit
ETFB	1.0624366	1.8921709	0.0140953	0.0001281	enriched candidate	enriched hit
LY6K	0.8385584	1.2372256	0.0142151	0.0008218	enriched candidate	enriched hit
NOMO1 NOMO3 NOMO2	0.9539389	1.3588072	0.0146567	0.0011730	enriched candidate	enriched hit
BASP1	1.9995488	2.4353819	0.0148356	0.0041320	enriched candidate	enriched hit
PRKCSH	0.6993345	0.2732514	0.0151703	0.3087731	enriched candidate	no hit
GANAB	0.7327816	0.9974384	0.0155799	0.0018765	enriched candidate	enriched candidate
COX4I1	0.9876078	1.3284838	0.0165074	0.0022412	enriched candidate	enriched hit
EIF4B	-1.6765027	-2.0360043	0.0166077	0.0048674	no hit	no hit
PLS3	0.6927140	0.6701795	0.0166470	0.0199473	enriched candidate	enriched candidate
HSPA9	1.2165599	1.9695718	0.0169997	0.0004665	enriched candidate	enriched hit
CD44	0.7504626	0.7995567	0.0172474	0.0119663	enriched candidate	enriched candidate
SLC25A5	1.0757471	1.9265948	0.0178012	0.0001863	enriched candidate	enriched hit
LDHA	-1.0940288	-1.1451179	0.0179713	0.0138860	no hit	no hit
CYP51A1	0.6923136	1.0379720	0.0183088	0.0010615	enriched candidate	enriched hit
BST2	-0.5837096	-0.8496488	0.0183943	0.0013782	no hit	no hit
SERPIN5	-1.2072295	-1.3448798	0.0187761	0.0100150	no hit	no hit
RDH11	0.9828302	1.1454376	0.0190882	0.0076554	enriched candidate	enriched hit
STEAP4	0.6904106	0.7080156	0.0192346	0.0167519	enriched candidate	enriched candidate
RAB35	0.9938404	1.3126777	0.0195449	0.0032748	enriched candidate	enriched hit
NUDT5	-1.1725917	-1.1996755	0.0196409	0.0173414	no hit	no hit
HPD	-0.8261069	-1.1001446	0.0197387	0.0031206	no hit	no hit
FH	1.0869163	1.9067402	0.0201251	0.0002889	enriched candidate	enriched hit
STX4	1.1623278	1.1191094	0.0204003	0.0248381	enriched candidate	enriched candidate
PPP2CA	-0.6038101	-0.5655153	0.0204561	0.0285701	no hit	no hit
CMBL	-0.8246131	-1.0986435	0.0205955	0.0033027	no hit	no hit
AXL	0.6605263	0.7116850	0.0211588	0.0139980	enriched candidate	enriched candidate
RAB18	-0.6475098	-0.6559605	0.0215452	0.0201149	no hit	no hit
NUTF2	-0.8619663	-0.9661471	0.0218436	0.0114805	no hit	no hit
LDHB	-1.0726842	-1.2577723	0.0218544	0.0086771	no hit	no hit
ABHD14B	-0.8417298	-0.8629057	0.0225916	0.0198159	no hit	no hit
GSTO1	-1.4148474	-1.6603257	0.0227676	0.0090753	no hit	no hit
SCCPDH	0.7664889	1.0578445	0.0228555	0.0029388	enriched candidate	enriched hit
GDI2	-0.6969195	-0.6372051	0.0232498	0.0359314	no hit	no hit
PNP	-0.8627469	-1.0972216	0.0232774	0.0054741	no hit	no hit
PRSS21	0.6963114	0.9508782	0.0233809	0.0032925	enriched candidate	enriched candidate

gene_name	logFC_PA	logFC_PE	pvalue_PA	pvalue_PE	hit_annotation_PA	hit_annotation_PE
ANP32B	-1.3860798	-1.4036057	0.0236871	0.0221968	no hit	no hit
SLC25A6	1.1797124	1.7670341	0.0238151	0.0016322	enriched candidate	enriched hit
CPS1	1.0270738	1.6495991	0.0239479	0.0009057	enriched candidate	enriched hit
ANP32A	-1.1868057	-1.0616081	0.0244341	0.0413937	no hit	no hit
AIFM1	1.0483436	1.7119607	0.0246193	0.0008197	enriched candidate	enriched hit
TXN	-0.8956316	-1.0405750	0.0247717	0.0107042	no hit	no hit
YWHAB	-0.8802779	-1.1334477	0.0248553	0.0054920	no hit	no hit
PDHB	1.0699200	1.7764359	0.0248684	0.0007183	enriched candidate	enriched hit
PTGES	0.5018075	0.5596113	0.0250710	0.0138701	no hit	no hit
PTPRJ	0.5950299	0.5901194	0.0251618	0.0262311	enriched candidate	enriched candidate
CLPTM1L	1.0283125	1.5259723	0.0256774	0.0019886	enriched candidate	enriched hit
SCAMP3	-0.6761965	-0.7810753	0.0257679	0.0116302	no hit	no hit
CLIC4	0.4297073	0.2735500	0.0265122	0.1415954	no hit	no hit
PPP2R1A	-0.9015254	-0.7913703	0.0269971	0.0488287	no hit	no hit
KRAS	0.7409604	0.5669426	0.0275758	0.0833111	enriched candidate	no hit
ATP5F1	0.8173218	1.2246776	0.0276858	0.0020778	enriched candidate	enriched hit
CLTA	-0.8395670	-1.0333273	0.0277006	0.0085783	no hit	no hit
ACAT1	1.0392981	1.6812198	0.0277856	0.0011031	enriched candidate	enriched hit
ATP5C1	1.1618019	1.8541359	0.0279490	0.0012522	enriched candidate	enriched hit
TRAP1	1.2101336	1.7001014	0.0280957	0.0035008	enriched candidate	enriched hit
CD46	0.5601800	0.2873589	0.0281057	0.2367035	no hit	no hit
UBA1	-0.8405999	-0.9717312	0.0293119	0.0135212	no hit	no hit
PSME3	-0.7459810	-0.8403125	0.0303332	0.0163339	no hit	no hit
UQCRC2	0.9581527	1.2745486	0.0313243	0.0060700	enriched candidate	enriched hit
PLIN3	-1.0299114	-1.3996025	0.0315516	0.0052927	no hit	no hit
ADPGK	0.4577273	0.5923353	0.0316733	0.0074157	no hit	enriched candidate
YBX1	-1.7691166	-1.5395923	0.0320330	0.0582983	no hit	no hit
ICAM1	0.6716955	0.6189284	0.0323045	0.0465526	enriched candidate	enriched candidate
TUBB4B	-0.6867938	-0.6738949	0.0324495	0.0354415	no hit	no hit
APOL2	0.7718817	0.8687097	0.0326253	0.0178734	enriched candidate	enriched candidate
SAR1A	-0.7370703	-0.5664139	0.0327720	0.0925463	no hit	no hit
YWHAE	-0.7459078	-0.9455276	0.0330316	0.0089787	no hit	no hit
ACTC1 ACTA1	0.8024025	1.1429917	0.0333403	0.0041133	enriched candidate	enriched hit
SSR4	0.5855332	0.7930475	0.0335823	0.0059367	enriched candidate	enriched candidate
GPI	-0.7734076	-0.4952956	0.0336305	0.1582710	no hit	no hit
ABCG2	1.2601713	1.3966358	0.0336884	0.0201581	enriched candidate	enriched candidate
CALM1	0.7661187	0.5945353	0.0337566	0.0915021	enriched candidate	no hit
IGSF8	0.8283054	0.7600261	0.0340433	0.0496476	enriched candidate	enriched candidate
PGD	-0.8701061	-0.7006273	0.0341524	0.0815206	no hit	no hit
CD58	0.7876075	0.6673019	0.0347561	0.0689490	enriched candidate	enriched candidate
SERPINB6	-0.7724718	-1.0582488	0.0363172	0.0061664	no hit	no hit
PGAM1	-1.0205799	-1.0660334	0.0364536	0.0297145	no hit	no hit
HSD17B4	0.7042386	1.1843335	0.0365094	0.0012970	enriched candidate	enriched hit
PLXNB2	0.5541265	0.6764503	0.0367329	0.0130200	no hit	enriched candidate
ATP5O	0.9459344	1.6234003	0.0378524	0.0011672	enriched candidate	enriched hit
GLUD1	1.1635431	1.4708045	0.0378675	0.0109963	enriched candidate	enriched candidate
SRPRA	0.8512058	0.8844125	0.0392771	0.0329737	enriched candidate	enriched candidate
CACYBP	-0.8579596	-0.9174785	0.0393082	0.0287563	no hit	no hit
TFG	-1.1244618	-1.1206098	0.0396581	0.0402656	no hit	no hit
BTF3	-1.2375595	-1.7200158	0.0404243	0.0065740	no hit	no hit
ZNF598	-0.7775675	-0.9992775	0.0410730	0.0111141	no hit	no hit
S100A6	-1.3047142	-1.6077461	0.0411125	0.0142806	no hit	no hit

gene_name	logFC_PA	logFC_PE	pvalue_PA	pvalue_PE	hit_annotation_PA	hit_annotation_PE
S100A11	-1.3524704	-2.2091287	0.0412764	0.0020713	no hit	no hit
TALDO1	-1.3120526	-1.6459841	0.0413439	0.0129596	no hit	no hit
NPEPPS	-0.6058937	-0.5433176	0.0414172	0.0645348	no hit	no hit
GNAI3	0.8393447	0.9391857	0.0415973	0.0244602	enriched candidate	enriched candidate
FKBP4	-0.6903636	-0.3854934	0.0416527	0.2367259	no hit	no hit
PTGR1	-0.7531171	-0.9903760	0.0417106	0.0098556	no hit	no hit
SERBP1	-1.8079280	-2.5061499	0.0427470	0.0072845	no hit	no hit
CSE1L	-0.8647388	-0.7954495	0.0431564	0.0607079	no hit	no hit
MIF	-1.0441700	-1.4407526	0.0435434	0.0077227	no hit	no hit
ECH1	1.0900183	1.5722015	0.0437041	0.0057688	enriched candidate	enriched hit
B4GALT1	-0.7047253	-0.8345779	0.0438584	0.0193717	no hit	no hit
ANXA1	-0.5224248	-0.2255554	0.0441086	0.3627332	no hit	no hit
CTTN	0.9015442	0.8124718	0.0445032	0.0673960	enriched candidate	enriched candidate
PTGFRN	0.7274874	0.5533771	0.0448288	0.1184281	enriched candidate	no hit
IQGAP1	1.3980589	1.3611695	0.0448654	0.0501907	enriched candidate	enriched candidate
TXNDC5	0.6153251	0.8399299	0.0449580	0.0086885	enriched candidate	enriched candidate
MDH2	0.8705424	1.3314963	0.0449768	0.0039903	enriched candidate	enriched hit
UQCRC1	0.7136781	1.1517412	0.0451219	0.0026798	enriched candidate	enriched hit
MYL6	0.5961698	0.5520476	0.0457694	0.0623811	enriched candidate	no hit
PUF60	-0.4712617	-0.4207790	0.0460849	0.0718511	no hit	no hit
RDX	1.3039637	1.1493159	0.0461561	0.0753589	enriched candidate	enriched candidate
GNG12	0.5021224	0.2823064	0.0462213	0.2445786	no hit	no hit
ATP5A1	0.8481773	1.6104386	0.0485491	0.0007948	no hit	enriched hit
RAP1A	0.5320556	0.7579538	0.0490914	0.0075436	no hit	enriched candidate
AGL	-1.0040286	-1.2029550	0.0494766	0.0212008	no hit	no hit
SKP1	-0.7393452	-0.8009505	0.0498820	0.0351854	no hit	no hit
GLOD4	-0.8477743	-0.9762664	0.0500377	0.0263486	no hit	no hit
TXNRD1	-0.6101066	-0.6128501	0.0505713	0.0496451	no hit	no hit
RPN2	0.7968537	1.3097488	0.0507365	0.0028882	no hit	enriched hit
PPP1CA	0.4903157	0.3873057	0.0512769	0.1165183	no hit	no hit
HSPH1	-0.5318265	-0.4065802	0.0531840	0.1311818	no hit	no hit
SLC25A24	0.9698108	1.1350588	0.0535950	0.0264327	no hit	enriched candidate
KPNB1	-0.6698115	-0.6399123	0.0538990	0.0643890	no hit	no hit
TM9SF2	-0.9274344	-1.0517459	0.0541365	0.0312049	no hit	no hit
HSPA4	-0.7347511	-0.4536348	0.0542675	0.2200571	no hit	no hit
ITGA6	0.6160650	0.5598786	0.0546545	0.0781872	no hit	no hit
DHCR7	0.8628836	1.1478017	0.0555554	0.0139149	no hit	enriched candidate
BPNT1	-0.5667511	-0.5567825	0.0562577	0.0603012	no hit	no hit
YWHAH	-0.7761973	-1.1368576	0.0565507	0.0079065	no hit	no hit
NMT1	-1.1620870	-1.7092048	0.0570214	0.0077993	no hit	no hit
RP2	0.6859755	0.4805714	0.0590441	0.1751859	no hit	no hit
CIB1	0.4424269	0.0767560	0.0602315	0.7321770	no hit	no hit
TRIM28	0.6867347	0.7648885	0.0605151	0.0386461	no hit	enriched candidate
MSLN	0.5925356	0.4150970	0.0607018	0.1781403	no hit	no hit
NECTIN2	0.4771873	0.2047078	0.0613481	0.4035085	no hit	no hit
AKR1B1	-0.7648907	-0.9349887	0.0617305	0.0254600	no hit	no hit
SLC25A3	0.8302348	1.5530089	0.0623183	0.0015558	no hit	enriched hit
ADAM10	0.4694021	0.7025148	0.0627386	0.0081764	no hit	enriched candidate
TPD52L2	-0.7235519	-1.0737492	0.0629491	0.0086830	no hit	no hit
GTF2I	0.7782688	1.0808547	0.0631256	0.0131048	no hit	enriched candidate
PPIF	0.9239184	1.6091492	0.0645972	0.0029664	no hit	enriched hit
HMBOX2	0.4829780	0.5548688	0.0668045	0.0378085	no hit	no hit

gene_name	logFC_PA	logFC_PE	pvalue_PA	pvalue_PE	hit_annotation_PA	hit_annotation_PE
GOLT1B	-0.5355459	-0.5745379	0.0676244	0.0514464	no hit	no hit
PARK7	-0.7473461	-0.8083441	0.0691631	0.0510112	no hit	no hit
ACO2	0.6691561	1.0844205	0.0696929	0.0058022	no hit	enriched hit
YWHAG	-0.4642422	-0.8470333	0.0697281	0.0024270	no hit	no hit
ETFA	0.7791291	1.1731190	0.0700165	0.0094913	no hit	enriched candidate
WDR1	1.1206443	1.1555536	0.0702509	0.0626577	no hit	enriched candidate
SHMT2	1.1096423	1.8917486	0.0715130	0.0042664	no hit	enriched hit
GNG5	0.5357813	0.3309812	0.0717179	0.2527440	no hit	no hit
AP1B1	-0.4693235	-0.8364574	0.0726385	0.0031716	no hit	no hit
RAB31	0.4759150	0.6653932	0.0729057	0.0157856	no hit	enriched candidate
RBBP4	0.5423190	0.2505057	0.0732154	0.3913247	no hit	no hit
ATP1A1	0.5687790	0.8566751	0.0735322	0.0103066	no hit	enriched candidate
SDHA	0.9086139	1.6885254	0.0736665	0.0023670	no hit	enriched hit
POR	0.6752719	1.2822349	0.0747595	0.0020604	no hit	enriched hit
EIF5A	-1.3670257	-1.6858074	0.0755064	0.0318463	no hit	no hit
LIFR	0.4648637	0.4255133	0.0757462	0.1016881	no hit	no hit
MME	-0.4869324	-0.9887385	0.0762257	0.0012362	no hit	no hit
ITGA5	0.6907537	0.6910638	0.0768046	0.0766832	no hit	enriched candidate
SFXN1	0.8439585	1.3278179	0.0772622	0.0085487	no hit	enriched hit
PPA1	-0.9022483	-1.0180095	0.0774740	0.0488178	no hit	no hit
RAP2C	0.4012618	0.4555885	0.0779790	0.0479289	no hit	no hit
GLO1	-0.9432437	-1.2287457	0.0804913	0.0266674	no hit	no hit
PA2G4	-1.0323648	-1.3580830	0.0813144	0.0257705	no hit	no hit
DSG2	0.5092099	0.5182017	0.0815305	0.0767096	no hit	no hit
LAMC1	0.5137819	0.2155576	0.0816605	0.4493452	no hit	no hit
GSTM3	-0.7007375	-0.4917216	0.0820878	0.2127673	no hit	no hit
GOT2	0.8470544	1.5142310	0.0823144	0.0040398	no hit	enriched hit
SLC43A3	0.5485201	0.0663466	0.0826897	0.8267207	no hit	no hit
OXCT1	0.6595150	1.3439306	0.0831710	0.0014839	no hit	enriched hit
CS	1.4016306	2.2800407	0.0834149	0.0079509	no hit	enriched hit
PRDX1	-0.8641678	-1.0643709	0.0842449	0.0370733	no hit	no hit
USP14	-0.6021440	-0.7050309	0.0850444	0.0468237	no hit	no hit
RMDN1	0.7151034	1.2567316	0.0852800	0.0049203	no hit	enriched hit
PGK1	-0.7322022	-0.8622865	0.0870973	0.0470823	no hit	no hit
BUB3	-0.4248345	-0.3829254	0.0872845	0.1205178	no hit	no hit
HSP90B1	0.8768021	1.3699159	0.0874302	0.0111871	no hit	enriched candidate
UBXN4	0.5163635	0.6651792	0.0887183	0.0323534	no hit	enriched candidate
CAPZA1	-0.5595352	-0.3641191	0.0889270	0.2573339	no hit	no hit
ACSL3	1.0994523	1.4123138	0.0890577	0.0329646	no hit	enriched candidate
SLC44A2	0.8047551	0.7306552	0.0904399	0.1217162	no hit	no hit
PEBP1	-1.0342547	-1.3508123	0.0915596	0.0317146	no hit	no hit
TRMT10C	0.7804957	1.3265029	0.0921464	0.0072551	no hit	enriched hit
NEGR1	0.3925125	0.2330619	0.0943592	0.3084358	no hit	no hit
MLEC	0.5586669	0.9309872	0.0946951	0.0087084	no hit	enriched candidate
QARS	0.3944565	0.2932767	0.0972788	0.2099295	no hit	no hit
ENO1	-0.6567392	-0.5858189	0.0973372	0.1361995	no hit	no hit
GDA	-0.6464967	-0.6086386	0.0986695	0.1184982	no hit	no hit
RPS28	-0.6225026	-0.9282649	0.0987896	0.0181941	no hit	no hit
ARFGAP1	-0.5605887	-0.9075345	0.0993044	0.0114400	no hit	no hit
ECI1	0.8083904	1.1499630	0.1000294	0.0238445	no hit	enriched candidate
DAG1	0.6328029	0.4841418	0.1001741	0.2015386	no hit	no hit
F11R	0.6703346	0.5786599	0.1011202	0.1531764	no hit	no hit

gene_name	logFC_PA	logFC_PE	pvalue_PA	pvalue_PE	hit_annotation_PA	hit_annotation_PE
TUFM	1.1617206	1.7057189	0.1027527	0.0211509	no hit	enriched candidate
HSPA1B HSPA1A	-0.4351823	-0.1209898	0.1032678	0.6391645	no hit	no hit
MAT2A	-0.6444786	-0.7286590	0.1032697	0.0681141	no hit	no hit
SLC1A5	0.4066043	0.1795620	0.1039616	0.4594581	no hit	no hit
ALDH3A2	0.7284483	1.1699565	0.1045580	0.0132371	no hit	enriched candidate
PRDX3	1.1454577	1.5097689	0.1060583	0.0376813	no hit	enriched candidate
CLINT1	-1.0843148	-1.6696676	0.1061654	0.0173164	no hit	no hit
CAPN2	-0.4646363	-0.3366213	0.1093045	0.2381256	no hit	no hit
CD59	0.5405265	0.5149523	0.1099009	0.1265537	no hit	no hit
ATL2	0.5416945	0.7326634	0.1101676	0.0354658	no hit	enriched candidate
EIF3M	-0.5956659	-0.7569095	0.1116491	0.0475652	no hit	no hit
MYDGF	0.6411100	0.4473981	0.1119904	0.2588817	no hit	no hit
CAPRIN1	-1.1131676	-1.8752007	0.1139290	0.0118013	no hit	no hit
DLD	0.9607469	1.4164378	0.1139656	0.0247059	no hit	enriched candidate
RAN	-0.3879245	-0.1126817	0.1141586	0.6355767	no hit	no hit
GIGYF2	-0.8588753	-1.3041414	0.1155944	0.0217537	no hit	no hit
DSP	-0.7004315	-0.8915726	0.1169136	0.0503811	no hit	no hit
LSS	0.3643852	0.4395606	0.1178693	0.0630021	no hit	no hit
CDH10	0.5228095	0.4905615	0.1191043	0.1420662	no hit	no hit
SLC38A5	0.5757868	0.3688671	0.1195638	0.3091078	no hit	no hit
USP10	-0.7552357	-1.2279646	0.1196238	0.0159862	no hit	no hit
MCAM	0.7428621	0.8024138	0.1198088	0.0946603	no hit	no hit
MSN	1.4877823	1.3495103	0.1198543	0.1558913	no hit	no hit
TLN1	0.4964995	0.5474012	0.1200941	0.0887615	no hit	no hit
ALG5	0.6799184	1.0268735	0.1205670	0.0241057	no hit	enriched candidate
SUPT16H	0.3565489	0.2253326	0.1207534	0.3171152	no hit	no hit
CCT8	0.5130406	0.1856713	0.1210070	0.5633561	no hit	no hit
MMP15	0.4099008	0.2804082	0.1213524	0.2807919	no hit	no hit
ADAM9	0.4688802	0.5977875	0.1214535	0.0528125	no hit	enriched candidate
TAPBP	0.5379738	1.0205991	0.1215162	0.0063619	no hit	enriched hit
BZW2	-0.5642821	-0.3594154	0.1219288	0.3150239	no hit	no hit
DDOST	0.5872560	0.8253849	0.1225850	0.0351435	no hit	enriched candidate
EPB41L2	0.9540247	0.9189382	0.1226985	0.1361664	no hit	no hit
SUCLG2	0.8475886	1.2854421	0.1232421	0.0245393	no hit	enriched candidate
LRPPRC	0.8803241	1.4431776	0.1235478	0.0162604	no hit	enriched candidate
G3BP2	-1.3005146	-1.7375196	0.1238397	0.0447151	no hit	no hit
RPN1	0.9055281	1.2928639	0.1245692	0.0335417	no hit	enriched candidate
RAB8A	0.3653774	0.3123164	0.1251734	0.1861486	no hit	no hit
C17orf75	-0.3864451	-0.4159497	0.1263078	0.1015336	no hit	no hit
HNRNPA2B1	-0.5177406	-0.4120945	0.1267995	0.2188629	no hit	no hit
CAPZB	-0.4487241	-0.2896496	0.1270582	0.3155881	no hit	no hit
HSD17B10	0.6434498	0.9512938	0.1279775	0.0297473	no hit	enriched candidate
FLOT2	0.7160830	0.7804755	0.1282138	0.0992654	no hit	no hit
VDAC2	0.6761461	0.7611357	0.1286019	0.0897448	no hit	no hit
SLIRP	0.8045309	1.4909460	0.1291731	0.0085609	no hit	enriched hit
ANXA3	-0.6137583	-0.8338470	0.1298005	0.0447137	no hit	no hit
STT3A	0.5832009	1.0951797	0.1305010	0.0080497	no hit	enriched hit
COX5A	0.6865719	1.0359832	0.1308077	0.0279850	no hit	enriched candidate
CD320	0.3318795	0.5271437	0.1317788	0.0218707	no hit	no hit
EIF4A1	-1.0769287	-1.4921220	0.1320805	0.0422135	no hit	no hit
HSPA5	0.7608667	1.0473646	0.1340677	0.0444530	no hit	enriched candidate
ARL15	0.4211931	0.4453741	0.1348650	0.1151489	no hit	no hit

gene_name	logFC_PA	logFC_PE	pvalue_PA	pvalue_PE	hit_annotation_PA	hit_annotation_PE
FAM234A	0.4876238	0.1647107	0.1354343	0.6041060	no hit	no hit
SGTA	-0.6912632	-1.0949960	0.1355253	0.0233942	no hit	no hit
ACTR3	0.7209652	0.7582484	0.1361174	0.1181581	no hit	no hit
GPX8	0.7813264	0.8794929	0.1384419	0.0979550	no hit	no hit
NSDHL	0.6104310	0.9967437	0.1396551	0.0211687	no hit	enriched candidate
SAE1	-0.6869693	-0.9734499	0.1399645	0.0420202	no hit	no hit
TPI1	-0.8752863	-1.3146029	0.1403100	0.0324097	no hit	no hit
GNB2	0.9235087	1.1148611	0.1415669	0.0798367	no hit	no hit
PHB	1.0004014	1.5166908	0.1415971	0.0315096	no hit	enriched candidate
ALDOC	-0.4623600	-0.3477376	0.1417159	0.2629377	no hit	no hit
DNPB1	-0.5491632	-0.8279897	0.1432261	0.0330101	no hit	no hit
BSG	0.7674527	0.5553078	0.1432631	0.2827719	no hit	no hit
NUDT21	0.3128488	0.4548815	0.1436832	0.0391836	no hit	no hit
CNOT1	-0.9773670	-1.1739267	0.1438879	0.0829808	no hit	no hit
EZR	1.2053525	0.9549854	0.1447796	0.2428373	no hit	no hit
RPS12	-0.5167728	-0.8568059	0.1453146	0.0211430	no hit	no hit
ERP29	0.8413553	1.0042259	0.1453974	0.0859217	no hit	no hit
RHOA	0.3476848	0.1425033	0.1455950	0.5409533	no hit	no hit
FLOT1	0.7270289	0.7289149	0.1458074	0.1448243	no hit	no hit
KDELC2	0.4823694	0.5089700	0.1460138	0.1262608	no hit	no hit
GCN1	-1.0153633	-1.3456809	0.1481564	0.0604547	no hit	no hit
STX6	-0.3582669	-0.5070005	0.1487628	0.0466926	no hit	no hit
GSS	-0.5830147	-0.7431179	0.1490047	0.0705628	no hit	no hit
RPS10	-1.0015419	-1.6051252	0.1493796	0.0265737	no hit	no hit
CPM	0.6025927	0.6217837	0.1507395	0.1388656	no hit	no hit
NAA15	-1.1184321	-1.2229087	0.1511476	0.1184855	no hit	no hit
SBDS	-0.6783491	-0.9443653	0.1515137	0.0514816	no hit	no hit
DKFZp566H1924 NPTN	0.7993142	0.6960397	0.1515462	0.2086499	no hit	no hit
CNP	1.0902907	0.9573946	0.1517786	0.2052775	no hit	no hit
PLOD3	0.7053834	0.7502766	0.1517808	0.1287650	no hit	no hit
SYNGR2	-0.5886332	-0.7269089	0.1522276	0.0813050	no hit	no hit
TUBB	-0.6155474	-0.7689170	0.1551852	0.0802265	no hit	no hit
HSPD1	0.9014326	1.9121910	0.1561475	0.0056146	no hit	enriched hit
TPP2	0.8148830	0.9129634	0.1562630	0.1146645	no hit	no hit
PSME2	-0.6709449	-0.7246149	0.1574189	0.1284819	no hit	no hit
TMEM43	0.3461815	0.6961019	0.1575705	0.0082253	no hit	enriched candidate
FOLR1	0.7011765	0.5161595	0.1580814	0.2926925	no hit	no hit
MDH1	-0.5272863	-0.7207143	0.1583154	0.0593683	no hit	no hit
PMPCB	0.6668214	1.0407801	0.1590304	0.0340044	no hit	enriched candidate
COLGALT1	0.8325576	0.9915497	0.1591766	0.0972406	no hit	no hit
ARPC3	0.3714443	0.3898731	0.1598194	0.1411710	no hit	no hit
ATP5H	0.8068191	1.3281275	0.1600204	0.0266435	no hit	enriched candidate
LGALS1	0.4184166	0.3770910	0.1604680	0.2036356	no hit	no hit
RTN4RL2	0.4518794	0.1716733	0.1605016	0.5851250	no hit	no hit
CAPZA2	-0.3140864	-0.2204797	0.1619901	0.3196500	no hit	no hit
TPM3 DKFZp686J1372	0.6399644	0.7849955	0.1623590	0.0907110	no hit	no hit
FAM120A	-0.6677745	-1.0003940	0.1667286	0.0445130	no hit	no hit
ATP11C	0.3302766	0.3856727	0.1685136	0.1110997	no hit	no hit
CNPY3	0.4335020	0.3995845	0.1691744	0.2033025	no hit	no hit
PSME1	-0.8286533	-1.0987392	0.1701342	0.0742297	no hit	no hit
EIF5B	-0.9652211	-1.4702232	0.1713992	0.0435545	no hit	no hit
DSTN	0.4122759	0.4583294	0.1724723	0.1316024	no hit	no hit

gene_name	logFC_PA	logFC_PE	pvalue_PA	pvalue_PE	hit_annotation_PA	hit_annotation_PE
ATP5B	0.6481431	0.9215067	0.1725493	0.0584757	no hit	enriched candidate
TXNL1	-0.5509991	-0.8439840	0.1734693	0.0434590	no hit	no hit
PRDX2	-0.7865315	-1.1430588	0.1757150	0.0552915	no hit	no hit
HSPA13	0.4182579	0.6785729	0.1760926	0.0345871	no hit	enriched candidate
SERPINH1	0.9489722	1.1811706	0.1769333	0.0972135	no hit	no hit
AHCY	-0.3680976	-0.1397386	0.1802514	0.6032224	no hit	no hit
WDR61	-0.5347530	-0.8538863	0.1806211	0.0390773	no hit	no hit
DYNC1H1	-0.9744223	-1.1785718	0.1809552	0.1095142	no hit	no hit
PHB2	1.0352517	1.5160953	0.1812454	0.0565630	no hit	enriched candidate
CAT	0.5579615	0.9047239	0.1814100	0.0367822	no hit	enriched candidate
EIF3K	-0.3610334	-0.8200624	0.1814260	0.0053934	no hit	no hit
PRKAR2A	-0.2634099	-0.4239554	0.1821578	0.0383458	no hit	no hit
RPL38	-1.3763703	-1.1037475	0.1822352	0.2805586	no hit	no hit
ACSL4	0.9251326	0.7330185	0.1822896	0.2862276	no hit	no hit
NPR3	0.3784486	0.4070312	0.1824100	0.1530885	no hit	no hit
HLA-C	0.3664717	0.1795401	0.1843322	0.5075474	no hit	no hit
LARP4	-0.8570415	-1.3631832	0.1843746	0.0413741	no hit	no hit
XPO1	-0.4884276	-0.1528032	0.1849720	0.6715277	no hit	no hit
PRMT1	-0.4148341	-0.7798299	0.1861481	0.0186331	no hit	no hit
ITGA3	0.4757438	0.3885013	0.1862523	0.2765854	no hit	no hit
RACGAP1	1.2548032	1.0570651	0.1863014	0.2622452	no hit	no hit
RPLP1	-0.6976493	-0.9099714	0.1880194	0.0910683	no hit	no hit
MYO1B	1.0768574	1.1413346	0.1884016	0.1645073	no hit	no hit
SLC35B2	-0.4295009	-0.2921223	0.1891595	0.3656743	no hit	no hit
HSPA8	-0.3693488	-0.2270991	0.1905722	0.4140493	no hit	no hit
PSMA2	-0.3567348	-0.2878853	0.1908187	0.2871562	no hit	no hit
AP2A1	0.4433187	0.2973237	0.1915044	0.3748292	no hit	no hit
TOR1AIP2	0.4197331	0.3163467	0.1921655	0.3207269	no hit	no hit
ACTN1	0.9289429	1.1353098	0.1938871	0.1163550	no hit	no hit
PGRMC1	0.4523851	0.5333885	0.1948146	0.1297050	no hit	no hit
ACTN4	1.2041321	1.3633746	0.1955819	0.1453544	no hit	no hit
PABPC4	-0.6944954	-1.1678814	0.1959278	0.0364560	no hit	no hit
G3BP1	-0.9409152	-1.5250690	0.1964417	0.0431590	no hit	no hit
ADRM1	-0.5774512	-0.7601194	0.1966368	0.0944389	no hit	no hit
P4HA1	0.4905861	0.7315302	0.1977732	0.0614149	no hit	enriched candidate
CMPK1	-0.5004241	-0.7324657	0.1978787	0.0659533	no hit	no hit
HPRT1	-0.6949907	-0.5934223	0.1993951	0.2702627	no hit	no hit
GRB2	-0.5558618	-0.6632522	0.2007440	0.1304002	no hit	no hit
SLC6A9	0.3530572	0.0430949	0.2012579	0.8732198	no hit	no hit
NASP	-0.5373574	-0.8833073	0.2024011	0.0431240	no hit	no hit
ECHS1	0.7161459	1.2456994	0.2028539	0.0336037	no hit	enriched candidate
FDFT1	0.5369991	0.9065920	0.2040962	0.0390194	no hit	enriched candidate
CRELD1	0.3407067	0.1745879	0.2045007	0.5085792	no hit	no hit
PTPRF	0.7766446	0.8001789	0.2048545	0.1920595	no hit	no hit
SLC2A1	0.3761336	0.2777946	0.2057072	0.3451433	no hit	no hit
EIF4A3	-0.7338368	-0.9888043	0.2057364	0.0937620	no hit	no hit
MYO1C	1.2340096	1.3361376	0.2060303	0.1725278	no hit	no hit
MGST1	0.6989488	0.9786733	0.2068239	0.0832118	no hit	no hit
TXLNG	-0.8441387	-1.4115810	0.2068484	0.0418560	no hit	no hit
GORASP2	-0.5605087	0.0462007	0.2071039	0.9153207	no hit	no hit
SEPT7	-1.2334307	-1.5199100	0.2071909	0.1242262	no hit	no hit
ASPH	0.9251205	1.2596332	0.2073504	0.0917313	no hit	no hit

gene_name	logFC_PA	logFC_PE	pvalue_PA	pvalue_PE	hit_annotation_PA	hit_annotation_PE
GDPD3	0.3772271	0.3725936	0.2077590	0.2131561	no hit	no hit
SNTB2	0.5476806	0.7260393	0.2080427	0.1004546	no hit	no hit
HPCAL1	-0.5952747	-0.6338699	0.2081707	0.1814264	no hit	no hit
CLPTM1	0.4093705	0.6133579	0.2088599	0.0664599	no hit	enriched candidate
SEPT2	-0.8926841	-1.0904602	0.2095095	0.1292285	no hit	no hit
DNAJB11	0.9098420	0.9897602	0.2109674	0.1752513	no hit	no hit
TMEM259	0.4572342	0.5374831	0.2135374	0.1468733	no hit	no hit
CD276	0.3194928	0.2672407	0.2136433	0.2951536	no hit	no hit
ITGA1	0.7363086	0.7095578	0.2178101	0.2342999	no hit	no hit
CKAP4	1.0374425	1.3524718	0.2187040	0.1138606	no hit	no hit
ALDOA	-0.4578697	-0.6252609	0.2198786	0.0996045	no hit	no hit
VASN	0.3945106	0.2133211	0.2206697	0.5015023	no hit	no hit
TXLNA	-0.7825708	-1.3905142	0.2223436	0.0373870	no hit	no hit
LGALS3	0.3152423	0.2921546	0.2228815	0.2572663	no hit	no hit
ECI2	0.7559716	1.1563790	0.2230628	0.0693628	no hit	enriched candidate
AUP1	0.7653565	0.9183123	0.2247176	0.1487121	no hit	no hit
KIF23	1.3762028	1.1455282	0.2249349	0.3094339	no hit	no hit
DDX39B	-0.4483316	-0.0884175	0.2278352	0.8083495	no hit	no hit
ARPC2	0.8387718	0.9420930	0.2294064	0.1792502	no hit	no hit
PSMB4	-0.4262704	-0.3543919	0.2300335	0.3153738	no hit	no hit
FKBP10	0.4576698	0.6133966	0.2301868	0.1132303	no hit	no hit
MBOAT7	0.5866982	0.9957172	0.2301932	0.0492205	no hit	enriched candidate
CLPP	0.4817375	0.7479977	0.2305996	0.0698576	no hit	enriched candidate
LIMA1	0.7611764	0.9203629	0.2311615	0.1512981	no hit	no hit
PODXL2	0.3814965	0.3655090	0.2315324	0.2509176	no hit	no hit
TKT	-0.3688553	-0.4913761	0.2315713	0.1163288	no hit	no hit
DDX6	-0.8606561	-1.1429265	0.2327959	0.1183436	no hit	no hit
HMGB1	-0.7689009	-1.0217888	0.2341188	0.1191183	no hit	no hit
ATP2A2	0.5280694	0.9832882	0.2350848	0.0343790	no hit	enriched candidate
RSU1	-0.5293020	-0.4237555	0.2352318	0.3385930	no hit	no hit
S100A16	-0.3952593	-0.8653984	0.2363937	0.0151367	no hit	no hit
CCDC47	0.9389928	1.2682447	0.2368414	0.1156282	no hit	no hit
HADHA	0.4662461	0.9638485	0.2393573	0.0214936	no hit	enriched candidate
MTHFD1	-0.9865059	-1.2043627	0.2396704	0.1548941	no hit	no hit
PSMA7	-0.2666472	-0.0195521	0.2407575	0.9301211	no hit	no hit
ITGB1	0.6028352	0.6285449	0.2430567	0.2242890	no hit	no hit
CAP1	-0.4675020	-0.3160625	0.2434228	0.4256011	no hit	no hit
ATP6AP2	0.4593696	0.4762395	0.2458170	0.2295416	no hit	no hit
NRAS	-0.3555890	-0.6062246	0.2459363	0.0556734	no hit	no hit
ABCF2	-0.8384770	-1.2729247	0.2464148	0.0855027	no hit	no hit
SLC22A18	0.4999536	0.6506782	0.2465142	0.1363421	no hit	no hit
MYO1E	1.0374950	1.0311746	0.2482288	0.2510173	no hit	no hit
PGRMC2	0.5230338	0.4461151	0.2494738	0.3235609	no hit	no hit
CD109	0.5226382	0.2843424	0.2494741	0.5255844	no hit	no hit
PABPC1	-0.7657607	-1.2853266	0.2502205	0.0613787	no hit	no hit
COMT	0.3793053	0.5558602	0.2502978	0.0986723	no hit	no hit
SACM1L	0.6798284	0.8889034	0.2504870	0.1378444	no hit	no hit
GARS	-0.5564182	-0.6178410	0.2531211	0.2063277	no hit	no hit
REEP6	-0.3948524	-0.5485894	0.2555428	0.1200405	no hit	no hit
CSPG4	0.3372564	0.2071553	0.2574308	0.4818129	no hit	no hit
RPL18A	-0.8012599	-1.0647002	0.2577255	0.1377294	no hit	no hit
WLS	0.3405494	0.6001163	0.2585101	0.0544451	no hit	enriched candidate

gene_name	logFC_PA	logFC_PE	pvalue_PA	pvalue_PE	hit_annotation_PA	hit_annotation_PE
HNRNPA1	-0.7122415	-0.0891362	0.2596919	0.8858464	no hit	no hit
CXADR	0.3314016	0.1803730	0.2596961	0.5344966	no hit	no hit
TMX3	0.3871463	0.4835278	0.2613083	0.1646260	no hit	no hit
SCAMP1	-0.3356148	-0.5459533	0.2623313	0.0759383	no hit	no hit
EIF1AY EIF1AX	-0.9107681	-1.1709613	0.2623737	0.1540957	no hit	no hit
TAP1	0.5026019	1.0862074	0.2644086	0.0226909	no hit	enriched candidate
RBMX	-0.6463810	0.0391064	0.2654104	0.9453388	no hit	no hit
CLTC	-0.6017355	-0.9168297	0.2672966	0.0980671	no hit	no hit
TM9SF4	-0.3620671	-0.3815750	0.2680679	0.2440042	no hit	no hit
FXR1	-0.8131010	-1.0024651	0.2688156	0.1764772	no hit	no hit
ERH	-0.5510695	-0.0124216	0.2701238	0.9798265	no hit	no hit
ANXA4	-0.3897706	-1.0457973	0.2713977	0.0069116	no hit	no hit
VAMP3	-0.3572429	-0.5252880	0.2717534	0.1126949	no hit	no hit
LDLR	-0.3726042	-0.4455738	0.2733777	0.1933577	no hit	no hit
SEPT10	-0.8078085	-1.0533540	0.2742079	0.1585877	no hit	no hit
PODXL	0.4364640	0.4962518	0.2764118	0.2180638	no hit	no hit
CFL1	0.3755804	0.6947909	0.2771756	0.0526751	no hit	enriched candidate
GEMIN5	-0.9234248	-1.1881832	0.2773421	0.1665755	no hit	no hit
CNPY2 F8W031	0.6198838	0.6623748	0.2774079	0.2468770	no hit	no hit
VIM	-0.7550759	0.2748573	0.2776430	0.6885019	no hit	no hit
RPS25	-1.0555336	-1.4913347	0.2778374	0.1311902	no hit	no hit
SLC44A1	0.5331593	0.3191940	0.2799447	0.5133502	no hit	no hit
TM9SF3	-0.4410135	-0.2820623	0.2804642	0.4858499	no hit	no hit
VDAC1	0.4891815	0.6999095	0.2832936	0.1308736	no hit	no hit
METAP2	-1.1672268	-1.7239209	0.2838974	0.1200882	no hit	no hit
AP2M1	0.6692516	0.4596463	0.2839912	0.4580464	no hit	no hit
NCEH1	0.3895530	0.4323896	0.2842689	0.2363231	no hit	no hit
GPRC5A	0.5835683	0.7300156	0.2844384	0.1843865	no hit	no hit
SCAMP2	-0.3611587	-0.7141227	0.2845094	0.0425531	no hit	no hit
APMAP	0.4756683	0.4846636	0.2868441	0.2781128	no hit	no hit
GPD2	0.7016824	1.3088019	0.2878149	0.0558469	no hit	enriched candidate
RPS7	-0.8317582	-1.1847248	0.2886797	0.1367301	no hit	no hit
PSMB1	-0.3880081	-0.1190548	0.2891161	0.7414412	no hit	no hit
SLC16A1	0.2446925	0.1246826	0.2914283	0.5865823	no hit	no hit
P4HB	0.5295123	0.5141162	0.2925002	0.3063375	no hit	no hit
ANXA2	0.2289044	0.0315289	0.2959714	0.8838129	no hit	no hit
FARSB	-0.6211158	-0.9754518	0.2960562	0.1081376	no hit	no hit
RAB27B	0.3835296	0.2493259	0.2963088	0.4934005	no hit	no hit
VAPA	0.5013389	0.9139444	0.2965477	0.0655578	no hit	enriched candidate
RAB1B	-0.3824102	-0.4802344	0.2980556	0.1950401	no hit	no hit
SEPT9	-0.9908514	-1.1495393	0.2982647	0.2298990	no hit	no hit
DEGS1	0.3264638	0.5725459	0.3008159	0.0779586	no hit	no hit
DLG1	0.2685080	0.4981249	0.3014211	0.0638309	no hit	no hit
ZMPSTE24	0.4647001	0.7210685	0.3040662	0.1179194	no hit	no hit
RABAC1	-0.4214853	-0.4863726	0.3040845	0.2378858	no hit	no hit
CSDE1	-0.8677602	-1.3081679	0.3051104	0.1288399	no hit	no hit
SCD	0.4187249	0.8347019	0.3058105	0.0498486	no hit	enriched candidate
SLC5A6	-0.2534202	-0.5117102	0.3077571	0.0480789	no hit	no hit
HMGF	-0.3794429	-0.7799302	0.3080303	0.0447058	no hit	no hit
FAU	-1.2183756	-1.5092772	0.3086996	0.2107272	no hit	no hit
S100A13	-0.5376245	-0.9305155	0.3089895	0.0865794	no hit	no hit
RPL5	-0.6903833	-1.1747547	0.3097510	0.0920863	no hit	no hit

gene_name	logFC_PA	logFC_PE	pvalue_PA	pvalue_PE	hit_annotation_PA	hit_annotation_PE
PLD3	0.2875705	0.3640653	0.3098410	0.2023372	no hit	no hit
TPM4	0.4376922	0.5770425	0.3109776	0.1861186	no hit	no hit
RPS14	-0.7317541	-1.1634865	0.3128199	0.1159482	no hit	no hit
STT3B	1.2871175	1.3664882	0.3142492	0.2861883	no hit	no hit
FUBP1	-0.3619687	-0.6758808	0.3153676	0.0695858	no hit	no hit
SFPQ	-0.5062834	-0.0471734	0.3154967	0.9244352	no hit	no hit
ESYT1	0.6876612	0.9129691	0.3183955	0.1898051	no hit	no hit
M6PR	-0.5028284	-0.6549505	0.3205010	0.1998450	no hit	no hit
FLVCR1	0.3130558	0.0821283	0.3209768	0.7919818	no hit	no hit
RUVBL2	-0.5663251	-0.7702881	0.3221846	0.1830327	no hit	no hit
CORO1C	0.5854411	0.6345545	0.3242751	0.2864592	no hit	no hit
RPL14	-1.0125213	-1.3067001	0.3250588	0.2080305	no hit	no hit
TMEM165	-0.4216952	-0.4595446	0.3262406	0.2858887	no hit	no hit
NCL	0.3709587	0.7250099	0.3266669	0.0642066	no hit	enriched candidate
IKBIP	0.7831438	1.1417357	0.3269566	0.1589767	no hit	no hit
EIF2A	-0.6542443	-1.0084641	0.3272351	0.1378801	no hit	no hit
SEC61B	0.3143726	0.2599649	0.3276498	0.4163027	no hit	no hit
PSMA3	-0.4040460	-0.5553528	0.3279420	0.1837614	no hit	no hit
CYBSR3	0.4456785	0.7990912	0.3290754	0.0887368	no hit	no hit
AK2	0.5170853	0.9504375	0.3293545	0.0817618	no hit	no hit
RPL24	-0.9191877	-1.3019531	0.3362564	0.1786114	no hit	no hit
RPL36A RPL36A-HNRNPH2	-0.8823112	-1.3371821	0.3364819	0.1517261	no hit	no hit
ARPC4-TTL3 ARPC4	0.3463547	0.4158419	0.3367566	0.2514127	no hit	no hit
DDX3X	-0.7297179	-1.0153922	0.3378197	0.1873957	no hit	no hit
HLA-A	0.2389993	0.0103419	0.3387667	0.9665554	no hit	no hit
TMX2	0.3317400	0.9467155	0.3411925	0.0120021	no hit	enriched candidate
STX10	-0.3488578	-0.4856360	0.3420549	0.1910114	no hit	no hit
CALR	0.3275359	0.5172317	0.3420856	0.1406136	no hit	no hit
PPP3CA	-0.2388980	-0.3992380	0.3423152	0.1203675	no hit	no hit
EIF3G	-0.8235661	-1.2972172	0.3423820	0.1418085	no hit	no hit
RPLP0	-0.6730905	-1.0651957	0.3433146	0.1407894	no hit	no hit
SLC7A2	-0.2848604	-0.3995457	0.3448875	0.1903705	no hit	no hit
SLC31A1	0.2908689	-0.0560104	0.3458152	0.8542247	no hit	no hit
RPS8	-0.8715098	-1.1752908	0.3461180	0.2083535	no hit	no hit
TMED5	-0.4449062	-0.1431350	0.3470317	0.7596693	no hit	no hit
RPL35	-0.9043925	-1.1620853	0.3480880	0.2315781	no hit	no hit
SCP2	0.5047331	1.0237617	0.3484288	0.0664381	no hit	enriched candidate
E9PAM4 PI4K2A	-0.3162002	-0.4878897	0.3495461	0.1555436	no hit	no hit
RPL11	-0.8546576	-1.1890316	0.3500932	0.1985455	no hit	no hit
RPL15	-0.7978020	-0.9475853	0.3502915	0.2696080	no hit	no hit
TSPAN4	0.6361595	0.2973885	0.3508632	0.6597311	no hit	no hit
RPS20	-0.8739130	-1.3810225	0.3543163	0.1502141	no hit	no hit
TECR	0.7546452	0.8234753	0.3547755	0.3136913	no hit	no hit
NAPA	-0.2622515	-0.3380945	0.3551982	0.2368901	no hit	no hit
KDSR	0.3551705	0.4978699	0.3584189	0.2029220	no hit	no hit
ITGA2	0.5012052	0.2802604	0.3592761	0.6053160	no hit	no hit
XRCC5	-0.5917313	-0.7128302	0.3605306	0.2731589	no hit	no hit
SYNCRIP	-0.5910552	-0.8579058	0.3608183	0.1902191	no hit	no hit
SURF4	-0.2996728	-0.2397919	0.3612315	0.4631764	no hit	no hit
SYPL1	-0.5468150	-0.3614096	0.3617302	0.5440042	no hit	no hit
FKBP9	0.3855950	0.3653033	0.3620501	0.3873045	no hit	no hit
RPL7	-0.8038363	-1.2803383	0.3623667	0.1537990	no hit	no hit

gene_name	logFC_PA	logFC_PE	pvalue_PA	pvalue_PE	hit_annotation_PA	hit_annotation_PE
MICA	0.3456726	0.3609124	0.3624216	0.3421447	no hit	no hit
RPL36	-0.9026262	-1.1684220	0.3626459	0.2422200	no hit	no hit
RPS3A	-0.7393476	-1.0960594	0.3650739	0.1851519	no hit	no hit
CYB5B	0.5613273	0.6710972	0.3671943	0.2832957	no hit	no hit
RHEB	0.2058517	0.2394298	0.3682448	0.2972043	no hit	no hit
SEC61A1	0.2966841	0.6914496	0.3688266	0.0454093	no hit	enriched candidate
PDIA4	0.6446313	0.8142042	0.3688550	0.2594935	no hit	no hit
P4HA2	0.4168585	0.5944729	0.3718328	0.2078787	no hit	no hit
PSMA4	-0.2404741	-0.0015543	0.3721474	0.9953458	no hit	no hit
UQCRB	0.7334598	1.1612093	0.3729699	0.1651250	no hit	no hit
RPL23A	-0.7721570	-1.0143976	0.3731138	0.2456676	no hit	no hit
RPS17	-0.8838204	-1.4228098	0.3731412	0.1586376	no hit	no hit
RPS3	-0.7743381	-1.1823833	0.3734615	0.1802986	no hit	no hit
PLEC	-0.5750348	0.1088815	0.3758303	0.8654216	no hit	no hit
LGALS3BP	0.2572816	0.5519703	0.3772971	0.0677993	no hit	no hit
EEF2	-0.6237502	-0.9191843	0.3809253	0.2021019	no hit	no hit
RAB1A	-0.2464567	-0.3929116	0.3811400	0.1693721	no hit	no hit
RPS11	-0.7354220	-1.2214507	0.3814275	0.1533688	no hit	no hit
RPS2	-0.8145821	-1.2056922	0.3816428	0.2008708	no hit	no hit
TMEM33	0.2773073	0.7626371	0.3817426	0.0238227	no hit	enriched candidate
RPL13	-0.8333597	-1.1379202	0.3820103	0.2368046	no hit	no hit
RPL22	-0.7907898	-1.3428734	0.3822431	0.1455192	no hit	no hit
CLCC1	0.3326902	0.6428979	0.3825695	0.1006723	no hit	no hit
RPS9	-0.8120057	-1.3552671	0.3860102	0.1552954	no hit	no hit
RPS24	-0.8573689	-1.2758859	0.3870024	0.2035100	no hit	no hit
RPL34	-0.9369821	-1.1988690	0.3878728	0.2723436	no hit	no hit
EIF3F	-0.3842297	-0.8356300	0.3878973	0.0701140	no hit	no hit
MATR3	-0.3896702	-0.3518068	0.3880900	0.4349733	no hit	no hit
NIT2	-0.2491599	-0.1309036	0.3897615	0.6489310	no hit	no hit
S100A10	0.2886700	0.2487605	0.3912761	0.4588628	no hit	no hit
HTATIP2	0.4882925	0.4114694	0.3912981	0.4687401	no hit	no hit
FAM3C	-0.2530116	-0.3495352	0.3918667	0.2411073	no hit	no hit
LRRC59	1.0666575	1.7379222	0.3938065	0.1715984	no hit	no hit
REEP5	-0.3843386	-0.3321109	0.3954758	0.4616551	no hit	no hit
RPL28	-0.7495031	-1.0767428	0.3972160	0.2287000	no hit	no hit
RPL7A	-0.7597630	-1.0601064	0.3974695	0.2420791	no hit	no hit
RPL26	-0.8335416	-1.2629444	0.3979554	0.2059466	no hit	no hit
RPL29	-0.9636526	-1.1746680	0.3982230	0.3054071	no hit	no hit
IGF2BP3	-0.6259536	-0.9819136	0.3999283	0.1928785	no hit	no hit
TXNDC12	0.3124914	0.5234791	0.4003237	0.1660708	no hit	no hit
AP2B1	0.2743329	0.2643168	0.4018140	0.4188954	no hit	no hit
RPS13	-0.7244270	-1.2016797	0.4021990	0.1716846	no hit	no hit
CDC42	0.2414787	0.0214432	0.4050529	0.9404895	no hit	no hit
SLC2A3	0.3829006	0.2428679	0.4054841	0.5956313	no hit	no hit
DARS	0.4621965	0.3120175	0.4060339	0.5728485	no hit	no hit
MPZL1	0.3868072	0.3173118	0.4065007	0.4945634	no hit	no hit
GLG1	-0.2772624	-0.1132116	0.4072998	0.7330449	no hit	no hit
RPL13A	-0.7918771	-1.1281656	0.4074574	0.2424523	no hit	no hit
HDLBP	-0.5052360	-0.8107209	0.4094137	0.1919928	no hit	no hit
RPL19	-0.6723126	-1.1177523	0.4099860	0.1776871	no hit	no hit
RPL8	-0.9069136	-1.3424516	0.4102002	0.2279142	no hit	no hit
HM13	0.3749500	0.5093270	0.4111289	0.2679455	no hit	no hit

gene_name	logFC_PA	logFC_PE	pvalue_PA	pvalue_PE	hit_annotation_PA	hit_annotation_PE
CPNE3	-0.2338397	-0.3214158	0.4113480	0.2627167	no hit	no hit
RPS18	-0.6707669	-1.1811845	0.4127722	0.1569838	no hit	no hit
VKORC1L1	0.3571129	0.3562727	0.4136751	0.4147544	no hit	no hit
RPL10A	-0.7421003	-1.0748685	0.4145078	0.2419216	no hit	no hit
SCARB1	0.2631376	0.2606525	0.4145667	0.4189073	no hit	no hit
SCRIB	0.2345346	0.2165163	0.4172461	0.4533172	no hit	no hit
RPL21	-0.7406006	-1.0599002	0.4179388	0.2507942	no hit	no hit
FLNB	0.3995931	0.6712528	0.4183074	0.1809192	no hit	no hit
RPLP2	-0.5543999	-1.1430867	0.4185280	0.1048435	no hit	no hit
RCC2	-0.6522001	-0.9090149	0.4198138	0.2648305	no hit	no hit
FLNA	0.7026479	0.8370706	0.4200562	0.3385726	no hit	no hit
RPL27	-0.7488666	-0.9817767	0.4204064	0.2939087	no hit	no hit
ENG	0.2534421	0.2120423	0.4205430	0.4992127	no hit	no hit
RANGAP1	0.2681333	0.1640025	0.4209500	0.6205792	no hit	no hit
RPL17 RPL17-C18orf32	-0.7280410	-0.9930729	0.4211520	0.2761759	no hit	no hit
RPS4X	-0.6505533	-0.9780111	0.4211750	0.2317113	no hit	no hit
SQSTM1	0.5265306	0.5998086	0.4211832	0.3607753	no hit	no hit
RPS6	-0.7129250	-1.1310338	0.4213852	0.2081219	no hit	no hit
CD151	0.3682590	0.1048861	0.4234917	0.8182084	no hit	no hit
RPL3	-0.6693002	-0.9505590	0.4244043	0.2608037	no hit	no hit
GAA	-0.2220331	-0.0226581	0.4247618	0.9345054	no hit	no hit
STX7	-0.2426743	-0.3327488	0.4253528	0.2780365	no hit	no hit
VAPB	0.2270465	0.4803762	0.4278509	0.1031251	no hit	no hit
RPS23	-0.6949735	-1.2703006	0.4285290	0.1559076	no hit	no hit
TBL2	0.6729672	1.0830149	0.4288388	0.2090324	no hit	no hit
PSMB6	-0.3647889	-0.5897653	0.4317972	0.2098741	no hit	no hit
RPL4	-0.7205831	-1.0077362	0.4330908	0.2767951	no hit	no hit
ATP6AP1	0.3615237	0.4814670	0.4346768	0.3012787	no hit	no hit
GOLPH3	-0.2477797	-0.2444842	0.4351813	0.4412116	no hit	no hit
RPS5	-0.6805561	-1.0576074	0.4360541	0.2315500	no hit	no hit
ACLY	-0.5805583	-0.7639730	0.4379443	0.3103029	no hit	no hit
VAT1	-0.2925052	-0.3899011	0.4435068	0.3100714	no hit	no hit
DPM3	0.3892319	0.5039774	0.4447278	0.3250270	no hit	no hit
HNRNPL	-0.4353905	-0.1985422	0.4456955	0.7263335	no hit	no hit
ARF3 ARF1	-0.2104515	-0.2488867	0.4511670	0.3743768	no hit	no hit
RPL23	-0.7737745	-1.2370109	0.4528072	0.2356275	no hit	no hit
RPS16	-0.6640048	-1.1339480	0.4546834	0.2082472	no hit	no hit
RPS27A	-0.6527722	-1.1415464	0.4574746	0.2006963	no hit	no hit
RPL30	-0.6703706	-1.0763097	0.4574993	0.2384601	no hit	no hit
RPS19	-0.6157550	-1.3013651	0.4576796	0.1259548	no hit	no hit
TMED10	-0.3098274	-0.4499838	0.4577882	0.2848884	no hit	no hit
CYFIP1	0.6069145	0.6194631	0.4592128	0.4501244	no hit	no hit
RHOB	0.2059062	0.0250409	0.4599029	0.9278470	no hit	no hit
RPL6	-0.6616957	-1.0933862	0.4600713	0.2281481	no hit	no hit
RPL27A	-0.6422145	-1.0844665	0.4613297	0.2197720	no hit	no hit
HNRNPK	-0.3659242	-0.6599319	0.4638106	0.1936588	no hit	no hit
RPL10	-0.7253314	-1.1898856	0.4657692	0.2372063	no hit	no hit
EIF2S3	-0.5852716	-1.0671759	0.4664822	0.1915754	no hit	no hit
CASC4	-0.2819521	-0.4943941	0.4665198	0.2084111	no hit	no hit
MARS	0.2854450	0.3787247	0.4684803	0.3387717	no hit	no hit
RTN3	-0.3459618	-0.3808997	0.4692280	0.4262640	no hit	no hit
TNFRSF10A	0.1756454	-0.1066146	0.4695083	0.6591751	no hit	no hit

gene_name	logFC_PA	logFC_PE	pvalue_PA	pvalue_PE	hit_annotation_PA	hit_annotation_PE
RPL35A	-0.7198064	-1.0699368	0.4697412	0.2867419	no hit	no hit
RPS15A	-0.5864656	-0.8310171	0.4719482	0.3115354	no hit	no hit
RPS26	-0.7209519	-1.3299764	0.4730815	0.1930296	no hit	no hit
XRCC6	-0.4768411	-0.6544365	0.4740420	0.3288321	no hit	no hit
RTN4	-0.3502438	-0.9253006	0.4781009	0.0715115	no hit	no hit
PSMA1	-0.1557183	-0.2073236	0.4801690	0.3497639	no hit	no hit
PSEN1	0.2247999	0.0490752	0.4807261	0.8768522	no hit	no hit
HNRNPC	-0.5231644	-0.2451348	0.4828231	0.7409500	no hit	no hit
ITGAV	0.2860721	0.2204525	0.4832110	0.5879407	no hit	no hit
SLC29A1	0.3318377	0.0671470	0.4856465	0.8870697	no hit	no hit
CLUH	-0.3909244	-1.0259678	0.4858443	0.0780417	no hit	no hit
LAMTOR2	-0.3259802	0.0370592	0.4865540	0.9365280	no hit	no hit
RPSA	-0.3792508	-1.0851253	0.4889121	0.0581950	no hit	no hit
LPCAT3	0.2804523	0.4758574	0.4895819	0.2467825	no hit	no hit
RPL9	-0.6884048	-1.1384194	0.4906998	0.2597373	no hit	no hit
RAB21	0.1589412	0.3823176	0.4951388	0.1110940	no hit	no hit
RAB5A	0.1992319	0.4798704	0.4966859	0.1118641	no hit	no hit
RPL12	-0.5505902	-0.8483631	0.4974307	0.2999692	no hit	no hit
FERMT2	0.3726710	0.2277756	0.4990936	0.6783076	no hit	no hit
PVR	0.3589297	0.3156166	0.4998772	0.5524322	no hit	no hit
BAIAP2L1	0.3747394	0.1782274	0.5004852	0.7474485	no hit	no hit
UPF1	-0.5501691	-0.8731530	0.5025846	0.2918223	no hit	no hit
ANTXR1	0.1650726	-0.1052309	0.5028140	0.6681052	no hit	no hit
HRAS	0.2489713	-0.0020219	0.5035072	0.9956380	no hit	no hit
RPL32	-0.6227703	-0.8883385	0.5037478	0.3432933	no hit	no hit
CCT7	0.5706808	0.4732419	0.5061346	0.5806681	no hit	no hit
C14orf166	-0.3182618	-0.7046305	0.5064785	0.1506105	no hit	no hit
LYPLA1	-0.2256490	-0.1602324	0.5092508	0.6382971	no hit	no hit
PCYOX1	0.2782876	0.4072001	0.5101205	0.3384499	no hit	no hit
RPL37A	-0.6954517	-1.0447554	0.5127835	0.3290567	no hit	no hit
RAB27A	0.3211234	0.4518342	0.5132547	0.3603960	no hit	no hit
BCAP31	0.2063963	0.3408285	0.5154459	0.2876308	no hit	no hit
TMED7-TICAM2 TICAM2 TMED7	-0.3779983	-0.1717446	0.5154567	0.7665532	no hit	no hit
ELAVL1	-0.3535949	-0.3485923	0.5175210	0.5233957	no hit	no hit
DAGLB	-0.2105249	-0.1672868	0.5185555	0.6071934	no hit	no hit
EIF3A	-0.6053218	-1.0504894	0.5249494	0.2752273	no hit	no hit
DERL2	0.2379586	0.4816663	0.5267406	0.2076798	no hit	no hit
SLC38A2	-0.2491920	-0.4364245	0.5286826	0.2752243	no hit	no hit
RPL31	-0.6298237	-1.0987274	0.5323827	0.2812822	no hit	no hit
RPL18	-0.6172557	-0.9497302	0.5330238	0.3409919	no hit	no hit
SLC35F6	-0.3537498	-0.2156407	0.5388883	0.7070423	no hit	no hit
EIF2S1	-0.4435920	-0.9023143	0.5423632	0.2225104	no hit	no hit
VPS35	-0.3582235	-0.3605282	0.5447318	0.5421733	no hit	no hit
SNAP23	0.2137274	-0.0457802	0.5496468	0.8975413	no hit	no hit
CCT2	0.4682346	0.3322103	0.5502757	0.6709352	no hit	no hit
ATP6V0A1	0.1337670	0.2310992	0.5503550	0.3068558	no hit	no hit
ATL3	0.1245788	0.3934117	0.5551268	0.0735579	no hit	no hit
IGF2BP1	-0.4315657	-1.0102529	0.5560470	0.1771116	no hit	no hit
EIF3D	-0.4998896	-0.8500947	0.5578465	0.3232649	no hit	no hit
GGH	-0.1890147	0.0564856	0.5584220	0.8605734	no hit	no hit
ERO1A	0.3354980	0.4630809	0.5607380	0.4239533	no hit	no hit
UBL3	0.2265038	0.3035245	0.5615101	0.4382518	no hit	no hit

gene_name	logFC_PA	logFC_PE	pvalue_PA	pvalue_PE	hit_annotation_PA	hit_annotation_PE
TMED2	-0.2907201	-0.3564787	0.5640917	0.4804389	no hit	no hit
LMAN2	-0.2106224	-0.1845720	0.5645599	0.6132973	no hit	no hit
DDX1	-0.4124819	-0.7219445	0.5669151	0.3207356	no hit	no hit
RAB6A	-0.1664209	-0.0169600	0.5672999	0.9533015	no hit	no hit
SIGMAR1	0.2962249	0.4722193	0.5673811	0.3652529	no hit	no hit
FUBP3	-0.4103971	-0.8228288	0.5684371	0.2591701	no hit	no hit
IMPDH2	0.2808336	0.3462835	0.5700142	0.4846863	no hit	no hit
HNRNPH1	-0.3395556	-0.2258633	0.5706895	0.7053390	no hit	no hit
RAB2A	-0.2076822	-0.1124195	0.5709976	0.7583336	no hit	no hit
ILF3	-0.3088510	-0.1062830	0.5719814	0.8452011	no hit	no hit
ERGIC3	-0.2366223	-0.3786691	0.5732864	0.3706778	no hit	no hit
TSPAN3	-0.1988471	-0.3616053	0.5750057	0.3127074	no hit	no hit
CTSC	-0.1696138	0.0799476	0.5753976	0.7910740	no hit	no hit
ECE1	0.2436509	0.3316790	0.5767782	0.4490837	no hit	no hit
RAB10	0.1196336	0.0514575	0.5799264	0.8111795	no hit	no hit
SLC1A4	0.1957858	0.2219732	0.5804725	0.5314052	no hit	no hit
DAD1	0.3187158	0.6055691	0.5823772	0.3013035	no hit	no hit
ERAP1	0.2364970	0.6005637	0.5824052	0.1719888	no hit	no hit
ERGIC1	-0.1197406	0.0770924	0.5872175	0.7260678	no hit	no hit
MVP	-0.3002642	-0.2576867	0.5889087	0.6424437	no hit	no hit
ITGB5	0.1654753	0.0670563	0.5889623	0.8260941	no hit	no hit
FEN1	-0.3557630	-0.5590130	0.5933270	0.4041246	no hit	no hit
ABCE1	-0.4342123	-0.5719330	0.5938391	0.4836823	no hit	no hit
RARS	0.2529848	0.4231013	0.5947519	0.3769824	no hit	no hit
EIF3L	-0.4397572	-0.8659140	0.5954088	0.3011011	no hit	no hit
RECQL	-0.3839392	-0.8720744	0.5962141	0.2361780	no hit	no hit
ADAM15	0.1665389	0.4820007	0.6013394	0.1409790	no hit	no hit
TMED4	-0.2026178	-0.1669862	0.6029584	0.6677787	no hit	no hit
RACK1	-0.3163594	-0.8285872	0.6055898	0.1853885	no hit	no hit
HNRNPM	-0.2284365	-0.1313169	0.6104499	0.7690945	no hit	no hit
VAMP8	0.2013502	-0.2019220	0.6123575	0.6113554	no hit	no hit
EIF3B	-0.3456909	-0.6229093	0.6132557	0.3662121	no hit	no hit
MOV10	-0.2701311	-0.6603730	0.6144185	0.2260206	no hit	no hit
ATP6V0D1	0.1265341	0.0733311	0.6150837	0.7702152	no hit	no hit
VAMP7	-0.1345636	-0.0231325	0.6183823	0.9315266	no hit	no hit
TMED1	-0.2071635	-0.1182927	0.6201655	0.7766722	no hit	no hit
SLC38A7	-0.1965712	0.1262036	0.6209824	0.7504144	no hit	no hit
NEU1	0.1858993	0.4126054	0.6236370	0.2822999	no hit	no hit
LMNA	-0.3391932	-0.1354718	0.6244000	0.8445276	no hit	no hit
SPTBN1	0.3289097	0.8697761	0.6251740	0.2050876	no hit	no hit
CTNNA1	0.2857709	-0.1691800	0.6273821	0.7733563	no hit	no hit
EIF3H	-0.3836413	-0.9723089	0.6368290	0.2391415	no hit	no hit
HEXB	-0.2378309	-0.1260650	0.6387268	0.8030471	no hit	no hit
GALNT7	-0.1505094	0.0871305	0.6409552	0.7867553	no hit	no hit
ATP1B3	0.2190781	0.1101010	0.6514213	0.8200051	no hit	no hit
ALDH7A1	0.2236469	0.4709680	0.6521379	0.3470851	no hit	no hit
EIF3C	-0.2961329	-0.7628475	0.6553519	0.2574795	no hit	no hit
TCP1	0.4514777	0.3813473	0.6560926	0.7065899	no hit	no hit
SMC2	-0.2794817	-0.8232297	0.6566057	0.1994572	no hit	no hit
HNRNPUL1	-0.1974225	-0.1817665	0.6611425	0.6864037	no hit	no hit
EIF3E	-0.2842945	-0.7451165	0.6633951	0.2611863	no hit	no hit
CCT5	0.4482578	0.2526310	0.6650111	0.8068653	no hit	no hit

gene_name	logFC_PA	logFC_PE	pvalue_PA	pvalue_PE	hit_annotation_PA	hit_annotation_PE
MYOF	0.1932061	0.1651339	0.6668746	0.7127568	no hit	no hit
SLC7A6	0.1513299	-0.0722096	0.6678963	0.8374706	no hit	no hit
SLC7A5	0.1709859	-0.1663057	0.6695683	0.6780564	no hit	no hit
HNRNPR	-0.1750734	-0.1816969	0.6715339	0.6599363	no hit	no hit
RAB3D	0.1302096	0.2047058	0.6736617	0.5094630	no hit	no hit
CSTB	-0.1945916	-0.4572256	0.6736634	0.3277294	no hit	no hit
DDB1	0.1141053	0.2921831	0.6738516	0.2876371	no hit	no hit
TMEM109	0.2182279	0.2585744	0.6739565	0.6184753	no hit	no hit
MPDU1 HBEBP2BPA	0.2067031	0.2904126	0.6740426	0.5555073	no hit	no hit
PKN2	0.2695960	0.3285979	0.6749463	0.6096717	no hit	no hit
VCP	0.2506833	0.5938006	0.6751043	0.3261464	no hit	no hit
EPHX1	0.1923847	0.4878827	0.6782723	0.2989744	no hit	no hit
POFUT1	0.1123747	0.5126925	0.6804018	0.0720001	no hit	no hit
RPS21	-0.1579725	-0.9200207	0.6815525	0.0256978	no hit	no hit
IGF2R	0.1628472	0.1507547	0.6816050	0.7039930	no hit	no hit
CCT6A	0.4234097	0.3213645	0.6831860	0.7565114	no hit	no hit
ALYREF	-0.2216727	0.0557840	0.6838348	0.9181977	no hit	no hit
LNPEP	-0.1679683	-0.1241197	0.6866621	0.7654046	no hit	no hit
SEC23IP	-0.3008969	-0.8502318	0.6891947	0.2656788	no hit	no hit
ABCB6	0.1280243	0.5408159	0.6910477	0.1049927	no hit	no hit
SDCBP	0.1579079	0.5806899	0.6944958	0.1592729	no hit	no hit
HNRNPD	-0.1530716	0.0555533	0.6949514	0.8866181	no hit	no hit
TMED9	-0.2031202	-0.1722856	0.6954228	0.7396826	no hit	no hit
HSP90AB1	-0.1497072	-0.0897142	0.7006019	0.8175263	no hit	no hit
DDR1	0.1085571	-0.0233097	0.7048318	0.9350488	no hit	no hit
RAB14	-0.1168015	-0.1611457	0.7085982	0.6067444	no hit	no hit
TMEM106B	0.1905441	0.3989278	0.7094183	0.4382704	no hit	no hit
CCT4	0.3877967	0.3081591	0.7116036	0.7687670	no hit	no hit
SCARB2	0.2273036	0.4324196	0.7119085	0.4845055	no hit	no hit
CCT3	0.3421406	0.2573196	0.7150574	0.7834786	no hit	no hit
FASN	-0.1526562	-0.2757642	0.7181876	0.5161753	no hit	no hit
SCPEP1	-0.1711656	-0.0589112	0.7251300	0.9035318	no hit	no hit
PARP1	0.2223683	0.1464677	0.7261308	0.8173600	no hit	no hit
HADHB	0.1485002	0.3449166	0.7287938	0.4240061	no hit	no hit
RTCB	-0.2222065	-0.5982079	0.7288995	0.3557466	no hit	no hit
NSUN2	-0.1779332	-0.6447477	0.7301176	0.2202538	no hit	no hit
CTSA	-0.1614620	-0.1374767	0.7307816	0.7694417	no hit	no hit
NCS1	0.1121921	0.2713215	0.7311936	0.4097841	no hit	no hit
ARL6IP5	0.1643239	0.2463498	0.7320364	0.6084416	no hit	no hit
GLA	0.1524022	0.3790152	0.7329649	0.4000791	no hit	no hit
ALDH9A1	-0.1314803	0.2161166	0.7359400	0.5803803	no hit	no hit
RAB9A	-0.0811041	0.0540906	0.7365420	0.8223089	no hit	no hit
SND1	-0.3123217	-0.4387089	0.7411713	0.6431635	no hit	no hit
RAB7A	0.0957545	0.2065882	0.7432851	0.4822033	no hit	no hit
AHNAK	0.1050165	0.0956885	0.7474240	0.7691359	no hit	no hit
GYS1	-0.1905551	-0.6397497	0.7494363	0.2904905	no hit	no hit
TFRC	-0.1011998	0.0034287	0.7522457	0.9914545	no hit	no hit
NAGLU	0.0951769	-0.0308454	0.7526414	0.9185460	no hit	no hit
ATP6V1A	0.0742893	-0.0399806	0.7530904	0.8654360	no hit	no hit
ATP2C1	-0.0894692	-0.1061876	0.7535843	0.7096200	no hit	no hit
DDR2	-0.0790369	-0.1574708	0.7537581	0.5336436	no hit	no hit
RRBP1	-0.1804930	0.0653534	0.7558633	0.9102602	no hit	no hit

gene_name	logFC_PA	logFC_PE	pvalue_PA	pvalue_PE	hit_annotation_PA	hit_annotation_PE
TMX1	-0.1233157	0.0220703	0.7594880	0.9562475	no hit	no hit
PROCR	0.1166713	0.3599981	0.7595767	0.3502955	no hit	no hit
SLC38A1	-0.1333432	-0.3693581	0.7596577	0.4008171	no hit	no hit
EIF3I	-0.1215991	-0.9098980	0.7605745	0.0324603	no hit	no hit
PSMB5	-0.0850333	-0.1225236	0.7613040	0.6620449	no hit	no hit
PSAP	-0.1355137	-0.0082476	0.7637644	0.9853880	no hit	no hit
PTBP1	-0.1697549	-0.6011508	0.7646098	0.2957882	no hit	no hit
MYH9	0.1865761	0.2804252	0.7655799	0.6545573	no hit	no hit
DNAJA1	-0.2204496	-0.5552552	0.7661762	0.4567880	no hit	no hit
EPRS	-0.1125805	-0.1252850	0.7684147	0.7432274	no hit	no hit
BANF1	-0.0760968	-0.4917480	0.7708271	0.0718836	no hit	no hit
PKM	-0.1189707	0.1021601	0.7719871	0.8034319	no hit	no hit
CD97	0.1270715	-0.0022931	0.7727485	0.9958372	no hit	no hit
TPP1	-0.1131493	0.1202320	0.7737645	0.7600598	no hit	no hit
FAM49B	0.1053502	-0.0407488	0.7764432	0.9124582	no hit	no hit
CPA4	0.1315341	0.3069382	0.7779513	0.5125877	no hit	no hit
AIMP1	0.0843026	0.2273129	0.7852047	0.4652897	no hit	no hit
TOMM40	0.1558069	0.3128903	0.7962343	0.6050823	no hit	no hit
ATPSL	0.1392492	0.5384218	0.7968649	0.3257173	no hit	no hit
YARS	0.0936667	0.0917299	0.7984965	0.8025687	no hit	no hit
HEXA	-0.1304777	0.0904322	0.7994882	0.8601895	no hit	no hit
LRP1	-0.0884887	-0.1882392	0.8024890	0.5957946	no hit	no hit
PSMA6	-0.0790482	-0.1002187	0.8025318	0.7513365	no hit	no hit
HFE	-0.0633784	-0.1349335	0.8126730	0.6148657	no hit	no hit
CSRP1	-0.1441540	0.3807524	0.8143225	0.5369149	no hit	no hit
ARL8B	-0.0789700	-0.1170163	0.8170548	0.7319887	no hit	no hit
SRP9	-0.0628013	-0.2270302	0.8244172	0.4263129	no hit	no hit
PDLIM1	0.0628402	0.3823953	0.8247736	0.1882691	no hit	no hit
SLC39A14	0.0772715	-0.1539015	0.8265446	0.6631376	no hit	no hit
PDCD4	-0.1259747	-0.4801519	0.8317181	0.4218920	no hit	no hit
PPT1	-0.0854106	0.0349463	0.8379196	0.9332663	no hit	no hit
CDC2 CDK1	-0.1187053	-0.3084831	0.8424946	0.6067294	no hit	no hit
CTSD	-0.0898063	-0.1605212	0.8463845	0.7294295	no hit	no hit
GBA	0.0825128	0.2852768	0.8464854	0.5056893	no hit	no hit
NSF	-0.1223320	-0.1084306	0.8513473	0.8680612	no hit	no hit
SLC7A1	-0.0636021	-0.3317820	0.8565324	0.3512966	no hit	no hit
VLDLR	-0.0737174	-0.3844171	0.8565649	0.3515650	no hit	no hit
PRPF19	0.0708285	0.1949323	0.8592001	0.6263926	no hit	no hit
ZDHHC20	0.0430560	-0.1573023	0.8599042	0.5212706	no hit	no hit
DHX9	-0.1075302	0.2282740	0.8607339	0.7099837	no hit	no hit
GALNT2	0.0812879	0.0380946	0.8675514	0.9376862	no hit	no hit
PPA2	0.0608126	0.2148074	0.8682336	0.5595905	no hit	no hit
RAB5C	0.0517004	0.1389822	0.8700332	0.6607945	no hit	no hit
KPNA2	0.0419851	0.0983180	0.8709110	0.7040141	no hit	no hit
SLC16A3	-0.0699334	-0.4148181	0.8714253	0.3429709	no hit	no hit
ACP2	0.0928626	0.3662572	0.8763927	0.5415403	no hit	no hit
HIST1H4A	-0.1222180	0.2442689	0.8797828	0.7626573	no hit	no hit
YIF1B	-0.0600393	-0.2527999	0.8836737	0.5398689	no hit	no hit
PRKDC	0.0878348	0.0620125	0.8876082	0.9205066	no hit	no hit
KHSRP	-0.0261144	-0.2753133	0.8918171	0.1629189	no hit	no hit
IARS	0.0727343	0.2864244	0.8929414	0.5974649	no hit	no hit
SLC3A2	0.0435545	-0.0473317	0.9004529	0.8918751	no hit	no hit

gene_name	logFC_PA	logFC_PE	pvalue_PA	pvalue_PE	hit_annotation_PA	hit_annotation_PE
HNRNPU	0.0680859	0.2218324	0.9049979	0.6979303	no hit	no hit
ILF2	-0.0524385	-0.1386280	0.9057428	0.7545349	no hit	no hit
SEC22B	-0.0333094	-0.0596189	0.9063033	0.8332149	no hit	no hit
CLIC1	-0.0262637	-0.4724710	0.9088678	0.0510675	no hit	no hit
CPD	-0.0400661	-0.2129421	0.9107310	0.5531499	no hit	no hit
DDX5	-0.0598607	0.3519765	0.9112142	0.5144844	no hit	no hit
NPC1	0.0517273	0.2383349	0.9151675	0.6246705	no hit	no hit
GLB1	0.0356149	0.2081011	0.9373261	0.6468527	no hit	no hit
SERINC1	0.0357022	0.1605051	0.9426638	0.7467786	no hit	no hit
PRSS56	-0.0237832	-0.1718653	0.9443177	0.6149892	no hit	no hit
COTL1	-0.0221659	-0.2204299	0.9488216	0.5255920	no hit	no hit
SRP14	-0.0416633	-0.0499319	0.9502728	0.9404222	no hit	no hit
NAPG	-0.0155178	-0.3614983	0.9519423	0.1714763	no hit	no hit
RAB4A	0.0141311	-0.1636162	0.9522990	0.4914075	no hit	no hit
ERP44	0.0170711	-0.0037553	0.9549588	0.9900864	no hit	no hit
IL6ST	0.0147408	-0.0802392	0.9589332	0.7794830	no hit	no hit
LAMP1	-0.0208422	0.2776255	0.9605424	0.5124250	no hit	no hit
EIF3J	-0.0234196	-0.5000801	0.9611731	0.3056907	no hit	no hit
HSP90AA1	-0.0190077	-0.1032756	0.9632116	0.8022820	no hit	no hit
SRP72	0.0201781	0.0322529	0.9688414	0.9502171	no hit	no hit
FSCN1	0.0184615	0.2082420	0.9713632	0.6862032	no hit	no hit
PRDX4	-0.0146193	0.4215892	0.9714058	0.3083293	no hit	no hit
STK26	-0.0033419	0.0810178	0.9840069	0.6281173	no hit	no hit
CD63	0.0088463	0.2716092	0.9888679	0.6691684	no hit	no hit
SPTAN1	0.0098815	0.5237709	0.9892468	0.4781006	no hit	no hit
LMAN1	-0.0089397	-0.0809709	0.9903722	0.9129827	no hit	no hit
DDX17	0.0016574	-0.1396869	0.9962328	0.6913271	no hit	no hit
GAPDH	0.0024854	-0.0249406	0.9968991	0.9688910	no hit	no hit
RRAS	0.0003442	0.3152153	0.9991908	0.3586577	no hit	no hit
HNRNPF	-0.0001318	-0.4538482	0.9998786	0.6018054	no hit	no hit

References

1. Zhang Y, Rozsa M, Liang Y, Bushey D, Wei Z, Zheng J, et al. Fast and sensitive GCaMP calcium indicators for imaging neural populations. *Nature*. 2023;615(7954):884-91.
2. Kell DB, Oliver SG. Here is the evidence, now what is the hypothesis? The complementary roles of inductive and hypothesis-driven science in the post-genomic era. *Bioessays*. 2004;26(1):99-105.
3. Succi S, Coveney PV. Big data: the end of the scientific method? *Philos Trans A Math Phys Eng Sci*. 2019;377(2142):20180145.
4. Tsien RY. Breeding and building molecules to spy on cells and tumors. *Keio J Med*. 2006;55(4):127-40.
5. Koide Y, Urano Y, Hanaoka K, Piao W, Kusakabe M, Saito N, et al. Development of NIR fluorescent dyes based on Si-rhodamine for in vivo imaging. *J Am Chem Soc*. 2012;134(11):5029-31.
6. Chai X, Cui X, Wang B, Yang F, Cai Y, Wu Q, et al. Near-Infrared Phosphorus-Substituted Rhodamine with Emission Wavelength above 700 nm for Bioimaging. *Chemistry*. 2015;21(47):16754-8.
7. Grimm JB, English BP, Chen J, Slaughter JP, Zhang Z, Revyakin A, et al. A general method to improve fluorophores for live-cell and single-molecule microscopy. *Nat Methods*. 2015;12(3):244-50, 3 p following 50.
8. Lincoln R, Bossi ML, Remmel M, D'Este E, Butkevich AN, Hell SW. A general design of caging-group-free photoactivatable fluorophores for live-cell nanoscopy. *Nat Chem*. 2022;14(9):1013-20.
9. Sakabe M, Asanuma D, Kamiya M, Iwatate RJ, Hanaoka K, Terai T, et al. Rational design of highly sensitive fluorescence probes for protease and glycosidase based on precisely controlled spirocyclization. *J Am Chem Soc*. 2013;135(1):409-14.
10. Grimm JB, Gruber TD, Ortiz G, Brown TA, Lavis LD. Virginia Orange: A Versatile, Red-Shifted Fluorescein Scaffold for Single- and Dual-Input Fluorogenic Probes. *Bioconjug Chem*. 2016;27(2):474-80.
11. Lavis LD. Teaching Old Dyes New Tricks: Biological Probes Built from Fluoresceins and Rhodamines. *Annu Rev Biochem*. 2017;86:825-43.
12. Paradiso AM, Tsien RY, Machen TE. Na⁺-H⁺ exchange in gastric glands as measured with a cytoplasmic-trapped, fluorescent pH indicator. *Proc Natl Acad Sci U S A*. 1984;81(23):7436-40.
13. Cohen LB, Salzberg BM. Optical measurement of membrane potential. *Rev Physiol Biochem Pharmacol*. 1978;83:35-88.
14. Grynkiewicz G, Poenie M, Tsien RY. A new generation of Ca²⁺ indicators with greatly improved fluorescence properties. *J Biol Chem*. 1985;260(6):3440-50.
15. Tsien RY. Fluorescent probes of cell signaling. *Annu Rev Neurosci*. 1989;12:227-53.
16. Tsien RY. New calcium indicators and buffers with high selectivity against magnesium and protons: design, synthesis, and properties of prototype structures. *Biochemistry*. 1980;19(11):2396-404.
17. Minta A, Kao JP, Tsien RY. Fluorescent indicators for cytosolic calcium based on rhodamine and fluorescein chromophores. *J Biol Chem*. 1989;264(14):8171-8.

18. Zhou X, Belavek KJ, Miller EW. Origins of Ca(2+) Imaging with Fluorescent Indicators. *Biochemistry*. 2021;60(46):3547-54.
19. Rehberg M, Lepier A, Solchenberger B, Osten P, Blum R. A new non-disruptive strategy to target calcium indicator dyes to the endoplasmic reticulum. *Cell Calcium*. 2008;44(4):386-99.
20. Liu Z, Lavis LD, Betzig E. Imaging live-cell dynamics and structure at the single-molecule level. *Mol Cell*. 2015;58(4):644-59.
21. Shimomura O, Johnson FH, Saiga Y. Extraction, purification and properties of aequorin, a bioluminescent protein from the luminous hydromedusa, *Aequorea*. *J Cell Comp Physiol*. 1962;59:223-39.
22. Chalfie M, Tu Y, Euskirchen G, Ward WW, Prasher DC. Green fluorescent protein as a marker for gene expression. *Science*. 1994;263(5148):802-5.
23. Heim R, Cubitt AB, Tsien RY. Improved green fluorescence. *Nature*. 1995;373(6516):663-4.
24. Heim R, Prasher DC, Tsien RY. Wavelength mutations and posttranslational autoxidation of green fluorescent protein. *Proc Natl Acad Sci U S A*. 1994;91(26):12501-4.
25. Ormo M, Cubitt AB, Kallio K, Gross LA, Tsien RY, Remington SJ. Crystal structure of the *Aequorea victoria* green fluorescent protein. *Science*. 1996;273(5280):1392-5.
26. Förster T. Zwischenmolekulare energiewanderung und fluoreszenz. *Annalen der physik*. 1948;437(1-2):55-75.
27. Rodriguez EA, Campbell RE, Lin JY, Lin MZ, Miyawaki A, Palmer AE, et al. The Growing and Glowing Toolbox of Fluorescent and Photoactive Proteins. *Trends Biochem Sci*. 2017;42(2):111-29.
28. Rodriguez EA, Tran GN, Gross LA, Crisp JL, Shu X, Lin JY, et al. A far-red fluorescent protein evolved from a cyanobacterial phycobiliprotein. *Nat Methods*. 2016;13(9):763-9.
29. Stryer L, Haugland RP. Energy transfer: a spectroscopic ruler. *Proc Natl Acad Sci U S A*. 1967;58(2):719-26.
30. Bolbat A, Schultz C. Recent developments of genetically encoded optical sensors for cell biology. *Biol Cell*. 2017;109(1):1-23.
31. Depry C, Allen MD, Zhang J. Visualization of PKA activity in plasma membrane microdomains. *Mol Biosyst*. 2011;7(1):52-8.
32. Ponsioen B, Zhao J, Riedl J, Zwartkuis F, van der Krogt G, Zaccolo M, et al. Detecting cAMP-induced Epac activation by fluorescence resonance energy transfer: Epac as a novel cAMP indicator. *EMBO Rep*. 2004;5(12):1176-80.
33. Lin CW, Jao CY, Ting AY. Genetically encoded fluorescent reporters of histone methylation in living cells. *J Am Chem Soc*. 2004;126(19):5982-3.
34. Carrillo LD, Froemming JA, Mahal LK. Targeted in vivo O-GlcNAc sensors reveal discrete compartment-specific dynamics during signal transduction. *J Biol Chem*. 2011;286(8):6650-8.
35. Peng Q, Lu S, Shi Y, Pan Y, Limsakul P, Chernov AV, et al. Coordinated histone modifications and chromatin reorganization in a single cell revealed by FRET biosensors. *Proc Natl Acad Sci U S A*. 2018;115(50):E11681-E90.
36. Komatsu N, Aoki K, Yamada M, Yukinaga H, Fujita Y, Kamioka Y, et al. Development of an optimized backbone of FRET biosensors for kinases and GTPases. *Mol Biol Cell*. 2011;22(23):4647-56.

37. Piljic A, de Diego I, Wilmanns M, Schultz C. Rapid development of genetically encoded FRET reporters. *ACS Chem Biol.* 2011;6(7):685-91.
38. Miyawaki A, Niino Y. Molecular spies for bioimaging--fluorescent protein-based probes. *Mol Cell.* 2015;58(4):632-43.
39. Zhang J, Ma Y, Taylor SS, Tsien RY. Genetically encoded reporters of protein kinase A activity reveal impact of substrate tethering. *Proc Natl Acad Sci U S A.* 2001;98(26):14997-5002.
40. Herbst KJ, Allen MD, Zhang J. Luminescent kinase activity biosensors based on a versatile bimolecular switch. *J Am Chem Soc.* 2011;133(15):5676-9.
41. Baird GS, Zacharias DA, Tsien RY. Circular permutation and receptor insertion within green fluorescent proteins. *Proc Natl Acad Sci U S A.* 1999;96(20):11241-6.
42. Nagai T, Sawano A, Park ES, Miyawaki A. Circularly permuted green fluorescent proteins engineered to sense Ca²⁺. *Proc Natl Acad Sci U S A.* 2001;98(6):3197-202.
43. Nakai J, Ohkura M, Imoto K. A high signal-to-noise Ca(2+) probe composed of a single green fluorescent protein. *Nat Biotechnol.* 2001;19(2):137-41.
44. Hilger D, Masureel M, Kobilka BK. Structure and dynamics of GPCR signaling complexes. *Nat Struct Mol Biol.* 2018;25(1):4-12.
45. Rasmussen SG, DeVree BT, Zou Y, Kruse AC, Chung KY, Kobilka TS, et al. Crystal structure of the beta2 adrenergic receptor-Gs protein complex. *Nature.* 2011;477(7366):549-55.
46. Patriarchi T, Cho JR, Merten K, Howe MW, Marley A, Xiong WH, et al. Ultrafast neuronal imaging of dopamine dynamics with designed genetically encoded sensors. *Science.* 2018;360(6396).
47. Sun F, Zhou J, Dai B, Qian T, Zeng J, Li X, et al. Next-generation GRAB sensors for monitoring dopaminergic activity in vivo. *Nat Methods.* 2020;17(11):1156-66.
48. Feng J, Zhang C, Lischinsky JE, Jing M, Zhou J, Wang H, et al. A Genetically Encoded Fluorescent Sensor for Rapid and Specific In Vivo Detection of Norepinephrine. *Neuron.* 2019;102(4):745-61 e8.
49. Wan J, Peng W, Li X, Qian T, Song K, Zeng J, et al. A genetically encoded sensor for measuring serotonin dynamics. *Nat Neurosci.* 2021;24(5):746-52.
50. Jing M, Li Y, Zeng J, Huang P, Skirzewski M, Kljakic O, et al. An optimized acetylcholine sensor for monitoring in vivo cholinergic activity. *Nat Methods.* 2020;17(11):1139-46.
51. Nasu Y, Shen Y, Kramer L, Campbell RE. Structure- and mechanism-guided design of single fluorescent protein-based biosensors. *Nat Chem Biol.* 2021;17(5):509-18.
52. Ghosh I, Hamilton AD, Regan L. Antiparallel leucine zipper-directed protein reassembly: application to the green fluorescent protein. *Journal of the American Chemical Society.* 2000;122(23):5658-9.
53. Shyu YJ, Suarez CD, Hu CD. Visualization of ternary complexes in living cells by using a BiFC-based FRET assay. *Nat Protoc.* 2008;3(11):1693-702.
54. Kerppola TK. Visualization of molecular interactions using bimolecular fluorescence complementation analysis: characteristics of protein fragment complementation. *Chem Soc Rev.* 2009;38(10):2876-86.
55. Plamont MA, Billon-Denis E, Maurin S, Gauron C, Pimenta FM, Specht CG, et al. Small fluorescence-activating and absorption-shifting tag for tunable protein imaging in vivo. *Proc Natl Acad Sci U S A.* 2016;113(3):497-502.

56. Tebo AG, Gautier A. A split fluorescent reporter with rapid and reversible complementation. *Nat Commun.* 2019;10(1):2822.
57. Keppler A, Gendreizig S, Gronemeyer T, Pick H, Vogel H, Johnsson K. A general method for the covalent labeling of fusion proteins with small molecules in vivo. *Nat Biotechnol.* 2003;21(1):86-9.
58. Keppler A, Pick H, Arrivoli C, Vogel H, Johnsson K. Labeling of fusion proteins with synthetic fluorophores in live cells. *Proc Natl Acad Sci U S A.* 2004;101(27):9955-9.
59. Yan Q, Bruchez MP. Advances in chemical labeling of proteins in living cells. *Cell Tissue Res.* 2015;360(1):179-94.
60. Gautier A, Juillerat A, Heinis C, Correa IR, Jr., Kindermann M, Beaufils F, et al. An engineered protein tag for multiprotein labeling in living cells. *Chem Biol.* 2008;15(2):128-36.
61. Los GV, Encell LP, McDougall MG, Hartzell DD, Karassina N, Zimprich C, et al. HaloTag: a novel protein labeling technology for cell imaging and protein analysis. *ACS Chem Biol.* 2008;3(6):373-82.
62. Shaner NC, Steinbach PA, Tsien RY. A guide to choosing fluorescent proteins. *Nat Methods.* 2005;2(12):905-9.
63. Ai HW, Hazelwood KL, Davidson MW, Campbell RE. Fluorescent protein FRET pairs for ratiometric imaging of dual biosensors. *Nat Methods.* 2008;5(5):401-3.
64. Piljic A, Schultz C. Simultaneous recording of multiple cellular events by FRET. *ACS Chem Biol.* 2008;3(3):156-60.
65. Brun MA, Tan KT, Nakata E, Hinner MJ, Johnsson K. Semisynthetic fluorescent sensor proteins based on self-labeling protein tags. *J Am Chem Soc.* 2009;131(16):5873-84.
66. Brun MA, Griss R, Reymond L, Tan KT, Piguet J, Peters RJ, et al. Semisynthesis of fluorescent metabolite sensors on cell surfaces. *J Am Chem Soc.* 2011;133(40):16235-42.
67. Masharina A, Reymond L, Maurel D, Umezawa K, Johnsson K. A fluorescent sensor for GABA and synthetic GABA(B) receptor ligands. *J Am Chem Soc.* 2012;134(46):19026-34.
68. Schena A, Johnsson K. Sensing acetylcholine and anticholinesterase compounds. *Angew Chem Int Ed Engl.* 2014;53(5):1302-5.
69. Sallin O, Reymond L, Gondrand C, Raith F, Koch B, Johnsson K. Semisynthetic biosensors for mapping cellular concentrations of nicotinamide adenine dinucleotides. *Elife.* 2018;7.
70. Wilhelm J, Kuhn S, Tarnawski M, Gotthard G, Tunnermann J, Tanzer T, et al. Kinetic and Structural Characterization of the Self-Labeling Protein Tags HaloTag7, SNAP-tag, and CLIP-tag. *Biochemistry.* 2021;60(33):2560-75.
71. Frei MS, Tarnawski M, Roberti MJ, Koch B, Hiblot J, Johnsson K. Engineered HaloTag variants for fluorescence lifetime multiplexing. *Nat Methods.* 2022;19(1):65-70.
72. Ohana RF, Encell LP, Zhao K, Simpson D, Slater MR, Urh M, et al. HaloTag7: a genetically engineered tag that enhances bacterial expression of soluble proteins and improves protein purification. *Protein Expr Purif.* 2009;68(1):110-20.
73. Murakoshi H, Shibata ACE, Nakahata Y, Nabekura J. A dark green fluorescent protein as an acceptor for measurement of Forster resonance energy transfer. *Sci Rep.* 2015;5:15334.

74. Hellweg L, Edenhofer A, Barck L, Huppertz MC, Frei MS, Tarnawski M, et al. A general method for the development of multicolor biosensors with large dynamic ranges. *Nat Chem Biol.* 2023;19(9):1147-57.
75. Grimm JB, Muthusamy AK, Liang Y, Brown TA, Lemon WC, Patel R, et al. A general method to fine-tune fluorophores for live-cell and in vivo imaging. *Nat Methods.* 2017;14(10):987-94.
76. Deo C, Abdelfattah AS, Bhargava HK, Berro AJ, Falco N, Farrants H, et al. The HaloTag as a general scaffold for far-red tunable chemigenetic indicators. *Nat Chem Biol.* 2021;17(6):718-23.
77. Conti E, Franks NP, Brick P. Crystal structure of firefly luciferase throws light on a superfamily of adenylate-forming enzymes. *Structure.* 1996;4(3):287-98.
78. Dacres H, Wang J, Dumancic MM, Trowell SC. Experimental determination of the Forster distance for two commonly used bioluminescent resonance energy transfer pairs. *Anal Chem.* 2010;82(1):432-5.
79. Perroy J, Pontier S, Charest PG, Aubry M, Bouvier M. Real-time monitoring of ubiquitination in living cells by BRET. *Nat Methods.* 2004;1(3):203-8.
80. Jiang LI, Collins J, Davis R, Lin KM, DeCamp D, Roach T, et al. Use of a cAMP BRET sensor to characterize a novel regulation of cAMP by the sphingosine 1-phosphate/G13 pathway. *J Biol Chem.* 2007;282(14):10576-84.
81. Suzuki K, Nagai T. Recent progress in expanding the chemiluminescent toolbox for bioimaging. *Curr Opin Biotechnol.* 2017;48:135-41.
82. Yao Z, Zhang BS, Prescher JA. Advances in bioluminescence imaging: new probes from old recipes. *Curr Opin Chem Biol.* 2018;45:148-56.
83. Yang J, Cumberbatch D, Centanni S, Shi SQ, Winder D, Webb D, et al. Coupling optogenetic stimulation with NanoLuc-based luminescence (BRET) Ca(++) sensing. *Nat Commun.* 2016;7:13268.
84. Yoshida T, Kakizuka A, Imamura H. BTeam, a Novel BRET-based Biosensor for the Accurate Quantification of ATP Concentration within Living Cells. *Sci Rep.* 2016;6:39618.
85. Inagaki S, Tsutsui H, Suzuki K, Agetsuma M, Arai Y, Jinno Y, et al. Genetically encoded bioluminescent voltage indicator for multi-purpose use in wide range of bioimaging. *Sci Rep.* 2017;7:42398.
86. Komatsu N, Terai K, Imanishi A, Kamioka Y, Sumiyama K, Jin T, et al. A platform of BRET-FRET hybrid biosensors for optogenetics, chemical screening, and in vivo imaging. *Sci Rep.* 2018;8(1):8984.
87. Schreier B, Stumpp C, Wiesner S, Hocker B. Computational design of ligand binding is not a solved problem. *Proc Natl Acad Sci U S A.* 2009;106(44):18491-6.
88. Tinberg CE, Khare SD, Dou J, Doyle L, Nelson JW, Schena A, et al. Computational design of ligand-binding proteins with high affinity and selectivity. *Nature.* 2013;501(7466):212-6.
89. Polizzi NF, DeGrado WF. A defined structural unit enables de novo design of small-molecule-binding proteins. *Science.* 2020;369(6508):1227-33.
90. Quijano-Rubio A, Yeh HW, Park J, Lee H, Langan RA, Boyken SE, et al. De novo design of modular and tunable protein biosensors. *Nature.* 2021;591(7850):482-7.
91. Zhang JZ, Nguyen WH, Greenwood N, Rose JC, Ong SE, Maly DJ, et al. Computationally designed sensors detect endogenous Ras activity and signaling effectors at subcellular resolution. *Nat Biotechnol.* 2024.

92. Huisgen R. Kinetics and mechanism of 1, 3-dipolar cycloadditions. *Angewandte Chemie International Edition in English*. 1963;2(11):633-45.
93. Rostovtsev VV, Green LG, Fokin VV, Sharpless KB. A stepwise huisgen cycloaddition process: copper(I)-catalyzed regioselective "ligation" of azides and terminal alkynes. *Angew Chem Int Ed Engl*. 2002;41(14):2596-9.
94. Sletten EM, Bertozzi CR. Bioorthogonal chemistry: fishing for selectivity in a sea of functionality. *Angew Chem Int Ed Engl*. 2009;48(38):6974-98.
95. Wang Q, Chan TR, Hilgraf R, Fokin VV, Sharpless KB, Finn MG. Bioconjugation by copper(I)-catalyzed azide-alkyne [3 + 2] cycloaddition. *J Am Chem Soc*. 2003;125(11):3192-3.
96. Patel PL, Rana NK, Patel MR, Kozuch SD, Sabatino D. Nucleic Acid Bioconjugates in Cancer Detection and Therapy. *ChemMedChem*. 2016;11(3):252-69.
97. Hsu TL, Hanson SR, Kishikawa K, Wang SK, Sawa M, Wong CH. Alkynyl sugar analogs for the labeling and visualization of glycoconjugates in cells. *Proc Natl Acad Sci U S A*. 2007;104(8):2614-9.
98. Agard NJ, Prescher JA, Bertozzi CR. A strain-promoted [3 + 2] azide-alkyne cycloaddition for covalent modification of biomolecules in living systems. *J Am Chem Soc*. 2004;126(46):15046-7.
99. Blackman ML, Royzen M, Fox JM. Tetrazine ligation: fast bioconjugation based on inverse-electron-demand Diels-Alder reactivity. *J Am Chem Soc*. 2008;130(41):13518-9.
100. Devaraj NK, Thurber GM, Keliher EJ, Marinelli B, Weissleder R. Reactive polymer enables efficient in vivo bioorthogonal chemistry. *Proc Natl Acad Sci U S A*. 2012;109(13):4762-7.
101. Rossin R, Verkerk PR, van den Bosch SM, Vulderson RC, Verel I, Lub J, et al. In vivo chemistry for pretargeted tumor imaging in live mice. *Angew Chem Int Ed Engl*. 2010;49(19):3375-8.
102. Selvaraj R, Fox JM. trans-Cyclooctene--a stable, voracious dienophile for bioorthogonal labeling. *Curr Opin Chem Biol*. 2013;17(5):753-60.
103. Beliu G, Kurz AJ, Kuhlemann AC, Behringer-Pliess L, Meub M, Wolf N, et al. Bioorthogonal labeling with tetrazine-dyes for super-resolution microscopy. *Commun Biol*. 2019;2:261.
104. Patterson DM, Nazarova LA, Xie B, Kamber DN, Prescher JA. Functionalized cyclopropenes as bioorthogonal chemical reporters. *J Am Chem Soc*. 2012;134(45):18638-43.
105. Mattheisen JM, Limberakis C, Ruggeri RB, Dowling MS, Am Ende CW, Ceraudo E, et al. Bioorthogonal Tethering Enhances Drug Fragment Affinity for G Protein-Coupled Receptors in Live Cells. *J Am Chem Soc*. 2023;145(20):11173-84.
106. Klan P, Solomek T, Bochet CG, Blanc A, Givens R, Rubina M, et al. Photoremovable protecting groups in chemistry and biology: reaction mechanisms and efficacy. *Chem Rev*. 2013;113(1):119-91.
107. Givens RS, Matuszewski B, Athey PS, Stoner MR. Photochemistry of phosphate esters: an efficient method for the generation of electrophiles. *Journal of the American Chemical Society*. 1990;112(16):6016-21.
108. Amatrudo JM, Olson JP, Lur G, Chiu CQ, Higley MJ, Ellis-Davies GC. Wavelength-selective one- and two-photon uncaging of GABA. *ACS Chem Neurosci*. 2014;5(1):64-70.

109. Kobauri P, Dekker FJ, Szymanski W, Feringa BL. Rational Design in Photopharmacology with Molecular Photoswitches. *Angew Chem Int Ed Engl.* 2023;62(30):e202300681.
110. Broichhagen J, Frank JA, Trauner D. A roadmap to success in photopharmacology. *Acc Chem Res.* 2015;48(7):1947-60.
111. Schoenberger M, Damijonaitis A, Zhang Z, Nagel D, Trauner D. Development of a new photochromic ion channel blocker via azologization of fomocaine. *ACS Chem Neurosci.* 2014;5(7):514-8.
112. Beharry AA, Woolley GA. Azobenzene photoswitches for biomolecules. *Chem Soc Rev.* 2011;40(8):4422-37.
113. Frank JA, Moroni M, Moshourab R, Sumser M, Lewin GR, Trauner D. Photoswitchable fatty acids enable optical control of TRPV1. *Nat Commun.* 2015;6:7118.
114. Frank JA, Yushchenko DA, Hodson DJ, Lipstein N, Nagpal J, Rutter GA, et al. Photoswitchable diacylglycerols enable optical control of protein kinase C. *Nat Chem Biol.* 2016;12(9):755-62.
115. Chakrabarti P, Khorana G. A new approach to the study of phospholipid-protein interactions in biological membranes. Synthesis of fatty acids and phospholipids containing photosensitive groups. *Biochemistry.* 1975;14(23):5021-33.
116. Xia Y, Peng L. Photoactivatable lipid probes for studying biomembranes by photoaffinity labeling. *Chem Rev.* 2013;113(10):7880-929.
117. Blencowe A, Hayes W. Development and application of diazirines in biological and synthetic macromolecular systems. *Soft Matter.* 2005;1(3):178-205.
118. West AV, Muncipinto G, Wu HY, Huang AC, Labenski MT, Jones LH, et al. Labeling Preferences of Diazirines with Protein Biomolecules. *J Am Chem Soc.* 2021;143(17):6691-700.
119. Schultz C, Farley SE, Tafesse FG. "Flash & Click": Multifunctionalized Lipid Derivatives as Tools To Study Viral Infections. *J Am Chem Soc.* 2022;144(31):13987-95.
120. Gubbens J, Ruijter E, de Fays LE, Damen JM, de Kruijff B, Slijper M, et al. Photocrosslinking and click chemistry enable the specific detection of proteins interacting with phospholipids at the membrane interface. *Chem Biol.* 2009;16(1):3-14.
121. Niphakis MJ, Lum KM, Cognetta AB, 3rd, Correia BE, Ichu TA, Olucha J, et al. A Global Map of Lipid-Binding Proteins and Their Ligandability in Cells. *Cell.* 2015;161(7):1668-80.
122. Muir TW. Semisynthesis of proteins by expressed protein ligation. *Annu Rev Biochem.* 2003;72:249-89.
123. Hecht SM, Alford BL, Kuroda Y, Kitano S. "Chemical aminoacylation" of tRNA's. *J Biol Chem.* 1978;253(13):4517-20.
124. Link AJ, Tirrell DA. Cell surface labeling of Escherichia coli via copper(I)-catalyzed [3+2] cycloaddition. *J Am Chem Soc.* 2003;125(37):11164-5.
125. Liu DR, Schultz PG. Progress toward the evolution of an organism with an expanded genetic code. *Proc Natl Acad Sci U S A.* 1999;96(9):4780-5.
126. Santoro SW, Wang L, Herberich B, King DS, Schultz PG. An efficient system for the evolution of aminoacyl-tRNA synthetase specificity. *Nat Biotechnol.* 2002;20(10):1044-8.
127. Liu CC, Schultz PG. Adding new chemistries to the genetic code. *Annu Rev Biochem.* 2010;79:413-44.

128. Saks ME, Sampson JR, Nowak MW, Kearney PC, Du F, Abelson JN, et al. An engineered Tetrahymena tRNAGln for in vivo incorporation of unnatural amino acids into proteins by nonsense suppression. *J Biol Chem.* 1996;271(38):23169-75.
129. Davis L, Chin JW. Designer proteins: applications of genetic code expansion in cell biology. *Nat Rev Mol Cell Biol.* 2012;13(3):168-82.
130. Zhang M, Lin S, Song X, Liu J, Fu Y, Ge X, et al. A genetically incorporated crosslinker reveals chaperone cooperation in acid resistance. *Nat Chem Biol.* 2011;7(10):671-7.
131. Hoffmann JE, Dziuba D, Stein F, Schultz C. A Bifunctional Noncanonical Amino Acid: Synthesis, Expression, and Residue-Specific Proteome-wide Incorporation. *Biochemistry.* 2018;57(31):4747-52.
132. Lemke EA, Summerer D, Geierstanger BH, Brittain SM, Schultz PG. Control of protein phosphorylation with a genetically encoded photocaged amino acid. *Nat Chem Biol.* 2007;3(12):769-72.
133. Gautier A, Deiters A, Chin JW. Light-activated kinases enable temporal dissection of signaling networks in living cells. *J Am Chem Soc.* 2011;133(7):2124-7.
134. Nikić I, Plass T, Schraidt O, Szymanski J, Briggs JA, Schultz C, et al. Minimal tags for rapid dual-color live-cell labeling and super-resolution microscopy. *Angew Chem Int Ed Engl.* 2014;53(8):2245-9.
135. Sauer M, Heilemann M. Single-Molecule Localization Microscopy in Eukaryotes. *Chem Rev.* 2017;117(11):7478-509.
136. Schmied WH, Elsasser SJ, Uttamapinant C, Chin JW. Efficient multisite unnatural amino acid incorporation in mammalian cells via optimized pyrrolysyl tRNA synthetase/tRNA expression and engineered eRF1. *J Am Chem Soc.* 2014;136(44):15577-83.
137. Reinkemeier CD, Girona GE, Lemke EA. Designer membraneless organelles enable codon reassignment of selected mRNAs in eukaryotes. *Science.* 2019;363(6434).
138. Cohen MS, Chang P. Insights into the biogenesis, function, and regulation of ADP-ribosylation. *Nat Chem Biol.* 2018;14(3):236-43.
139. Chang P, Jacobson MK, Mitchison TJ. Poly(ADP-ribose) is required for spindle assembly and structure. *Nature.* 2004;432(7017):645-9.
140. DaRosa PA, Wang Z, Jiang X, Pruneda JN, Cong F, Klevit RE, et al. Allosteric activation of the RNF146 ubiquitin ligase by a poly(ADP-ribosylation) signal. *Nature.* 2015;517(7533):223-6.
141. Barkauskaite E, Jankevicius G, Ahel I. Structures and Mechanisms of Enzymes Employed in the Synthesis and Degradation of PARP-Dependent Protein ADP-Ribosylation. *Mol Cell.* 2015;58(6):935-46.
142. Hottiger MO, Hassa PO, Luscher B, Schuler H, Koch-Nolte F. Toward a unified nomenclature for mammalian ADP-ribosyltransferases. *Trends Biochem Sci.* 2010;35(4):208-19.
143. Bock FJ, Chang P. New directions in poly(ADP-ribose) polymerase biology. *FEBS J.* 2016;283(22):4017-31.
144. Gibson BA, Kraus WL. New insights into the molecular and cellular functions of poly(ADP-ribose) and PARPs. *Nat Rev Mol Cell Biol.* 2012;13(7):411-24.
145. El-Khamisy SF, Masutani M, Suzuki H, Caldecott KW. A requirement for PARP-1 for the assembly or stability of XRCC1 nuclear foci at sites of oxidative DNA damage. *Nucleic Acids Res.* 2003;31(19):5526-33.

146. Langelier MF, Planck JL, Roy S, Pascal JM. Crystal structures of poly(ADP-ribose) polymerase-1 (PARP-1) zinc fingers bound to DNA: structural and functional insights into DNA-dependent PARP-1 activity. *J Biol Chem.* 2011;286(12):10690-701.
147. Min W, Bruhn C, Grigaravicius P, Zhou ZW, Li F, Kruger A, et al. Poly(ADP-ribose) binding to Chk1 at stalled replication forks is required for S-phase checkpoint activation. *Nat Commun.* 2013;4:2993.
148. Hanzlikova H, Kalasova I, Demin AA, Pennicott LE, Cihlarova Z, Caldecott KW. The Importance of Poly(ADP-Ribose) Polymerase as a Sensor of Unligated Okazaki Fragments during DNA Replication. *Mol Cell.* 2018;71(2):319-31 e3.
149. Lonskaya I, Potaman VN, Shlyakhtenko LS, Oussatcheva EA, Lyubchenko YL, Soldatenkov VA. Regulation of poly(ADP-ribose) polymerase-1 by DNA structure-specific binding. *J Biol Chem.* 2005;280(17):17076-83.
150. Koczor CA, Saville KM, Andrews JF, Clark J, Fang Q, Li J, et al. Temporal dynamics of base excision/single-strand break repair protein complex assembly/disassembly are modulated by the PARP/NAD(+)/SIRT6 axis. *Cell Rep.* 2021;37(5):109917.
151. Ray Chaudhuri A, Nussenzweig A. The multifaceted roles of PARP1 in DNA repair and chromatin remodelling. *Nat Rev Mol Cell Biol.* 2017;18(10):610-21.
152. Genoix MM, Gagne JP, Yasuhara T, Jackson J, Saxena S, Langelier MF, et al. CARM1 regulates replication fork speed and stress response by stimulating PARP1. *Mol Cell.* 2021;81(4):784-800 e8.
153. Houl JH, Ye Z, Brosey CA, Balapiti-Modarage LPF, Namjoshi S, Bacolla A, et al. Selective small molecule PARG inhibitor causes replication fork stalling and cancer cell death. *Nat Commun.* 2019;10(1):5654.
154. Bryant HE, Schultz N, Thomas HD, Parker KM, Flower D, Lopez E, et al. Specific killing of BRCA2-deficient tumours with inhibitors of poly(ADP-ribose) polymerase. *Nature.* 2005;434(7035):913-7.
155. Farmer H, McCabe N, Lord CJ, Tutt AN, Johnson DA, Richardson TB, et al. Targeting the DNA repair defect in BRCA mutant cells as a therapeutic strategy. *Nature.* 2005;434(7035):917-21.
156. Ruf A, Rolli V, de Murcia G, Schulz GE. The mechanism of the elongation and branching reaction of poly(ADP-ribose) polymerase as derived from crystal structures and mutagenesis. *J Mol Biol.* 1998;278(1):57-65.
157. Tao Z, Gao P, Liu HW. Identification of the ADP-ribosylation sites in the PARP-1 automodification domain: analysis and implications. *J Am Chem Soc.* 2009;131(40):14258-60.
158. Li P, Zhen Y, Yu Y. Site-specific analysis of the Asp- and Glu-ADP-ribosylated proteome by quantitative mass spectrometry. *Methods Enzymol.* 2019;626:301-21.
159. Zhang Y, Wang J, Ding M, Yu Y. Site-specific characterization of the Asp- and Glu-ADP-ribosylated proteome. *Nat Methods.* 2013;10(10):981-4.
160. Leidecker O, Bonfiglio JJ, Colby T, Zhang Q, Atanassov I, Zaja R, et al. Serine is a new target residue for endogenous ADP-ribosylation on histones. *Nat Chem Biol.* 2016;12(12):998-1000.
161. Bonfiglio JJ, Fontana P, Zhang Q, Colby T, Gibbs-Seymour I, Atanassov I, et al. Serine ADP-Ribosylation Depends on HPF1. *Mol Cell.* 2017;65(5):932-40 e6.

162. Suskiewicz MJ, Zobel F, Ogden TEH, Fontana P, Ariza A, Yang JC, et al. HPF1 completes the PARP active site for DNA damage-induced ADP-ribosylation. *Nature*. 2020;579(7800):598-602.
163. Hendriks IA, Buch-Larsen SC, Prokhorova E, Elsborg JD, Rebak A, Zhu K, et al. The regulatory landscape of the human HPF1- and ARH3-dependent ADP-ribosylome. *Nat Commun*. 2021;12(1):5893.
164. Ray Chaudhuri A, Callen E, Ding X, Gogola E, Duarte AA, Lee JE, et al. Replication fork stability confers chemoresistance in BRCA-deficient cells. *Nature*. 2016;535(7612):382-7.
165. Chen Q, Kassab MA, Dantzer F, Yu X. PARP2 mediates branched poly ADP-ribosylation in response to DNA damage. *Nat Commun*. 2018;9(1):3233.
166. Fontana P, Bonfiglio JJ, Palazzo L, Bartlett E, Matic I, Ahel I. Serine ADP-ribosylation reversal by the hydrolase ARH3. *Elife*. 2017;6.
167. Martello R, Leutert M, Jungmichel S, Bilan V, Larsen SC, Young C, et al. Proteome-wide identification of the endogenous ADP-ribosylome of mammalian cells and tissue. *Nat Commun*. 2016;7:12917.
168. Bonfiglio JJ, Leidecker O, Dauben H, Longarini EJ, Colby T, San Segundo-Acosta P, et al. An HPF1/PARP1-Based Chemical Biology Strategy for Exploring ADP-Ribosylation. *Cell*. 2020;183(4):1086-102 e23.
169. Gibson BA, Conrad LB, Huang D, Kraus WL. Generation and Characterization of Recombinant Antibody-like ADP-Ribose Binding Proteins. *Biochemistry*. 2017;56(48):6305-16.
170. Daniels CM, Ong SE, Leung AK. The Promise of Proteomics for the Study of ADP-Ribosylation. *Mol Cell*. 2015;58(6):911-24.
171. Longarini EJ, Dauben H, Locatelli C, Wondisford AR, Smith R, Muench C, et al. Modular antibodies reveal DNA damage-induced mono-ADP-ribosylation as a second wave of PARP1 signaling. *Mol Cell*. 2023;83(10):1743-60 e11.
172. Challa S, Ryu KW, Whitaker AL, Abshier JC, Camacho CV, Kraus WL. Development and characterization of new tools for detecting poly(ADP-ribose) in vitro and in vivo. *Elife*. 2022;11.
173. Weis WI, Kobilka BK. The Molecular Basis of G Protein-Coupled Receptor Activation. *Annu Rev Biochem*. 2018;87:897-919.
174. Lagerstrom MC, Schioth HB. Structural diversity of G protein-coupled receptors and significance for drug discovery. *Nat Rev Drug Discov*. 2008;7(4):339-57.
175. Fredriksson R, Lagerstrom MC, Lundin LG, Schioth HB. The G-protein-coupled receptors in the human genome form five main families. Phylogenetic analysis, paralogon groups, and fingerprints. *Mol Pharmacol*. 2003;63(6):1256-72.
176. Wootten D, Christopoulos A, Marti-Solano M, Babu MM, Sexton PM. Mechanisms of signalling and biased agonism in G protein-coupled receptors. *Nat Rev Mol Cell Biol*. 2018;19(10):638-53.
177. Gurevich VV, Gurevich EV. Biased GPCR signaling: Possible mechanisms and inherent limitations. *Pharmacol Ther*. 2020;211:107540.
178. Lazar AM, Irannejad R, Baldwin TA, Sundaram AB, Gutkind JS, Inoue A, et al. G protein-regulated endocytic trafficking of adenylyl cyclase type 9. *Elife*. 2020;9.
179. Stoeber M, Jullie D, Lobingier BT, Laeremans T, Steyaert J, Schiller PW, et al. A Genetically Encoded Biosensor Reveals Location Bias of Opioid Drug Action. *Neuron*. 2018;98(5):963-76 e5.

180. Lobingier BT, von Zastrow M. When trafficking and signaling mix: How subcellular location shapes G protein-coupled receptor activation of heterotrimeric G proteins. *Traffic*. 2019;20(2):130-6.
181. Puri NM, Romano GR, Lin TY, Mai QN, Irannejad R. The organic cation transporter 2 regulates dopamine D1 receptor signaling at the Golgi apparatus. *Elife*. 2022;11.
182. Radoux-Mergault A, Oberhauser L, Aureli S, Gervasio FL, Stoeber M. Subcellular location defines GPCR signal transduction. *Sci Adv*. 2023;9(16):eadf6059.
183. Devane WA, Dysarz FA, 3rd, Johnson MR, Melvin LS, Howlett AC. Determination and characterization of a cannabinoid receptor in rat brain. *Mol Pharmacol*. 1988;34(5):605-13.
184. Ashton JC, Zheng Y, Liu P, Darlington CL, Smith PF. Immunohistochemical characterisation and localisation of cannabinoid CB1 receptor protein in the rat vestibular nucleus complex and the effects of unilateral vestibular deafferentation. *Brain Res*. 2004;1021(2):264-71.
185. Piomelli D. The molecular logic of endocannabinoid signalling. *Nat Rev Neurosci*. 2003;4(11):873-84.
186. Howlett AC, Barth F, Bonner T, Cabral G, Casellas P, Devane W, et al. International Union of Pharmacology. XXVII. Classification of cannabinoid receptors. *Pharmacological reviews*. 2002;54(2):161-202.
187. Araque A, Castillo PE, Manzoni OJ, Tonini R. Synaptic functions of endocannabinoid signaling in health and disease. *Neuropharmacology*. 2017;124:13-24.
188. Eldeeb K, Leone-Kabler S, Howlett AC. CB1 cannabinoid receptor-mediated increases in cyclic AMP accumulation are correlated with reduced Gi/o function. *J Basic Clin Physiol Pharmacol*. 2016;27(3):311-22.
189. Calandra B, Portier M, Kerneis A, Delpech M, Carillon C, Le Fur G, et al. Dual intracellular signaling pathways mediated by the human cannabinoid CB1 receptor. *Eur J Pharmacol*. 1999;374(3):445-55.
190. Lauckner JE, Hille B, Mackie K. The cannabinoid agonist WIN55,212-2 increases intracellular calcium via CB1 receptor coupling to Gq/11 G proteins. *Proc Natl Acad Sci U S A*. 2005;102(52):19144-9.
191. Krishna Kumar K, Shalev-Benami M, Robertson MJ, Hu H, Banister SD, Hollingsworth SA, et al. Structure of a Signaling Cannabinoid Receptor 1-G Protein Complex. *Cell*. 2019;176(3):448-58 e12.
192. Khajehali E, Malone DT, Glass M, Sexton PM, Christopoulos A, Leach K. Biased Agonism and Biased Allosteric Modulation at the CB1 Cannabinoid Receptor. *Mol Pharmacol*. 2015;88(2):368-79.
193. Zhu X, Finlay DB, Glass M, Duffull SB. Evaluation of the profiles of CB(1) cannabinoid receptor signalling bias using joint kinetic modelling. *Br J Pharmacol*. 2020;177(15):3449-63.
194. Leo LM, Abood ME. CB1 Cannabinoid Receptor Signaling and Biased Signaling. *Molecules*. 2021;26(17).
195. Andersson H, D'Antona AM, Kendall DA, Von Heijne G, Chin CN. Membrane assembly of the cannabinoid receptor 1: impact of a long N-terminal tail. *Mol Pharmacol*. 2003;64(3):570-7.

196. Fay JF, Farrens DL. The membrane proximal region of the cannabinoid receptor CB1 N-terminus can allosterically modulate ligand affinity. *Biochemistry*. 2013;52(46):8286-94.
197. Ryberg E, Vu HK, Larsson N, Groblewski T, Hjorth S, Elebring T, et al. Identification and characterisation of a novel splice variant of the human CB1 receptor. *FEBS Lett*. 2005;579(1):259-64.
198. Shire D, Carillon C, Kaghad M, Calandra B, Rinaldi-Carmona M, Le Fur G, et al. An amino-terminal variant of the central cannabinoid receptor resulting from alternative splicing. *J Biol Chem*. 1995;270(8):3726-31.
199. Grimsey NL, Graham ES, Dragunow M, Glass M. Cannabinoid Receptor 1 trafficking and the role of the intracellular pool: implications for therapeutics. *Biochem Pharmacol*. 2010;80(7):1050-62.
200. Brailoiu GC, Oprea TI, Zhao P, Abood ME, Brailoiu E. Intracellular cannabinoid type 1 (CB1) receptors are activated by anandamide. *J Biol Chem*. 2011;286(33):29166-74.
201. Benard G, Massa F, Puente N, Lourenco J, Bellocchio L, Soria-Gomez E, et al. Mitochondrial CB(1) receptors regulate neuronal energy metabolism. *Nat Neurosci*. 2012;15(4):558-64.
202. Jimenez-Blasco D, Busquets-Garcia A, Hebert-Chatelain E, Serrat R, Vicente-Gutierrez C, Ioannidou C, et al. Glucose metabolism links astroglial mitochondria to cannabinoid effects. *Nature*. 2020;583(7817):603-8.
203. Grimsey NL, Goodfellow CE, Scotter EL, Dowie MJ, Glass M, Graham ES. Specific detection of CB1 receptors; cannabinoid CB1 receptor antibodies are not all created equal! *J Neurosci Methods*. 2008;171(1):78-86.
204. Steyaert J, Kobilka BK. Nanobody stabilization of G protein-coupled receptor conformational states. *Curr Opin Struct Biol*. 2011;21(4):567-72.
205. Irannejad R, Tomshine JC, Tomshine JR, Chevalier M, Mahoney JP, Steyaert J, et al. Conformational biosensors reveal GPCR signalling from endosomes. *Nature*. 2013;495(7442):534-8.
206. Ring AM, Manglik A, Kruse AC, Enos MD, Weis WI, Garcia KC, et al. Adrenaline-activated structure of beta2-adrenoceptor stabilized by an engineered nanobody. *Nature*. 2013;502(7472):575-9.
207. Hayashi T, Hamachi I. Traceless affinity labeling of endogenous proteins for functional analysis in living cells. *Acc Chem Res*. 2012;45(9):1460-9.
208. Arttamangkul S, Plazek A, Platt EJ, Jin H, Murray TF, Birdsong WT, et al. Visualizing endogenous opioid receptors in living neurons using ligand-directed chemistry. *Elife*. 2019;8.
209. Mach L, Omran A, Bouma J, Radetzki S, Sykes DA, Guba W, et al. Highly Selective Drug-Derived Fluorescent Probes for the Cannabinoid Receptor Type 1 (CB(1)R). *J Med Chem*. 2024;67(14):11841-67.
210. Varnai P, Thyagarajan B, Rohacs T, Balla T. Rapidly inducible changes in phosphatidylinositol 4,5-bisphosphate levels influence multiple regulatory functions of the lipid in intact living cells. *J Cell Biol*. 2006;175(3):377-82.
211. Horchani H, de Saint-Jean M, Barelli H, Antonny B. Interaction of the Spo20 membrane-sensor motif with phosphatidic acid and other anionic lipids, and influence of the membrane environment. *PLoS One*. 2014;9(11):e113484.
212. Thiele C, Papan C, Hoelper D, Kusserow K, Gaebler A, Schoene M, et al. Tracing fatty acid metabolism by click chemistry. *ACS Chem Biol*. 2012;7(12):2004-11.

213. Klymchenko AS, Kreder R. Fluorescent probes for lipid rafts: from model membranes to living cells. *Chem Biol.* 2014;21(1):97-113.
214. Wang TY, Silvius JR. Different sphingolipids show differential partitioning into sphingolipid/cholesterol-rich domains in lipid bilayers. *Biophys J.* 2000;79(3):1478-89.
215. Sezgin E, Levental I, Grzybek M, Schwarzmann G, Mueller V, Honigsmann A, et al. Partitioning, diffusion, and ligand binding of raft lipid analogs in model and cellular plasma membranes. *Biochim Biophys Acta.* 2012;1818(7):1777-84.
216. Neef AB, Schultz C. Selective fluorescence labeling of lipids in living cells. *Angew Chem Int Ed Engl.* 2009;48(8):1498-500.
217. Kuerschner L, Ejsing CS, Ekroos K, Shevchenko A, Anderson KI, Thiele C. Polyene-lipids: a new tool to image lipids. *Nat Methods.* 2005;2(1):39-45.
218. Ancajas CF, Ricks TJ, Best MD. Metabolic labeling of glycerophospholipids via clickable analogs derivatized at the lipid headgroup. *Chem Phys Lipids.* 2020;232:104971.
219. Wu H, Volponi JV, Oliver AE, Parikh AN, Simmons BA, Singh S. In vivo lipidomics using single-cell Raman spectroscopy. *Proc Natl Acad Sci U S A.* 2011;108(9):3809-14.
220. Wei L, Hu F, Shen Y, Chen Z, Yu Y, Lin CC, et al. Live-cell imaging of alkyne-tagged small biomolecules by stimulated Raman scattering. *Nat Methods.* 2014;11(4):410-2.
221. Fu D, Yu Y, Folick A, Currie E, Farese RV, Jr., Tsai TH, et al. In vivo metabolic fingerprinting of neutral lipids with hyperspectral stimulated Raman scattering microscopy. *J Am Chem Soc.* 2014;136(24):8820-8.
222. Haberkant P, Holthuis JC. Fat & fabulous: bifunctional lipids in the spotlight. *Biochim Biophys Acta.* 2014;1841(8):1022-30.
223. Haberkant P, Rajmakers R, Wildwater M, Sachsenheimer T, Brugger B, Maeda K, et al. In vivo profiling and visualization of cellular protein-lipid interactions using bifunctional fatty acids. *Angew Chem Int Ed Engl.* 2013;52(14):4033-8.
224. Best MD, Rowland MM, Bostic HE. Exploiting bioorthogonal chemistry to elucidate protein-lipid binding interactions and other biological roles of phospholipids. *Acc Chem Res.* 2011;44(9):686-98.
225. Bockelmann S, Mina JGM, Korneev S, Hassan DG, Muller D, Hilderink A, et al. A search for ceramide binding proteins using bifunctional lipid analogs yields CERT-related protein StarD7. *J Lipid Res.* 2018;59(3):515-30.
226. Mentel M, Laketa V, Subramanian D, Gillandt H, Schultz C. Photoactivatable and cell-membrane-permeable phosphatidylinositol 3,4,5-trisphosphate. *Angew Chem Int Ed Engl.* 2011;50(16):3811-4.
227. Laguerre A, Hauke S, Qiu J, Kelly MJ, Schultz C. Photorelease of 2-Arachidonoylglycerol in Live Cells. *J Am Chem Soc.* 2019;141(42):16544-7.
228. Hoglinger D, Nadler A, Haberkant P, Kirkpatrick J, Schifferer M, Stein F, et al. Trifunctional lipid probes for comprehensive studies of single lipid species in living cells. *Proc Natl Acad Sci U S A.* 2017;114(7):1566-71.
229. Muller R, Citir M, Hauke S, Schultz C. Synthesis and Cellular Labeling of Caged Phosphatidylinositol Derivatives. *Chemistry.* 2020;26(2):384-9.
230. Farley SE, Hashimoto R, Evangelista J, Stein F, Haberkant P, Kikuchi K, et al. Trifunctional fatty acid derivatives: the impact of diazirine placement. *Chem Commun (Camb).* 2024;60(52):6651-4.

231. Farley S, Stein F, Haberkant P, Tafesse FG, Schultz C. Trifunctional Sphinganine: A New Tool to Dissect Sphingolipid Function. *ACS Chem Biol.* 2024;19(2):336-47.
232. Thomas A, Upadhyaya K, Bejan D, Adoff H, Cohen M, Schultz C. A Genetically Encoded Sensor for Real-Time Monitoring of Poly-ADP-Ribosylation Dynamics In Vitro and in Cells. *ACS Sens.* 2024;9(10):5246-52.
233. Pascal JM. The comings and goings of PARP-1 in response to DNA damage. *DNA Repair (Amst).* 2018;71:177-82.
234. Langelier MF, Planck JL, Roy S, Pascal JM. Structural basis for DNA damage-dependent poly(ADP-ribosylation) by human PARP-1. *Science.* 2012;336(6082):728-32.
235. Alvarez-Gonzalez R, Jacobson MK. Characterization of polymers of adenosine diphosphate ribose generated in vitro and in vivo. *Biochemistry.* 1987;26(11):3218-24.
236. Leung AKL. Poly(ADP-ribose): A Dynamic Trigger for Biomolecular Condensate Formation. *Trends Cell Biol.* 2020;30(5):370-83.
237. Abplanalp J, Leutert M, Frugier E, Nowak K, Feurer R, Kato J, et al. Proteomic analyses identify ARH3 as a serine mono-ADP-ribosylhydrolase. *Nat Commun.* 2017;8(1):2055.
238. Slade D, Dunstan MS, Barkauskaite E, Weston R, Lafite P, Dixon N, et al. The structure and catalytic mechanism of a poly(ADP-ribose) glycohydrolase. *Nature.* 2011;477(7366):616-20.
239. Serebrovskaya EO, Podvalnaya NM, Dudenkova VV, Efremova AS, Gurskaya NG, Gorbachev DA, et al. Genetically Encoded Fluorescent Sensor for Poly-ADP-Ribose. *Int J Mol Sci.* 2020;21(14).
240. Krastev DB, Pettitt SJ, Campbell J, Song F, Tanos BE, Stoyanov SS, et al. Coupling bimolecular PARylation biosensors with genetic screens to identify PARylation targets. *Nat Commun.* 2018;9(1):2016.
241. Bejan DS, Sundalam S, Jin H, Morgan RK, Kirby IT, Siordia IR, et al. Structure-guided design and characterization of a clickable, covalent PARP16 inhibitor. *Chem Sci.* 2022;13(46):13898-906.
242. Schindelin J, Arganda-Carreras I, Frise E, Kaynig V, Longair M, Pietzsch T, et al. Fiji: an open-source platform for biological-image analysis. *Nat Methods.* 2012;9(7):676-82.
243. Wang Z, Michaud GA, Cheng Z, Zhang Y, Hinds TR, Fan E, et al. Recognition of the iso-ADP-ribose moiety in poly(ADP-ribose) by WWE domains suggests a general mechanism for poly(ADP-ribosylation)-dependent ubiquitination. *Genes Dev.* 2012;26(3):235-40.
244. Zhang Y, Liu S, Mickanin C, Feng Y, Charlat O, Michaud GA, et al. RNF146 is a poly(ADP-ribose)-directed E3 ligase that regulates axin degradation and Wnt signalling. *Nat Cell Biol.* 2011;13(5):623-9.
245. Kistemaker HA, Nardoza AP, Overkleeft HS, van der Marel GA, Ladurner AG, Filippov DV. Synthesis and Macrodomein Binding of Mono-ADP-Ribosylated Peptides. *Angew Chem Int Ed Engl.* 2016;55(36):10634-8.
246. Lambrecht MJ, Brichacek M, Barkauskaite E, Ariza A, Ahel I, Hergenrother PJ. Synthesis of dimeric ADP-ribose and its structure with human poly(ADP-ribose) glycohydrolase. *J Am Chem Soc.* 2015;137(10):3558-64.
247. Palazzo L, Thomas B, Jemth AS, Colby T, Leidecker O, Feijs KL, et al. Processing of protein ADP-ribosylation by Nudix hydrolases. *Biochem J.* 2015;468(2):293-301.

248. Wang L, Yang C, Xie C, Jiang J, Gao M, Fu L, et al. Pharmacologic characterization of fluzoparib, a novel poly(ADP-ribose) polymerase inhibitor undergoing clinical trials. *Cancer Sci.* 2019;110(3):1064-75.
249. Johannes JW, Balazs A, Barratt D, Bista M, Chuba MD, Cosulich S, et al. Discovery of 5-4-[(7-Ethyl-6-oxo-5,6-dihydro-1,5-naphthyridin-3-yl)methyl]piperazin-1-yl-N-methylpyridine-2-carboxamide (AZD5305): A PARP1-DNA Trapper with High Selectivity for PARP1 over PARP2 and Other PARPs. *J Med Chem.* 2021;64(19):14498-512.
250. Thorsell AG, Ekblad T, Karlberg T, Low M, Pinto AF, Tresaugues L, et al. Structural Basis for Potency and Promiscuity in Poly(ADP-ribose) Polymerase (PARP) and Tankyrase Inhibitors. *J Med Chem.* 2017;60(4):1262-71.
251. Buntz A, Wallrodt S, Gwosch E, Schmalz M, Beneke S, Ferrando-May E, et al. Real-Time Cellular Imaging of Protein Poly(ADP-ribos)ylation. *Angew Chem Int Ed Engl.* 2016;55(37):11256-60.
252. Kruger A, Burkle A, Hauser K, Mangerich A. Real-time monitoring of PARP1-dependent PARylation by ATR-FTIR spectroscopy. *Nat Commun.* 2020;11(1):2174.
253. Hurst V, Gasser SM. The study of protein recruitment to laser-induced DNA lesions can be distorted by photoconversion of the DNA binding dye Hoechst. *F1000Res.* 2019;8:104.
254. Kukulj E, Kaufmann T, Dick AE, Zeillinger R, Gerlich DW, Slade D. PARP inhibition causes premature loss of cohesion in cancer cells. *Oncotarget.* 2017;8(61):103931-51.
255. Forst AH, Karlberg T, Herzog N, Thorsell AG, Gross A, Feijs KL, et al. Recognition of mono-ADP-ribosylated ARTD10 substrates by ARTD8 macrodomains. *Structure.* 2013;21(3):462-75.
256. Rack JGM, Zorzini V, Zhu Z, Schuller M, Ahel D, Ahel I. Viral macrodomains: a structural and evolutionary assessment of the pharmacological potential. *Open Biol.* 2020;10(11):200237.
257. Dukic N, Stromland O, Elsborg JD, Munnur D, Zhu K, Schuller M, et al. PARP14 is a PARP with both ADP-ribosyl transferase and hydrolase activities. *Sci Adv.* 2023;9(37):eadi2687.
258. Hendriks IA, Larsen SC, Nielsen ML. An Advanced Strategy for Comprehensive Profiling of ADP-ribosylation Sites Using Mass Spectrometry-based Proteomics. *Mol Cell Proteomics.* 2019;18(5):1010-26.
259. Alesmasova EE, Lavrik OI. Poly(ADP-ribosylation) by PARP1: reaction mechanism and regulatory proteins. *Nucleic Acids Res.* 2019;47(8):3811-27.
260. Marsischky GT, Wilson BA, Collier RJ. Role of glutamic acid 988 of human poly-ADP-ribose polymerase in polymer formation. Evidence for active site similarities to the ADP-ribosylating toxins. *J Biol Chem.* 1995;270(7):3247-54.
261. Langelier MF, Billur R, Sverzhinsky A, Black BE, Pascal JM. HPF1 dynamically controls the PARP1/2 balance between initiating and elongating ADP-ribose modifications. *Nat Commun.* 2021;12(1):6675.
262. Prokhorova E, Zobel F, Smith R, Zentout S, Gibbs-Seymour I, Schutzenhofer K, et al. Serine-linked PARP1 auto-modification controls PARP inhibitor response. *Nat Commun.* 2021;12(1):4055.

263. Deeksha W, Abhishek S, Rajakumara E. PAR recognition by PARP1 regulates DNA-dependent activities and independently stimulates catalytic activity of PARP1. *FEBS J.* 2023;290(21):5098-113.
264. Ali AAE, Timinszky G, Arribas-Bosacoma R, Kozlowski M, Hassa PO, Hassler M, et al. The zinc-finger domains of PARP1 cooperate to recognize DNA strand breaks. *Nat Struct Mol Biol.* 2012;19(7):685-92.
265. Eustermann S, Wu WF, Langelier MF, Yang JC, Easton LE, Riccio AA, et al. Structural Basis of Detection and Signaling of DNA Single-Strand Breaks by Human PARP-1. *Mol Cell.* 2015;60(5):742-54.
266. Rouleau-Turcotte E, Krastev DB, Pettitt SJ, Lord CJ, Pascal JM. Captured snapshots of PARP1 in the active state reveal the mechanics of PARP1 allostery. *Mol Cell.* 2022;82(16):2939-51 e5.
267. Helleday T. The underlying mechanism for the PARP and BRCA synthetic lethality: clearing up the misunderstandings. *Mol Oncol.* 2011;5(4):387-93.
268. Lord CJ, Ashworth A. PARP inhibitors: Synthetic lethality in the clinic. *Science.* 2017;355(6330):1152-8.
269. Rudolph J, Roberts G, Luger K. Histone Parylation factor 1 contributes to the inhibition of PARP1 by cancer drugs. *Nat Commun.* 2021;12(1):736.
270. Stojanovic P, Luger K, Rudolph J. Slow Dissociation from the PARP1-HPF1 Complex Drives Inhibitor Potency. *Biochemistry.* 2023;62(16):2382-90.
271. Gopal AA, Fernandez B, Delano J, Weissleder R, Dubach JM. PARP trapping is governed by the PARP inhibitor dissociation rate constant. *Cell Chem Biol.* 2024.
272. Sriram K, Insel PA. G Protein-Coupled Receptors as Targets for Approved Drugs: How Many Targets and How Many Drugs? *Mol Pharmacol.* 2018;93(4):251-8.
273. Maudsley S, Martin B, Luttrell LM. The origins of diversity and specificity in g protein-coupled receptor signaling. *J Pharmacol Exp Ther.* 2005;314(2):485-94.
274. Smith JS, Lefkowitz RJ, Rajagopal S. Biased signalling: from simple switches to allosteric microprocessors. *Nat Rev Drug Discov.* 2018;17(4):243-60.
275. Fernandez TJ, De Maria M, Lobingier BT. A cellular perspective of bias at G protein-coupled receptors. *Protein Sci.* 2020;29(6):1345-54.
276. Lane JR, May LT, Parton RG, Sexton PM, Christopoulos A. A kinetic view of GPCR allostery and biased agonism. *Nat Chem Biol.* 2017;13(9):929-37.
277. Jong YJ, Sergin I, Purgert CA, O'Malley KL. Location-dependent signaling of the group 1 metabotropic glutamate receptor mGlu5. *Mol Pharmacol.* 2014;86(6):774-85.
278. Irannejad R, Pessino V, Mika D, Huang B, Wedegaertner PB, Conti M, et al. Functional selectivity of GPCR-directed drug action through location bias. *Nat Chem Biol.* 2017;13(7):799-806.
279. Ibsen MS, Connor M, Glass M. Cannabinoid CB(1) and CB(2) Receptor Signaling and Bias. *Cannabis Cannabinoid Res.* 2017;2(1):48-60.
280. Diez-Alarcia R, Ibarra-Lecue I, Lopez-Cardona AP, Meana J, Gutierrez-Adan A, Callado LF, et al. Biased Agonism of Three Different Cannabinoid Receptor Agonists in Mouse Brain Cortex. *Front Pharmacol.* 2016;7:415.
281. Busquets-Garcia A, Bains J, Marsicano G. CB(1) Receptor Signaling in the Brain: Extracting Specificity from Ubiquity. *Neuropsychopharmacology.* 2018;43(1):4-20.
282. Freund TF, Katona I, Piomelli D. Role of endogenous cannabinoids in synaptic signaling. *Physiol Rev.* 2003;83(3):1017-66.

283. Wittmann G, Deli L, Kallo I, Hrabovszky E, Watanabe M, Liposits Z, et al. Distribution of type 1 cannabinoid receptor (CB1)-immunoreactive axons in the mouse hypothalamus. *J Comp Neurol*. 2007;503(2):270-9.
284. Marsicano G, Kuner R. Anatomical Distribution of Receptors, Ligands and Enzymes in the Brain and in the Spinal Cord: Circuitries and Neurochemistry. In: Köfalvi A, editor. *Cannabinoids and the Brain*. Boston, MA: Springer US; 2008. p. 161-201.
285. Steindel F, Lerner R, Haring M, Ruehle S, Marsicano G, Lutz B, et al. Neuron-type specific cannabinoid-mediated G protein signalling in mouse hippocampus. *J Neurochem*. 2013;124(6):795-807.
286. Finlay DB, Cawston EE, Grimsey NL, Hunter MR, Korde A, Vemuri VK, et al. Galpha(s) signalling of the CB(1) receptor and the influence of receptor number. *Br J Pharmacol*. 2017;174(15):2545-62.
287. Horvath VB, Soltesz-Katona E, Wisniewski E, Rajki A, Halasz E, Enyedi B, et al. Optimization of the Heterologous Expression of the Cannabinoid Type-1 (CB(1)) Receptor. *Front Endocrinol (Lausanne)*. 2021;12:740913.
288. Hebert-Chatelain E, Desprez T, Serrat R, Bellocchio L, Soria-Gomez E, Busquets-Garcia A, et al. A cannabinoid link between mitochondria and memory. *Nature*. 2016;539(7630):555-9.
289. Guan XM, Kobilka TS, Kobilka BK. Enhancement of membrane insertion and function in a type IIIb membrane protein following introduction of a cleavable signal peptide. *J Biol Chem*. 1992;267(31):21995-8.
290. Kato Y. Translational Control using an Expanded Genetic Code. *Int J Mol Sci*. 2019;20(4).
291. DiPilato LM, Zhang J. The role of membrane microdomains in shaping beta2-adrenergic receptor-mediated cAMP dynamics. *Mol Biosyst*. 2009;5(8):832-7.
292. Qin JY, Zhang L, Clift KL, Hular I, Xiang AP, Ren BZ, et al. Systematic comparison of constitutive promoters and the doxycycline-inducible promoter. *PLoS One*. 2010;5(5):e10611.
293. Keith DE, Murray SR, Zaki PA, Chu PC, Lissin DV, Kang L, et al. Morphine activates opioid receptors without causing their rapid internalization. *J Biol Chem*. 1996;271(32):19021-4.
294. von Zastrow M, Kobilka BK. Ligand-regulated internalization and recycling of human beta 2-adrenergic receptors between the plasma membrane and endosomes containing transferrin receptors. *J Biol Chem*. 1992;267(5):3530-8.
295. Novy B, Adoff H, Maria MD, Kampmann M, Tsvetanova NG, Zastrow Mv, et al. A genome-wide CRISPR interference screen using an engineered trafficking biosensor reveals a role for RME-8 in opioid receptor regulation. *bioRxiv*. 2022:2022.10.11.511646.
296. Klarenbeek J, Goedhart J, van Batenburg A, Groenewald D, Jalink K. Fourth-generation epac-based FRET sensors for cAMP feature exceptional brightness, photostability and dynamic range: characterization of dedicated sensors for FLIM, for ratiometry and with high affinity. *PLoS One*. 2015;10(4):e0122513.
297. Tsvetanova NG, von Zastrow M. Spatial encoding of cyclic AMP signaling specificity by GPCR endocytosis. *Nat Chem Biol*. 2014;10(12):1061-5.
298. Ramil CP, Dong M, An P, Lewandowski TM, Yu Z, Miller LJ, et al. Spirohexene-Tetrazine Ligation Enables Bioorthogonal Labeling of Class B G Protein-Coupled Receptors in Live Cells. *J Am Chem Soc*. 2017;139(38):13376-86.

299. Erb L, Weisman GA. Coupling of P2Y receptors to G proteins and other signaling pathways. *Wiley Interdiscip Rev Membr Transp Signal*. 2012;1(6):789-803.
300. Li C, Jones PM, Persaud SJ. Cannabinoid receptors are coupled to stimulation of insulin secretion from mouse MIN6 beta-cells. *Cell Physiol Biochem*. 2010;26(2):187-96.
301. Daniel H, Crepel F. Control of Ca(2+) influx by cannabinoid and metabotropic glutamate receptors in rat cerebellar cortex requires K(+) channels. *J Physiol*. 2001;537(Pt 3):793-800.
302. Dudok B, Barna L, Ledri M, Szabo SI, Szabadits E, Pinter B, et al. Cell-specific STORM super-resolution imaging reveals nanoscale organization of cannabinoid signaling. *Nat Neurosci*. 2015;18(1):75-86.
303. Katona I, Sperlagh B, Sik A, Kafalvi A, Vizi ES, Mackie K, et al. Presynaptically located CB1 cannabinoid receptors regulate GABA release from axon terminals of specific hippocampal interneurons. *J Neurosci*. 1999;19(11):4544-58.
304. Leterrier C, Bonnard D, Carrel D, Rossier J, Lenkei Z. Constitutive endocytic cycle of the CB1 cannabinoid receptor. *J Biol Chem*. 2004;279(34):36013-21.
305. Martini L, Waldhoer M, Pusch M, Kharazia V, Fong J, Lee JH, et al. Ligand-induced down-regulation of the cannabinoid 1 receptor is mediated by the G-protein-coupled receptor-associated sorting protein GASP1. *FASEB J*. 2007;21(3):802-11.
306. Rinaldi-Carmona M, Le Duigou A, Oustric D, Barth F, Bouaboula M, Carayon P, et al. Modulation of CB1 cannabinoid receptor functions after a long-term exposure to agonist or inverse agonist in the Chinese hamster ovary cell expression system. *J Pharmacol Exp Ther*. 1998;287(3):1038-47.
307. Wente W, Stroth T, Beaudet A, Richter D, Kreienkamp HJ. Interactions with PDZ domain proteins PIST/GOPC and PDZK1 regulate intracellular sorting of the somatostatin receptor subtype 5. *J Biol Chem*. 2005;280(37):32419-25.
308. Koliwer J, Park M, Bauch C, von Zastrow M, Kreienkamp HJ. The golgi-associated PDZ domain protein PIST/GOPC stabilizes the beta1-adrenergic receptor in intracellular compartments after internalization. *J Biol Chem*. 2015;290(10):6120-9.
309. Strothman MJ, Maeda S, Hilger D, Masureel M, Du Y, Kobilka BK. Local membrane charge regulates beta(2) adrenergic receptor coupling to G(i3). *Nat Commun*. 2019;10(1):2234.
310. Hernandez EH, Manglik A, Irannejad R. Anionic phospholipids determine G protein coupling selectivity at distinct subcellular membrane compartments. *bioRxiv*. 2023:2023.08.31.555797.
311. Adham N, Ellerbrock B, Hartig P, Weinshank RL, Branchek T. Receptor reserve masks partial agonist activity of drugs in a cloned rat 5-hydroxytryptamine1B receptor expression system. *Mol Pharmacol*. 1993;43(3):427-33.
312. Yen YC, Li Y, Chen CL, Klose T, Watts VJ, Dessauer CW, et al. Structure of adenylyl cyclase 5 in complex with Gbetagamma offers insights into ADCY5-related dyskinesia. *Nat Struct Mol Biol*. 2024.
313. Nehme R, Carpenter B, Singhal A, Strega A, Edwards PC, White CF, et al. Mini-G proteins: Novel tools for studying GPCRs in their active conformation. *PLoS One*. 2017;12(4):e0175642.
314. Steiert F, Schultz P, Hofinger S, Muller TD, Schwille P, Weidemann T. Insights into receptor structure and dynamics at the surface of living cells. *Nat Commun*. 2023;14(1):1596.

315. Wan Q, Okashah N, Inoue A, Nehme R, Carpenter B, Tate CG, et al. Mini G protein probes for active G protein-coupled receptors (GPCRs) in live cells. *J Biol Chem*. 2018;293(19):7466-73.
316. Liccardo F, Morstein J, Lin TY, Pampel J, Shokat KM, Irannejad R. Selective activation of intracellular beta1AR using a spatially restricted antagonist. *bioRxiv*. 2023.
317. Elsasser SJ, Ernst RJ, Walker OS, Chin JW. Genetic code expansion in stable cell lines enables encoded chromatin modification. *Nat Methods*. 2016;13(2):158-64.
318. Meineke B, Heimgartner J, Caridha R, Block MF, Kimler KJ, Pires MF, et al. Dual stop codon suppression in mammalian cells with genomically integrated genetic code expansion machinery. *Cell Rep Methods*. 2023;3(11):100626.
319. Vance JE. Phospholipid synthesis and transport in mammalian cells. *Traffic*. 2015;16(1):1-18.
320. Bleijerveld OB, Brouwers J, Vaandrager AB, Helms JB, Houweling M. The CDP-ethanolamine pathway and phosphatidylserine decarboxylation generate different phosphatidylethanolamine molecular species. *J Biol Chem*. 2007;282(39):28362-72.
321. Shiao YJ, Lupo G, Vance JE. Evidence that phosphatidylserine is imported into mitochondria via a mitochondria-associated membrane and that the majority of mitochondrial phosphatidylethanolamine is derived from decarboxylation of phosphatidylserine. *J Biol Chem*. 1995;270(19):11190-8.
322. Fullerton MD, Hakimuddin F, Bakovic M. Developmental and metabolic effects of disruption of the mouse CTP:phosphoethanolamine cytidyltransferase gene (*Pcvt2*). *Mol Cell Biol*. 2007;27(9):3327-36.
323. Steenbergen R, Nanowski TS, Beigneux A, Kulinski A, Young SG, Vance JE. Disruption of the phosphatidylserine decarboxylase gene in mice causes embryonic lethality and mitochondrial defects. *J Biol Chem*. 2005;280(48):40032-40.
324. Tasseva G, Bai HD, Davidescu M, Haromy A, Michelakis E, Vance JE. Phosphatidylethanolamine deficiency in Mammalian mitochondria impairs oxidative phosphorylation and alters mitochondrial morphology. *J Biol Chem*. 2013;288(6):4158-73.
325. Horvath SE, Daum G. Lipids of mitochondria. *Prog Lipid Res*. 2013;52(4):590-614.
326. Lahiri S, Chao JT, Tavassoli S, Wong AK, Choudhary V, Young BP, et al. A conserved endoplasmic reticulum membrane protein complex (EMC) facilitates phospholipid transfer from the ER to mitochondria. *PLoS Biol*. 2014;12(10):e1001969.
327. Vance JE. Phospholipid synthesis in a membrane fraction associated with mitochondria. *J Biol Chem*. 1990;265(13):7248-56.
328. van den Brink-van der Laan E, Killian JA, de Kruijff B. Nonbilayer lipids affect peripheral and integral membrane proteins via changes in the lateral pressure profile. *Biochim Biophys Acta*. 2004;1666(1-2):275-88.
329. Bottinger L, Horvath SE, Kleinschroth T, Hunte C, Daum G, Pfanner N, et al. Phosphatidylethanolamine and cardiolipin differentially affect the stability of mitochondrial respiratory chain supercomplexes. *J Mol Biol*. 2012;423(5):677-86.
330. Emoto K, Umeda M. An essential role for a membrane lipid in cytokinesis. Regulation of contractile ring disassembly by redistribution of phosphatidylethanolamine. *J Cell Biol*. 2000;149(6):1215-24.
331. Nair U, Yen WL, Mari M, Cao Y, Xie Z, Baba M, et al. A role for Atg8-PE deconjugation in autophagosome biogenesis. *Autophagy*. 2012;8(5):780-93.

332. Mueller R, Kojic A, Citir M, Schultz C. Synthesis and cellular labeling of multifunctional phosphatidylinositol bis- and trisphosphate derivatives. *Angew Chem*, in revision.
333. Bolte S, Cordelieres FP. A guided tour into subcellular colocalization analysis in light microscopy. *J Microsc.* 2006;224(Pt 3):213-32.
334. Franken H, Mathieson T, Childs D, Sweetman GM, Werner T, Togel I, et al. Thermal proteome profiling for unbiased identification of direct and indirect drug targets using multiplexed quantitative mass spectrometry. *Nat Protoc.* 2015;10(10):1567-93.
335. Savitski MM, Wilhelm M, Hahne H, Kuster B, Bantscheff M. A Scalable Approach for Protein False Discovery Rate Estimation in Large Proteomic Data Sets. *Mol Cell Proteomics.* 2015;14(9):2394-404.
336. Huber W, von Heydebreck A, Sultmann H, Poustka A, Vingron M. Variance stabilization applied to microarray data calibration and to the quantification of differential expression. *Bioinformatics.* 2002;18 Suppl 1:S96-104.
337. Muller R, Kojic A, Citir M, Schultz C. Synthesis and Cellular Labeling of Multifunctional Phosphatidylinositol Bis- and Trisphosphate Derivatives. *Angew Chem Int Ed Engl.* 2021;60(36):19759-65.
338. Subramanian D, Laketa V, Muller R, Tischer C, Zarbakhsh S, Pepperkok R, et al. Activation of membrane-permeant caged PtdIns(3)P induces endosomal fusion in cells. *Nat Chem Biol.* 2010;6(5):324-6.
339. Walter AM, Muller R, Tawfik B, Wierda KD, Pinheiro PS, Nadler A, et al. Phosphatidylinositol 4,5-bisphosphate optical uncaging potentiates exocytosis. *Elife.* 2017;6.
340. Citir M, Muller R, Hauke S, Traynor-Kaplan A, Schultz C. Monitoring the cellular metabolism of a membrane-permeant photo-caged phosphatidylinositol 3,4,5-trisphosphate derivative. *Chem Phys Lipids.* 2021;241:105124.
341. Athenstaedt K, Daum G. Phosphatidic acid, a key intermediate in lipid metabolism. *Eur J Biochem.* 1999;266(1):1-16.
342. Rebane AA, Ziltener P, LaMonica LC, Bauer AH, Zheng H, Lopez-Montero I, et al. Liquid-liquid phase separation of the Golgi matrix protein GM130. *FEBS Lett.* 2020;594(7):1132-44.
343. Jahn H, Bartos L, Dearden GI, Dittman JS, Holthuis JCM, Vacha R, et al. Phospholipids are imported into mitochondria by VDAC, a dimeric beta barrel scramblase. *Nat Commun.* 2023;14(1):8115.
344. Shin HW, Takatsu H. Substrates of P4-ATPases: beyond aminophospholipids (phosphatidylserine and phosphatidylethanolamine). *FASEB J.* 2019;33(3):3087-96.
345. Shinzawa-Itoh K, Aoyama H, Muramoto K, Terada H, Kurauchi T, Tadehara Y, et al. Structures and physiological roles of 13 integral lipids of bovine heart cytochrome c oxidase. *EMBO J.* 2007;26(6):1713-25.
346. Hao J, Wang T, Cao C, Li X, Li H, Gao H, et al. LPCAT3 exacerbates early brain injury and ferroptosis after subarachnoid hemorrhage in rats. *Brain Res.* 2024;1832:148864.
347. Feng H, Stockwell BR. Unsolved mysteries: How does lipid peroxidation cause ferroptosis? *PLoS Biol.* 2018;16(5):e2006203.
348. Bernier I, Tresca JP, Jolles P. Ligand-binding studies with a 23 kDa protein purified from bovine brain cytosol. *Biochim Biophys Acta.* 1986;871(1):19-23.

349. Ye Y, Tyndall ER, Bui V, Bewley MC, Wang G, Hong X, et al. Multifaceted membrane interactions of human Atg3 promote LC3-phosphatidylethanolamine conjugation during autophagy. *Nat Commun.* 2023;14(1):5503.
350. Cui Z, Vance JE, Chen MH, Voelker DR, Vance DE. Cloning and expression of a novel phosphatidylethanolamine N-methyltransferase. A specific biochemical and cytological marker for a unique membrane fraction in rat liver. *J Biol Chem.* 1993;268(22):16655-63.
351. Chan EY, McQuibban GA. Phosphatidylserine decarboxylase 1 (Psd1) promotes mitochondrial fusion by regulating the biophysical properties of the mitochondrial membrane and alternative topogenesis of mitochondrial genome maintenance protein 1 (Mgm1). *J Biol Chem.* 2012;287(48):40131-9.
352. Yan B, Ai Y, Sun Q, Ma Y, Cao Y, Wang J, et al. Membrane Damage during Ferroptosis Is Caused by Oxidation of Phospholipids Catalyzed by the Oxidoreductases POR and CYB5R1. *Mol Cell.* 2021;81(2):355-69 e10.
353. Kagan VE, Mao G, Qu F, Angeli JP, Doll S, Croix CS, et al. Oxidized arachidonic and adrenic PEs navigate cells to ferroptosis. *Nat Chem Biol.* 2017;13(1):81-90.
354. Freitas FP, Alborzinia H, Dos Santos AF, Nepachalovich P, Pedrera L, Zilka O, et al. 7-Dehydrocholesterol is an endogenous suppressor of ferroptosis. *Nature.* 2024;626(7998):401-10.
355. Gallegos AM, Atshaves BP, Storey SM, Starodub O, Petrescu AD, Huang H, et al. Gene structure, intracellular localization, and functional roles of sterol carrier protein-2. *Prog Lipid Res.* 2001;40(6):498-563.
356. Peretti D, Dahan N, Shimoni E, Hirschberg K, Lev S. Coordinated lipid transfer between the endoplasmic reticulum and the Golgi complex requires the VAP proteins and is essential for Golgi-mediated transport. *Mol Biol Cell.* 2008;19(9):3871-84.
357. Kim YJ, Guzman-Hernandez ML, Wisniewski E, Balla T. Phosphatidylinositol-Phosphatidic Acid Exchange by Nir2 at ER-PM Contact Sites Maintains Phosphoinositide Signaling Competence. *Dev Cell.* 2015;33(5):549-61.
358. Shulga YV, Topham MK, Epanand RM. Regulation and functions of diacylglycerol kinases. *Chem Rev.* 2011;111(10):6186-208.
359. Selvy PE, Lavieri RR, Lindsley CW, Brown HA. Phospholipase D: enzymology, functionality, and chemical modulation. *Chem Rev.* 2011;111(10):6064-119.
360. Reinisch KM, Prinz WA. Mechanisms of nonvesicular lipid transport. *J Cell Biol.* 2021;220(3).
361. Wong LH, Gatta AT, Levine TP. Lipid transfer proteins: the lipid commute via shuttles, bridges and tubes. *Nat Rev Mol Cell Biol.* 2019;20(2):85-101.
362. Li P, Lees JA, Lusk CP, Reinisch KM. Cryo-EM reconstruction of a VPS13 fragment reveals a long groove to channel lipids between membranes. *J Cell Biol.* 2020;219(5).
363. Kainu V, Hermansson M, Hanninen S, Hokynar K, Somerharju P. Import of phosphatidylserine to and export of phosphatidylethanolamine molecular species from mitochondria. *Biochim Biophys Acta.* 2013;1831(2):429-37.
364. Raturi A, Simmen T. Where the endoplasmic reticulum and the mitochondrion tie the knot: the mitochondria-associated membrane (MAM). *Biochim Biophys Acta.* 2013;1833(1):213-24.
365. Ventura R, Martinez-Ruiz I, Hernandez-Alvarez MI. Phospholipid Membrane Transport and Associated Diseases. *Biomedicines.* 2022;10(5).

366. Belgareh-Touze N, Cavellini L, Cohen MM. Ubiquitination of ERMES components by the E3 ligase Rsp5 is involved in mitophagy. *Autophagy*. 2017;13(1):114-32.
367. Yang M, Li C, Yang S, Xiao Y, Xiong X, Chen W, et al. Mitochondria-Associated ER Membranes - The Origin Site of Autophagy. *Front Cell Dev Biol*. 2020;8:595.
368. Ichimura Y, Kirisako T, Takao T, Satomi Y, Shimonishi Y, Ishihara N, et al. A ubiquitin-like system mediates protein lipidation. *Nature*. 2000;408(6811):488-92.
369. Rockenfeller P, Koska M, Pietrocola F, Minois N, Knittelfelder O, Sica V, et al. Phosphatidylethanolamine positively regulates autophagy and longevity. *Cell Death Differ*. 2015;22(3):499-508.
370. Fadeel B, Xue D. The ins and outs of phospholipid asymmetry in the plasma membrane: roles in health and disease. *Crit Rev Biochem Mol Biol*. 2009;44(5):264-77.
371. Ruprecht JJ, Kunji ERS. The SLC25 Mitochondrial Carrier Family: Structure and Mechanism. *Trends Biochem Sci*. 2020;45(3):244-58.
372. Janer A, Prudent J, Paupe V, Fahiminiya S, Majewski J, Sgarioto N, et al. SLC25A46 is required for mitochondrial lipid homeostasis and cristae maintenance and is responsible for Leigh syndrome. *EMBO Mol Med*. 2016;8(9):1019-38.
373. Gallegos AM, Schoer JK, Starodub O, Kier AB, Billheimer JT, Schroeder F. A potential role for sterol carrier protein-2 in cholesterol transfer to mitochondria. *Chem Phys Lipids*. 2000;105(1):9-29.
374. Vila A, Levchenko VV, Korytowski W, Girotti AW. Sterol carrier protein-2-facilitated intermembrane transfer of cholesterol- and phospholipid-derived hydroperoxides. *Biochemistry*. 2004;43(39):12592-605.
375. Yang WS, Stockwell BR. Ferroptosis: Death by Lipid Peroxidation. *Trends Cell Biol*. 2016;26(3):165-76.
376. Doll S, Proneth B, Tyurina YY, Panzilius E, Kobayashi S, Ingold I, et al. ACSL4 dictates ferroptosis sensitivity by shaping cellular lipid composition. *Nat Chem Biol*. 2017;13(1):91-8.
377. Dai T, Xue X, Huang J, Yang Z, Xu P, Wang M, et al. SCP2 mediates the transport of lipid hydroperoxides to mitochondria in chondrocyte ferroptosis. *Cell Death Discov*. 2023;9(1):234.
378. Calzada E, Avery E, Sam PN, Modak A, Wang C, McCaffery JM, et al. Phosphatidylethanolamine made in the inner mitochondrial membrane is essential for yeast cytochrome bc(1) complex function. *Nat Commun*. 2019;10(1):1432.
379. Gallion LA, Wang Y, Massaro A, Yao M, Petersen BV, Zhang Q, et al. "Fix and Click" for Assay of Sphingolipid Signaling in Single Primary Human Intestinal Epithelial Cells. *Anal Chem*. 2022;94(3):1594-600.
380. Dixon SJ, Lemberg KM, Lamprecht MR, Skouta R, Zaitsev EM, Gleason CE, et al. Ferroptosis: an iron-dependent form of nonapoptotic cell death. *Cell*. 2012;149(5):1060-72.
381. Yang WS, Stockwell BR. Synthetic lethal screening identifies compounds activating iron-dependent, nonapoptotic cell death in oncogenic-RAS-harboring cancer cells. *Chem Biol*. 2008;15(3):234-45.
382. D'Souza K, Kim YJ, Balla T, Epand RM. Distinct properties of the two isoforms of CDP-diacylglycerol synthase. *Biochemistry*. 2014;53(47):7358-67.